Development of Quantitative Myocardial Tissue Characterization

by

Kelvin Chow

A thesis submitted in partial fulfillment of the requirements for the degree of

Doctor of Philosophy

Medical Sciences – Biomedical Engineering

University of Alberta

Abstract

Diffuse myocardial fibrosis and other remodeling of the extracellular volume (ECV) in the heart are common pathological features in a variety of cardiac diseases. These microscopic alterations can be imaged non-invasively via changes in the spin-lattice (T_1) relaxation time in magnetic resonance imaging (MRI). A growing body of literature supports the hypothesis that myocardial T_1 and derived ECV measurements are correlated with fibrosis and disease severity in a variety of cardiomyopathies and that ECV may be an independent predictor of mortality. ECV is a promising biomarker for assessing cardiac disease and could potentially be a therapeutic target for medical interventions aimed at controlling fibrosis progression.

The widely used "MOLLI" T_1 imaging technique is known to have numerous systematic errors that increase measurement variability and may lead to erroneous interpretations of fibrosis. A thorough understanding of these confounding effects is essential to support translation of ECV measurements to routine clinical practice. The goal of this thesis was to gain analytic insight into factors affecting MOLLI T_1 values and the development and optimization of a new T_1 imaging technique which is robust against these potential confounders.

A simple analytical model of the MOLLI technique was developed, describing the apparent spin-lattice relaxation rate ($1/T_1^*$) as the time-weighted average (TWA) of two distinctive relaxation rates. The TWA model was validated through simulations and experimental data and the model characterizes the relationship between the measured MOLLI T_1^* and the true T_1 as a function of several confounding factors. In contrast to existing literature that phenomenologically describes many of these confounders in isolation, the TWA model provides a unified theory for the effect of these factors as well as their interaction.

A novel cardiac T_1 measurement technique termed SASHA was developed and validated through simulations and experimental data. SASHA T_1 measurements were found to be accurate and robust against changes in heart rate, spin-spin relaxation time (T_2), flip angle, and off-resonance, which are known sources of error in MOLLI T_1 values. Normal ranges for SASHA T_1 values were established in a group of healthy controls and altered T_1 values consistent with fibrosis were found in small study of patients with heart failure.

Precision of SASHA measurements can be significantly improved using a 2-parameter model to calculate T_1 values at the expense of greater systematic errors, particularly due to incomplete magnetization saturation. Robust saturation pulses were developed using hard pulse trains with numerically optimized flip angles and experimentally validated to result in less than 1% residual magnetization over the range of B_0 and B_1 magnetic field inhomogeneities expected at common imaging field strengths.

A variable flip angle (VFA) imaging readout was also designed to reduce SASHA T_1 errors caused by readout effects when using a 2-parameter model. SASHA-VFA was found to significantly reduce the magnitude of T_1 errors in phantom experiments and consistently reduce image artifacts due to off-resonance. Together, robust saturation pulse trains and VFA readouts minimize systematic errors in 2-parameter SASHA T_1 values, enabling accurate in-vivo T_1 measurements with comparable precision to the existing MOLLI technique.

ECV quantification using T_1 measurements can be easily added to existing clinical MRI protocols and can potentially provide clinically useful information due to the ubiquitous presence of myocardial fibrosis in cardiac disease. The characterization and development of improved T_1 measurement techniques in this thesis directly translate to more reliable ECV measurements that may drive its clinical adoption.

Preface

A portion of Chapter 2 has been previously published: Chow K, Thompson RB. An Analytic Description of Factors Affecting MOLLI's Accuracy Using a Time-Weighted Average Model of T_1 Relaxation. *Proc Intl Soc Mag Reson Med.* 2014;**22**:2453. I was responsible for conception of the model, experimental validation, data analysis, and manuscript composition. Richard Thompson was the supervisory author and contributed to study design and manuscript revision.

A version of Chapter 3 has been previously published: Chow K, Flewitt JA, Green JD, Pagano JJ, Friedrich MG, Thompson RB. Saturation Recovery Single-Shot Acquisition (SASHA) for Myocardial T_1 Mapping. *Magn Reson Med.* 2014;**71**:2082–2095. I was responsible for MRI sequence design and validation, contributed to in-vivo study protocol design, and acquired data in some subjects. Data analysis was performed by both myself and Richard Thompson and I was responsible for manuscript composition. Jacqueline Flewitt assisted in data acquisition, Jordin Green provided technical resources for MRI sequence implementation, and Joseph Pagano contributed to the study design. Matthias Friedrich was a principal investigator in the Alberta HEART study, from which this chapter used a subset of subjects. Richard Thompson was the supervisory author and involved in study design, data analysis, and manuscript drafting. All authors read and approved the final version of the submitted manuscript. The in-vivo studies were approved by the University of Calgary Conjoint Health Research Ethics Board with Ethics ID numbers 18800 and 22657.

A version of Chapter 4 has been submitted for review: Chow K, Kellman P, Spottiswoode BS, Thompson RB. Saturation Pulse Design for Quantitative Cardiac Imaging. *Mag Reson Med.* Submitted 26 August 2014. A portion of Chapter 5 has been previously published: Chow K, Spottiswoode BS, Pagano JJ, Thompson RB. Improved precision in SASHA T_1 mapping with a variable flip angle readout. *J Cardiovasc Magn Reson.* 2014;**16**(Suppl 1):M9. These chapters are part of a research collaboration between the University of Alberta, the National Institutes of Health, and Siemens Healthcare. In both studies, I was responsible for sequence design, experimental validation, data analysis, and manuscript composition. Peter Kellman contributed to study design and sequence development and Bruce Spottiswoode provided technical resources for sequence implementations. Richard Thompson was the supervisory author and contributed to overall study design and manuscript drafting. All authors read and approved the final version of the submitted manuscripts.

The great thing about science is that you can get it wrong over and over again because what you're after — call it truth or understanding — waits patiently for you. Ultimately, you'll find the answer because it doesn't change.

Dudley Herschbach, Nobel Prize Laureate

Acknowledgments

Although a doctoral thesis has a single author, it is only made possible through the efforts of many. I have been lucky enough to work alongside countless people who have provided me with support and guidance throughout my program. It has been an absolute pleasure to work with you all.

This research would not have been possible without the support of various funding agencies. I would like to acknowledge the Natural Sciences and Engineering Research Council of Canada, the University of Alberta, and the Faculty of Medicine for stipend funding during my program. Operational funding was provided by the Canadian Institutes of Health Research and Alberta Innovates – Health Solutions.

I would like to thank my supervisor, Dr. Richard Thompson for the countless hours spent teaching me everything that I know about MRI and research. Your scientific curiosity has inspired me and your advice has guided me throughout my program. I am truly proud of the work that we have accomplished together and I could not have done it without you.

Special thanks are also needed for the other members of my supervisory committee, Dr. Alan Wilman and Dr. Ian Paterson. Alan, thank you for treating me as an academic peer long before I felt I had earned it. The scientific insights you have shared with me are paralleled only by the advice you have given me about academia itself. Thank you Ian for providing me with an invaluable clinical perspective throughout my program. You treated every moment we shared as a teaching moment and always found the time to answer my questions despite your incredibly busy schedule.

Much of my research was conducted at the Peter S. Allen MRI Centre and I am thankful to Karim, Peter, and Carol for all the work they do in ensuring the smooth operation of the centre. I am also grateful to the entire team of MRI technologists and nursing staff, particularly Tracey and Priya, for their helpful assistance in all of our patient studies. A number of experiments in this thesis were performed at the Elko Cardiac MRI Unit, which would not have been possible without the generous support of Dr. Richard Coulden, Emer Sonnex and the rest of the staff there.

Thank you to my exceptional clinical collaborators for their time and effort in designing and managing patient studies. Application of new techniques into actual patient studies is the ultimate goal of translational research and your support has made that goal an every day reality for the work done in our lab. I would especially like to thank the research coordinators: Marleen, Lisa, Edie, and Margo. Your tireless efforts in recruiting and coordinating our research subjects should win you awards for logistical planning and I thank you for being such a pleasure to work with over the past years. The hundreds of clinical patient studies

we have been able to do are truly a testament to your hard work and dedication.

I am extremely grateful to Dr. Matthias Friedrich, Dr. James White, and the rest of the wonderful individuals at the Stephenson CMR Centre in Calgary. Thank you Matthias for your initial suggestion of trying T_1 mapping which has become the focus of this thesis. Your unqualified support of my research and generosity in allowing me the use of the resources at the Stephenson were immensely helpful in our initial investigations of the MOLLI sequence. James, thank you for the continued support of our collaboration and I hope that the work that we have done together so far is just the beginning. I am also grateful to all the senior staff at the Stephenson for their support and numerous discussions over the years.

It is difficult to say enough about the support that I have received from Jackie Flewitt. You have helped me in virtually all aspects of doing research in Calgary, from scanning my complex research protocols to looking after mundane details, and always with smile. I am forever grateful for your support and friendship. Thank you to Loreen and Jian-Nong for all your efforts in scanning and thanks to Rosa, Sandra, and Michelle for handling all the messy details involved in getting our research projects off the ground. To everyone I've worked with in Calgary, thank you for genuinely making me feel like part of the family.

Optimization of the SASHA sequence was a collaborative effort with Dr. Peter Kellman at the National Institutes of Health and Dr. Bruce Spottiswoode at Siemens Healthcare. I am grateful to Peter for taking the time to share his insights and considerable expertise. Thank you Bruce for providing an incredible amount of technical support in the last two years. Your effort in incorporating SASHA into a Siemens works-in-progress distribution has brought our technique to a worldwide audience that many researchers can only wish for.

I have been fortunate enough to work alongside many supportive and talented graduate students. I have learned so much from all of you and am honoured to call you both my colleagues and my friends. I would like to especially thank the students in our lab, Dr. June Cheng Baron, Dr. Joseph Pagano, Kory Mathewson, and Sarah Thiesson, for their support and making it a pleasure to come to work every day. June, I greatly enjoyed sharing an office with you for many years and appreciated our many discussions together and your always thoughtful advice. Joe, thank you for the countless coffees and all the time and stress you've saved me by sharing the scanning responsibilities with me. I am also grateful to our department administrators, Maisie and Catherine, for their assistance in managing the little details of the graduate program itself so that I had the time to focus on research itself.

Finally, I am thankful to my friends and family for their emotional support and always providing much needed distractions whenever I needed to get away from work. Mom and dad, I am eternally grateful for your love and support during my degree. You were the first to believe in me, and it means the world to me.

Table of Contents

1 Introduction **1**

1.1 Overview . . . 1

1.2 Nuclear Magnetic Resonance . . . 2

1.2.1 Spins, Magnetization, and Magnetic Fields . . . 2

1.3 MRI Image Acquisition . . . 4

1.3.1 Magnetic Field Gradients . . . 4

1.3.2 Slice Selection . . . 4

1.3.3 Frequency Encoding . . . 5

1.3.4 Phase Encoding . . . 5

1.3.5 k-space . . . 5

1.3.6 Pulse Sequences . . . 6

1.3.7 Cardiac Imaging . . . 7

1.4 Relaxation . . . 7

1.4.1 Spin-Lattice (T_1) Relaxation . . . 8

1.4.2 Spin-Spin (T_2) Relaxation . . . 9

1.4.3 T_1 and T_2 Relaxation in Pure Matter . . . 10

1.4.4 T_1 and T_2 Relaxation in Biological Tissue . . . 11

1.4.5 Image Contrast with T_1 and T_2 . . . 12

1.5 T_1 Relaxation Measurements . . . 13

1.5.1 Inversion Recovery . . . 13

1.5.2 Saturation Recovery . . . 13

1.5.3 Look-Locker . . . 14

1.5.4 Modified-Look-Locker Inversion Recovery (MOLLI) . . . 16

1.6 Myocardial Fibrosis . . . 18

1.6.1 Late Gadolinium Enhancement . . . 20

1.6.2 Post-contrast T_1 Mapping . . . 21

1.6.3 Extracellular Volume Fraction Imaging . . . 22

1.6.4 Native Myocardial T_1 Mapping . . . 23

1.6.5 Clinical Studies with T_1 Mapping . . . 23

1.7 Scope of Thesis . . . 25

1.8 References . . . 26

2 An Analytic Model of Factors Affecting MOLLI T_1 Accuracy Using a Time-Weighted Average Model of Relaxation **35**
2.1 Introduction . . . 35
2.2 Theory . . . 36
2.2.1 Time-Weighted Average Model of Apparent T_1^* Relaxation . . . 37
2.2.2 Apparent Starting Magnetization . . . 39
2.2.3 Slice Profile Effects . . . 40
2.2.4 Relationship Between Apparent T_1^* and True T_1 In MOLLI . . . 42
2.3 Methods . . . 43
2.3.1 Simulation Validation . . . 43
2.3.2 Phantom Experiments . . . 44
2.3.3 Data Analysis . . . 44
2.4 Results . . . 45
2.4.1 Simulation Validation of the Time-Weighted Average Model . . . 45
2.4.2 Phantom Experiments . . . 45
2.5 Discussion . . . 47
2.5.1 Validation of the TWA Model . . . 47
2.5.2 Calculation of True T_1 Values . . . 51
2.5.3 Further Development of the TWA Model . . . 52
2.5.4 MOLLI and the Look-Locker Correction . . . 53
2.6 Conclusion . . . 54
2.7 References . . . 55

3 Saturation Recovery Single-Shot Acquisition (SASHA) for Myocardial T_1 Mapping **59**
3.1 Introduction . . . 59
3.2 Theory . . . 61
3.3 Methods . . . 61
3.3.1 Pulse Sequence . . . 61
3.3.2 Calculation of T_1 Values . . . 63
3.3.3 Simulations . . . 63
3.3.4 Phantom Experiments . . . 64
3.3.5 In-Vivo Studies . . . 65
3.3.6 In-Vivo Image Analysis . . . 65
3.3.7 Myocardial and Blood T_1 Variability . . . 66
3.3.8 Inter- and Intra-Observer Reproducibility . . . 66

3.3.9 Statistics . . . 66
3.4 Results . . . 67
3.4.1 Simulations . . . 67
3.4.2 Phantom Experiments . . . 68
3.4.3 In-Vivo Studies . . . 70
3.4.4 Post-Contrast Time-Course Sub-Study . . . 73
3.4.5 Heart Failure Sub-Study . . . 75
3.4.6 Inter- and Intra-Observer Reproducibility . . . 76
3.5 Discussion . . . 76
3.5.1 Myocardial and Blood T_1 Values . . . 76
3.5.2 Partition Coefficient . . . 77
3.5.3 Inter- and Intra-Observer Reproducibility . . . 78
3.5.4 Image Quality . . . 78
3.5.5 T_1 Variability and Pulse Sequence Limitations . . . 78
3.5.6 Study Limitations . . . 80
3.6 Conclusions . . . 81
3.7 Appendix: Origin of Apparent Changes in Saturation Efficiency in SASHA . . . 81
3.7.1 Saturation Recovery Preparation . . . 81
3.7.2 Effect of a bSSFP Readout . . . 82
3.7.3 Effect of a Flip Angle Distribution . . . 83
3.8 References . . . 85

4 Saturation Pulse Design for Quantitative Cardiac Imaging 91
4.1 Introduction . . . 91
4.2 Theory . . . 92
4.2.1 Geometric Pulse Train Design . . . 92
4.3 Methods . . . 94
4.3.1 B_1 Field Strength Limitations . . . 94
4.3.2 Spoiler Gradient Design . . . 94
4.3.3 Numerical Pulse Train Design . . . 96
4.3.4 BIR4-90 Pulse Optimization . . . 97
4.3.5 RF Power Calculation . . . 97
4.3.6 Phantom Validation . . . 97
4.3.7 SASHA Sequence Simulation . . . 98
4.4 Results . . . 99
4.4.1 B_1 Field Strength Limitations . . . 99

4.4.2 BIR4-90 Pulses . . . 99
4.4.3 Numerically Optimized Pulse Trains . . . 99
4.4.4 Pulse Train Ordering Effects . . . 101
4.4.5 T_1 Relaxation Effects . . . 101
4.4.6 Phantom Validation . . . 103
4.5 Discussion . . . 106
4.5.1 BIR4-90 Pulse Design . . . 106
4.5.2 Pulse Train Design . . . 107
4.6 Conclusions . . . 109
4.7 References . . . 110

5 Optimization of SASHA T_1 Mapping Using Variable Flip Angle Readouts 113
5.1 Introduction . . . 113
5.2 Methods . . . 115
5.2.1 Variable Flip Angle Readout Design Simulations . . . 115
5.2.2 Phantom Experiments . . . 117
5.2.3 In-Vivo Studies . . . 118
5.2.4 Image Analysis . . . 118
5.2.5 Statistics . . . 119
5.3 Results . . . 119
5.3.1 Variable Flip Angle Readout Performance . . . 119
5.3.2 Variable Flip Angle Length Optimization . . . 121
5.3.3 Phantom Experiments . . . 123
5.3.4 In-Vivo Studies . . . 125
5.4 Discussion . . . 127
5.4.1 Accuracy of 2-parameter SASHA T_1 Values . . . 127
5.4.2 Variable Flip Angle Readout Performance . . . 128
5.4.3 Phantom Experiments . . . 129
5.4.4 In-Vivo Studies . . . 129
5.4.5 Limitations . . . 130
5.5 Conclusions . . . 131
5.6 References . . . 132

6 Discussion and Conclusions 136
6.1 Summary . . . 136
6.2 T_1 Measurements and Fibrosis . . . 137
6.2.1 Random and Systematic Errors in T_1 Measurements . . . 137

6.2.2 Sensitivity and Specificity of T_1 and ECV Measurements 139
6.2.3 Interpretation of T_1 and ECV Measurements 140
6.3 Limitations 140
6.4 Recent Developments in SASHA T_1 mapping 141
6.4.1 Selection of SASHA Saturation Recovery Times 141
6.5 Future Directions 143
6.5.1 MOLLI and the TWA Model 143
6.5.2 Segmented Acquisitions 143
6.5.3 Alternative Image Reconstruction 144
6.6 Conclusions 144
6.7 References 146

Complete Bibliography **152**

List of Tables

3 Saturation Recovery Single-Shot Acquisition (SASHA) for Myocardial T_1 Mapping **59**

3.1 T_1 and T_2 values of agarose phantoms, as determined by spin echo and SASHA 71

3.2 Subject characteristics 73

4 Saturation Pulse Design for Quantitative Cardiac Imaging **91**

4.1 Summary of characteristics for Bloch simulation numerically optimized saturation pulses 100

5 Optimization of SASHA T_1 Mapping Using Variable Flip Angle Readouts **113**

5.1 Myocardial and blood T_1 values in 4 healthy volunteers 131

List of Figures

1 Introduction **1**

1.1 Spin-lattice (T_1) relaxation . . . 8
1.2 Spin-spin (T_2) relaxation . . . 9
1.3 Molecular motion frequency distribution . . . 10
1.4 T_1 and T_2 relaxation with motion frequency . . . 11
1.5 Dynamic range of inversion and saturation recovery . . . 14
1.6 MOLLI sequence diagram . . . 17
1.7 MOLLI and SASHA T_1 errors with various confounders . . . 19
1.8 In-vivo native T_1 map . . . 24

2 An Analytic Model of Factors Affecting MOLLI T_1 Accuracy Using a Time-Weighted Average Model of Relaxation **35**

2.1 Time-weighted average (TWA) model schematic . . . 37
2.2 MOLLI magnetization with TI increments . . . 40
2.3 RF pulse slice profile . . . 41
2.4 TWA model in single flip angle simulations . . . 46
2.5 TWA model in multipe flip angle simulations accounting for slice profile . . . 47
2.6 TWA T_1^* error as a function of R_1'/R_1 . . . 48
2.7 Comparison of simulated, TWA, and measured T_1^* values in phantom experiments . . . 49
2.8 Comparison of spin-echo, TWA, and Look-Locker corrected T_1 values in phantom experiments . . . 50
2.9 Comparison of predicted and measured apparent R_1^* and driven R_1' in phantoms 51

3 Saturation Recovery Single-Shot Acquisition (SASHA) for Myocardial T_1 Mapping **59**

3.1 SASHA sequence diagram . . . 62
3.2 SASHA saturation efficiency dependence . . . 68
3.3 SASHA SNR dependence (box and whiskers) . . . 69
3.4 SASHA SNR dependence (median and IQR) . . . 70
3.5 SASHA in-vivo example (native) . . . 72
3.6 SASHA in-vivo example (post-contrast) . . . 74

3.7 SASHA time-course 75

4 Saturation Pulse Design for Quantitative Cardiac Imaging 91
4.1 Geometric pulse train design 93
4.2 Saturation pulse sequence diagrams 95
4.3 Saturation pulse train design comparison 101
4.4 Saturation pulse performance with B_1 102
4.5 Saturation pulse performance with flip angle permutations 103
4.6 Saturation pulse performance with T_1 104
4.7 Measured saturation pulse performance with B_0 and B_1 105
4.8 SASHA T_1 error with saturation pulse performance 106

5 Optimization of SASHA T_1 Mapping Using Variable Flip Angle Readouts 113
5.1 VFA flip angle pattern 116
5.2 Constant and variable flip angle signal with off-resonance 120
5.3 Characteristics of CFA and VFA with off-resonance 120
5.4 Point spread functions of CFA and VFA readouts 121
5.5 Simulated performance of VFA readouts 122
5.6 Accuracy of SASHA-VFA in phantoms 124
5.7 Comparison of SASHA-VFA accuracy in phantoms to simulations 125
5.8 Summary of SASHA-VFA accuracy in phantoms 126
5.9 In-vivo example of SASHA-CFA and SASHA-VFA 127

List of Abbreviations

2SX	2 site exchange
ACS	autocalibration signal
AHA	American Heart Association
BIR4	B_1 independent rotation RF pulse
bpm	beats per minute
BPP	Bloembergen-Pound-Purcell
bSSFP	balanced steady state free precession
CFA	constant flip angle
CT	computed tomography
CV	coefficient of variation
CVD	cardiovascular disease
D	duty cycle
DE	delayed enhancement
DTPA	diethylene triamine pentaacetic acid
ECG	electrocardiogram
ECM	extracellular matrix
ECV	extracellular volume
EPI	echo planar imaging
FE	frequency encoding
FID	free induction decay
FLASH	fast low angle shot
FOV	field of view
FPD	fast proton diffusion
FWHM	full width half maximum
Gd	gadolinium
GRAPPA	generalized autocalibrating partially parallel acquisitions
GRE	gradient recalled echo
Hct	hematocrit
ICC	intraclass correlation
IQR	inter-quartile range
IR	inversion recovery
LGE	late gadolinium enhancement
LL	Look-Locker
NMR	nuclear magnetic resonance
MLLSR	modified Look-Locker acquisition with saturation recovery
MOLLI	modified Look-Locker inversion recovery
MRI	magnetic resonance imaging
MT	magnetization transfer
PE	phase encoding
PET	positron emission tomography
PSF	point spread function
RF	radiofrequency

RAS	renin-angiotension system
ROI	region of interest
SAP-T_1	short acquisition period T_1
SAR	specific absorption rate
SASHA	saturation-recovery single-shot acquisition
SD	standard deviation
SDAM	saturated double angle method
SE	spin echo
SENSE	sensitivity encoding
ShMOLLI	shortened MOLLI
SNR	signal to noise ratio
SPECT	single photon emission computed tomography
SSFP	steady state free precession
SR	saturation recovery
SRTFL	saturation recovery turbo FLASH
TGF-β	transforming growth factor-β
TNF-α	tumor necrosis factor-α
TE	echo time
TI	inversion recovery time
TR	repetition time
TrueFISP	true fast imaging with steady-state precession
TS	saturation recovery time
TTC	triphenyltetrazolium chloride
TWA	time-weighted average
VFA	variable flip angle

List of Symbols

B_0	main magnetic field
B_1	radiofrequency field
$\hat{\mathrm{B}}_1$	normalized radiofrequency field scale factor
f_h	hydration phase fraction
f_w	free water phase fraction
G_r	gradient field
k	k-space position
$M(0)$	starting magnetization
M_0	equilibrium longitudinal magnetization
M_{XY}	transverse magnetization
M_Z	longitudinal magnetization
M_Z/M_0	residual longitudinal magnetization
r_1	relaxivity constant
R_1	spin-lattice relaxation rate
R_1^*	apparent spin-lattice relaxation rate
R_1'	driven spin-lattice relaxation rate
R_2	spin-spin relaxation rate
R_2^*	apparent spin-spin relaxation rate
T_1	spin-lattice relaxation time
T_1^*	apparent spin-lattice relaxation time
T_1'	driven spin-lattice relaxation time
T_2	spin-spin relaxation time
T_2^*	apparent spin-spin relaxation time
$\hbar$	Planck's constant
t	time
η	saturation efficiency
γ	gyromagnetic ratio
ω	Larmor frequency
ω_c	molecular motion frequency
λ	blood-tissue partition coefficient
τ_c	molecular motion correlation time
θ	flip angle

Chapter 1

Introduction

1.1 Overview

Cardiovascular disease (CVD) is the leading cause of death worldwide [1] and the second leading cause of death in Canada [2], with an average of 1 death in Canada every 8 minutes [2] and 1 death every 40 seconds in the United States [3] attributed to CVD. Of the cardiovascular diseases, diseases of the heart were the largest portion, accounting for 72% CVD related deaths. Over 1 in 3 Americans have CVD, with an estimated total cost (direct and indirect) of $315 billion USD in 2010 [3].

Medical imaging plays a central role in not only the diagnosis of cardiovascular disease, but also the staging of disease severity and guiding treatment. A variety of imaging modalities are available for cardiac imaging, each with specific strengths and weaknesses. X-ray computed tomography (CT) provides high-resolution anatomical images of the heart and coronary arteries, useful in the diagnosis of coronary artery disease. It is one of the fastest imaging modalities, but is used sparingly in serial follow-up studies due to ionizing radiation exposure. Single photon emission computed tomography (SPECT) and positron emission tomography (PET) imaging modalities involve the injection of a radionuclide into a subject to quantify metabolic information and identify regions of reduced myocardial perfusion, but PET has high associated costs and both expose patients to ionizing radiation. Echocardiography is one of the most common cardiac imaging modalities due to its low cost and portability and is widely used to acquire structural and functional information about the heart.

Magnetic resonance imaging (MRI) is increasingly popular due to its ability to generate relatively sub-millimeter three-dimensional images without the use of ionizing radiation. MRI has excellent soft tissue contrast and is also unique in that its image contrast can be easily manipulated during a scan by adjusting acquisition parameters without the need for

exogenous contrast agents. Although MRI is a relatively new imaging modality, technical advances over the last two decades have made it the diagnostic standard in many diseases. For example, cardiac MRI is widely used for the assessment of heart chamber volumes and cardiac performance due to low inter- and intra-observer variability. The late gadolinium enhancement technique with MRI is also considered the clinical standard for the detection and quantification of myocardial scarring with ischemic heart disease.

Quantitative tissue characterization is an emerging research area in cardiac MRI. Measured signal intensities in MRI are modulated by intrinsic tissue parameters that are sensitive to the underlying microscopic tissue structure, a property used to generate images with high visual contrast between soft tissues. Cellular and microstructural changes in tissue with disease result in changes in these so-called relaxation parameters and are often visually detectable in MRI images. However, early stages of disease result in only small changes in relaxation parameters, which may only be detectable using careful quantitative measurements and are difficult to visually identify.

Recent interest in myocardial T_1 relaxation has been spurred by promising correlations with myocardial fibrosis and the widespread availability of quantitative T_1 mapping techniques. Fibrosis is a common microstructural feature in the progression of many cardiac diseases and could potentially be used to detect early stages of disease when medical therapy may be more useful.

The overall theme of this thesis was the development of an accurate T_1 mapping technique that could be robustly used in clinical patient populations. Sections 1.2 and 1.3 provide general background information about MRI imaging theory, Section 1.4 describes the theoretical basis of MRI relaxation phenomena, and Section 1.5 details the basic techniques for measuring T_1 relaxation. Section 1.6 reviews the literature about myocardial fibrosis and its measurement using MRI.

1.2 Nuclear Magnetic Resonance

1.2.1 Spins, Magnetization, and Magnetic Fields

The principle of nuclear magnetic resonance (NMR) was first discovered in molecular beams by Isidor Rabi in 1938 and subsequently expanded upon in condensed matter independently by Felix Bloch and Edward Purcell in 1946, for which all three received Nobel prizes. In the classical description of NMR, nuclei having a net non-zero quantum property of "spin" resonate at a characteristic frequency in the presence of a magnetic field. This Larmor frequency (ω) is proportional to the strength of the magnetic field (B_0), multiplied

by the gyromagnetic ratio (γ), a constant for each nuclei:

$$\omega = \gamma B_0 \tag{1.1}$$

For the commonly imaged proton at a typical MRI magnetic field strength of 1.5T, γ= 42.58 MHz/T and thus the Larmor frequency is 63.87 MHz. Spins are classically represented as small magnetic dipoles that interact with external magnetic fields by aligning parallel or anti-parallel to the direction of the external field. Protons are a spin ½ nuclei with a difference in energy states of:

$$\Delta E = \gamma \hbar B_0 \tag{1.2}$$

where $\hbar$ is Planck's constant and the parallel alignment has a lower energy state. The relative proportion of these states can be characterized with the Boltzmann distribution, determined by the difference in their energy states and the temperature of the system:

$$\frac{N_{\text{parallel}}}{N_{\text{anti-parallel}}} = e^{\frac{-\Delta E}{\text{kT}}} \tag{1.3}$$

where k is Boltzmann's constant and T is the temperature. At room temperature of 20°C and a magnetic field strength of 1.5T, the number of parallel spins only slightly exceeds the number of anti-parallel spins, with only approximately 5 more parallel spins for every 1,000,000 spins. However, the human body is composed of approximately 70% water, with two hydrogen protons per molecule. Therefore for every 1g of water, there are 3×10^{17} more parallel spins than anti-parallel, leading to an appreciable equilibrium net magnetization vector, M_0, along the direction of the main magnetic field. Magnetization is expressed as the number of magnetic dipole moments per unit volume and has units of A/m.

By convention, the direction of the main magnetic field, B_0, is along the longitudinal (Z) direction and the transverse plane (XY) is oriented perpendicular to it. The spin-system can be excited using radiofrequency (RF) pulse at the Larmor frequency to create an additional magnetic field, B_1, perpendicular to B_0. The B_1 field rotates the net magnetization, M_0, toward the transverse plane with a rotational frequency that can be expressed using the Larmor equation, similar to Eq. 1.1:

$$\omega = \gamma B_1 \tag{1.4}$$

The angle of rotation, θ, is equal to the accumulated phase of this rotation over the duration of the B_1 field, t:

$$\theta = \omega t \tag{1.5}$$

This angle is commonly referred to as the tip angle or flip angle, and can be written more compactly by combining Eq. 1.4 and 1.5:

$$\theta = \gamma B_1 t \tag{1.6}$$

The longitudinal and transverse components of the net magnetization following excitation can be expressed as:

$$M_Z = M_0 \cos(\theta) \tag{1.7}$$

$$M_{XY} = M_0 \sin(\theta) \tag{1.8}$$

The excited transverse magnetization, M_{XY}, also precesses at the Larmor frequency (Eq. 1.1) and therefore emits a radiofrequency signal at this frequency. This time-varying signal, known as the free induction decay (FID), can be measured in a nearby antenna coil as a magnetically induced electrical current.

1.3 MRI Image Acquisition

1.3.1 Magnetic Field Gradients

Spatially resolved images are generated in MRI by varying the magnetic field strength in a known, spatially dependent manner. This is commonly achieved using adjustable magnetic field gradients, named for the linear spatial gradient generated. Magnetic field components of the gradients are oriented parallel or anti-parallel with the main magnetic field, thus changing the net field strength but not direction. An MRI system consists of three sets of gradient coils, capable of generating spatial gradients in three orthogonal directions, and thus the magnetic field strength can be made to vary in any arbitrary direction. When a gradient is applied in the direction r, the resonant frequency becomes spatially varying in that direction and is defined by:

$$\omega = \gamma B_0 + \gamma G_r r \tag{1.9}$$

1.3.2 Slice Selection

Spins are excited only when the frequency of the applied RF pulse is at or near the Larmor frequency. In the absence of spatial gradients and large magnetic field inhomogeneties, all spins have a similar resonant frequency and are all excited by an RF pulse at

the Larmor frequency. If a gradient is applied during the RF pulse, the spatial variation in resonant frequency causes excitation only in the spatial plane where the resonant frequency matches the RF frequency. By adjusting the gradient field direction and the frequency and bandwidth of the RF pulse, the excited slice can have any arbitrary orientation, location, and width.

1.3.3 Frequency Encoding

If a gradient is applied after an excitation, spatial variations in resonant frequency cause the FID to be the superposition of signals with multiple frequencies. The relative strength of each of these signals is proportional to the number of excited spins precessing at that frequency, and thus proportional to the spin density at a given spatial location. Therefore, the acquired signal in the frequency domain is a 1-dimensional projection of the imaged object in an axis perpendicular to the gradient. It can be shown that the real-space projection can be obtained by applying a Fourier transform on the acquired time-domain signal.

1.3.4 Phase Encoding

Phase encoding gradients are applied after excitation for a short duration and turned off prior to the acquisition of the FID signal. The phase accumulated during the phase encoding gradient is proportional to the resonant frequency and the duration, and thus variation in resonant frequency cause spins at different locations to accumulate different amount of phase. If the acquisition is repeated with various phase encoding gradient strengths, it can be shown that the 1D projection of the imaged object perpendicular to the phase encoding gradient can be obtained by applying a Fourier transform, analogous to frequency encoding.

1.3.5 k-space

Slice selective excitation is often used together with frequency and phase encoding in orthogonal directions to resolve a 2-dimensional image. The frequency and phase encoded FID signal are referred to as "k-space", where frequency encoding (FE) and phase encoding (PE) are in orthogonal directions. The position in k-space is proportional to the gradient

amplitude and durations in each direction:

$$k_x = \gamma G_{\mathrm{FE}} t_{\mathrm{FE}} \tag{1.10}$$

$$k_y = \gamma G_{\mathrm{PE}} t_{\mathrm{PE}} \tag{1.11}$$

In conventional Cartesian sampling, lines of k_x are acquired one line at a time, repeated with multiple phase encoding strengths to sample the k_y dimension, filling in a 2-dimensional matrix. The k-space data is then converted into a 2D image in the spatial domain by applying a 2D Fourier transform.

The resolution and field of view of the resulting image is determined by the k-space sampling pattern. The spatial resolution is determined by the extent of the frequency domain sampled, while the field of view is determined by the distance between k-space samples:

$$\Delta x = 2\pi / k_{x,max} \tag{1.12}$$

$$FOV = 2\pi / \Delta k_x \tag{1.13}$$

with similar definitions for the phase encoded k_y direction.

As a result, images with higher resolution require more lines of k-space to be acquired and consequently a longer total imaging duration. Typical in-vivo cardiac imaging uses imaging matrix sizes with 50–250 acquired lines of k-space depending on the size of the imaged object and the desired resolution. Images can be acquired in a single shot, where all of k-space is collected in a continuous interval, or in a segmented fashion, where data acquisition is split up into multiple segments.

1.3.6 Pulse Sequences

An MRI pulse sequence is defined by the pattern of RF pulses and gradients used and can result in images with a wide variety of contrasts. For example, a spoiled gradient recalled echo (GRE) sequence uses a low flip angle excitation RF pulse and a large "spoiler" gradient following the k-space readout to dephase any remaining transverse magnetization. The balanced steady-state free precession (bSSFP) sequence is similar to the GRE sequence, but uses "balanced" gradients following the k-space readout to reverse the frequency and phase encoding gradients, preserving much of the transverse magnetization, resulting in higher signal intensity. An excellent textbook describing the technical aspects of various pulse sequences and their design has been written by Bernstein *et al* [4].

1.3.7 Cardiac Imaging

In-vivo MR imaging of the heart is challenging due to constant cardiac and respiratory motion. Breath-holds are often used to minimize respiratory motion but limit the total acquisition duration to approximately 10–15 seconds, with shorter durations often needed in patients. Images acquired in separate breath-holds may be combined but are susceptible to mis-registration due to inconsistency in the breath-hold respiratory phase.

Respiratory motion can also be addressed with gated imaging, where the respiratory phase is continuously monitored either through an external respiratory belt or using specialized MRI acquisitions. Subjects are instructed to breath normally and images are automatically acquired when a target respiratory phase is acquired. Respiratory-gated acquisitions are easier in younger subjects or patients with reduced pulmonary function, although the total study duration is often longer than breath-hold imaging as the target respiratory phase is typically only reached <50% of the time.

The constant motion of the beating heart presents a greater challenge to acquiring high quality cardiac images, as there is no extended duration in which the heart remains motionless. Instead, the cardiac phase is typically monitored using electrocardiography (ECG) or pulse oximetry and image acquisition is gated. By using segmented acquisitions synchronized to the cardiac phase, the motion of the heart can be temporally resolved into a time-series of images over the cardiac cycle commonly referred to as a "cine". Segmented acquisitions implicitly assume that there is no physical motion between each segment and image quality can be degraded with breath-hold motion, irregular heart rhythms, or poor cardiac triggering.

Single images are also often acquired during the diastasis phase, where there is the least amount of motion for the longest duration. These single images can also be segmented, with the same limitations as described above, or acquired in a "single shot" during the diastasis phase of a single heartbeat (~200 ms). Single-shot images are often used when many images need to be acquired during a single breath-hold, but often have reduced spatial resolution to minimize any residual cardiac phase motion during the acquisition.

1.4 Relaxation

Following excitation or any perturbation, the spin system returns to its equilibrium state (M_{XY}=0, M_Z=M_0) through a process known as relaxation. While a quantum mechanical treatment is required to understand the nuances of this process, it can generally be well described classically through a set of characteristic phenomenological equations developed

by Felix Bloch [5].

1.4.1 Spin-Lattice (T_1) Relaxation

An excited spin system exchanges energy through interactions with its surroundings, inducing transitions in the spins' energy state and slowly restoring the Boltzmann distribution equilibrium in Eq. 1.3. This process is known as spin-lattice relaxation. At any given point in time (t), a system with longitudinal magnetization M_Z relaxes toward its equilibrium value (M_0) at a rate (R_1) proportional to the difference in magnetization:

$$\frac{dM_z(t)}{dt} = -\left(M_Z - M_0\right) R_1 \tag{1.14}$$

This expression can be integrated to describe M_Z as a function of time:

$$M_Z(t) = M_0 - \left[M_0 - M_Z(0)\right] e^{-t/T_1} \tag{1.15}$$

where T_1 is known as the characteristic spin-lattice relaxation time and equal to $1/R_1$. Following a saturation pulse, M_Z=0 and the T_1 is equal to the time required for M_Z to reach 63% (=1-e^{-1}) of its equilibrium (Fig. 1.1).

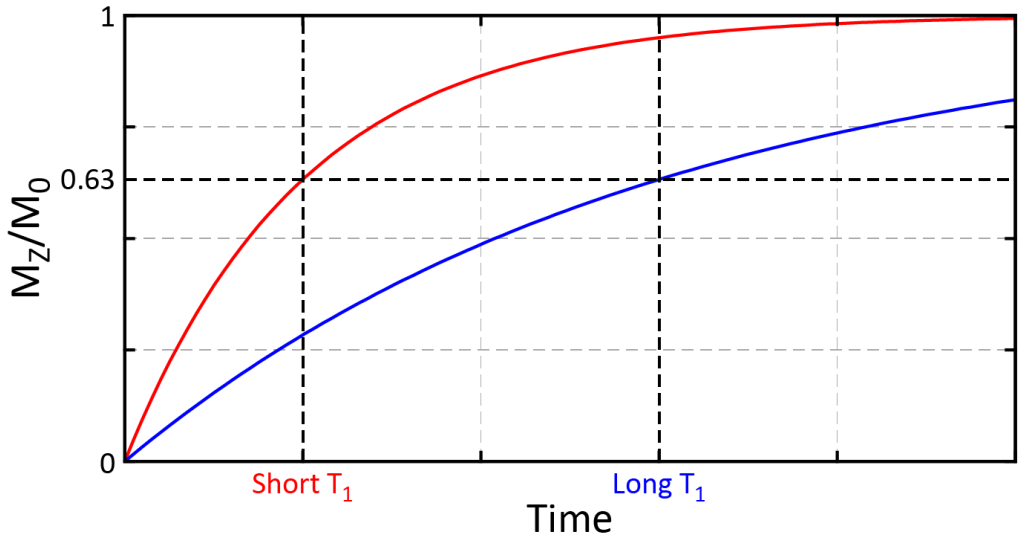

Figure 1.1: Recovery of longitudinal magnetization (M_Z) following a saturation pulse is characterized by the spin-lattice relaxation (T_1) time.

1.4.2 Spin-Spin (T_2) Relaxation

Immediately following excitation, spins have coherent phase and net magnetization in the transverse plane (M_{XY}). Interactions between these spins result in a progressive loss of phase coherence, leading to decay in net transverse magnetization. This "spin-spin relaxation" occurs at a characteristic rate (R_2) proportional to the transverse magnetization (M_{XY}):

$$\frac{dM_{XY}(t)}{dt} = -M_{XY}R_2 \tag{1.16}$$

This expression can also be integrated to describe M_{XY} as a function of time:

$$M_{XY}(t) = M_{XY}(0)e^{-t/T_2} \tag{1.17}$$

where T_2 ($=1/R_2$) is known as the characteristic spin-spin relaxation time and is the time it takes for M_{XY} to decay to 37% ($=e^{-1}$) of its original value (Fig. 1.2).

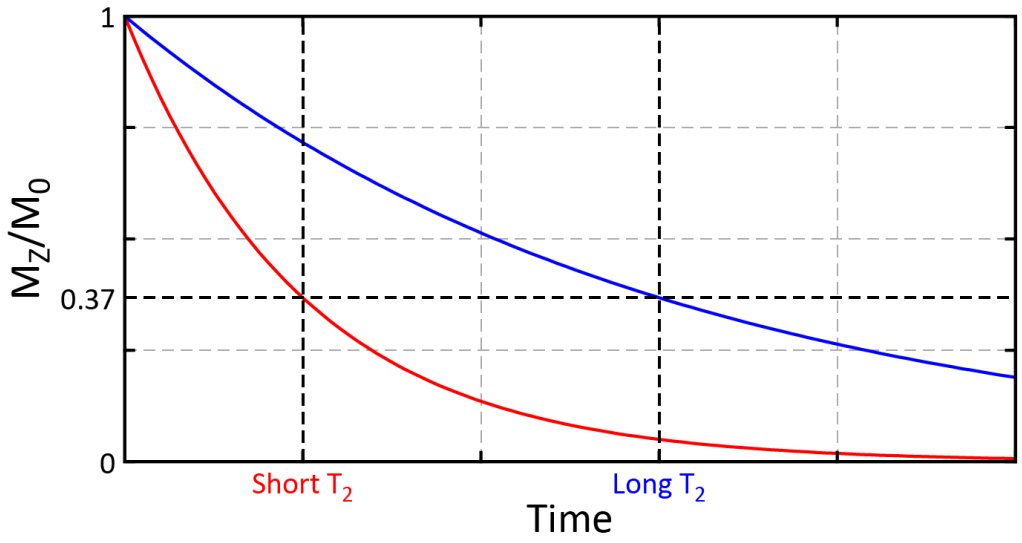

Figure 1.2: Decay of transverse magnetization (M_{XY}) is characterized by the spin-spin (T_2) relaxation time.

In practice, magnetic field inhomogeneities cause an additional loss of phase coherence in the transverse plane. The overall apparent relaxation rate (R_2^*) is therefore equal to R_2 plus the additional relaxation rate (R_2') and follows the same relationships described in Eq. 1.16 and 1.17.

1.4.3 T_1 and T_2 Relaxation in Pure Matter

The relaxation properties of pure matter can be related to the motion of its particles with the Bloembergen-Pound-Purcell (BPP) theory [6]. It is based on dipole-dipole interactions, where an individual spin is affected by the local magnetic fields produced by nearby spins. In a system with a non-zero temperature, molecules undergo random Brownian motion. This molecular motion can be characterized with a correlation time, τ_c, which may be intuitively conceptualized as a characteristic duration that two spins are in close enough proximity to interact. The motion can also be expressed as a molecular frequency ω_c, where $\omega_c=1/\tau_c$, which is dependent on both the temperature of the system as well as its physical structure.

Due to the stochastic nature of Brownian motion, molecular frequencies within a system are distributed within a spectrum. Highly restricted motion in solid matter leads to a narrow distribution of low frequencies (long correlation times), whereas unrestricted motion in liquids leads to a broad distribution with higher frequencies (Fig. 1.3). Viscous fluids have partially restricted motion with intermediate frequencies.

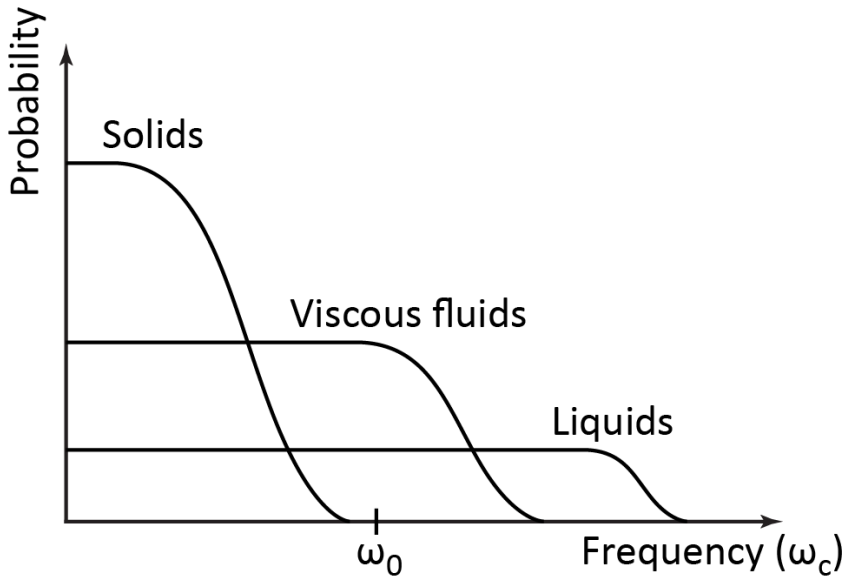

Figure 1.3: Distribution of molecular motion frequency (ω_c) in solid matter, viscous fluids, and liquids.

The motion of individual spins results in a fluctuating magnetic field at the frequency of its molecular motion. When this frequency is equal to the Larmor frequency (ω_0), it induces energy level transitions in nearby spins, facilitating T_1 recovery and T_2 decay. The relaxation times T_1 and T_2 are characteristically related to ω_c as shown in Fig. 1.4. In

liquids where there is a broad distribution of ω_c, there is a relatively low probability that the motion occurs at the Larmor frequency (Fig. 1.3). In solids, the narrow distribution of short ω_c results an even lower probability that the motion occurs at the Larmor frequency. However, viscous fluids have an intermediate frequency distribution with a relatively large probability of motion at the Larmor frequency, leading to short T_1 and T_2 values. If the strength of the main magnetic field increases, the Larmor frequency also increases, reducing the frequency distribution overlap and increasing T_1 and T_2 values.

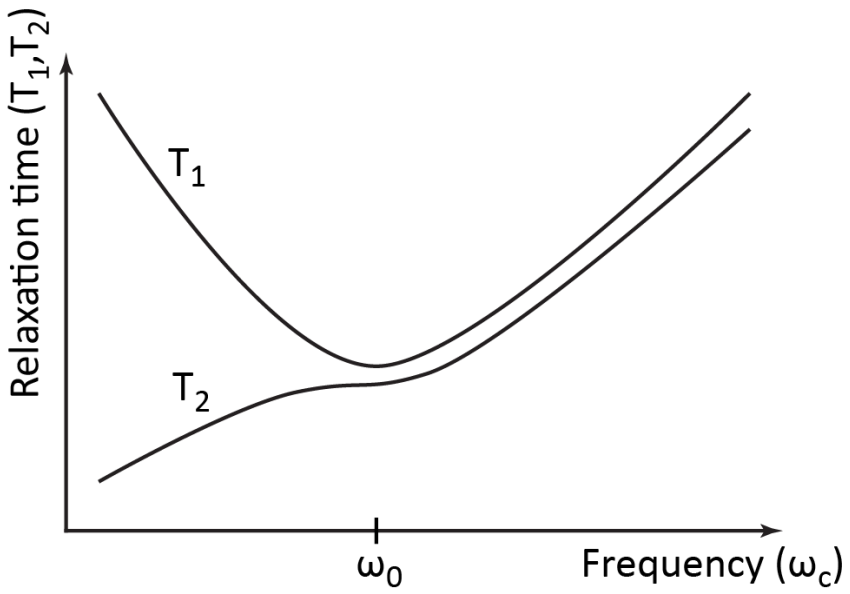

Figure 1.4: T_1 and T_2 relaxation times as a function of motion frequency.

1.4.4 T_1 and T_2 Relaxation in Biological Tissue

While the BPP theory provides an intuitive understanding of relaxation in uniform materials, biological tissues are highly heterogenous structures. The relaxation characteristics of tissues can be understood with Fullerton's Fast Proton Diffusion (FPD) model [7]. In the FPD model, water within tissues may be classified in one of three compartments: free water, hydration water, and crystalline water. Free water is sufficiently far away from the macromolecular structure to be analogous to a liquid in the BPP model and has long T_1 and T_2 values. Crystalline water is tightly bound to the macromolecules and thus has properties similar to solids, with long T_1 values and short T_2 values. The hydration layer is refers to water that is loosely bound to the macromolecules, and thus is analogous to a viscous fluid with intermediate T_1 and T_2 values.

The long T_1 and short T_2 values of the crystalline water result in the observed spin-

lattice relaxation rate being dominated by the T_1 values of the free and hydration water, which are in fast exchange. Therefore, as described by the Zimmerman-Brittin model [8] for multi-phase systems in fast exchange, the effective T_1 relaxation time is:

$$\frac{1}{T_{1,eff}} = \frac{f_w}{T_{1,w}} + \frac{f_h}{T_{1,h}} \tag{1.18}$$

where f_w and f_h are fraction of water in the free and hydration phase respectively, and $T_{1,w}$ and $T_{1,h}$ are the relaxation times of water in the free and hydration phase respectively.

The short T_2 value of the crystalline water results in intermediate exchange with free and hydration water that can be approximated with the slow exchange limit. As the free and hydration water are in fast exchange with much longer T_2 values than the crystalline water, the effective T_2 value of the system is:

$$\frac{1}{T_{2,eff}} = \frac{f_w}{T_{2,w}} + \frac{f_h}{T_{2,h}} \tag{1.19}$$

with analogous definitions to Eq. 1.18.

The T_1 and T_2 of the hydration water are much shorter than those of free water and depend on the hydrated protein. Together, Eq. 1.18 and 1.19 describe how the relaxation rates in tissues depend on the macromolecules (proteins) within the tissue as well as the hydration fraction of those macromolecules.

1.4.5 Image Contrast with T_1 and T_2

Together with the proton density, T_1 and T_2 are the fundamental image contrast mechanisms in magnetic resonance imaging. While all protons are identical, the wide spectrum of microscopic environments within the body results in a diverse range of relaxation values. In this way, each proton acts as a small probe into its local environment, revealing far more information than is available from the proton density itself. MRI images can be produced with different relaxation weighting by altering acquisition parameters, allowing a variety of contrasts between tissues.

1.5 T_1 Relaxation Measurements

1.5.1 Inversion Recovery

The T_1 of a spin system is classically measured using an inversion recovery (IR) experiment. Starting at the equilibrium state with M_Z=M_0, an inversion pulse is applied to fully invert the longitudinal magnetization, i.e. $M_Z(0)$=-M_0. After a specified delay termed the inversion time, TI, the longitudinal magnetization is sampled by an imaging readout. The system is allowed to fully recover to equilibrium by waiting a sufficiently long time (>5T_1), typically several seconds, and the experiment is repeated. By varying the TI, the longitudinal magnetization recovery curve is sampled at multiple points and the characteristic T_1 time can be computed by fitting the sampled data to the exponential recovery curve in Eq. 1.15 with $M_Z(0)$=-M_0:

$$M_Z(t) = M_0\left(1 - 2e^{-t/T_1}\right) \tag{1.20}$$

1.5.2 Saturation Recovery

The IR experiment is time inefficient as long wait times are needed in order to allow full recovery before the experiment can be repeated. A saturation recovery (SR) experiment utilizes a saturation preparation pulse instead of inversion as well as short delay times before the next saturation/readout pair. M_Z recovers at the same rate, R_1, in both IR and SR experiments but with $M_Z(0)$=0 in SR experiments instead. Conceptually, both sequences require that the starting magnetization following the preparation pulse (inversion or saturation) be well known. For IR experiments, the starting magnetization uses long wait times to ensure M_Z=M_0 prior to the inversion pulse, and thus M_Z=- M_0 afterwards. For SR sequences, the saturation pulse results in M_Z=0 regardless of the starting magnetization, therefore the long wait times are not necessary and the total time required is considerably reduced. However, T_1 measurements with saturation recovery experiments are less precise than with inversion recovery experiments as they have half the dynamic range in measured signal (Fig. 1.5). Furthermore, the reduction in dynamic range results in decreased image contrast between tissues with different T_1 values.

By varying the delay between saturation and readout, now termed the saturation recovery time, TS, the T_1 can be computed by fitting the sampled data to the exponential recovery curve in Eq. 1.15 with $M_Z(0)$=-M_0:

$$M_Z(t) = M_0\left(1 - e^{-t/T_1}\right) \tag{1.21}$$

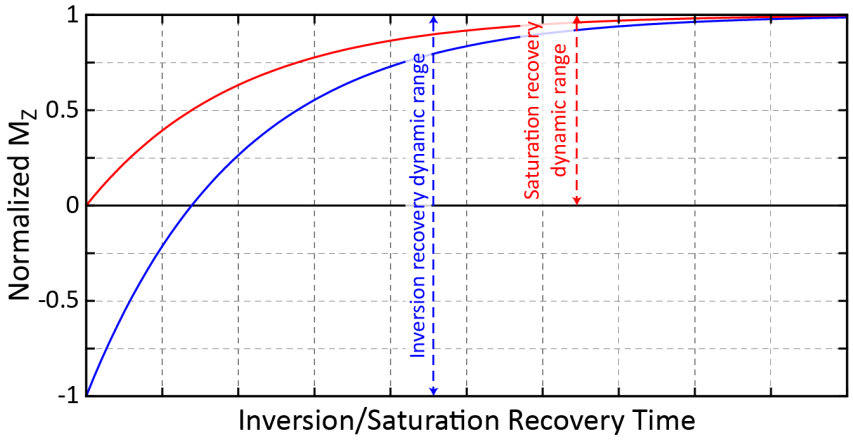

Figure 1.5: Saturation recovery (red) has half the range of longitudinal magnetization values as inversion recovery (blue).

Ideal IR and SR experiments assume that the measured imaging readout signal is directly proportional to the longitudinal magnetization described by Eq. 1.20 and Eq. 1.21. This requirement is only met for imaging sequences that use a single excitation RF pulse, such as a gradient echo or spin echo where a single line of k-space is acquired per readout. In segmented imaging sequences where multiple excitation RF pulses are used to acquire several lines of k-space, T_1 recovery during imaging alters the signal intensity for later readouts and causes systematic errors the calculated T_1 value. Therefore, the gold-standard experiment for quantifying T_1 is an inversion or saturation recovery sequence with a gradient or spin echo readout, with a single line of k-space acquired at a time.

1.5.3 Look-Locker

Both inversion and saturation recovery methods acquire a single sample on the T_1 recovery curve in each repetition, which can be time consuming as single k-space line readouts often require many lengthy repetitions in order to produce a single image. These acquisitions must also be repeated with multiple TI or TS times in order to properly sample the recovery curve.

In 1970, Look and Locker described an accelerated technique for measuring T_1 in which multiple periodic spoiled RF excitations can be used following an inversion pulse without waiting for full magnetization recovery [9]. As each excitation reduces the longitudinal magnetization, the magnetization time course does not follow the standard inversion recovery T_1 recovery curve described in Eq. 1.20. With small flip angle excitations, Diechmann and Hasse showed that the magnetization time course can still be characterized by an

exponential recovery function [10]:

$$M_Z = M_\infty(1 - M_\infty)e^{-t/T_1^*} \tag{1.22}$$

$$M_\infty = M_0 \frac{1 - e^{-TR/T_1}}{1 - e^{-TR/T_1^*}} \tag{1.23}$$

where the repetition time (TR) is the time between excitation pulses.

The magnetization time-course during a Look-Locker experiment thus has a reduced apparent steady-state value, M_∞, and reduced apparent relaxation time constant, T_1^*. It can also be shown the true T_1 time can be calculated using the experimental data with no additional prior information by re-writing Eq. 1.22 as:

$$M_Z = A - Be^{-t/T_1^*} \tag{1.24}$$

$$T_1 = \left({}^{B}/_{A} - 1\right) T_1^* \tag{1.25}$$

where "${}^{B}/_{A} - 1$" is commonly referred to as the "Look-Locker correction factor".

Using this Look-Locker approach, the efficiency of T_1 measurements is greatly increased, as the apparent recovery curve can be sampled many times following a single inversion pulse.

Inversion-recovery spoiled gradient echo Look-Locker techniques have been used to quantify myocardial T_1 values in-vivo [11, 12], with an inversion pulse applied after detection of the QRS complex in ECG gating and spoiled gradient echo images acquired with 15–30 phases (TI times) spanning several cardiac cycles. Look-Locker-like imaging with inversion-recovery balanced SSFP readouts [13, 14] are also routinely used in clinical practice to determine the optimal inversion time for late gadolinium enhanced imaging (Section 1.6.1) and as a method for quantifying cardiac function and fibrosis in a single sequence [15, 16]. The apparent T_1* in this sequence was found to have excellent correlation to histological measures of fibrosis in an ex-vivo swine model [17], although true T_1 values cannot be calculated using Eq. 1.24 and Eq. 1.25 due to the influence of T_2 from the magnetization refocusing of the balanced SSFP readout.

Analysis of in-vivo data from both gradient echo and bSSFP Look-Locker techniques is limited to region of interest (ROI) analysis due to cardiac phase motion over the time-series and time consuming, as the ROIs must be adjusted for each TI time. These techniques may also be confounded by through-plane motion, as the physical slice of interest does not experience a continuous consistent flip angle excitation if it moves outside of the excitation plane during the cardiac cycle.

1.5.4 Modified-Look-Locker Inversion Recovery (MOLLI)

The MOdified Look-Locker Inversion recovery (MOLLI) sequence proposed by Messroghli *et al.* [18] addresses several weaknesses of standard Look-Locker imaging in cardiac applications by using single-shot balanced steady-state free precession (bSSFP) image readouts. The single-shot images are ECG triggered to maintain a consistent diastasis cardiac phase, allowing T_1 pixel maps to be generated and a single analysis ROI to be drawn if a stable breath-hold is maintained. Balanced SSFP readouts also have improved blood-tissue contrast and have higher overall signal-to-noise ratios compared to spoiled gradient echo images typically used in Look-Locker experiments.

The MOLLI sequence consists of several "Look-Locker sets", each containing an inversion pulse followed by several ECG triggered single-shot images at diastasis (Fig. 1.6a). Look-Locker sets are separated by several heartbeats for longitudinal magnetization recovery and a variable delay is inserted between the inversion pulse and first image to increment the TI time of the first image between sets. Implementation of MOLLI sequences often alter the number of images in each set, number of sets, and delay between sets to reduce the breath-hold duration and improve sampling for shorter T_1 values [19–21]. A standardized nomenclature has been proposed [22] to describe the sampling pattern, where 3(3)3(3)5 denotes three sets of 3, 3, and 5 images respectively separated by 3 heartbeats (values in parentheses) for recovery. Standard MOLLI analysis fits Eq. 1.24 to combined data from all Look-Locker sets, with the Look-Locker correction (Eq. 1.25) applied to calculate the true T_1 values (Fig. 1.6b).

The accuracy of T_1 values with standard MOLLI sequences is known to be heart rate dependent [18, 19], with greater errors at higher heart rates and long T_1 times. This can be largely attributed to incomplete magnetization recovery between sets, as the typical 3 heartbeat recovery duration can vary significantly with heart rate. Kellman *et al.* recently proposed a 5(3s)3 protocol, denoting two sets of 5 and 3 images separated by at least 3 seconds for recovery [22]. By acquiring the longer set first and ensuring a minimum recovery time of at least 3 seconds, the heart rate variability is greatly reduced at the expense of a slightly longer breath-hold duration.

A conditional fitting algorithm is used for the 5(1)1(1)1 shortened MOLLI ("ShMOLLI") variant [19]. Due to the 1 heartbeat recovery durations, standard MOLLI analysis would be significantly more heart-rate sensitive than other MOLLI protocols with 3 heartbeat recovery durations. The conditional fitting algorithm used for ShMOLLI performs iterative per-pixel analysis to determine the estimated T_1 value and then only include data from the 2^{nd} and 3^{rd} sets if the T_1 is sufficiently short such that there is nearly full M_Z recovery in the 1 heart-

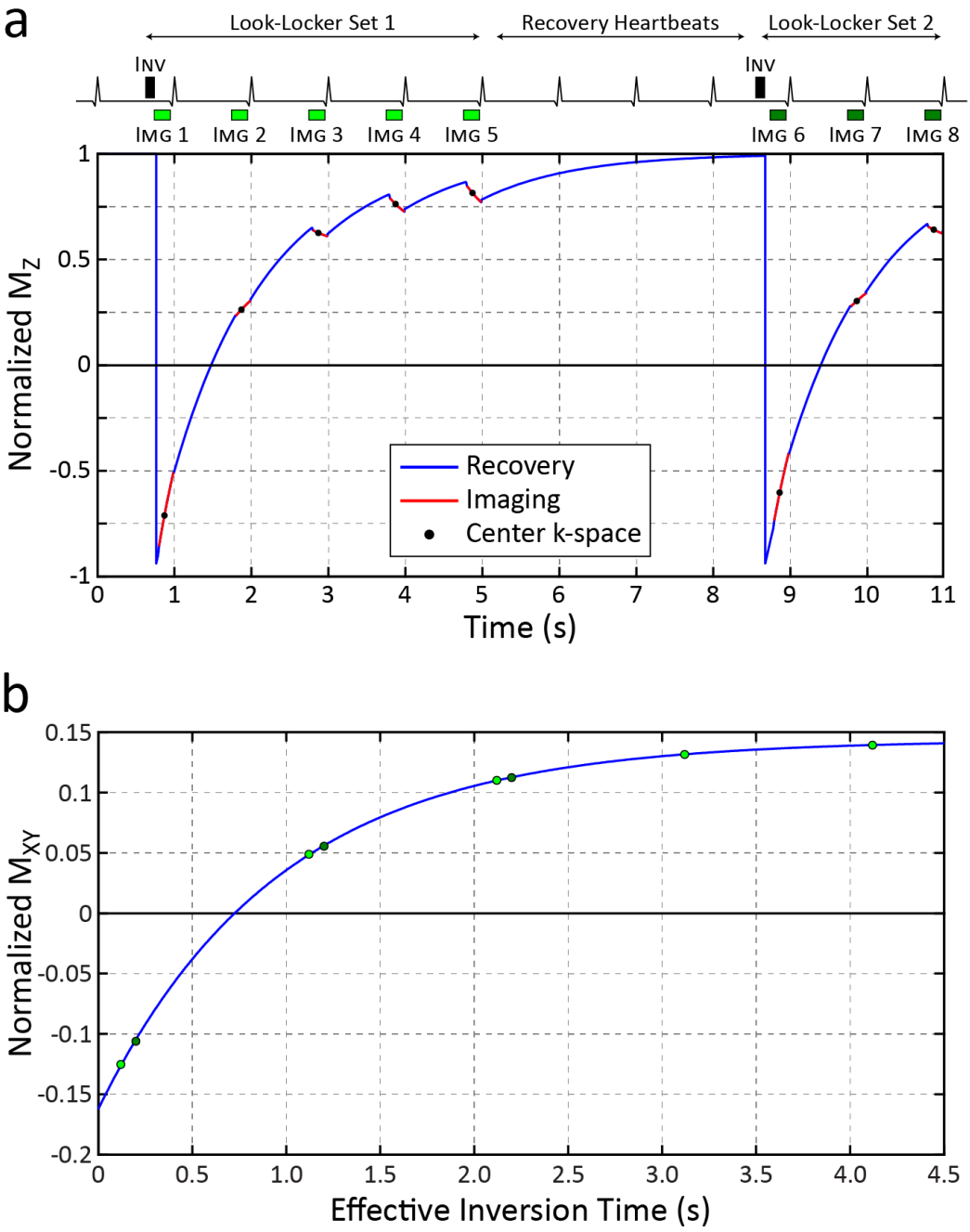

Figure 1.6: **a)** 5(3)3 MOLLI with 2 Look-Locker sets of 5 and 3 images separated by 3 recovery heartbeats. Longitudinal magnetization is perturbed during imaging (red) and follows normal T_1 recovery between images (blue). **b)** Data from both Look-Locker sets are combined and Eq. 1.24 is fit to determine the apparent T_1^* time. True T_1 times are calculated using Eq. 1.25

beat recovery duration. This approach was shown to have reduced heart-rate dependence compared to standard analysis [19], but long T_1 values in the native (non-contrast) setting typically include data only from the first Look-Locker set resulting in reduced precision compared to other MOLLI sampling patterns [22].

MOLLI uses the Look-Locker correction factor to account for the magnetization perturbation caused by the imaging readout. However, as the correction factor was derived for a continuous spoiled gradient echo readout instead of the discrete single-shot bSSFP readouts, significant errors in MOLLI T_1 values can occur. The accuracy of MOLLI T_1 values has been shown to be affected by numerous other sources of error such as T_2 values [23, 24], T_1 values [18, 19, 24], flip angle [25, 26], inversion efficiency [23, 27], off-resonance [28], magnetization transfer [29], and number of phase encode lines in the image readout [26].

The relative effect of these parameters on MOLLI T_1 errors are summarized in Fig. 1.7 using data from Bloch equation simulations of native myocardium with a typical 3(3)5 MOLLI sequence. In each subplot, a single parameter is varied with all other parameters held constant to characterize MOLLI's T_1 error with that parameter alone. Circles indicate the nominal value used when that parameter is held constant. MOLLI's sources of error generally cause underestimation of T_1 values and are in good agreement with the literature described above. T_1 errors are also shown SASHA, another T_1 mapping sequence presented in Chapter 3. While it is useful to characterize these sources of error in isolation, in-vivo experiments are likely affected by all of these factors to various degrees and the interaction of these sources of error is not well understood. MOLLI has been used extensively in clinical studies of myocardial fibrosis, and it is likely that these factors contributed variability and systematic errors to the measured T_1 values. Careful interpretation of MOLLI T_1 values is necessary, as factors such as heart rates, myocardial T_2, and magnetization transfer are often systematically altered with disease [30, 31]. As a result, simple univariate comparisons of MOLLI T_1 values in disease may be significantly confounded by MOLLI's systematic dependencies.

1.6 Myocardial Fibrosis

The cardiac extracellular matrix (ECM) is comprised of a complex collection of collagen and elastin fibers, macromolecules such as proteoglycans, and fibroblast cells. It is essential for maintaining the structure and efficient function of the myoardium and is a dynamic system that can be altered in response to pathological stress. Excessive collagen deposition in the ECM is a common feature of most cardiac diseases and is mediated through complex signaling pathways upregulated in cardiac damage such as the renin-angiotension

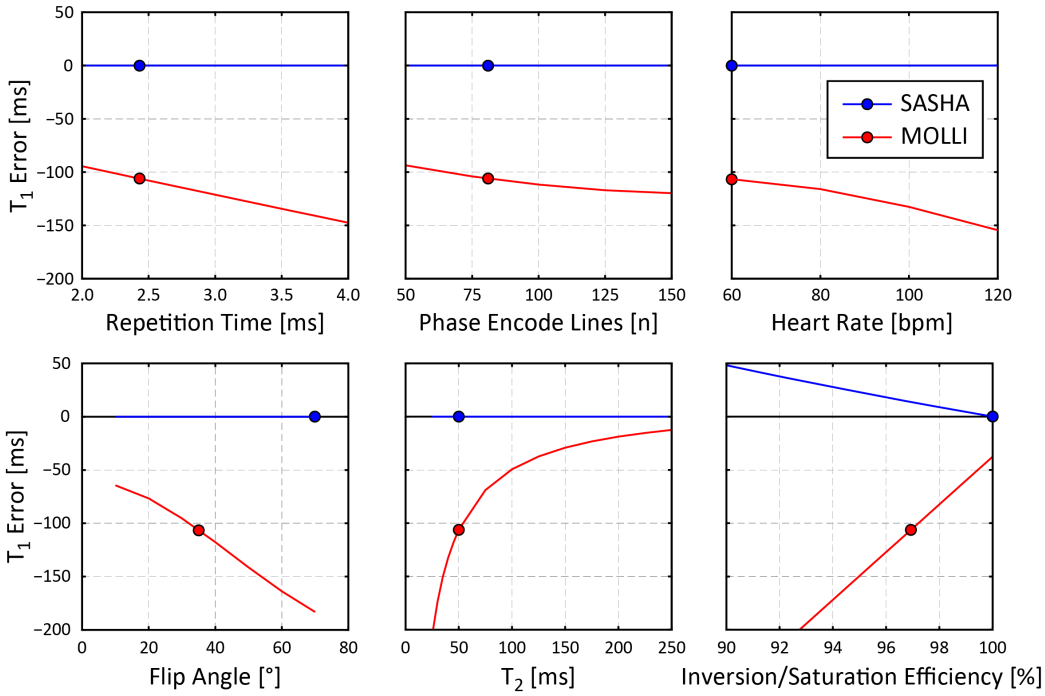

Figure 1.7: Errors in MOLLI and SASHA T_1 values with Bloch equation simulations of native myocardium. Subplots show T_1 errors as each parameter is varied while all other parameters are held constant at nominal values (circles).

system (RAS), transforming growth factor-β (TGF-β), and tumor necrosis factor-α (TNF-α) [32]. The origin of myocardial fibrosis, defined as an increase in collagen deposition in the ECM, can be classified into 3 groups: reactive fibrosis, infiltrative fibrosis, and replacement fibrosis [33]. Reactive fibrosis occurs in response to physiologic stresses to the heart, such as pressure overloading with aortic stenosis or volume overloading in heart failure. Infiltrative fibrosis is the pathological deposition of infiltrates into ECM, such as insoluble proteins in amyloidsis or glycosphingolipids in Anderson-Fabry disease. When functional cardiac myocytes are damaged, the accumulation of structural collagen fibers in their place is known as replacement fibrosis. This can occur in the case of ischemic heart disease, notably myocardial infarction where myocytes are starved of oxygen and undergo necrosis, resulting in a focal scar. However, replacement fibrosis can also occur in more advanced stages of reactive or infiltrative diseases when myocyte integrity is compromised, resulting in a mixed scarring pattern.

The ubiquity of myocardial fibrosis in cardiac disease makes it an important biomarker for assessing disease. Fibrotic remodeling of the heart impairs diastolic function by increasing stiffness, later leading to hypertrophy and systolic dysfunction [34]. It is an appealing target in cardiac disease therapy [35] and non-invasive fibrosis measurements may provide

relevant information to guide treatment. Early detection of pathological fibrosis may also help to identify patients that are at higher risk for further disease progression and require prophylactic treatment.

Myocardial fibrosis is traditionally assessed through histological analysis, particularly picrosirius red staining, which selectively visualizes collagen I and III fibers. While this provides gold standard measurements of collagen volume, it has limited clinical utility due to the need for an invasively obtained biopsy sample. Additionally, endomyocardial biopsies are generally obtained from the interventricular septum [36] and may not be representative of the whole heart, particularly in diseases with a heterogeneous fibrosis distribution.

1.6.1 Late Gadolinium Enhancement

Fibrosis is routinely assessed non-invasively with cardiac MRI using a contrast-enhanced technique called late gadolinium enhancement (LGE) or delayed enhancement (DE) imaging. Gadolinium is a highly paramagnetic ion with a large number of unpaired electrons that generate a large time-varying magnetic field due to its molecular motion. This shortens the T_1 and T_2 relaxations time of protons in its nearby vicinity, and thus provides an additional form of image contrast. However, free gadolinium ions are highly toxic and must be rendered biologically inactive by ligation to large macromolecules. Various ligates are widely used and their size and structure determine the distribution of the contrast agent when administered to a subject. For LGE imaging, common macromolecules are diethylene triamine pentaacetic acid (DTPA), and DO3A-butrol, which are large extracellular chelates that can move from the blood pool into interstitial spaces, but are too large to enter intracellular spaces.

LGE imaging visualizes myocardial scarring through a combination of two differences between scarred tissue and healthy tissue: increased extracellular volume and reduced blood flow. The T_1 shortening of the contrast agent is proportional to its concentration, and thus the myocardial T_1 is inversely proportional to its extracellular volume. Regions of large replacement fibrosis (focal scarring) are often poorly perfused, leading to delayed contrast washout kinetics, further increasing contrast between infarcted tissue, healthy myocardium, and the blood pool [37]. In practice, T_1-weighted images are acquired approximately 10–15 minutes following intravenous contrast administration to maximize the T_1 differences between infarcted and healthy myocardium, with hyperintensities in LGE imaging being an average of 485% brighter than that of normal myocardium [38]. The spatial extent of scarred myocardium has been validated with excellent correlation to gold standard triphenyltetrazolium chloride (TTC) histology staining for necrosis in an animal model [39] and spatial

location correlated with coronary artery territories identified with angiography in humans [40].

Cardiac MRI has become the gold standard for the non-invasive assessment of focal replacement myocardial fibrosis through the use of contrast-enhanced imaging. The phase sensitive inversion-recovery segmented gradient echo imaging sequence [41] has been found to generate robust high contrast images in clinical practice. An experienced radiologist or cardiologist often visually interprets LGE imaging, commonly noting infarct location, transmurality, and pattern in clinical reports. Advanced analysis of LGE imaging is also widely used, where semi-automated signal intensity analysis is used to identify scar regions and quantify the "grey-zone" regions of intermediate signal intensity. However, the fundamental principle of LGE imaging relies on generating contrast between fibrotic tissue and assumed healthy myocardium. In diffuse fibrosis, the extracellular volume is globally increased, resulting in a homogenously decreased T_1 value and thus no identifiable contrast in LGE images.

1.6.2 Post-contrast T_1 Mapping

T_1 mapping techniques have been used to assess diffuse fibrosis by quantifying myocardial T_1 values following contrast administration. Post-contrast T_1 values can be calculated as:

$$\frac{1}{T_{1,\text{post}}} = \frac{1}{T_{1,\text{pre}}} + r_1[Gd] \tag{1.26}$$

where $T_{1,\text{pre}}$ is the native (non-contrast) T_1 value, [Gd] is the gadolinium concentration, and r_1 is the relaxivity constant which is approximately 4.5 $mM^{-1} \cdot s^{-1}$ for Gd-DTPA. Assuming that pre-contrast myocardial T_1 values are constant, post-contrast myocardial T_1 values are thus inversely proportional to the contrast agent concentration.

It is important to note that for extracellular contrast agents typically used, protons in the intracellular and extracellular space have different T_1 relaxation values. It is generally assumed that for typical contrast agent concentrations and biological relevant permeability coefficients, there is fast proton exchange between these spaces and thus the combined spaces can be characterized with a single mono-exponential T_1 value and thus equation 1.26 is applicable. However, inter-extracellular exchange is appropriately classified as "intermediate to fast" [42], and is more appropriately modeled as intermediate exchange between two site (2SX) [43, 44]. Estimates of myocardial extracellular volume fraction (discussed below) in a mouse model using multiple post-contrast measurements starting at 4 minutes have shown better correlation with histological fibrosis measurements with a 2SX model than a fast exchange model [45].

Contrast agents are typically administered in a single bolus injection, with the dosage normalized to the subject's body weight in order to partially account for subject-to-subject variations in total blood volume. It has been shown that for myocardial blood flow rates above 0.5 $mL{\cdot}g^{-1}{\cdot}min^{-1}$, equilibrium is established between contrast concentrations in the blood and the tissue to within 1% by 3 minutes following contrast [11]. A study comparing extracellular volume measurements using a bolus injection and a continuous infusion of contrast [46] showed high agreement except in cases where the extracellular volume fraction exceeded 40% such as in amyloidosis or focal scarring in myocardial infarction or hypertrophic cardiomyopathy [47].

As most contrast agents are renally cleared from the body with an elimination half life of ~100 minutes, the myocardial and blood pool contrast concentration also depend on the time between contrast administration and imaging as well as kidney function. This effect can be partially mitigated by ensuring consistent timing of post-contrast imaging.

1.6.3 Extracellular Volume Fraction Imaging

The tissue-blood partition coefficient, λ, is defined as the ratio of contrast agent concentration in the myocardium divided by the blood concentration. These concentrations can be estimated by re-arranging Eq. 1.26 and using native and post-contrast T_1 values:

$$\lambda = \frac{[\mathrm{Gd}]_{\mathrm{myo}}}{[\mathrm{Gd}]_{\mathrm{blood}}}$$

$$\lambda = \frac{\left(\dfrac{1}{T_{1,\mathrm{tissue,post}}} - \dfrac{1}{T_{1,\mathrm{tissue,pre}}}\right) \Big/ r_{1,\mathrm{tissue}}}{\left(\dfrac{1}{T_{1,\mathrm{blood,post}}} - \dfrac{1}{T_{1,\mathrm{blood,pre}}}\right) \Big/ r_{1,blood}} \tag{1.27}$$

The relaxivity is often assumed to be the same in the blood and the tissue [42], simplifying the calculation to:

$$\lambda = \frac{\dfrac{1}{T_{1,\mathrm{tissue,post}}} - \dfrac{1}{T_{1,\mathrm{tissue,pre}}}}{\dfrac{1}{T_{1,\mathrm{blood,post}}} - \dfrac{1}{T_{1,\mathrm{blood,pre}}}} \tag{1.28}$$

Measurements of the partition coefficient are theoretically independent of the time interval between contrast administration and measurement, provided that the concentrations

in the blood and tissue have reached equilibrium. A recent consensus statement on T_1 mapping estimates of fibrosis recommends a delay of at least 15 minutes following contrast agent [48] to ensure equilibrium.

Within the blood pool, the contrast agent is distributed solely within the blood serum and does not enter red blood cells. Therefore blood samples with a larger red blood cell volume, commonly termed hematocrit, have lower overall contrast concentrations due to a lower serum volume fraction. The serum volume fraction can be determined using routine blood sample lab analysis and is equal to 1-Hct, and the hematocrit (Hct) is approximately equal to 0.44 for men and 0.40 for women. The extracellular volume (ECV) fraction can therefore be calculated as:

$$\mathrm{ECV} = \lambda(1 - \mathrm{Hct}) \tag{1.29}$$

ECV measurements using T_1 mapping are appealing in that they provide a physiologically relevant metric that can be compared directly to histological fibrosis measurements. ECV values are also appealing in that they are theoretically independent of contrast concentration and measurement time. However, four T_1 values plus a blood sample measurement are required, and thus ECV measurements may have larger variability due to error propagation than single measurements like post-contrast myocardial T_1 values directly.

1.6.4 Native Myocardial T_1 Mapping

Expansion of the extracellular volume causes an increase in the native (non-contrast) myocardial T_1 and T_2 relaxation times. The increase in relaxation times is a result of a relative increase in the free water proportion of the FPD model (Section 1.4.4), which has longer T_1 and T_2 times than the hydration layer. Quantification of fibrosis using native T_1 mapping is appealing as it does not require the use of contrast agents, which may cause adverse reactions in a small proportional of subjects [49] and is contraindicated in patients with impaired renal function due to the risk of nephrogenic systemic fibrosis [50]. However, as native relaxation values are reflective of the overall microstructural environment, myocardial T_1 values are influenced by not only by changes in ECV with fibrosis, but also other factors such as infiltrative depositions in amyloidosis, thalassemia, and Anderson-Fabry disease. A native T_1 map in a healthy volunteer is shown in Fig. 1.8.

1.6.5 Clinical Studies with T_1 Mapping

T_1 mapping has been used extensively to quantify fibrosis in many disease populations using all of the techniques described above and several excellent reviews of the literature have

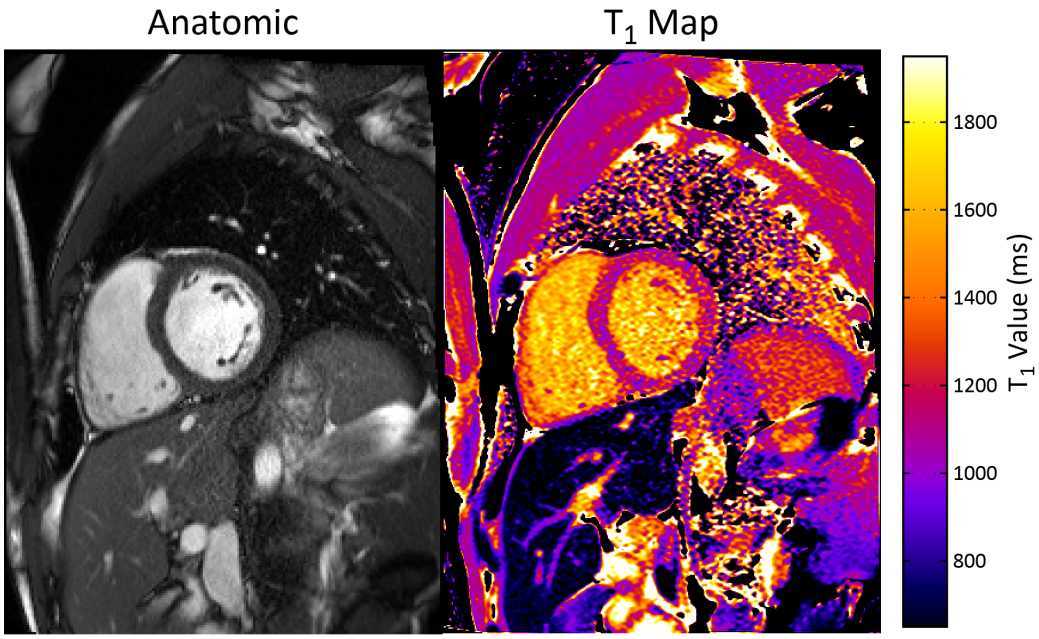

Figure 1.8: An short-axis view of the heart with an anatomic bSSFP image (left) and a native parametric T_1 map (right) in a healthy volunteer.

been written [33, 51, 52]. Briefly, studies have shown decreased post-contrast myocardial T_1 values and increased λ and ECV in patients with hypertrophic cardiomyopathy [46], dilated cardiomyopathy [11], aortic stenosis [46], and heart failure [53]. Larger changes in post-contrast myocardial T_1 values, λ, and ECV were found in patients with amyloidosis [51, 54] and acute myocardial infarction [51, 55, 56], suggesting greater expansion of the extracellular space. Native myocardial T_1 values were increased in most diseases such as hypertrophic and dilated cardiomyopathy [57], myocardial edema [58], and aortic stenosis [59], although reduced T_1 values were consistently found in Anderson-Fabry disease [60, 61] and attributed to the short T_1 values of the fatty infiltrates. Native and post-contrast myocardial T_1 as well as MRI-derived ECV have all been validated with histological measurements of collagen volume fraction in a post-mortem study [62], heart transplant recipients [53, 63], and patients with aortic stenosis [59] and amyloidosis [64].

In a prospective study with 793 consecutive patients referred for cardiac MRI, multivariate Cox regression found increased ECV to be an independent predictor of both all-cause mortality and a composite end point of heart transplant or ventricular assist device (VAD) free survival, with a hazard ratio magnitude similar to left ventricular ejection fraction [65]. This study suggests that ECV may therefore be a clinically relevant biomarker for disease severity that can be routinely assessed in cardiac MRI patients. Given its histological validation with myocardial fibrosis, ECV also has the potential to become a theraputic target

for angiotensin-converting-enzyme (ACE) inhibitor drugs such as lisinopril, which have been shown to reduce fibrosis in patients with hypertensive heart disease [66].

The vast majority of published studies use the MOLLI and ShMOLLI T_1 mapping sequences due to their availability and ease of analysis. However, known systematic dependencies of MOLLI sequences can result in changes in myocardial T_1 values that are unrelated to fibrosis, as described in Section 1.5.4. These confounders may result in increased variability of measured T_1 and ECV values, but may also cause systematic changes in T_1 values that are misinterpreted as fibrosis. Improvements in the accuracy, precision, and robustness of T_1 mapping techniques are essential for translation of T_1 fibrosis measurements into widespread clinical practice.

1.7 Scope of Thesis

This thesis focuses on the characterization of systematic sources of error in the MOLLI sequence and the development and optimization of a new T_1 mapping technique, SASHA, which is robust to systematic errors. Chapter 2 presents the time-weighted average model of relaxation for the MOLLI sequence that intuitively and analytically describes the influence and interaction of many of MOLLI's sources of error, which have only been described empirically in the current literature. Chapter 3 outlines the basic principles of the SAturation-recovery single-SHot Acqusition (SASHA) sequence using a 3-parameter model and describes its robustness against many of MOLLI's sources of error with a theoretical foundation and experimental validation with phantom experiments. Analysis of SASHA data using a 2-parameter model was found to yield higher precision in calculated T_1 values at the expense of introducing systematic biases. Chapter 4 and 5 focus on improvements to the SASHA sequence that minimize these systematic errors. Chapter 4 details the optimization of flip angles in saturation pulse trains, enabling robust magnetization saturation at commonly used 1.5T and 3T field strengths, with the goal of reducing saturation performance as a source of error in SASHA. Chapter 5 describes the development of a variable flip angle readout that was found to reduce these systematic biases and improves image quality. Finally, Chapter 6 concludes with a discussion about the interpretation and limitations of fibrosis measurements with MOLLI and SASHA and some possible directions for further development.

1.8 References

[1] World Health Organization. Global status report on noncommunicable diseases 2010. Technical report, Geneva, 2011. pg. 1

[2] Statistics Canada. Mortality, Summary List of Causes 2009. Technical report, July 2012. pg. 1, pg. 1

[3] A S Go, D Mozaffarian, V L Roger, E J Benjamin, J D Berry, M J Blaha, S Dai, E S Ford, C S Fox, S Franco, H J Fullerton, C Gillespie, S M Hailpern, J A Heit, V J Howard, M D Huffman, S E Judd, B M Kissela, S J Kittner, D T Lackland, J H Lichtman, L D Lisabeth, R H Mackey, D J Magid, G M Marcus, A Marelli, D B Matchar, D K McGuire, E R Mohler, C S Moy, M E Mussolino, R W Neumar, G Nichol, D K Pandey, N P Paynter, M J Reeves, P D Sorlie, J Stein, A Towfighi, T N Turan, S S Virani, N D Wong, D Woo, M B Turner, and on behalf of the American Heart Association Statistics Committee and Stroke Statistics Subcommittee. Heart Disease and Stroke Statistics–2014 Update: A Report From the American Heart Association. *Circulation*, 129(3):e28–e292, January 2014. pg. 1, pg. 1

[4] M A Bernstein, K F King, and X J Zhou. *Handbook of MRI Pulse Sequences*. Elsevier Science, 2004. pg. 6

[5] F Bloch. Nuclear Induction. *Physical Review*, 70(7-8):460–474, October 1946. pg. 8

[6] N Bloembergen, E Purcell, and R Pound. Relaxation Effects in Nuclear Magnetic Resonance Absorption. *Physical Review*, 73(7):679–712, April 1948. pg. 10

[7] Gary D Fullerton, Janet L Potter, and N Carol Dornbluth. NMR relaxation of protons in tissues and other macromolecular water solutions. *Magnetic resonance imaging*, 1(4):209–226, 1982. pg. 11

[8] J R Zimmerman and W E Brittin. Nuclear Magnetic Resonance Studies in Multiple Phase Systems: Lifetime of a Water Molecule in an Adsorbing Phase on Silica Gel. *The Journal of Physical Chemistry*, 61(10):1328–1333, October 1957. pg. 12

[9] D Look and D Locker. Time Saving in Measurement of NMR and EPR Relaxation Times. *Review of Scientific Instruments*, 41(2):250–251, 1970. pg. 14

[10] R Deichmann and Axel Haase. Quantification of T1 values by SNAPSHOT-FLASH NMR imaging. *Journal of Magnetic Resonance*, 96(3):608–612, February 1992. pg. 15

[11] Michael Jerosch-Herold, David C Sheridan, Jessica D Kushner, Deirdre Nauman, Donna Burgess, Diana Dutton, Rami Alharethi, Duanxiang Li, and Ray E Hershberger. Cardiac magnetic resonance imaging of myocardial contrast uptake and blood flow in patients affected with idiopathic or familial dilated cardiomyopathy. *American journal of physiology Heart and circulatory physiology*, 295(3):H1234–H1242, September 2008. pg. 15, pg. 22, pg. 24

[12] Craig S Broberg, Sumeet S Chugh, Catherine Conklin, David J Sahn, and Michael Jerosch-Herold. Quantification of diffuse myocardial fibrosis and its association with myocardial dysfunction in congenital heart disease. *Circulation: Cardiovascular Imaging*, 3(6):727–734, November 2010. pg. 15

[13] Peter Schmitt, Mark A Griswold, Peter M Jakob, Markus Kotas, Vikas Gulani, Michael Flentje, and Axel Haase. Inversion recovery TrueFISP: quantification of T(1), T(2), and spin density. *Magnetic Resonance in Medicine*, 51(4):661–667, April 2004. pg. 15

[14] Ankur Gupta, Vivian S Lee, Yiu-Cho Chung, James S Babb, and Orlando P Simonetti. Myocardial Infarction: Optimization of Inversion Times at Delayed Contrast-enhanced MR Imaging. *Radiology*, 233(3):921–926, December 2004. pg. 15

[15] J S Detsky, Jeffrey A Stainsby, R Vijayaraghavan, John J Graham, A J Dick, and G A Wright. Inversion-recovery-prepared SSFP for cardiac-phase-resolved delayed-enhancement MRI. *Magnetic Resonance in Medicine*, 58(2):365–372, July 2007. pg. 15

[16] Kim A Connelly, Jay S Detsky, John J Graham, Gideon Paul, Ram Vijayaragavan, Alexander J Dick, and Graham A Wright. Multicontrast late gadolinium enhancement imaging enables viability and wall motion assessment in a single acquisition with reduced scan times. *Journal of magnetic resonance imaging : JMRI*, 30(4):771–777, October 2009. pg. 15

[17] M Pop, V Ramanan, F Yang, L Zhang, S Newbigging, N Ghugre, and G Y1 Wright. High resolution 3D T1*-mapping and quantitative image analysis of gray zone in chronic fibrosis. *Biomedical Engineering, IEEE Transactions on*, PP(99):1–1, 2014. pg. 15

[18] Daniel R Messroghli, Aleksandra Radjenovic, Sebastian Kozerke, David M Higgins, Mohan U Sivananthan, and John P Ridgway. Modified Look-Locker inversion recovery

(MOLLI) for high-resolution T1 mapping of the heart. *Magnetic Resonance in Medicine*, 52(1):141–146, July 2004. pg. 16, pg. 16, pg. 18

[19] Stefan K Piechnik, Vanessa M Ferreira, Erica Dall'Armellina, Lowri E Cochlin, Andreas Greiser, Stefan Neubauer, and Matthew D Robson. Shortened Modified Look-Locker Inversion recovery (ShMOLLI) for clinical myocardial T1-mapping at 1.5 and 3 T within a 9 heartbeat breathhold. *Journal of cardiovascular magnetic resonance : official journal of the Society for Cardiovascular Magnetic Resonance*, 12:69, 2010. pg. 16, pg. 16, pg. 16, pg. 18, pg. 18

[20] Jason J Lee, Songtao Liu, Marcelo S Nacif, Martin Ugander, Jing Han, Nadine Kawel, Christopher T Sibley, Peter Kellman, Andrew E Arai, and David A Bluemke. Myocardial T1 and extracellular volume fraction mapping at 3 tesla. *Journal of cardiovascular magnetic resonance : official journal of the Society for Cardiovascular Magnetic Resonance*, 13:75, 2011.

[21] Erik B Schelbert, Stephen M Testa, Christopher G Meier, William J Ceyrolles, Joshua E Levenson, Alexander J Blair, Peter Kellman, Bobby L Jones, Daniel R Ludwig, David S Schwartzman, Sanjeev G Shroff, and Timothy C Wong. Myocardial extravascular extracellular volume fraction measurement by gadolinium cardiovascular magnetic resonance in humans: slow infusion versus bolus. *Journal of cardiovascular magnetic resonance : official journal of the Society for Cardiovascular Magnetic Resonance*, 13:16, 2011. pg. 16

[22] Peter Kellman and Michael Schacht Hansen. T1-mapping in the heart: accuracy and precision. *Journal of cardiovascular magnetic resonance : official journal of the Society for Cardiovascular Magnetic Resonance*, 16(1):2, January 2014. pg. 16, pg. 16, pg. 18

[23] Kelvin Chow, Jacqueline A Flewitt, Joseph J Pagano, Jordin D Green, Matthias G Friedrich, and Richard B Thompson. MOLLI T1 Values Have Systematic T2 and Inversion Efficiency Dependent Errors. In *Proceedings of the International Society for Magnetic Resonance in Medicine*, page 395, 2012. pg. 18, pg. 18

[24] Neville D Gai, Christian Stehning, Marcelo Nacif, and David A Bluemke. Modified Look-Locker T1 evaluation using Bloch simulations: human and phantom validation. *Magnetic Resonance in Medicine*, 69(2):329–336, February 2013. pg. 18, pg. 18

[25] Daniel R Messroghli, Andreas Greiser, Mirko Fröhlich, Rainer Dietz, and Jeanette Schulz-Menger. Optimization and validation of a fully-integrated pulse sequence for

modified look-locker inversion-recovery (MOLLI) T1 mapping of the heart. *Journal of magnetic resonance imaging : JMRI*, 26(4):1081–1086, October 2007. pg. 18

[26] Kelvin Chow, Joseph J Pagano, and Richard B Thompson. An Intuitive Model of Several Factors Affecting Accuracy of MOLLI T1 Values. In *Proceedings of the International Society for Magnetic Resonance in Medicine*, 2013. pg. 18, pg. 18

[27] Peter Kellman, Daniel A Herzka, and Michael Schacht Hansen. Adiabatic inversion pulses for myocardial T1 mapping. *Magnetic Resonance in Medicine*, 71(4):1428–1434, 2014. pg. 18

[28] Peter Kellman, Daniel A Herzka, Andrew E Arai, and Michael Schacht Hansen. Influence of Off-resonance in myocardial T1-mapping using SSFP based MOLLI method. *Journal of cardiovascular magnetic resonance : official journal of the Society for Cardiovascular Magnetic Resonance*, 15:63, 2013. pg. 18

[29] Matthew D Robson, Stefan K Piechnik, Elizabeth M Tunnicliffe, and Stefan Neubauer. T1 measurements in the human myocardium: The effects of magnetization transfer on the SASHA and MOLLI sequences. *Magnetic Resonance in Medicine*, July 2013. pg. 18

[30] C B Higgins, R Herfkens, M J Lipton, R Sievers, P Sheldon, L Kaufman, and L E Crooks. Nuclear magnetic resonance imaging of acute myocardial infarction in dogs: alterations in magnetic relaxation times. *The American journal of cardiology*, 52(1):184–188, July 1983. pg. 18

[31] Oliver M Weber, Peter Speier, Klaus Scheffler, and Oliver Bieri. Assessment of magnetization transfer effects in myocardial tissue using balanced steady-state free precession (bSSFP) cine MRI. *Magnetic Resonance in Medicine*, 62(3):699–705, 2009. pg. 18

[32] Hans J de Haas, Eloisa Arbustini, Valentin Fuster, Christopher M Kramer, and Jagat Narula. Molecular imaging of the cardiac extracellular matrix. *Circulation research*, 114(5):903–915, February 2014. pg. 19

[33] Nathan Mewton, Chia Ying Liu, Pierre Croisille, David A Bluemke, and João A C Lima. Assessment of myocardial fibrosis with cardiovascular magnetic resonance. *Journal of the American College of Cardiology*, 57(8):891–903, February 2011. pg. 19, pg. 24

[34] C A Souders, S L K Bowers, and T A Baudino. Cardiac Fibroblast: The Renaissance Cell. *Circulation research*, 105(12):1164–1176, December 2009. pg. 19

[35] Gabriela Kania, Przemyslaw Blyszczuk, and Urs Eriksson. Mechanisms of cardiac fibrosis in inflammatory heart disease. *Trends in cardiovascular medicine*, 19(8):247–252, November 2009. pg. 19

[36] Hossein Ardehali, Edward K Kasper, and Kenneth L Baughman. Diagnostic approach to the patient with cardiomyopathy: Whom to biopsy. *American heart journal*, 149(1):7–12, 2005. pg. 20

[37] Raymond Y Kwong and Hema Korlakunta. Diagnostic and prognostic value of cardiac magnetic resonance imaging in assessing myocardial viability. *Topics in magnetic resonance imaging : TMRI*, 19(1):15–24, February 2008. pg. 20

[38] O P Simonetti, R J Kim, D S Fieno, H B Hillenbrand, E Wu, J M Bundy, J P Finn, and R M Judd. An improved MR imaging technique for the visualization of myocardial infarction. *Radiology*, 218(1):215–223, 2001. pg. 20

[39] Raymond J Kim, David S Fieno, Todd B Parrish, Kathleen Harris, Enn-Ling Chen, Orlando Simonetti, Jeffrey Bundy, J Paul Finn, Francis J Klocke, and Robert M Judd. Relationship of MRI Delayed Contrast Enhancement to Irreversible Injury, Infarct Age, and Contractile Function. *Circulation*, 100(19):1992–2002, November 1999. pg. 20

[40] Edwin Wu, Robert M Judd, John D Vargas, Francis J Klocke, Robert O Bonow, and Raymond J Kim. Visualisation of presence, location, and transmural extent of healed Q-wave and non-Q-wave myocardial infarction. *The Lancet*, 357(9249):21–28, January 2001. pg. 21

[41] Peter Kellman, Andrew E Arai, Elliot R McVeigh, and Anthony H Aletras. Phase-sensitive inversion recovery for detecting myocardial infarction using gadolinium-delayed hyperenhancement. *Magnetic Resonance in Medicine*, 47(2):372–383, February 2002. pg. 21

[42] Kathleen M Donahue, R M Weisskoff, and D Burstein. Water diffusion and exchange as they influence contrast enhancement. *Journal of magnetic resonance imaging : JMRI*, 7(1):102–110, 1997. pg. 21, pg. 22

[43] C S Landis, X Li, F W Telang, P E Molina, I Palyka, G Vetek, and C S Springer. Equilibrium transcytolemmal water-exchange kinetics in skeletal muscle in vivo. *Magnetic Resonance in Medicine*, 42(3):467–478, September 1999. pg. 21

[44] C S Landis, X Li, F W Telang, J A Coderre, P L Micca, W D Rooney, L L Latour, G Vétek, I Pályka, and C S Springer. Determination of the MRI contrast agent

concentration time course in vivo following bolus injection: effect of equilibrium transcytolemmal water exchange. *Magnetic Resonance in Medicine*, 44(4):563–574, October 2000. pg. 21

[45] Otavio R Coelho-Filho, François-Pierre Mongeon, Richard Mitchell, Heitor Moreno, Wilson Nadruz, Raymond Y Kwong, and Michael Jerosch-Herold. Role of transcytolemmal water-exchange in magnetic resonance measurements of diffuse myocardial fibrosis in hypertensive heart disease. *Circulation: Cardiovascular Imaging*, 6(1):134–141, 2013. pg. 21

[46] Andrew S Flett, Martin P Hayward, Michael T Ashworth, Michael Schacht Hansen, Andrew M Taylor, Perry M Elliott, Christopher McGregor, and James Charles Moon. Equilibrium contrast cardiovascular magnetic resonance for the measurement of diffuse myocardial fibrosis: preliminary validation in humans. *Circulation*, 122(2):138–144, July 2010. pg. 22, pg. 24, pg. 24

[47] Steven K White, Daniel M Sado, Marianna Fontana, Sanjay M Banypersad, Viviana Maestrini, Andrew S Flett, Stefan K Piechnik, Matthew D Robson, Derek J Hausenloy, Amir M Sheikh, Philip Nigel Hawkins, and James Charles Moon. T1 Mapping for Myocardial Extracellular Volume Measurement by CMR: Bolus Only Versus Primed Infusion Technique. *JACC: Cardiovascular Imaging*, 6(9):955–962, April 2013. pg. 22

[48] James Charles Moon, Daniel R Messroghli, Peter Kellman, Stefan K Piechnik, Matthew D Robson, Martin Ugander, Peter D Gatehouse, Andrew E Arai, Matthias G Friedrich, Stefan Neubauer, Jeanette Schulz-Menger, and Erik B Schelbert. Myocardial T1 mapping and extracellular volume quantification: a Society for Cardiovascular Magnetic Resonance (SCMR) and CMR Working Group of the European Society of Cardiology consensus statement. *Journal of cardiovascular magnetic resonance : official journal of the Society for Cardiovascular Magnetic Resonance*, 15:92, 2013. pg. 23

[49] Martin R Prince, Honglei Zhang, Zhitong Zou, Ronald B Staron, and Paula W Brill. Incidence of immediate gadolinium contrast media reactions. *AJR American journal of roentgenology*, 196(2):W138–43, February 2011. pg. 23

[50] Zhitong Zou, Hong Lei Zhang, Giles H Roditi, Tim Leiner, Walter Kucharczyk, and Martin R Prince. Nephrogenic systemic fibrosis review of 370 biopsy-confirmed cases. *JACC: Cardiovascular Imaging*, 4(11):1206–1216, November 2011. pg. 23

[51] Daniel M Sado, Andrew S Flett, Sanjay M Banypersad, Steven K White, Viviana Maestrini, Giovanni Quarta, Robin H Lachmann, Elaine Murphy, Atul Mehta, Derralynn A Hughes, William J McKenna, Andrew M Taylor, Derek J Hausenloy, Philip Nigel Hawkins, Perry M Elliott, and James Charles Moon. Cardiovascular magnetic resonance measurement of myocardial extracellular volume in health and disease. *Heart (British Cardiac Society)*, 98(19):1436–1441, October 2012. pg. 24, pg. 24, pg. 24

[52] Martin Ugander, Abiola J Oki, Li-Yueh Hsu, Peter Kellman, Andreas Greiser, Anthony H Aletras, Christopher T Sibley, Marcus Y Chen, W Patricia Bandettini, and Andrew E Arai. Extracellular volume imaging by magnetic resonance imaging provides insights into overt and sub-clinical myocardial pathology. *European heart journal*, 33(10):1268–1278, May 2012. pg. 24

[53] Leah Iles, Heinz Pfluger, Arintaya Phrommintikul, Joshi Cherayath, Pelin Aksit, Sandeep N Gupta, David M Kaye, and Andrew J Taylor. Evaluation of diffuse myocardial fibrosis in heart failure with cardiac magnetic resonance contrast-enhanced T1 mapping. *Journal of the American College of Cardiology*, 52(19):1574–1580, November 2008. pg. 24, pg. 24

[54] Alicia Maria Maceira, Jayshree Joshi, Sanjay Kumar Prasad, James Charles Moon, Enrica Perugini, Idris Harding, Mary Noelle Sheppard, Philip Alexander Poole-Wilson, Philip Nigel Hawkins, and Dudley John Pennell. Cardiovascular magnetic resonance in cardiac amyloidosis. *Circulation*, 111(2):186–193, January 2005. pg. 24

[55] Sebastian J Flacke, S E Fischer, and C H Lorenz. Measurement of the gadopentetate dimeglumine partition coefficient in human myocardium in vivo: normal distribution and elevation in acute and chronic infarction. *Radiology*, 218(3):703–710, March 2001. pg. 24

[56] Daniel R Messroghli, Kevin Walters, Sven Plein, Patrick Sparrow, Matthias G Friedrich, John P Ridgway, and Mohan U Sivananthan. Myocardial T1 mapping: application to patients with acute and chronic myocardial infarction. *Magnetic Resonance in Medicine*, 58(1):34–40, July 2007. pg. 24

[57] Sairia Dass, Joseph J Suttie, Stefan K Piechnik, Vanessa M Ferreira, Cameron J Holloway, Rajarshi Banerjee, Masliza Mahmod, Lowri Cochlin, Theodoros D Karamitsos, Matthew D Robson, Hugh Watkins, and Stefan Neubauer. Myocardial tissue characterization using magnetic resonance noncontrast t1 mapping in hypertrophic and dilated

cardiomyopathy. *Circulation: Cardiovascular Imaging*, 5(6):726–733, November 2012. pg. 24

[58] Vanessa M Ferreira, Stefan K Piechnik, Erica Dall'Armellina, Theodoros D Karamitsos, Jane M Francis, Robin P Choudhury, Matthias G Friedrich, Matthew D Robson, and Stefan Neubauer. Non-contrast T1-mapping detects acute myocardial edema with high diagnostic accuracy: a comparison to T2-weighted cardiovascular magnetic resonance. *Journal of cardiovascular magnetic resonance : official journal of the Society for Cardiovascular Magnetic Resonance*, 14(1):42, June 2012. pg. 24

[59] Sacha Bull, Steven K White, Stefan K Piechnik, Andrew S Flett, Vanessa M Ferreira, Margaret Loudon, Jane M Francis, Theodoros D Karamitsos, Bernard D Prendergast, Matthew D Robson, Stefan Neubauer, James Charles Moon, and Saul G Myerson. Human non-contrast T1 values and correlation with histology in diffuse fibrosis. *Heart (British Cardiac Society)*, 99(13):932–937, July 2013. pg. 24, pg. 24

[60] Daniel M Sado, Steven K White, Stefan K Piechnik, Sanjay M Banypersad, Thomas Treibel, Gabriella Captur, Marianna Fontana, Viviana Maestrini, Andrew S Flett, Matthew D Robson, Robin H Lachmann, Elaine Murphy, Atul Mehta, Derralynn Hughes, Stefan Neubauer, Perry M Elliott, and James Charles Moon. Identification and assessment of Anderson-Fabry disease by cardiovascular magnetic resonance noncontrast myocardial T1 mapping. *Circulation: Cardiovascular Imaging*, 6(3):392–398, May 2013. pg. 24

[61] Richard B Thompson, Kelvin Chow, Aneal Khan, Alicia Chan, Miriam Shanks, Ian Paterson, and Gavin Y Oudit. T mapping with cardiovascular MRI is highly sensitive for Fabry disease independent of hypertrophy and sex. *Circulation: Cardiovascular Imaging*, 6(5):637–645, September 2013. pg. 24

[62] Elizabeth Kehr, Megan Sono, Sumeet S Chugh, and Michael Jerosch-Herold. Gadolinium-enhanced magnetic resonance imaging for detection and quantification of fibrosis in human myocardium in vitro. *The international journal of cardiovascular imaging*, 24(1):61–68, 2008. pg. 24

[63] Christopher A Miller, Josephine H Naish, Paul Bishop, Glyn Coutts, David Clark, Sha Zhao, Simon G Ray, Nizar Yonan, Simon G Williams, Andrew S Flett, James Charles Moon, Andreas Greiser, Geoffrey J M Parker, and Matthias Schmitt. Comprehensive Validation of Cardiovascular Magnetic Resonance Techniques for the Assessment of

Myocardial Extracellular Volume. *Circulation: Cardiovascular Imaging*, 6(3):373–383, May 2013. pg. 24

[64] Marianna Fontana, Steve K White, Sanjay M Banypersad, Daniel M Sado, Viviana Maestrini, Andrew S Flett, Stefan K Piechnik, Stefan Neubauer, Neil Roberts, and James Charles Moon. Comparison of T1 mapping techniques for ECV quantification. Histological validation and reproducibility of ShMOLLI versus multibreath-hold T1 quantification equilibrium contrast CMR. *Journal of cardiovascular magnetic resonance : official journal of the Society for Cardiovascular Magnetic Resonance*, 14:88, 2012. pg. 24

[65] Timothy C Wong, Kayla Piehler, Christopher G Meier, Stephen M Testa, Amanda M Klock, Ali A Aneizi, Jonathan Shakesprere, Peter Kellman, Sanjeev G Shroff, David S Schwartzman, Suresh R Mulukutla, Marc A Simon, and Erik B Schelbert. Association between extracellular matrix expansion quantified by cardiovascular magnetic resonance and short-term mortality. *Circulation*, 126(10):1206–1216, September 2012. pg. 24

[66] C G Brilla, R C Funck, and H Rupp. Lisinopril-mediated regression of myocardial fibrosis in patients with hypertensive heart disease. *Circulation*, 102(12):1388–1393, September 2000. pg. 25

Chapter 2

An Analytic Model of Factors Affecting MOLLI T_1 Accuracy Using a Time-Weighted Average Model of Relaxation[1]

2.1 Introduction

Diffuse myocardial fibrosis is a common feature of various cardiac pathologies including left ventricular remodeling in heart failure [1], dilated cardiomyopathy [2], and aortic stenosis [3] and its presence has been associated with worsened cardiac function [2, 4]. Quantitative myocardial T_1 mapping has been used to non-invasively assess fibrosis, where increased extracellular volume associated with collagen deposition has a higher concentration of gadolinium than healthy tissue following an intravenous contrast administration. The resulting shorter myocardial T_1 values have been associated with histological measurements of collagen content in patients following heart transplant, with dilated cardiomyopathy, and with aortic regurgitation. The blood-tissue partition coefficient, λ, is the ratio of myocardial to blood contrast concentration and is proportional to the underlying extracellular volume. λ can be calculated using myocardial and blood T_1 values pre- and post-contrast and is less sensitive to time of measurement following contrast administration than myocardial T_1 values alone, which increase over time as gadolinium is removed from circulation.

The MOdified Look-Locker Inversion recovery (MOLLI) technique [5] and its shorter variants [6–8] are widely used for cardiac T_1 and ECV mapping applications due to its widespread availability and high precision. All MOLLI sequences consist of multiple Look-Locker sets separated by several heartbeats, where each set consists of several ECG-triggered

[1] A portion of this chapter has been previously published: Chow K, Thompson RB. An Analytic Description of Factors Affecting MOLLI's Accuracy Using a Time-Weighted Average Model of T_1 Relaxation. *Proc Intl Soc Mag Reson Med.* 2014;**22**:2453.

single-shot diastasis images acquired in consecutive heartbeats following a single inversion pulse. Shorter variants change the length of and duration between Look-Locker sets, but all MOLLI techniques calculate an apparent T_1^* relaxation time from the acquired data and use the Look-Locker correction factor [9] to account for the magnetization perturbation by the image readout and estimate the true T_1 value.

Despite this correction factor, MOLLI T_1 values are known to have systematic errors sensitive to heart rate [5, 6], flip angle [10], T_1 [6], T_2 [11, 12], inversion efficiency [12], off-resonance [13], and magnetization transfer [14]. Analysis of these factors has been limited to empiric characterization of each factor independently or through Bloch equation simulations and the interaction between these factors is not well understood.

In this manuscript, we develop a time-weighted average (TWA) model of relaxation for MOLLI sequences that provides an analytic framework for understanding the effect and interaction of many of the sources of MOLLI T_1 errors. The model is compared against Bloch equation simulations of the MOLLI sequence and validated in phantom experiments. The relationship between apparent MOLLI T_1^* and the true T_1 is derived from the TWA model and used to calculate true T_1 values from MOLLI data in simulations and phantom experiments as a proof of concept.

2.2 Theory

The MOLLI sequence consists of several "Look-Locker sets", separated by a number of heartbeats to allow for magnetization recovery between them. A single Look-Locker set consists of an inversion pulse followed by a series of ECG-triggered single-shot balanced steady-state free precession (bSSFP) images. Images from all Look-Locker sets are combined, and the apparent relaxation time T_1^* is calculated by fitting a three-parameter exponential recovery model:

$$Signal = A - Be^{-TI/T_1^*} \tag{2.1}$$

where A and B are constants and TI is the inversion time.

To account for magnetization perturbation by the image readouts, the so-called "Look-Locker correction factor" [9] applied to calculate the true T_1 time:

$$T_1 = \left(B/A - 1\right) T_1^* \tag{2.2}$$

2.2.1 Time-Weighted Average Model of Apparent T_1^* Relaxation

The single-shot images during a Look-Locker set are ECG triggered and thus occur at regular intervals determined by the heart rate, separated by periods of unperturbed recovery (Fig. 2.1). The magnetization during each bSSFP readout can be characterized by a driven relaxation rate, R_1', which is a function of the true R_1 and R_2 relaxation rates and the bSSFP flip angle, θ [15]:

$$R_1' = R_1 \cos^2\left(\theta/2\right) + R_2 \sin^2\left(\theta/2\right) \tag{2.3}$$

where the relaxation rates R_1', R_1, and R_2 are the reciprocal of the relaxation times T_1', T_1, and T_2.

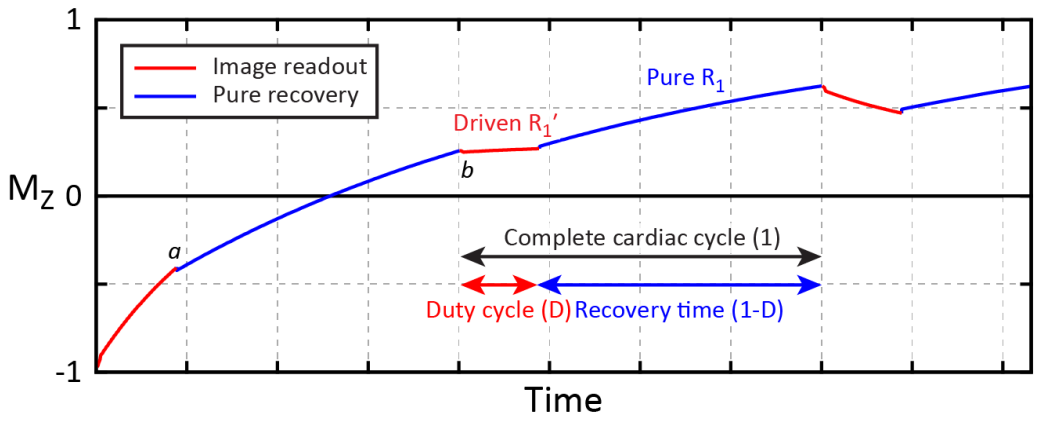

Figure 2.1: A Look-Locker set with three image readouts (red lines) having a driven relaxation rate R. The duty cycle (D) is defined as the fraction of the complete cardiac cycle during imaging.

The system illustrated in Fig. 2.1 can be described as alternating between two different phases, driven (D) and pure (P), each with a characteristic relaxation rate ($R_D = R_1'$, $R_P = R_1$ respectively) and equilibrium value (E_D, E_P). Given an initial starting longitudinal magnetization M(0), the longitudinal magnetization at time a (Fig. 2.1) is determined by only the driven phase:

$$M_a = E_D - [E_D - M(0)]e^{-t_D R_D} \tag{2.4}$$

At time b, after an additional time t_P in the pure relaxation phase, the longitudinal

magnetization is:

$$\begin{aligned} M_b &= E_P - \{E_P - M_a\}\, e^{-t_P R_P} \\ M_b &= E_P - \left\{E_P - E_D + [E_D - M(0)]e^{-t_D R_D}\right\} e^{-t_P R_P} \\ M_b &= E_P - [E_P - E_D]e^{-t_P R_P} - [E_D - M(0)]e^{-t_D R_D - t_P R_P} \end{aligned} \tag{2.5}$$

The overall behavior of the system can be described recursively by applying Eq. 2.5 over multiple time intervals T=D+P. The longitudinal magnetization after the n$^{\text{th}}$ interval is:

$$M_n = E_P - (E_P - E_D)\, e^{-t_P R_P} - (E_D - M_{n-1})\, e^{-t_D R_D - t_P R_P} \tag{2.6}$$

The overall system reaches its equilibrium value (E) when the magnetization at the end of an interval is the same as at the start of the interval, i.e. $M_n = M_{n-1}$:

$$\begin{aligned} E &= E_P - (E_P - E_D)\, e^{-t_P R_P} - (E_D - E)\, e^{-t_D R_D - t_P R_P} \\ E &= E_P - (E_P - E_D)\, e^{-t_P R_P} - E_D e^{-t_D R_D - t_P R_P} + E e^{-t_D R_D - t_P R_P} \\ E\left(1 - e^{-t_D R_D - t_P R_P}\right) &= E_P - (E_P - E_D)\, e^{-t_P R_P} - E_D e^{-t_D R_D - t_P R_P} \\ E &= \frac{E_P - (E_P - E_D)\, e^{-t_P R_P} - E_D e^{-t_D R_D - t_P R_P}}{1 - e^{-t_D R_D - t_P R_P}} \end{aligned} \tag{2.7}$$

It can be shown that the magnetization after the n$^{\text{th}}$ interval, described recursively in Eq. 2.6, can be written in closed form as:

$$\begin{aligned} M_n &= E - [E - M(0)]e^{-n(t_D R_D + t_P R_P)} \\ M_n &= E - [E - M(0)]e^{-n\left(\frac{t_D}{t_D + t_P} R_D + \frac{t_P}{t_D + t_P} R_P\right)(t_D + t_P)} \\ M_n &= E - [E - M(0)]e^{-n R_{\text{eff}} T} \end{aligned} \tag{2.8}$$

where

$$T = t_D + t_P \tag{2.9}$$

$$R_{\text{eff}} = \frac{t_D}{t_D + t_P} R_D + \frac{t_P}{t_D + t_P} R_P \tag{2.10}$$

Therefore the effective overall relaxation rate, R_{eff}, is the average of the relaxation

rates in each phase, weighted by the fractional amount of time spent in each pool. This is analogous to the Zimmerman-Brittin model of a two-phase system in fast exchange [16].

The time in the driven phase, t_D, is equal to the number of phase encode lines multiplied by the repetition time (echo spacing), while the time in the pure recovery phase, t_P, is R-R interval minus the time the imaging time. A duty cycle (D) can be defined as the imaging time normalized to the R-R interval (Fig. 2.1), and the apparent MOLLI relaxation rate, R_1^*, can be expressed as a function of pure R_1 and driven R_1' (Eq. 2.3) by re-writing Eq. 2.10 as:

$$R_1^* = DR_1' + (1 - D)\, R_1 \tag{2.11}$$

where D includes the effects of both the imaging duration as well as the heart rate.

The signal intensity of each image in a Look-Locker set is governed by the transverse magnetization during the center k-space readout. Equations 2.7–2.10 describe the magnetization at the end of each recovery phase, or equivalently, the start of each imaging phase. This corresponds to a centric-out k-space ordering, but it can be shown that for linear k-space ordering schemes, where the center k-space is acquired later in the image, the apparent relaxation rate, R_1^*, remains the same, but the equilibrium magnetization, E, changes.

2.2.2 Apparent Starting Magnetization

The time-weighted average (TWA) model is defined for arbitrary starting magnetization, M(0) (Eq. 2.8). Therefore, while MOLLI Look-Locker sets typically use inversion recovery preparation (M_0 = -1), the TWA model also applies for imperfect inversion pulses where $M_0 >$ -1. The TWA model can also be used with saturation recovery preparation ($M_0 = 0$) Look-Locker sets such as in the Modified Look-Locker acquisition with Saturation Recovery (MLLSR) sequence [17].

Look-Locker sets in MOLLI sequences are separated by a delay to allow for magnetization recovery, traditionally defined as a fixed number of heartbeats. It is commonly assumed that this delay is sufficiently long to allow for complete magnetization recovery and therefore that all Look-Locker sets have the same M(0) = -1. However, for high heart rates, incomplete recovery leads to different starting M(0) values for each Look-Locker set. As the apparent T_1^* and equilibrium value are independent of starting M(0) (Eq. 2.11 and Eq. 2.7, respectively), these values are shared between all Look-Locker sets. Therefore, assuming no change in the image readout or heart rate, data from multiple Look-Locker sets with different starting M(0) can be fit to:

$$Signal_i = A - B_i e^{-TI/T_1^*} \tag{2.12}$$

where i is the i^{th} Look-Locker set and there are n+2 independent fit parameters for a MOLLI data set with n Look-Locker sets.

The TI times in MOLLI Look-Locker sets is typically incremented by adding a variable delay between the inversion pulse and the first image in an effort to obtain better sampling for short T_1 values. This variable delay also causes a change in the apparent M_0 without affecting the apparent T_1^* or equilibrium value, as shown in Fig. 2.2. Therefore Eq. 2.12 can also be used to fit MOLLI data with TI increments.

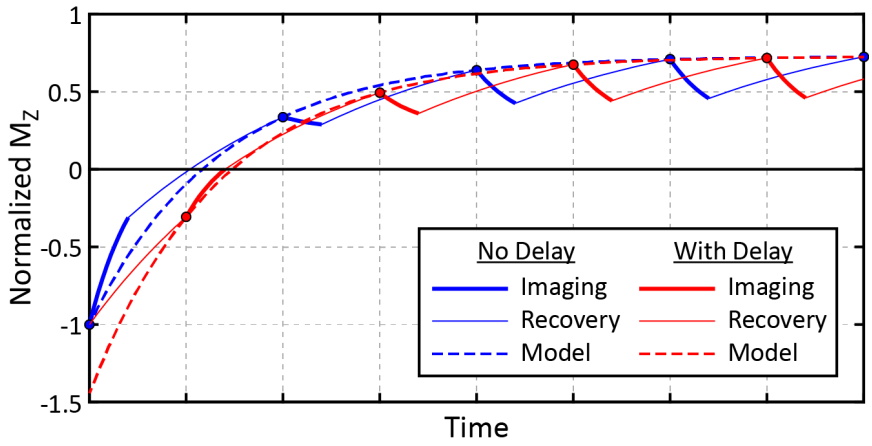

Figure 2.2: Look-Locker sets with no delay (blue) and with a delay between inversion and the first image (red) have the same steady-state equilibrium value and relaxation rate, but with a different apparent "B" value in Eq. 2.1 (dashed curves).

2.2.3 Slice Profile Effects

Excitation RF pulses used in bSSFP imaging have non-ideally shaped slice profiles due to the need for short TR durations, as shown in Fig. 2.3. A single slice contains many flip angles and many driven relaxation rates (R_1's), and therefore relaxation during imaging is multi-exponential. As the signal intensity varies with flip angle, the observed signal intensity is a weighted sum of multiple exponential recovery functions:

$$Signal = \sum_{i=1}^{n} \left\{ w_i \left(A_i - B_i e^{-R_{1i}' t} \right) \right\} \tag{2.13}$$

where there are n flip angles, w_i is the weighting function for each exponential recovery curve and $\sum w_i = 1$.

Using the first-order Taylor series expansion of $e^x = 1 + x$, Eq. 2.13 can be approxi-

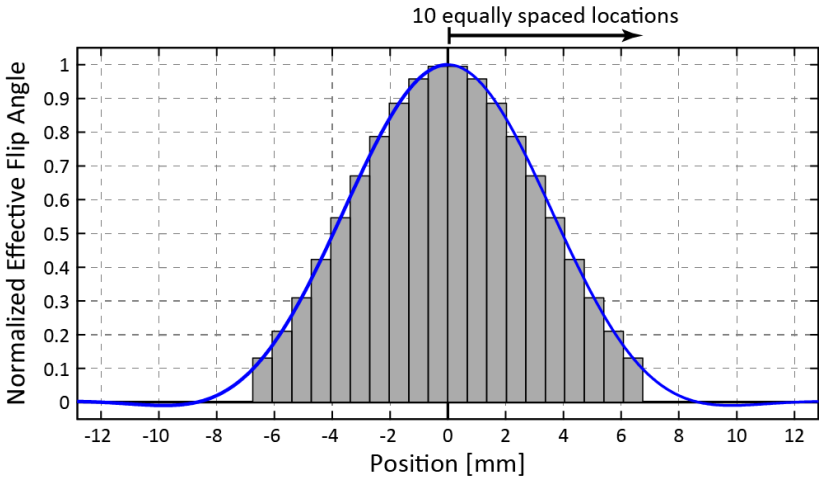

Figure 2.3: Slice profile of the excitation RF pulse using Bloch equation simulations (blue). Ten equally spaced "bins" are created starting at the center, extending to where the normalized effective flip angle reaches 10% of the maximum on one side. Slice profile simulations are performed by running simulations at each of these locations, using the flip angle at the center of each bin, and averaging the resulting magnetization.

mated as:

$$
\begin{aligned}
Signal &\approx \sum \left\{ w_i \left[A_i - B_i \left(1 - R'_{1i} t \right) \right] \right\} \\
Signal &\approx \sum \left\{ w_i A_i - \left(w_i B_i - w_i B_i R'_{1i} t \right) \right\} \\
Signal &\approx \sum w_i A_i - \left(\sum w_i B_i - \sum w_i B_i R'_{1i} t \right) \\
Signal &\approx \sum w_i A_i - \sum w_i B_i \left(1 - \frac{\sum w_i B_i R'_{1i}}{\sum w_i B_i} t \right) \\
Signal &\approx \sum w_i A_i - \left(\sum w_i B_i \right) e^{R'_{1,\text{eff}} t}
\end{aligned}
\tag{2.14}
$$

where

$$
R'_{1,\text{eff}} = \frac{\sum w_i B_i R'_{1i}}{\sum w_i B_i} \tag{2.15}
$$

Thus the observed sum of multi-exponential relaxation during an image readout may be approximated as the weighted sum of the individual relaxation rates. To calculate the effective driven $R'_{1,\text{eff}}$ for a slice profile, Eq. 2.3 can be substituted into Eq. 2.15, using the

substitution $w_i' = w_i B_i$ for simplicity:

$$R'_{1,\text{eff}} = \frac{\sum w_i' \left[R_1 \cos^2\left(\theta_i/2\right) + R_2 \sin^2\left(\theta_i/2\right) \right]}{\sum w_i B_i}$$

$$R'_{1,\text{eff}} = \frac{1}{\sum w_i'} \left\{ R_1 \sum w_i' \cos^2\left(\theta_i/2\right) + R_2 \sum w_i' \sin^2\left(\theta_i/2\right) \right\} \tag{2.16}$$

In practice, w_i' may be approximated as $\sin(\theta_i/2)$, the intensity at the first echo of a bSSFP train, and thus Eq. 2.16 becomes:

$$R'_{1,\text{eff}} = R_1 \frac{\sum \left[\sin\left(\theta_i/2\right) \cos^2\left(\theta_i/2\right) \right]}{\sum \sin\left(\theta_i/2\right)} + R_2 \frac{\sum \sin^3\left(\theta_i/2\right)}{\sum \sin\left(\theta_i/2\right)} \tag{2.17}$$

2.2.4 Relationship Between Apparent T_1^* and True T_1 In MOLLI

The TWA model states the apparent relaxation rate during a Look-Locker acquisition is the weighted average (Eq. 2.11) of the true longitudinal relaxation rate, R_1, and the driven relaxation rate, R_1', which is in turn dependent on R_1, R_2, and the flip angle (Eq. 2.3). For a single flip angle, the true relaxation rate can be calculated directly by substituting Eq. 2.3 into Eq. 2.11 and solving for R_1:

$$R_1^* = D\left[R_1 \cos^2\left(\theta/2\right) + R_2 \sin^2\left(\theta/2\right) \right] + \left(1 - D\right) R_1$$

$$R_1^* = DR_1 \cos^2\left(\theta/2\right) + DR_2 \sin^2\left(\theta/2\right) + \left(1 - D\right) R_1$$

$$R_1^* = R_1\left[D\cos^2\left(\theta/2\right) + 1 - D \right] + DR_2 \sin^2\left(\theta/2\right)$$

$$R_1 = \frac{R_1^* - DR_2 \sin^2\left(\theta/2\right)}{D\left[\cos^2\left(\theta/2\right) - 1\right] + 1}$$

$$R_1 = \frac{R_1^* - DR_2 \sin^2\left(\theta/2\right)}{1 - D\sin^2\left(\theta/2\right)} \tag{2.18}$$

For realistic slice profiles with multiple flip angles, Eq. 2.17 can be substituted into Eq. 2.3:

$$R_1^* = D\left\{ R_1 \frac{\sum \left[\sin\left(\theta_i/2\right) \cos^2\left(\theta_i/2\right) \right]}{\sum \sin\left(\theta_i/2\right)} + R_2 \frac{\sum \sin^3\left(\theta_i/2\right)}{\sum \sin\left(\theta_i/2\right)} \right\} + \left(1 - D\right) R_1$$

$$R_1^* = DR_1 \frac{\sum \left[\sin\left(\theta_i/2\right) \cos^2\left(\theta_i/2\right) \right]}{\sum \sin\left(\theta_i/2\right)} + DR_2 \frac{\sum \sin^3\left(\theta_i/2\right)}{\sum \sin\left(\theta_i/2\right)} + (1-D)\, R_1$$

$$R_1^* = R_1 \left\{ D \frac{\sum \left[\sin\left(\theta_i/2\right) \cos^2\left(\theta_i/2\right) \right]}{\sum \sin\left(\theta_i/2\right)} + 1 - D \right\} + DR_2 \frac{\sum \sin^3\left(\theta_i/2\right)}{\sum \sin\left(\theta_i/2\right)}$$

$$R_1 \left\{ D \frac{\sum \left[\sin\left(\theta_i/2\right) \cos^2\left(\theta_i/2\right) \right]}{\sum \sin\left(\theta_i/2\right)} + 1 - D \right\} = R_1^* - DR_2 \frac{\sum \sin^3\left(\theta_i/2\right)}{\sum \sin\left(\theta_i/2\right)}$$

$$R_1 = \frac{R_1^* - DR_2 \frac{\sum \sin^3\left(\theta_i/2\right)}{\sum \sin\left(\theta_i/2\right)}}{D \left[\frac{\sum \left[\sin\left(\theta_i/2\right) \cos^2\left(\theta_i/2\right) \right]}{\sum \sin\left(\theta_i/2\right)} - 1 \right] + 1} \tag{2.19}$$

Thus the true T_1 value can be theoretically be calculated from MOLLI data by calculating the duty cycle and with knowledge of the flip angle and T_2 value.

2.3 Methods

2.3.1 Simulation Validation

The TWA model was validated with Bloch equation simulations of the MOLLI sequence with typical parameters: 1.3 ms echo time (TE), 2.6 ms repetition time (TR), 5 linearly ramped preparation pulses with flip angle scaling factors of 10, 30, 50, 70, and 90%, 26 lines to the center of k-space, on-resonance, and ideal inversion pulses (M_0=-1). An atypical sampling scheme of 5-(10)-5-(10)-5 was chosen, denoting three Look-Locker sets of 5 images separated by 10 seconds to allow for more complete magnetization recovery between sets. Other parameters were varied over a wide range: 50–150 phase encode lines, 10–70° flip angle, 40–120 bpm heart rate, 300–2500 ms T_1, and 30–250 ms T_2, with all combinations within this space.

Bloch simulations were performed using a single flip angle as well as with consideration of multiple flip angles in typical slice profiles. For these simulations, a Bloch simulation of the excitation RF pulse was used to calculate the effective flip angle over spatial position. Ten equally sized bins were created between the zero position to the position where effective flip angle reached 10% of its maximum value, with each bin characterized by an effective flip angles equal to the value at its center (Fig. 2.3). To emulate slice profile effects, independent single flip angle Bloch equation simulations were computed for these 10 spatial locations and their simulated magnetization was averaged.

2.3.2 Phantom Experiments

14 $NiCl_2$-doped agarose phantoms with T_1 and T_2 value combinations similar to myocardium and blood [18] were imaging on a Siemens MAGNETOM 1.5T Aera MRI Scanner (Siemens Healthcare; Erlangen, Germany). Gold standard relaxometry was performed using spin echo experiments with common sequence parameters: 11 ms TE, 360×135 mm^2 field of view, 128×48 matrix size, 130 Hz/pixel bandwidth, 90° flip angle, and k-space acquired one line at a time with a 10 s TR. T_1 data had inversion recovery preparation with 14 TI values spanning 100–2000 ms and T_2 data had 7 TEs 11–200 ms from separate acquisitions.

MOLLI data was acquired with a 1.32/2.64ms TE/TR, 360×270 mm^2 field of view, 192×112 matrix size, 78% phase resolution, $7/8^{th}$ partial Fourier, 35° flip angle, 5 linear catalyzation pulses with 10, 30, 50, 70, and 90% scaling factors, 120 ms minimum TI, 80 ms TI increment, and a simulated heart rate of 60 bpm. A 5-(10)-5 acquisition scheme with 10 recovery heartbeats, the largest allowed by the sequence implementation, was used to ensure maximal magnetization recovery between sets. Additional acquisitions were made with flip angles from 10–70° to vary driven R_1' and with heart rates from 30–120 bpm to vary the duty cycle. Bloch simulations were also performed for each MOLLI experiment using spin echo T_1 and T_2 values, matching actual acquisition parameters, accounting for slice profile effects as described above. These simulations also included Bloch simulations of the hyperbolic secant inversion pulse to account for T_1 and T_2 dependence of inversion pulses [19].

2.3.3 Data Analysis

All image analysis was performed offline using MATLAB (R2013a, The MathWorks; Natick, USA). Regions of interest (ROIs) were traced for each phantom in experimental data and the parameter of interest was calculated using the average signal intensities within the ROI. Spin echo T_1 data was fit to:

$$Signal = A - Be^{-TI/T_1} \tag{2.20}$$

Spin echo T_2 data was fit to:

$$Signal = Ae^{-TE/T_2} \tag{2.21}$$

Both simulated and experimental MOLLI data was fit to Eq. 2.12, with different "B" values for each Look-Locker set. TWA model T_1^* values were calculated using Eq. 2.11, with driven R_1' values were calculated using Eq. 2.16 and Eq. 2.3 for simulations with and

without slice profile effects respectively. The duration of the 5 linear catalyzation pulses at the beginning of the image readout, in which relaxation occurs at an intermediate rate, was accounted for by adding 55% of its duration (determined empirically) to the image duty cycle when calculating D for Eq. 2.11. Experimental driven R_1' values were also calculated by solving Eq. 2.11 for R_1' and using measured R_1^* values with spin-echo R_1 values. T_1 values were calculated from MOLLI data with the TWA model using Eq. 2.18 for single flip angle simulations and Eq. 2.19 for experiments and simulations with slice profile effects, using known T_2 values. T_1 values were also calculated using the standard Look-Locker correction method (Eq. 2.2).

2.4 Results

2.4.1 Simulation Validation of the Time-Weighted Average Model

In single flip angle Bloch equation simulations of the MOLLI sequence, the TWA model T_1^* had excellent agreement with measured apparent T_1^*, with an average difference of 0.1±0.2 ms or 0.01%±0.02% as shown in Fig. 2.4a. The TWA model accurately calculated the true T_1 value with an average difference from input T_1 values of -0.4±1.5 ms (Fig. 2.4b), while the Look-Locker corrected T_1 values had moderate errors that both underestimated and overestimated the true T_1 values with a broader distribution of errors (Fig. 2.4c).

Simulations accounting for slice profile effects had poorer agreement between TWA T_1^* and measured T_1^*, but was still good overall, with a mean difference of -17.0±32.6 ms and 86% of simulations having less than 5% error (Fig. 2.5a). Figure 2.6 shows the correlation between the magnitude of error in TWA T_1^* values and the ratio of driven R_1' to pure R_1, with larger errors in apparent T_1^* when the driven R_1' rate is many times faster than the pure R_1 relaxation rate. These TWA T_1^* errors resulted in 3% of simulations having negative or T_1 values exceeding 7500 ms when using Eq. 2.19. Despite these erroneous T_1 values, 62% of the remaining simulations had less than 1% error in TWA T_1 values and 80% had less than 5% error (Fig. 2.5b). The Look-Locker corrected T_1 values had moderate errors with a similar pattern to single flip angle simulations (Fig. 2.5c).

2.4.2 Phantom Experiments

Apparent T_1^* values from Bloch simulations and the TWA model had good agreement with the measured T_1^* values in phantom data, with an average difference of 4.5±14.8 ms

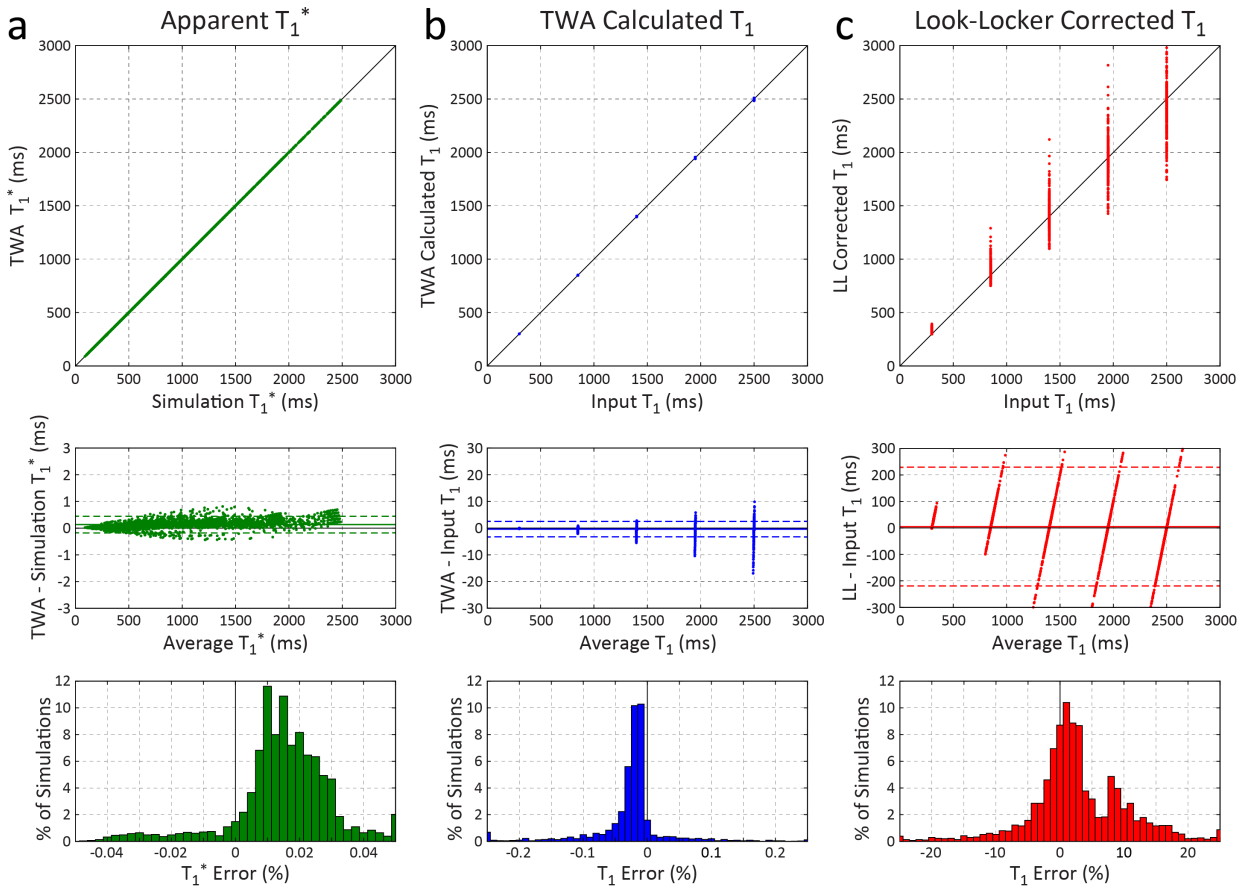

Figure 2.4: Comparison of apparent T_1^* (left) and pure T_1 (middle) using the TWA model and Look-Locker corrected pure T_1 values (right) with Bloch equation simulations using a single flip angle. X-Y plots are shown in the top row, Bland-Altman comparison in the middle row, and a histogram of percentage error for each parameter in the bottom row.

and -0.3±12.2 ms respectively (Fig. 2.7). True T_1 values calculated using the TWA model had good agreement with spin echo T_1 values (Fig. 2.8), with the exception of MOLLI experiments run at high (60–70°) flip angles (red circles, Fig. 2.7, Fig. 2.8), which were excluded from remaining statistics. The average difference between TWA and spin echo T_1 values was -2.5±29.2 ms, with 90% of experiments having an absolute TWA T_1 error of less than 5%. The standard Look-Locker corrected T_1 values were generally underestimated, with 50% of simulations having more than 5% error.

Apparent R_1^* values are plotted as a function of duty cycle for MOLLI experiments with varied heart rates in Fig. 2.9a. Measured R_1^* values (circles) have excellent agreement with the TWA model predictions (lines) with some discrepancies in phantoms with long R_1^* rates at low duty cycles, likely due to poor sampling of these short T_1^* values at a low heart rate. Figure 2.9b shows measured driven R_1' values (circles) as a function of flip angle

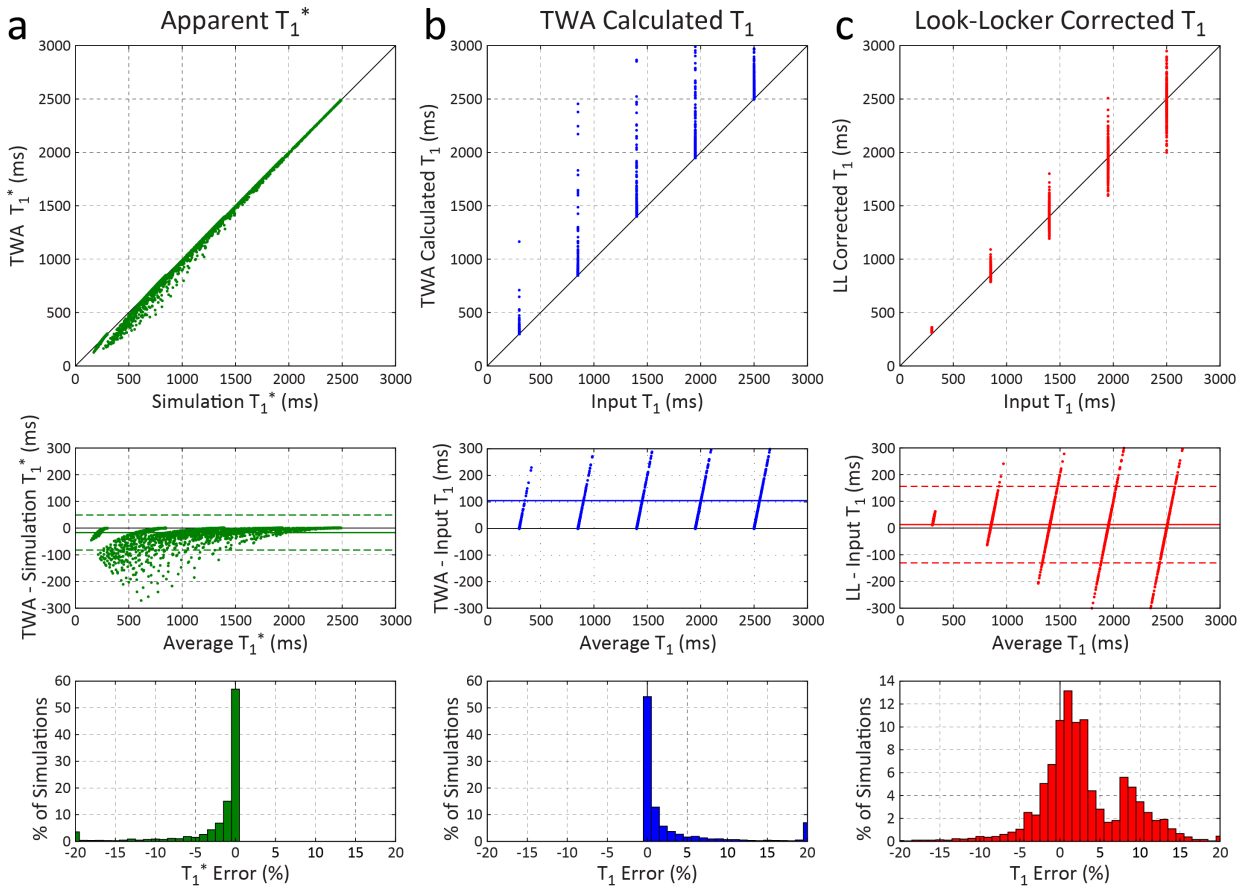

Figure 2.5: Comparison of apparent T_1^* (left) and pure T_1 (middle) using the TWA model and Look-Locker corrected pure T_1 values (right) with Bloch equation simulations with slice profile effects. X-Y plots are shown in the top row, Bland-Altman comparison in the middle row, and a histogram of percentage error for each parameter in the bottom row.

and R_1' values calculated from Eq. 2.11 using measured R_1^* values and spin echo R_1 values (lines). Measured R_1' values have excellent agreement with TWA model predictions. Data is displayed for odd numbered phantoms only to reduce clutter and even numbered phantoms had similar results.

2.5 Discussion

2.5.1 Validation of the TWA Model

TWA model T_1^* and T_1 values had excellent agreement with single flip angle Bloch equation simulations, implying that it is an accurate description of the magnetization time-course during a MOLLI sequence. The phantom data also provides experimental validation

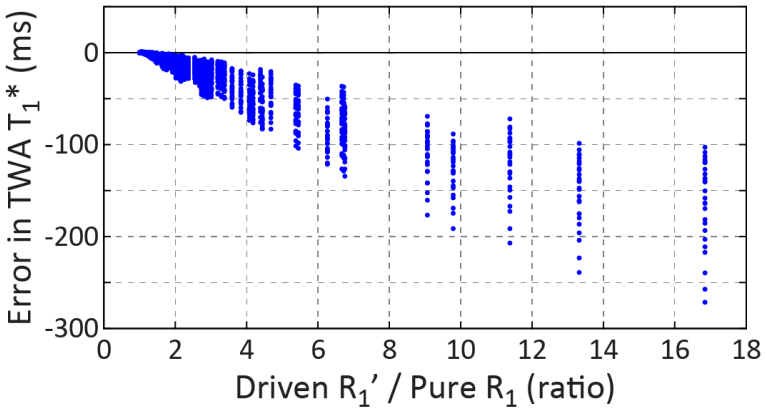

Figure 2.6: Error in TWA model T_1^* as a function of R_1'/R_1 in Bloch equation simulations with slice profile effects.

of the two fundamental concepts of the TWA model. First, the linear relationship between apparent R_1^* and duty cycle in Fig. 2.9a confirms that R_1^* is a weighted average of two relaxation rates as predicted in Eq. 2.11. Second, good agreement between the calculated driven R_1' and flip angle with theory in Fig. 2.9b confirms the ability to predict R_1' using Eq. 2.19.

Good agreement is found between TWA model predictions of T_1^* and T_1 values and experimental data in phantoms, which support the underlying assumptions made to account for slice profile effects in deriving Eq. 2.17 and Eq. 2.19. However, slice profile Bloch equation simulations over a much wider space of model parameters show substantial differences for certain combinations of parameters, revealing the limitations of these assumptions.

As the driven R_1' is a function of flip angle, the different flip angles in a slice profile result in a multitude of R_1' values and the net effect is fundamentally multi-exponential relaxation during each imaging readout. These multiple exponential relaxation curves are also weighted by their signal intensity, which vary over time, but is approximated as $\sin(\theta_i/2)$ in Eq. 2.17. Relaxation during the imaging is further approximated with an effective mono-exponential relaxation rate, $R_{1,\text{eff}}'$, in Eq. 2.15 for simplicity. These approximations appear to be inaccurate when the driven multi-exponential relaxation rates are much faster than the true relaxation rate, as shown in Fig. 2.6. Although these approximations could potentially be further improved, it is not necessarily clear that approximating a weighted sum of multi-exponentials with a single mono-exponential rate can be accurate over a wide range of values. Nevertheless, the TWA model was accurate in the large majority of simulations and phantom experiments and out-performed the Look-Locker correction.

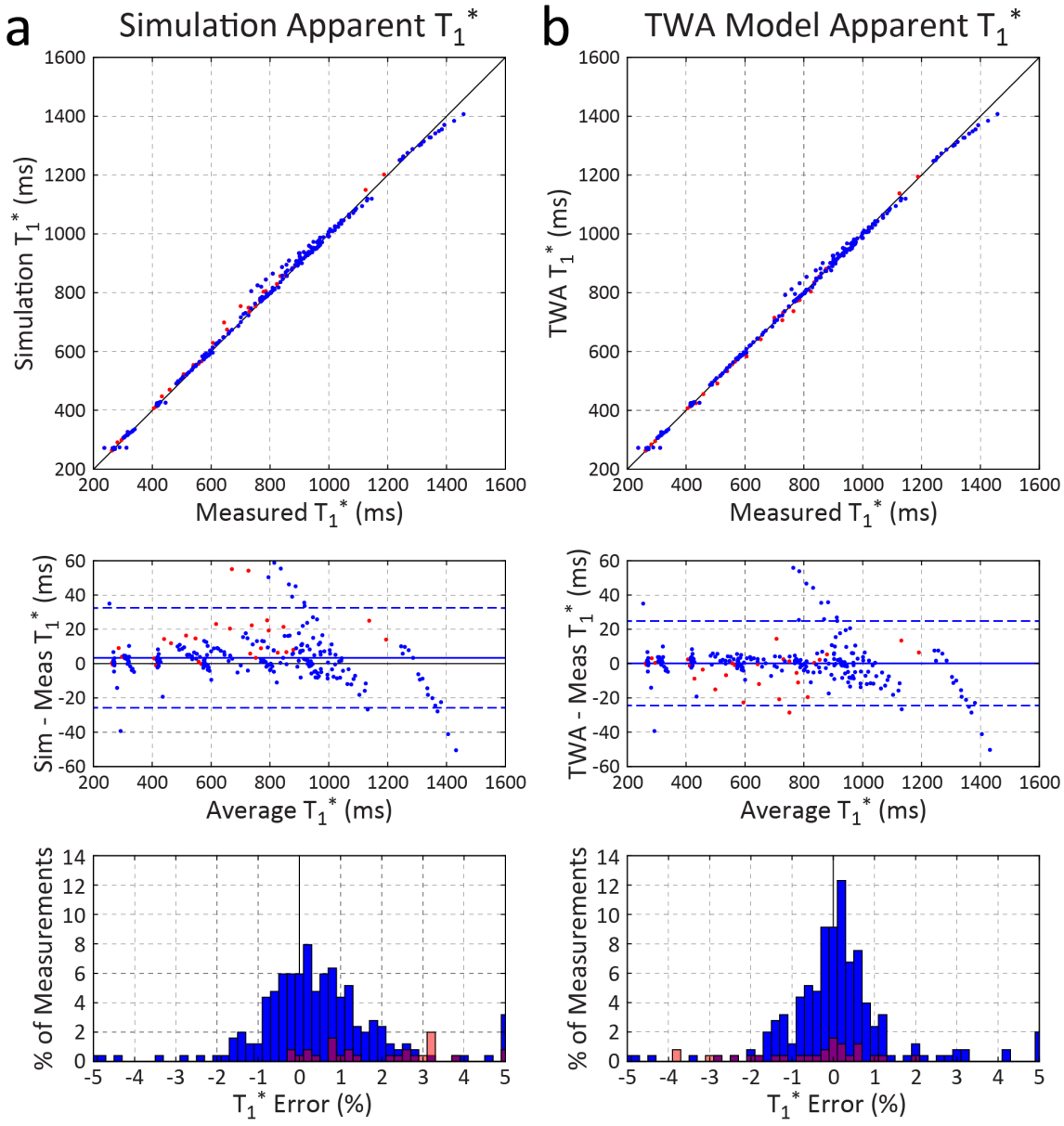

Figure 2.7: Comparison between measured apparent T_1^* with **(a)** Bloch equation simulations and (**b**) the TWA model. X-Y plots are shown in the top row, Bland-Altman comparison in the middle row, and a histogram of T_1^* error in the bottom row. Red dots and bars indicate data with a 60–70° flip angle.

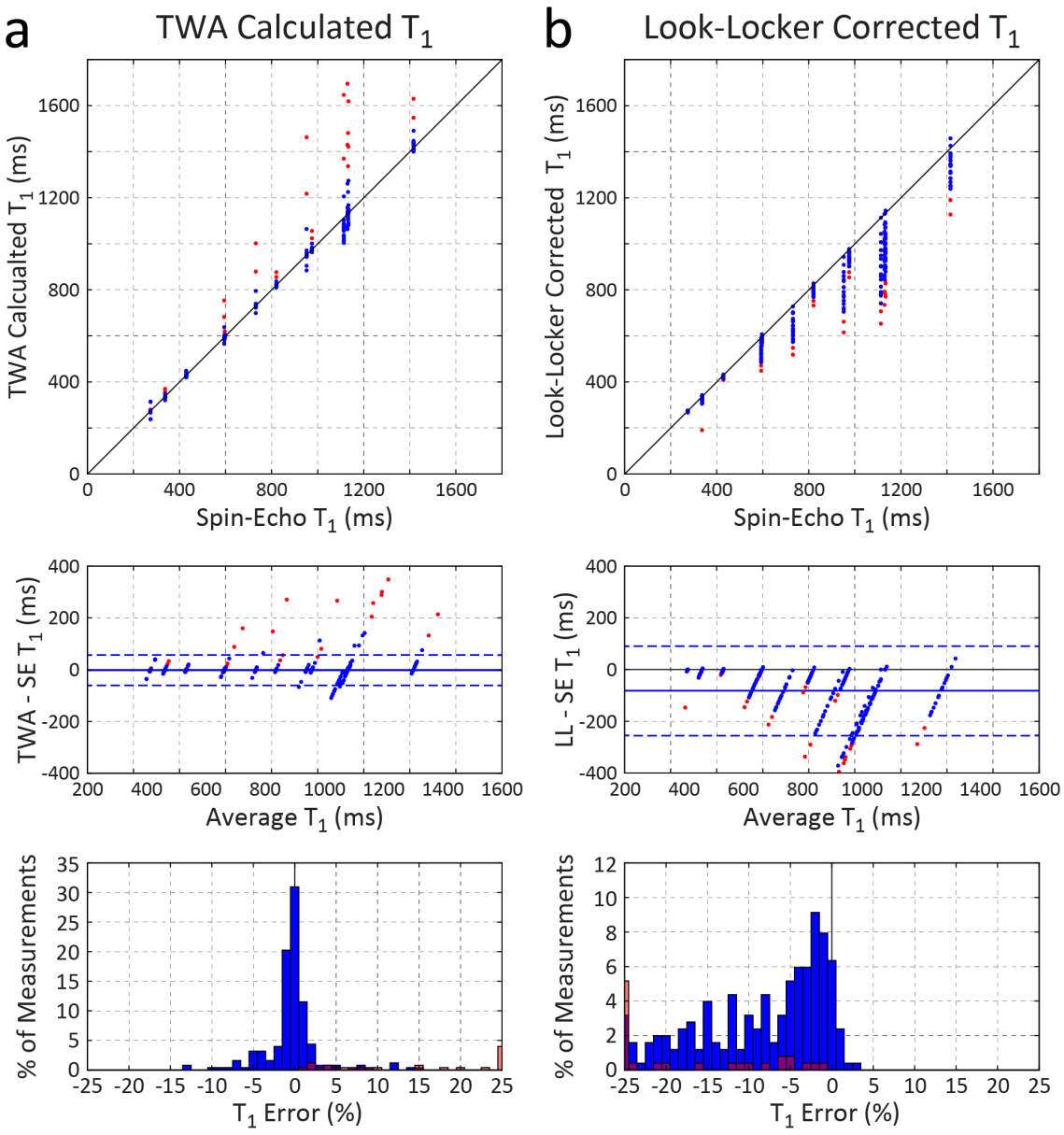

Figure 2.8: Comparison between spin-echo T_1 values and pure T_1 values calculated using **(a)** the TWA model and (**b**) the standard Look-Locker correction. X-Y plots are shown in the top row, Bland-Altman comparison in the middle row, and a histogram of T_1 error in the bottom row. Red dots and bars indicate data with a 60–70° flip angle.

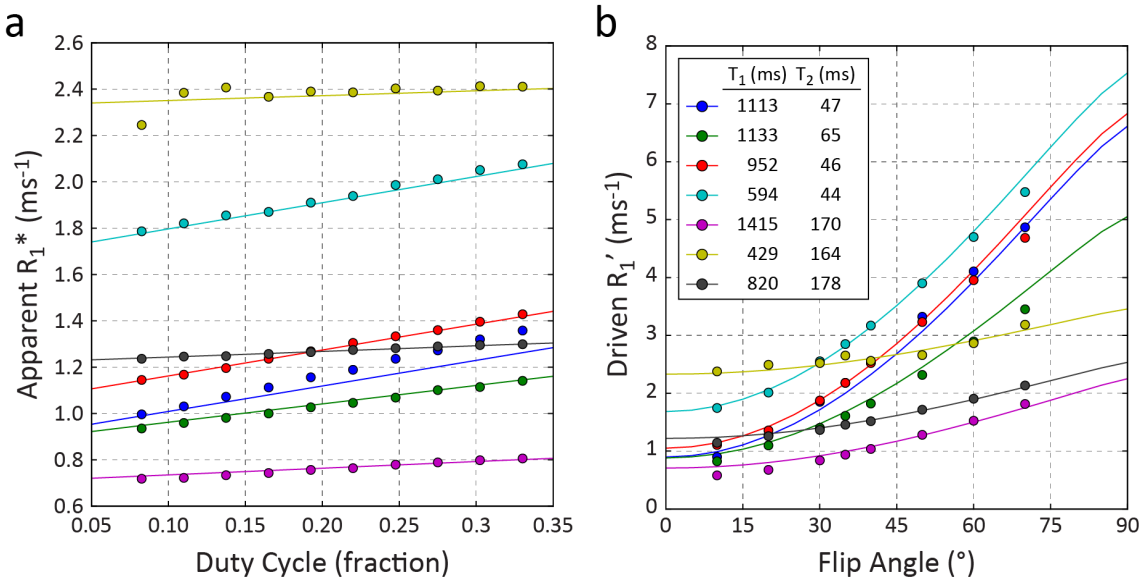

Figure 2.9: **a**) Predicted (lines) and measured (circles) apparent R_1^* as a function of duty cycle in phantom experiments with heart rates from 40–120 bpm. **b**) Predicted (lines) and measured (circles) driven R_1' as a function of flip angles in phantom experiments with flip angles from 10–70°.

2.5.2 Calculation of True T_1 Values

The equations of the TWA model can be used to calculate the true T_1 value using the measured apparent T_1^* value and assumed values for flip angle and its profile in space and T_2 using Eq. 2.18 and Eq. 2.19. This direct calculation of T_1 was extremely accurate in simulations with a single flip angle, but found to be unstable when applied over a wide range of input parameters in simulations incorporating slice profile effects, with 3% of simulations resulting in invalid T_1 values. However, the TWA calculated true T_1 value had less than 5% error in 80% of simulations, and 90% of phantom data, with significant outliers at higher flip angles. This is likely due to B_1 inhomogeneity over the phantom set and unpublished data acquired in a separate study using this phantom set has shown a reduction in B_1 of up to 15% at the sides where the outlier phantoms are located. Reduced flip angles result in a lower driven R_1' than predicted and higher calculated T_1 values as seen in the data.

Instability in the calculation of true T_1 values with the TWA model at can be partially understood by analyzing Eq. 2.3 and its visualization in Fig. 2.9b. At high flip angles, R_1' increases sharply until it reaches R_2 at 90° and therefore R_1' is highly sensitive to large flip angles and short T_2 values. Furthermore, if R_2 is much larger than R_1, then R_1' is also much larger than R_1 and the errors become compounded when solving Eq. 2.11 for R_1. Although the nominally 35° flip angle typically used in MOLLI experiments is fairly low,

the T_2 values in the myocardium are short compared to T_1 and neither flip angle nor T_2 are typically known with a high degree of precision *a priori*. Calculation of the true T_1 for in-vivo myocardium using this approach is likely to lead to significant variability and is therefore impractical.

Equation 2.11 suggests two additional ways that the true T_1 value can be calculated. As shown in Fig. 2.9a, the linear relationship between apparent R_1^* and duty cycle can be characterized by making multiple measurements at various duty cycles. The true R_1 value can then be calculated by fitting a straight line and taking the y-intercept, which may be intuitively thought of as the limit when the duty cycle approaches zero. In practice, MOLLI images are heart rate triggered and thus the duty cycle can only be decreased in integer multiples of the R-R interval by acquiring data every n^{th} heartbeat which may lead to poor sampling of the recovery curve.

Dummy RF pulses can also be used to increase the duty cycle without introducing bias from changing the k-space acquisition. If the number of dummy pulses is increased to the point where RF pulses are played continuously, the apparent R_1^* is in fact the driven R_1'. Combined with a standard Look-Locker set at a known duty cycle, the true R_1 can be then be calculated using Eq. 2.11 by solving for R_1. However, standard short-axis slices undergo significant through-plane motion, particularly in basal slices. As a result, continuous RF excitation at a given spatial plane does not necessarily result in continuous excitation of the imaging plane and the measured apparent driven R_1' is likely to be underestimated.

While the TWA model provides an intuitive description of the magnetization time-course during a MOLLI experiment, it cannot be easily used in its current form to calculate the true T_1 value from MOLLI measurements alone. The three approaches for doing so described above require precise and accurate assumptions or increase the complexity of data acquisition. Heart rate variations, particularly in subjects with arrhythmia, result in variable imaging duty cycle over the MOLLI acquisition and present an additional challenge in calculating the true T_1 value. Instead, alterative T_1 mapping sequences which are inherently less susceptible to systematic errors such as the recently proposed SAturation-recovery single-SHot Acquisition (SASHA) [18] technique may be a more reliable method for acquiring accurate in-vivo data.

2.5.3 Further Development of the TWA Model

The TWA model postulates that the measured relaxation rate is a weighted average of two distinct relaxation rates. The calculation of the driven relaxation rate, R_1', in Eq. 2.3 is strongly supported by experimental data with various flip angles in phantoms with a range

of T_1 and T_2 values. The TWA model could potentially be further expanded to incorporate the effects of other parameters on the driven relaxation rate. For example, off-resonance effects in bSSFP imaging can be modeled as change in the effective excitation flip angle, as proposed by Schmitt *et al* [20]. Magnetization transfer effects have also been shown to result in significant errors in Look-Locker corrected MOLLI T_1 values [14], but could also be potentially modeled an increase in the effective driven relaxation rate. These additions to the TWA model would provide a more complete description of practical confounders to the MOLLI sequence and could be useful if more stable techniques for calculating true T_1 values using the TWA model can be developed.

2.5.4 MOLLI and the Look-Locker Correction

Conventional MOLLI analysis uses the Look-Locker correction (Eq. 2.2), in which the apparent T_1^* is multiplied by a single value to calculate the true T_1 value. However, the relationship between the T_1 and T_1^* is accurately described by the TWA model in Eq. 2.18 for a single flip angle, which show R_1 and R_1^* have a linear relationship instead of the proportional relationship used in the Look-Locker correction. Nevertheless, the Look-Locker correction is at least partially effective at estimating the true T_1 value in some cases. It can be shown that "B/A-1" is equivalent to "-M_0/E", where E is the equilibrium value from Eq. 2.7. If a perfect inversion pulse can be assumed, M_0=-1, then the Look-Locker factor is simply equal to 1/E. Thus the Look-Locker correction effectively assumes that readout causes a reduction in the equilibrium value that equal to the reduction in the apparent T_1^*. Although this evidently does not hold in all scenarios, it may be possible to develop a more accurate method to estimate the true T_1 value using both the TWA model and the Look-Locker correction factor.

As the Look-Locker correction only partially corrects the apparent T_1^* values, the relationship between factors that affect T_1^* described by the TWA model provide some insight into the systematic errors observed in Look-Locker corrected MOLLI T_1 values. For example, the relationship between T_1, T_2, flip angle and their effect on driven R_1' (Eq. 2.3 and Fig. 2.9b) explains that previous observations of larger MOLLI T_1 errors with shorter T_2 values [11, 21] and longer T_1 values [6, 12] are a result of the difference in the R_1 and R_2 relaxation rates. Their relationship to the apparent R_1^* is modulated by flip angle, as observed in the initial optimization of the MOLLI sequence [10]. The weighted average aspect of the TWA model (Eq. 2.11) characterizes an intrinsic relationship between heart rate and T_1^* (Fig. 2.9a), although the MOLLI T_1 errors at higher heart rates are dominated by due to incomplete magnetization recovery between Look-Locker sets [22]. The weighted average

concept also illustrates a relationship between the number of phase encodes and T_1^*, which results in larger MOLLI T_1 errors for longer readouts such as with higher resolution [23].

2.6 Conclusion

The TWA model provides an analytic description of the apparent relaxation rate, R_1^*, during a MOLLI sequence as a time-weighted average of the true R_1 relaxation rate and a driven relaxation rate R_1' during bSSFP imaging. It had extremely good agreement with single flip angle Bloch equation simulations and could be used to predict T_1 values accurately if T_2 values and flip angles are known. Simplifications made to approximate multi-exponential relaxation in realistic slice profiles were found to have good agreement in a majority of simulations and phantom results, but calculations of the true T_1 value was found to be unstable at high flip angles and low T_2 values. Further work is necessary in order to develop a more robust method for calculating true T_1 values from MOLLI data using the TWA model.

2.7 References

[1] Leah Iles, Heinz Pfluger, Arintaya Phrommintikul, Joshi Cherayath, Pelin Aksit, Sandeep N Gupta, David M Kaye, and Andrew J Taylor. Evaluation of diffuse myocardial fibrosis in heart failure with cardiac magnetic resonance contrast-enhanced T1 mapping. *Journal of the American College of Cardiology*, 52(19):1574–1580, November 2008. pg. 35

[2] Michael Jerosch-Herold, David C Sheridan, Jessica D Kushner, Deirdre Nauman, Donna Burgess, Diana Dutton, Rami Alharethi, Duanxiang Li, and Ray E Hershberger. Cardiac magnetic resonance imaging of myocardial contrast uptake and blood flow in patients affected with idiopathic or familial dilated cardiomyopathy. *American journal of physiology Heart and circulatory physiology*, 295(3):H1234–H1242, September 2008. pg. 35, pg. 35

[3] Sacha Bull, Steven K White, Stefan K Piechnik, Andrew S Flett, Vanessa M Ferreira, Margaret Loudon, Jane M Francis, Theodoros D Karamitsos, Bernard D Prendergast, Matthew D Robson, Stefan Neubauer, James Charles Moon, and Saul G Myerson. Human non-contrast T1 values and correlation with histology in diffuse fibrosis. *Heart (British Cardiac Society)*, 99(13):932–937, July 2013. pg. 35

[4] Martin Ugander, Abiola J Oki, Li-Yueh Hsu, Peter Kellman, Andreas Greiser, Anthony H Aletras, Christopher T Sibley, Marcus Y Chen, W Patricia Bandettini, and Andrew E Arai. Extracellular volume imaging by magnetic resonance imaging provides insights into overt and sub-clinical myocardial pathology. *European heart journal*, 33(10):1268–1278, May 2012. pg. 35

[5] Daniel R Messroghli, Aleksandra Radjenovic, Sebastian Kozerke, David M Higgins, Mohan U Sivananthan, and John P Ridgway. Modified Look-Locker inversion recovery (MOLLI) for high-resolution T1 mapping of the heart. *Magnetic Resonance in Medicine*, 52(1):141–146, July 2004. pg. 35, pg. 36

[6] Stefan K Piechnik, Vanessa M Ferreira, Erica Dall'Armellina, Lowri E Cochlin, Andreas Greiser, Stefan Neubauer, and Matthew D Robson. Shortened Modified Look-Locker Inversion recovery (ShMOLLI) for clinical myocardial T1-mapping at 1.5 and 3 T within a 9 heartbeat breathhold. *Journal of cardiovascular magnetic resonance : official journal*

of the Society for Cardiovascular Magnetic Resonance, 12:69, 2010. pg. 35, pg. 36, pg. 36, pg. 53

[7] Jason J Lee, Songtao Liu, Marcelo S Nacif, Martin Ugander, Jing Han, Nadine Kawel, Christopher T Sibley, Peter Kellman, Andrew E Arai, and David A Bluemke. Myocardial T1 and extracellular volume fraction mapping at 3 tesla. *Journal of cardiovascular magnetic resonance : official journal of the Society for Cardiovascular Magnetic Resonance*, 13:75, 2011.

[8] Erik B Schelbert, Stephen M Testa, Christopher G Meier, William J Ceyrolles, Joshua E Levenson, Alexander J Blair, Peter Kellman, Bobby L Jones, Daniel R Ludwig, David S Schwartzman, Sanjeev G Shroff, and Timothy C Wong. Myocardial extravascular extracellular volume fraction measurement by gadolinium cardiovascular magnetic resonance in humans: slow infusion versus bolus. *Journal of cardiovascular magnetic resonance : official journal of the Society for Cardiovascular Magnetic Resonance*, 13:16, 2011. pg. 35

[9] R Deichmann and Axel Haase. Quantification of T1 values by SNAPSHOT-FLASH NMR imaging. *Journal of Magnetic Resonance*, 96(3):608–612, February 1992. pg. 36, pg. 36

[10] Daniel R Messroghli, Andreas Greiser, Mirko Fröhlich, Rainer Dietz, and Jeanette Schulz-Menger. Optimization and validation of a fully-integrated pulse sequence for modified look-locker inversion-recovery (MOLLI) T1 mapping of the heart. *Journal of magnetic resonance imaging : JMRI*, 26(4):1081–1086, October 2007. pg. 36, pg. 53

[11] Neville D Gai, Christian Stehning, Marcelo Nacif, and David A Bluemke. Modified Look-Locker T1 evaluation using Bloch simulations: human and phantom validation. *Magnetic Resonance in Medicine*, 69(2):329–336, February 2013. pg. 36, pg. 53

[12] Kelvin Chow, Jacqueline A Flewitt, Joseph J Pagano, Jordin D Green, Matthias G Friedrich, and Richard B Thompson. MOLLI T1 Values Have Systematic T2 and Inversion Efficiency Dependent Errors. In *Proceedings of the International Society for Magnetic Resonance in Medicine*, page 395, 2012. pg. 36, pg. 36, pg. 53

[13] Peter Kellman, Daniel A Herzka, Andrew E Arai, and Michael Schacht Hansen. Influence of Off-resonance in myocardial T1-mapping using SSFP based MOLLI method. *Journal of cardiovascular magnetic resonance : official journal of the Society for Cardiovascular Magnetic Resonance*, 15:63, 2013. pg. 36

[14] Matthew D Robson, Stefan K Piechnik, Elizabeth M Tunnicliffe, and Stefan Neubauer. T1 measurements in the human myocardium: The effects of magnetization transfer on the SASHA and MOLLI sequences. *Magnetic Resonance in Medicine*, July 2013. pg. 36, pg. 53

[15] Peter Schmitt, Mark A Griswold, Peter M Jakob, Markus Kotas, Vikas Gulani, Michael Flentje, and Axel Haase. Inversion recovery TrueFISP: quantification of T(1), T(2), and spin density. *Magnetic Resonance in Medicine*, 51(4):661–667, April 2004. pg. 37

[16] J R Zimmerman and W E Brittin. Nuclear Magnetic Resonance Studies in Multiple Phase Systems: Lifetime of a Water Molecule in an Adsorbing Phase on Silica Gel. *The Journal of Physical Chemistry*, 61(10):1328–1333, October 1957. pg. 39

[17] Ting Song, Jeffrey A Stainsby, Vincent B Ho, Maureen N Hood, and Glenn S Slavin. Flexible cardiac T(1) mapping using a modified look-locker acquisition with saturation recovery. *Magnetic Resonance in Medicine*, 67(3):622–627, March 2012. pg. 39

[18] Kelvin Chow, Jacqueline A Flewitt, Jordin D Green, Joseph J Pagano, Matthias G Friedrich, and Richard B Thompson. Saturation recovery single-shot acquisition (SASHA) for myocardial T1 mapping. *Magnetic Resonance in Medicine*, 71(6):2082–2095, 2014. pg. 44, pg. 52

[19] Peter Kellman, Daniel A Herzka, and Michael Schacht Hansen. Adiabatic inversion pulses for myocardial T1 mapping. *Magnetic Resonance in Medicine*, 71(4):1428–1434, 2014. pg. 44

[20] P Schmitt, Mark A Griswold, V Gulani, Axel Haase, M Flentje, and P M Jakob. A simple geometrical description of the TrueFISP ideal transient and steady-state signal. *Magnetic Resonance in Medicine*, 55(1):177–186, 2006. pg. 53

[21] Kelvin Chow, Jacqueline A Flewitt, Joseph J Pagano, Jordin D Green, Matthias G Friedrich, and Richard B Thompson. T2-dependent errors in MOLLI T1 values: simulations, phantoms, and in-vivo studies. *Journal of cardiovascular magnetic resonance : official journal of the Society for Cardiovascular Magnetic Resonance*, 14(Suppl 1):P281, 2012. pg. 53

[22] Peter Kellman and Michael Schacht Hansen. T1-mapping in the heart: accuracy and precision. *Journal of cardiovascular magnetic resonance : official journal of the Society for Cardiovascular Magnetic Resonance*, 16(1):2, January 2014. pg. 53

[23] Kelvin Chow, Joseph J Pagano, and Richard B Thompson. An Intuitive Model of Several Factors Affecting Accuracy of MOLLI T1 Values. In *Proceedings of the International Society for Magnetic Resonance in Medicine*, 2013. pg. 54

Chapter 3

Saturation Recovery Single-Shot Acquisition (SASHA) for Myocardial T_1 Mapping[1]

3.1 Introduction

Quantitative myocardial T_1 mapping, performed either pre- or post-gadolinium contrast administration, has proven to be an invaluable tool in the non-invasive assessment of cardiac remodeling. Increased non-contrast myocardial T_1 values have been related to the extent of tissue damage in acute myocardial infarction [1], while shortened post-contrast T_1 values from higher tissue gadolinium concentrations have been used to detect increased extracellular volume. In diseases with diffuse myocardial fibrosis, such as patients following heart transplantation [2], with aortic stenosis [3], and with hypertrophic cardiomyopathy [3], post-contrast myocardial T_1 values have shown good correlation with histological measures of fibrosis including biopsy measurements of myocardial collagen content [2] and collagen volume fraction [3].

However, post-contrast myocardial T_1 values are sensitive to both the time of measurement after contrast delivery [3–6] and the amount of contrast administered. The blood-tissue partition coefficient, λ, is the ratio of tissue contrast concentration to the blood concentration, and more accurately reflects the underlying tissue extracellular volume fraction. Tissue and blood contrast concentration can be derived using changes in T_1 from baseline to post contrast delivery [7]. Because λ is calculated using blood and tissue T_1 values before and after contrast, T_1 imaging sequences used for the measurement of λ should be accurate over the wide range of T_1 and T_2 values found in blood and tissue both pre- and post-contrast.

[1] A version of this chapter has been previously published: Chow K, Flewitt JA, Green JD, Pagano JJ, Friedrich MG, Thompson RB. Saturation Recovery Single-Shot Acquisition (SASHA) for Myocardial T_1 Mapping. *Magn Reson Med.* 2014;**71**:2082–2095. http://onlinelibrary.wiley.com/doi/10.1002/mrm.24878/abstract

Inversion recovery sequences are commonly used for T_1 mapping due to their use of the full dynamic range of signal intensities, but conventional methods require full T_1 recovery between acquisition and subsequent inversion pulses and thus total acquisition times are too long for breath-hold imaging. Look-Locker techniques [8] allow for faster imaging with continuous FLASH [9–11], EPI [12], or TrueFISP [13] readouts following a single inversion pulse. A correction factor [9] is used to account for magnetization attenuation due to image acquisition. Electrocardiogram (ECG) triggering allows for cardiac T_1 mapping with Look-Locker techniques; however, combining data from multiple cardiac phases [11] may introduce errors due to through-plane motion.

The MOdified Look-Locker Inversion recovery (MOLLI) sequence [6, 14, 15] consists of several "Look-Locker" sets, each containing several ECG-triggered single-shot images at the same cardiac phase in sequential heartbeats following a single inversion pulse. The MOLLI sequence, and its shorter breath-hold variants using different image sampling schemes [5, 16], have been used to calculate myocardial and blood T_1 values in healthy volunteers [5, 6, 16], patients with myocardial infarction [17, 18], chronic aortic regurgitation [19], and those with non-ischemic late enhancement lesions [18]. However, MOLLI sequences underestimate T_1 values by 4–10% in phantom studies [14–16] and are known to have greater underestimation in short T_2 tissues such as the myocardium [20, 21]. Saturation recovery variants of MOLLI have been developed but also have a systematic underestimation of ~5% [22], likely due to a similar magnetization attenuation effect from multiple image readouts after a single preparation pulse. Saturation recovery imaging with a single gradient echo image per saturation pulse, eliminating the magnetization attenuation effects in MOLLI approaches, have also been demonstrated in-vivo [23, 24]. However, gradient echo readouts are limited by both poor overall signal to noise (SNR) and poor blood-tissue contrast compared to the balanced steady-state free precession (bSSFP) readout used in MOLLI.

We present a similar SAturation recovery single-SHot Acquisition (SASHA) sequence for T_1 mapping using a single-shot bSSFP readout to provide good SNR and blood-tissue contrast. We propose that this approach will overcome the limitations of bSSFP Look-Locker sequences, where factors such as T_2 and heart rate affect the accuracy of calculated T_1 values in a complex manner. Accuracy of SASHA-derived T_1 values and their dependence on T_1, T_2, flip angle, off-resonance, heart rate, SNR, and saturation efficiency were evaluated using numerical simulations and validated in $NiCl_2$-agarose phantoms. The dependence of myocardial T_1 and λ on the time following contrast agent administration was characterized in a group of healthy volunteers. T_1 and λ values were also measured in patients with heart failure, a disease where diffuse fibrosis has been previously described [25, 26] and measured [2], and compared to a control group. Measurement reproducibility for in-vivo studies was

characterized with inter- and intra-observer variability statistics.

3.2 Theory

The SASHA pulse sequence consists of ten single-shot bSSFP images acquired over consecutive heartbeats, where the first image is acquired without magnetization preparation and the remaining images follow saturation pulses with variable saturation recovery times (TS) that uniformly span the R-R interval. TS is defined as the time from the end of the saturation radiofrequency (RF) pulse to the center line of k-space. Images are ECG-triggered and a variable trigger delay is added before each saturation pulse to obtain a consistent cardiac phase (diastasis) for all images (Fig. 3.1a).

The saturation recovery preparation results in a starting magnetization for each SASHA image (other than the first) defined by:

$$M(0) = 1 - \eta_{actual} e^{\frac{-(TS-\Delta)}{T_1}} \tag{3.1}$$

where η_{actual} is the saturation pulse efficiency ($\eta_{\text{actual}} = 1$ for perfect saturation) and Δ is the time from the start of imaging to the center of k-space. This magnetization is further modulated by multiple bSSFP radiofrequency pulses during imaging, as illustrated in Fig. 3.1b. However, the relationship between signal intensity, TS, and T_1 can still be expressed using a three-parameter exponential recovery model, as derived analytically in the Appendix (Eq. 3.14):

$$Signal = A\left(1 - \eta_{apparent} e^{\frac{-TS}{T_1}}\right) \tag{3.2}$$

where A is a scaling factor and η_{apparent} is the apparent saturation efficiency, which is η_{actual} multiplied by a constant determined by acquisition parameters, as detailed in Eq. 3.16. The overall effect of the bSSFP readout is an apparent change in saturation efficiency and scaling factor, while the exponential T_1 term remains unaffected. Changes in flip angle or the distribution of flip angles with realistic slice profiles both result in changes in η_{apparent} and the scaling factor while the T_1 term is again unaffected, as shown in the Appendix.

3.3 Methods

3.3.1 Pulse Sequence

The SASHA pulse sequence was implemented on a 1.5T MRI scanner (Avanto; Siemens Healthcare; Erlangen, Germany). Typical sequence parameters were: composite

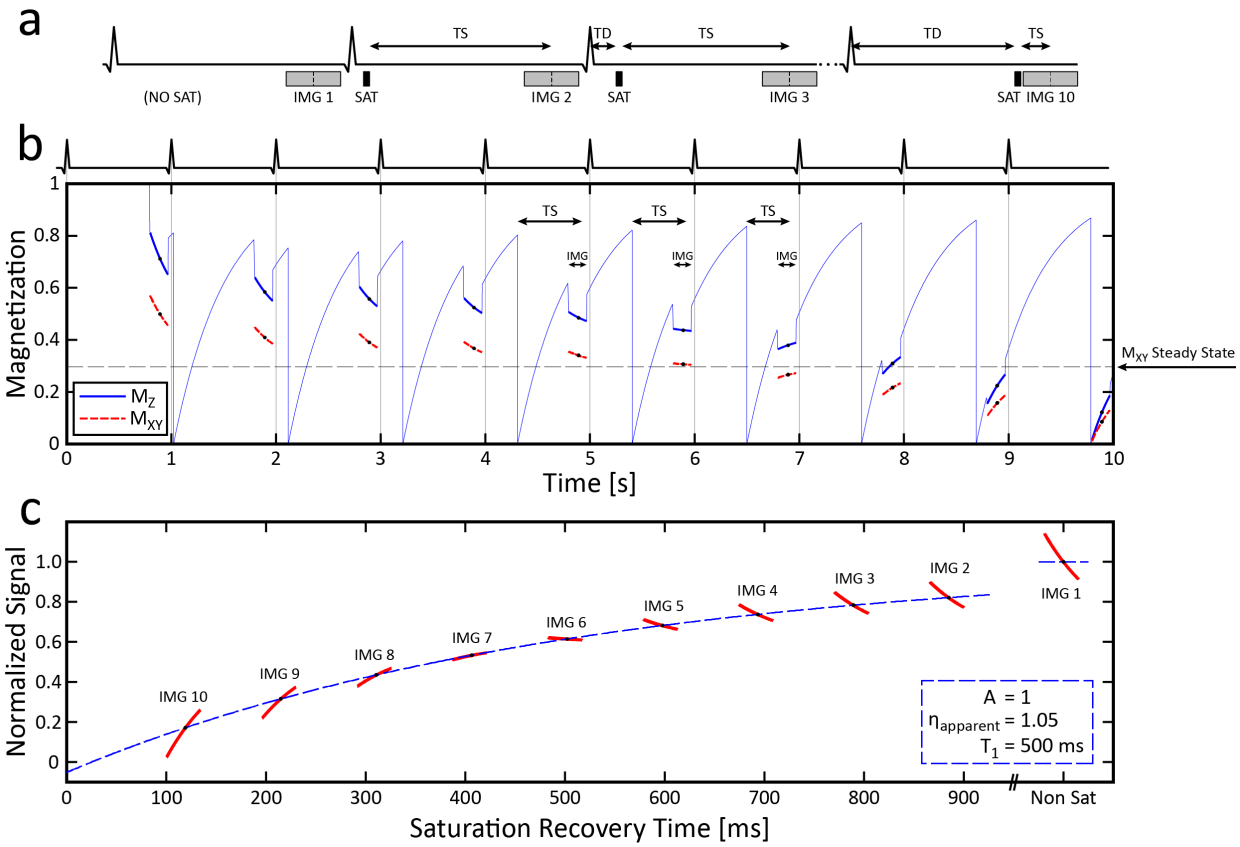

Figure 3.1: **(a)** Variable trigger delays (TD) are used to maintain constant cardiac phase for all images. Dashed vertical lines within each image readout represent the center of k-space. **(b)** Bloch equation simulation of longitudinal (M_Z) and transverse (M_{XY}) magnetization during the SASHA sequence for post-contrast blood with $T_2/T_1 = 180/500$ ms and ideal saturation ($\eta_{actual} = 1$). Bold lines indicate magnetization during imaging. **(c)** Magnetization curves for all images from panel b are shown scaled down in time by a factor of 5 and normalized to the signal intensity of the first image. The best-fit of Eq. 3.2 through the center of k-space for each image is shown with a dashed line.

saturation with 3 RF pulses, 70° flip angle, 3 preparation ramped start-up RF pulses with flip angle scaling factors of 1/6, 3/6, and 5/6 (of 70°), a closing $\alpha/2$ (35°) RF pulse following imaging, 1.3 ms echo time (TE), 2.6 ms repetition time (TR), 119–885 ms TS (for a heart rate of 60 bpm), 8 mm slice thickness, 270×360 mm field of view, 108×192 acquisition matrix size before interpolation, 75% phase resolution, and rate 2 k-space based parallel imaging for a ~175 ms imaging window. All imaging was performed with body coil RF transmission.

3.3.2 Calculation of T_1 Values

T_1 image analysis was performed offline using MATLAB R2009a (The MathWorks; Natick, USA). For all simulations, phantom, and in-vivo experiments, T_1 values were calculated by fitting image signal intensities to a three-parameter exponential recovery curve (Eq. 3.2). The first non-saturated image had the exponential term set to zero so that Signal = A. A Levenberg-Marquardt algorithm [27] was used to determine best-fit values for A, η_{apparent}, and T_1.

3.3.3 Simulations

The full SASHA pulse sequence was simulated using the Bloch equations in MATLAB with actual acquisition and timing parameters. Saturation pulses were implemented as complete spoiling of transverse magnetization and multiplication of longitudinal magnetization by (1-η_{actual}). Simulations were performed using ranges of heart rates (60–100 bpm), T_1s (300–2000 ms), T_2s (50–250 ms), η_{actual} (0.9–1.1), flip angles (30–90), and off-resonant frequencies (±0.375/TR, i.e. ±143 Hz) to determine the dependence of best-fit T_1 values on each parameter. Signal intensities from simulations with different flip angles were also combined as a weighted sum before calculating T_1 to emulate the effect of an excitation slice profile.

The range of SASHA TS times are determined by the R-R interval, where the sampling of the recovery curve will be reduced at higher heart rates and more so for longer T_1 values. Monte Carlo simulations were performed to examine the noise dependence of best-fit T_1s for blood (pre-contrast T_2/T_1: 240/1650 ms, post-contrast: 180/500 ms) and myocardium (pre-contrast T_2/T_1: 50/1175 ms, post-contrast: 50/725 ms). T_1s were selected to reflect baseline (non-contrast) T_1 values and those 15 minutes after a 0.1 mmol/kg bolus of a gadolinium. Non-contrast T_2s were selected based on literature values [28], and post-contrast T_2s were calculated using the relaxivity equation assuming matching relaxivity for T_1 and T_2. For each case, simulations were run with 100,000 repetitions for heart rates of 60 and 100 beats per minute (bpm) and SNR values of 20–120 in steps of 10. Simulated

signal intensities were calculated using the Bloch equations with TS times matching those calculated on the MRI scanner for the given heart rate and signal intensity was normalized to unity at the non-saturated time point. In each repetition, T_1 values were calculated using Rician distributed data with ν as normalized simulated signal intensities and σ as 1/SNR to represent magnitude reconstructed data. Based on this definition, the non-saturated image has the specified SNR value and remaining 9 SASHA images have lower SNR values due to reduced signal intensities, as determined by the TS time. The distributions of best-fit T_1 values are presented as normalized T_1 error (i.e. divided by the input T_1) to facilitate comparison between blood and tissue simulations with different input T_1 values. Variability and bias in best-fit T_1 errors are reported as the inter-quartile range (IQR) of normalized T_1 values and median of normalized T_1 values respectively.

3.3.4 Phantom Experiments

The accuracy of SASHA-derived T_1 values was evaluated in 14 $NiCl_2$-doped agarose phantoms [29] with T_1 and T_2 values spanning the wide range found in blood and myocardium with a normal range of gadolinium concentrations. Gold standard T_1 measurements were performed using inversion recovery spin echo experiments with 15 inversion times spanning 100–3000 ms, 11 ms TE, and one line of k-space acquired per inversion. Gold standard T_2 measurements were performed with spin echo experiments with 7 TEs spanning 11–200 ms, acquired in separate acquisitions. Common sequence parameters between all spin echo imaging were: 10 s TR, 129×360 mm field of view, 46×128 matrix size, 8 mm slice thickness, and a 90° excitation flip angle. Inversion recovery data was fit to Eq. 3.2 to determine T_1, while multiple TE data was fit to $S = A \exp\left(\frac{-TE}{T_2}\right)$ to determine T_2.

The experimentally achieved saturation efficiency (η_{actual}) was measured in phantoms using saturation recovery gradient echo images, acquired with one line of k-space per saturation pulse, with 4 images with TS times (3, 45, 87, 129 ms) and one image without saturation for a total of 5 images. Pulse sequence parameters were: 15° flip angle, 2.12 ms TE, 180×360 mm field of view, 64×128 matrix size, 8 mm slice thickness, and 10 s TR. Signal intensity was fit to Eq. 3.2 and best-fit η_{apparent} was taken to be η_{actual}.

SASHA T_1 mapping was performed using a simulated heart rate of 60 bpm and other acquisition parameters as described above. All phantoms were imaged using a 16-element posterior body coil. T_1, T_2, and η_{actual} values were calculated for each pixel within an ROI in each phantom using a Levenberg-Marquardt algorithm.

3.3.5 In-Vivo Studies

All subjects provided written informed consent with study approval from the University of Calgary Conjoint Health Research Ethics Board. Myocardial and blood T_1 values were measured in a mid-ventricular short-axis slice using SASHA with ECG-triggered diastasis imaging in a 10-heartbeat end-expiration breath-hold. All in-vivo imaging was performed using a 32-element (16 anterior and 16 posterior) body coil.

In a post-contrast time-course sub-study, SASHA T_1 measurements were obtained at baseline and every 1–4 minutes up to 15 minutes following a bolus injection of 0.1 mmol/kg Gd-DTPA (Magnevist; Bayer Healthcare, Toronto, Canada) in 19 healthy subjects without a history of heart disease. Slice thickness was 8–10 mm with other SASHA acquisition parameters the same as above.

In a patient sub-study, nine consecutive heart failure patients and ten consecutive healthy control subjects from an ongoing clinical study of heart failure (Alberta HEART, Alberta Heart Failure Etiology and Analysis Research Team) had SASHA T_1 measurements performed with acquisition parameters as above. T_1 measurements were obtained at baseline and approximately 25 minutes following 0.15 mmol/kg gadobutrol (Gadovist; Bayer HealthCare Pharmaceuticals, Montville, USA). Standard phase-sensitive inversion recovery late gadolinium enhancement imaging [30] was used to identify focal scaring and a short-axis stack of bSSFP cine images was used to calculate left-ventricular mass, volume, and ejection fraction with standard method of disks volumetric analysis using cmr^{42} (Circle Cardiovascular Imaging, Calgary, Canada).

3.3.6 In-Vivo Image Analysis

Saturation efficiency and T_1 image analysis was performed offline by a single individual (KC) using MATLAB. A non-rigid image registration algorithm [31] was used to co-register all 10 images within each SASHA data set. Endocardial and epicardial borders were manually traced on the co-registered images with the inferior right ventricular insertion point identified as a reference point to divide the myocardium into 18 equal circumferential segments, corresponding to each of the six mid-ventricular AHA standardized segments [32] subdivided into three. Images with ECG mis-triggering or residual motion following co-registration were excluded from analysis, with T_1 and λ calculated using the remaining SASHA images. Segments with artifacts or partial voluming of the myocardium were excluded from further analysis and segments with focal scarring identified in late enhancement images (in the patient sub-study) were analyzed separately. An ROI within the left ventricular cavity was traced for blood pool T_1 measurements.

The blood-tissue partition coefficient, λ, was obtained by normalizing the tissue contrast concentration to the blood concentration, where concentration was calculated using the change in T_1 from baseline to post-contrast delivery in both blood and tissue [7]:

$$\lambda = \frac{R_1\left(\text{myocardium}_{\text{post}}\right) - R_1\left(\text{myocardium}_{\text{pre}}\right)}{R_1\left(\text{blood}_{\text{post}}\right) - R_1\left(\text{blood}_{\text{pre}}\right)} \tag{3.3}$$

where:

$$R_1 = \frac{1}{T_1}$$

3.3.7 Myocardial and Blood T_1 Variability

Variability in pre-contrast T_1 values was characterized by calculating a parametric T_1 map for all myocardial and blood pixels using the co-registered SASHA images. The IQR of pixel T_1 values in each myocardial and blood ROI was normalized to the median T_1, as true "input" T_1 values are not known in-vivo. These values were compared the IQR of normalized T_1 values from Monte Carlo simulations.

3.3.8 Inter- and Intra-Observer Reproducibility

Myocardial and blood contours for all subjects were redrawn after at least one month by KC at both the pre-contrast and post-contrast time points (at only 15 minutes for time-course subjects) to assess intra-observer variability. All analysis was repeated by a second observer (RBT) to assess inter-observer variability.

3.3.9 Statistics

Myocardial T_1, λ, and T_1 variability for each subject were calculated as the average of these values from all included segments without focal scar in late enhancement imaging. Group values are expressed as mean ± standard deviation. Multiple regression analysis was used to determine the effects of gender and heart rate on pre-contrast myocardial and blood T_1 values in the post-contrast time-course sub-study population. Student's t-tests were used for statistical comparison of λ and T_1 between heart failure and control groups in the patient sub-study. Paired Student's t-tests were used for statistical comparison of λ and T_1 between scarred and remote segments in subjects with focal scarring. Inter- and intra-observer variability was assessed using the coefficient of variation (standard deviation of the differences divided by the mean) and intra-class correlation (ICC) using a two-way random effects model with absolute agreement for single measurements. The distribution

of best-fit T_1 values was tested for normality using the Lilliefors test. Statistical tests were performed using SPSS version 19 (IBM Software Group, Somers, United States) with statistical significance set at $P < 0.05$ for all tests.

3.4 Results

3.4.1 Simulations

Figure 3.1b shows the longitudinal and transverse magnetization from a SASHA Bloch equation simulation with the following input parameters: no added noise, ideal saturation pulses, on-resonance, 60 bpm heart rate, 500 ms T_1, and 180 ms T_2, reflecting post-contrast blood relaxation values. Abrupt changes observed in longitudinal magnetization before and after imaging are due to the start-up RF pulses and the $\alpha\pm/2$ closing pulse respectively. The large signal variation over each single-shot acquisition depends on the initial magnetization (determined by TS) relative to the steady state value (determined by T_1, T_2, and various pulse sequence parameters [33]).

The transverse magnetization curves from each image acquisition in the simulation are shown again in Fig. 3.1c, ordered by TS and scaled in time by a factor of 5 to fit on the time-scale. The best-fit curve of signal intensities at center k-space to Eq. 3.2 is also shown, with the calculated T_1 exactly matching the input T_1. The calculated apparent partial inversion ($\eta_{\text{apparent}} = 1.05$), despite the use of ideal saturation pulses, is due to the magnetization perturbation by the bSSFP readout, as described in the Appendix. Additional simulations with ideal saturation and every combination of heart rates, T_1s, T_2s, flip angles, and off-resonant frequencies up to ± 0.25/TR (± 96 Hz), as detailed in the methods above, all resulted in best-fit T_1 errors less than 0.5%. For off-resonant frequencies between ± 0.25/TR and ± 0.375/TR (± 143 Hz) best-fit T_1 errors were 5% or less in 99% of simulated parameter combinations, with errors reaching as high as 8% with flip angles of 90°. Simulations showed no best-fit T_1 dependence on flip angle distributions resulting from realistic slice excitation profiles, as expected from Eq. 3.18.

Numerical simulations with non-ideal saturation pulses showed small systematic errors in best-fit T_1 values, likely as a result of residual magnetization carried over between heartbeats. Figure 3.2 shows T_1 error as a function of η_{actual} and heart rate for pre- and post-contrast blood and myocardium, with true T_1 and T_2 values as described for Monte Carlo simulations in the Methods. The magnitude and direction (underestimation or overestimation) of the errors were different for blood and myocardium and also different with contrast. T_1 errors were mostly insensitive to heart rate, except for pre-contrast blood where

larger errors were found at a high heart rate of 100 bpm. All other errors were less than ~4% for the range of $\eta_{\text{actual}} = 0.9$–$1.1$.

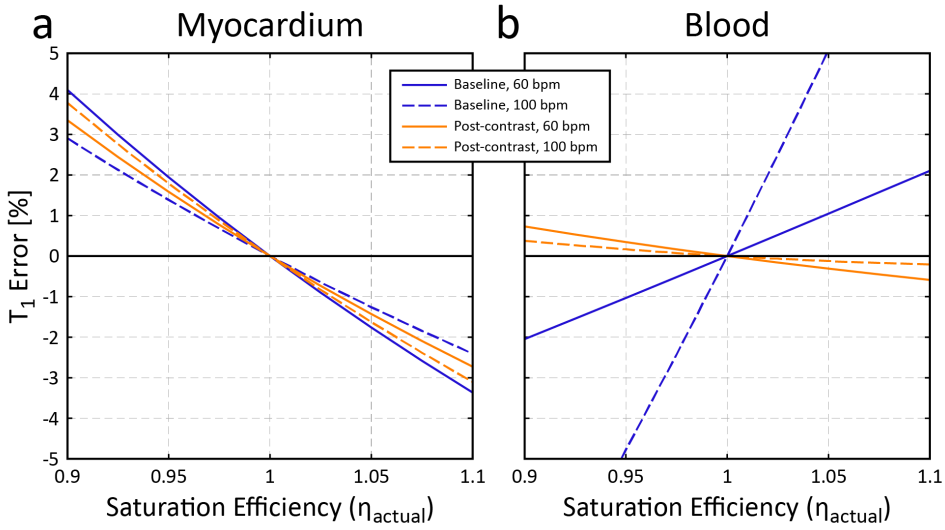

Figure 3.2: Error in SASHA-derived T_1 values with imperfect saturation pulses in the myocardium **(a)** and blood **(b)**, calculated using Bloch equation simulations.

Figure 3.3 shows box-plots of distributions of normalized best-fit T_1 errors from Monte Carlo simulations, as a function of SNR in the non-saturated SASHA image. Nearly all (150 of 152) combinations of heart rate, input T_1/T_2 values, and SNR resulted in non-normal distributions as determined by the Lilliefors test, with increasing skewness at lower SNRs and visualized by the unequal halves of boxes in Fig. 3.3. However, for SNR values greater than 50 at a heart rate of 60 bpm, distributions were approximately normal and the coefficient of variation (CV) could be approximated as normalized IQR divided by 1.35 with an error of less than 1% from the true CV. Median and inter-quartile ranges for simulations of pre-contrast myocardium and blood are re-plotted in Fig. 3.4 to allow for better visualization of bias and variability as a function of SNR. The inter-quartile range (variability) increased with decreasing SNR, but is overall larger in pre-contrast simulations, particularly in the blood at higher heart rates. Non-zero median T_1 errors indicate systematic overestimation of best-fit T_1 values following a similar trend, with appreciable overestimation in baseline blood T_1 values at 100 bpm and an SNR of 20 in the non-saturated SASHA image.

3.4.2 Phantom Experiments

The mean and standard deviation of T_1 and T_2 values calculated from the reference spin-echo experiments for all phantoms are shown in Table 3.1. Phantoms 1–8 had T_1 and T_2 values similar to in-vivo myocardial tissue, while phantoms 9–14 had values similar to

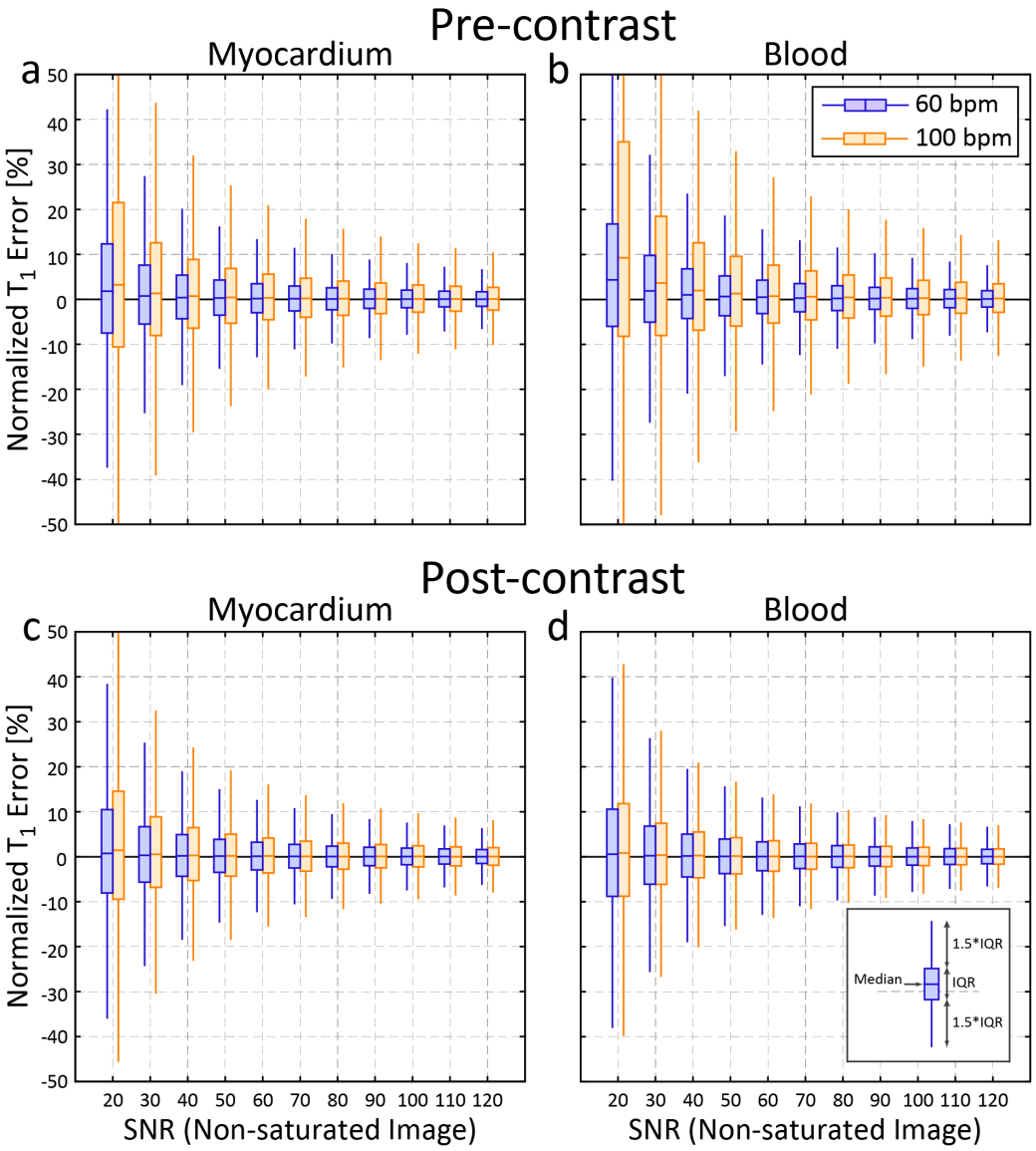

Figure 3.3: Box-and-whiskers plot of Monte Carlo simulations results using T_1/T_2 values representing myocardium (left) and blood (right) at baseline (top) and 15 minutes post-contrast (bottom) as a function of SNR values in non-saturated image. Plotted boxes indicate the median and inter-quartile range (IQR), while whiskers indicate the non-outlier bounds (furthest data points within 1.5 IQR of the upper and lower quartiles).

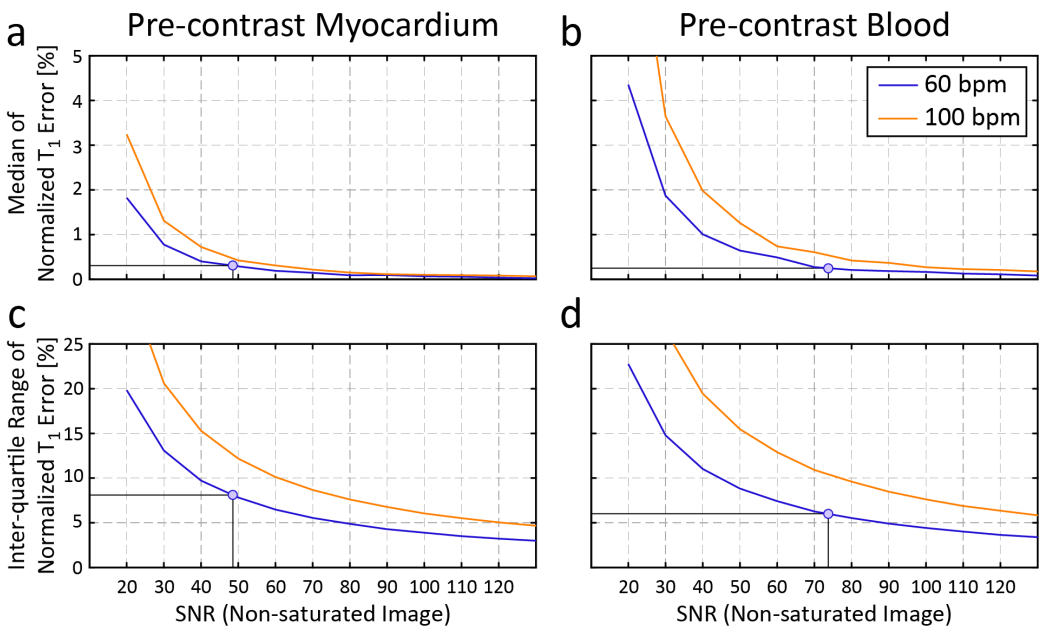

Figure 3.4: Median (top) and inter-quartile range (bottom) of Monte Carlo simulation results using T_1/T_2 values representing pre-contrast myocardium (left) and blood (right). Plotted data points indicate the measured normalized IQR from in-vivo data and the corresponding SNR and median normalized T_1 error.

blood. Bland-Altman analysis of SASHA T_1 values compared to gold standard spin-echo T_1 values showed a small positive bias of 5±5 ms with no significant trend. Errors in SASHA T_1 values did not show significant correlation with absolute T_1 or T_2 values. Excellent saturation efficiency was obtained in the phantoms, with a measured η_{actual} of 0.995±0.004 over pixels within all 14 phantoms.

3.4.3 In-Vivo Studies

Two heart failure patients were excluded for poor image quality; all remaining subjects from both time-course and patient sub-studies had analyzable SASHA T_1 data. One excluded patient had ghosting artifacts that obscured the majority of the left ventricle, and the second patient had severe ECG mis-triggering. Patient characteristics and imaging results for remaining subjects are summarized in Table 3.2.

Breath-holds averaged 10±2 seconds and were well tolerated in all subjects. ECG mis-triggering or motion uncorrectable by image registration resulted in the exclusion of 8 of 2730 images in 273 analyzed SASHA data sets. Presence of artifacts resulted in the exclusion of 3% of segments in the post-contrast time-course sub-study subjects, and 9% in controls and 8% in heart failure patients in the patient sub-study. 67% of excluded segments

Table 3.1: T_1 and T_2 values of agarose phantoms, as determined by spin echo and SASHA

	Spin-Echo		SASHA
Phantom Number	T_2 [ms]	T_1 [ms]	T_1 [ms]
Myocardial-like			
1	47.4 ± 0.2	1142 ± 4	1142 ± 19
2	58.0 ± 0.4	1154 ± 4	1159 ± 17
3	65.0 ± 0.6	1151 ± 5	1164 ± 22
4	74.5 ± 0.3	1144 ± 4	1160 ± 15
5	46.2 ± 0.3	963 ± 4	966 ± 18
6	45.2 ± 0.4	738 ± 3	741 ± 14
7	44.0 ± 0.3	602 ± 3	605 ± 13
8	50.0 ± 0.3	342 ± 2	344 ± 8
Blood-like			
9	172.4 ± 0.9	1470 ± 6	1466 ± 23
10	117.8 ± 0.4	279 ± 1	279 ± 5
11	165.5 ± 0.6	435 ± 1	440 ± 5
12	189.4 ± 0.7	606 ± 2	611 ± 9
13	177.6 ± 0.9	832 ± 3	848 ± 16
14	187.4 ± 0.9	991 ± 3	997 ± 18

were located in the anterior or inferolateral regions. The most common reason for segment exclusion was partial voluming of the myocardium, although occasional ghosting over the myocardium was also found in larger subjects. Positive late enhancement was found in 16% of segments for the heart failure patients and not found in any segments for the control subjects.

Figure 3.5a shows images at several TS times in a healthy subject pre-contrast along with myocardial segmentation contours. Good blood-tissue contrast is seen in the non-saturated image, but with reduced contrast at the endocardial border in saturation prepared images, typical of pre-contrast imaging. A typical best-fit recovery curve from a mid-septal segment is shown in Fig. 3.5b alongside a bull's-eye plot representing all myocardial and blood pool T_1 values from ROI analysis (Fig. 3.5c). A difference in best-fit η_{apparent} between myocardial and blood recovery curves is due to their difference in T_1 and T_2 values, as described in the Appendix. A pixel-by-pixel parametric T_1 map is shown in Fig. 3.5d. The average myocardial T_1 value of the 18 circumferential segments (1175±32 ms) was similar to the average T_1 value of individual pixels over entire myocardium (1179±58 ms).

SASHA images in a heart failure subject 33 minutes following contrast (Fig. 3.6a) show good blood tissue contrast in all images, typical of post-contrast imaging. Reduced post-contrast myocardial T_1 values in a bull's-eye plot (Fig. 3.6b) and pixel T_1 map (Fig.

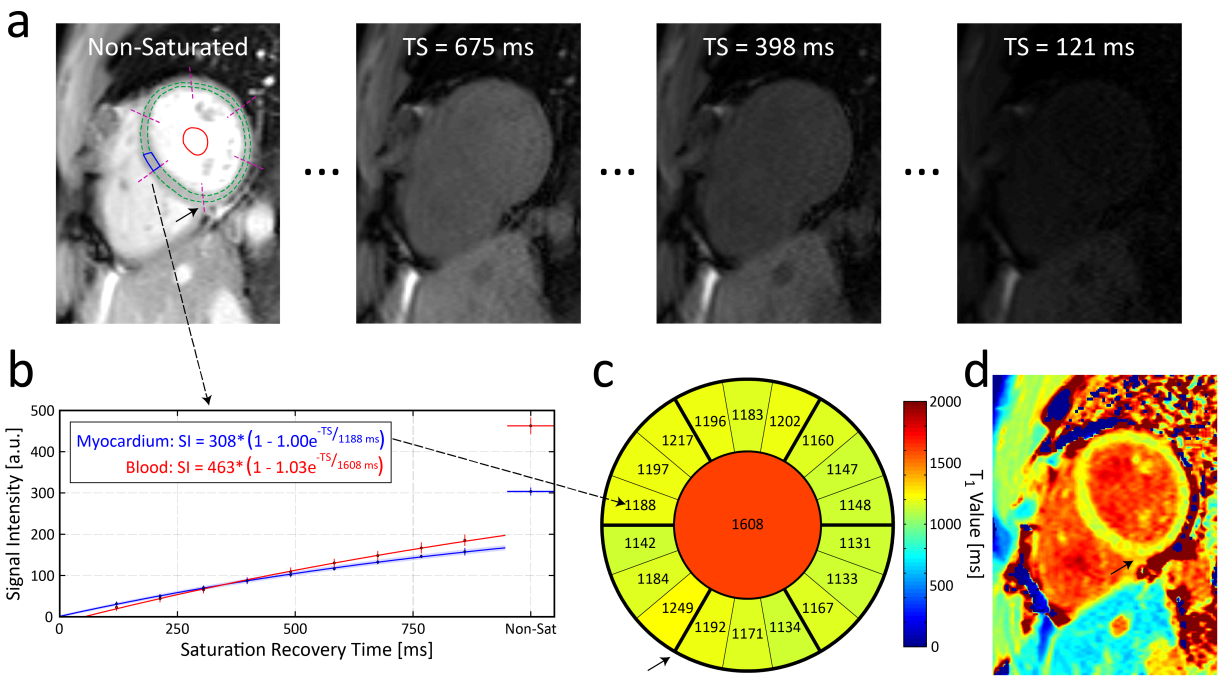

Figure 3.5: T_1 mapping in a healthy time-course sub-study subject before gadolinium contrast. **(a)** SASHA images from a short-axis slice at various saturation recovery times along with myocardial (dashed circles) and blood contours (solid circle), inferior right ventricular insertion point (black arrow), and circumferential segmentation (dashed lines). **(b)** Signal intensities from a septal segment (blue rectangle in panel a) and the blood pool ROI. Plotted circles and vertical lines indicate mean and ±2 standard deviations of signal intensities (in scanner units) within each ROI respectively. Best-fit curves of Eq. 3.2 are also shown. **(c)** T_1 values in the myocardium (circumferential segments) and blood pool (central circle). Black arrow indicates inferior right ventricular insertion point in panels a, c, and d. **(d)** Parametric T_1 map. Color map legend is matched between panels c and d.

Table 3.2: Subject characteristics

	Time-course sub-study	Patient sub-study	
		Control	Heart Failure
Age [years]	28 ± 6	54 ± 6	65 ± 9
Weight [kg]	73 ± 14	83 ± 20	87 ± 17
Heart rate [bpm]	65 ± 11	63 ± 8	71 ± 18
Left Ventricle			
End-diastolic volume [mL/m^2]		65 ± 9	96 ± 33
End-systolic volume [mL/m^2]		24 ± 4	57 ± 31
Stroke volume [mL/m^2]		41 ± 6	39 ± 6
Ejection fraction [%]		63 ± 4	43 ± 10
Myocardial T_1 [ms]			
Baseline	1174 ± 27	1170 ± 9	1200 ± 34
Post 0.1 mmol/kg Gd-DTPA	720 ± 48		
Post 0.15 mmol/kg gadobutrol		568 ± 40	538 ± 32
Blood T_1 [ms]			
Baseline	1655 ± 86	1613 ± 93	1678 ± 127
Post 0.1 mmol/kg Gd-DTPA	492 ± 42		
Post 0.15 mmol/kg gadobutrol		335 ± 44	340 ± 37
Normalized IQR [%]			
Baseline myocardial T_1	7.2 ± 1.9	7.8 ± 2.1	11.0 ± 4.6
Baseline blood T_1	5.4 ± 1.5	5.5 ± 1.5	8.5 ± 3.2
Post-contrast time [min]	15 ± 1	24 ± 2	28 ± 4
Partition coefficient (λ)	0.38 ± 0.04	0.38 ± 0.02	0.42 ± 0.04

3.6c) correspond to the transmural ischemic pattern scar in the inferior wall of the corresponding late enhancement image (white arrow, Fig. 3.6d).

The average normalized IQR of T_1 values within myocardial ROIs, excluding segments with artifact or positive late enhancement, was 8.8±2.8% over all subjects (Table 3.2), with less variability in healthy subjects than heart failure patients. T_1 variability was less in the blood pool than in the myocardium, with an average normalized IQR of 7.3±2.7% over all subjects.

3.4.4 Post-Contrast Time-Course Sub-Study

The time-course of blood T_1, myocardial T_1, and λ values after contrast injection is summarized in Fig. 3.7. The mean and standard deviation for all values are shown in one-minute intervals after contrast injection. Derived λ shows no significant trend from 5 to 15 minutes with an average value of 0.38±0.01 while blood and tissue T_1s increase considerably

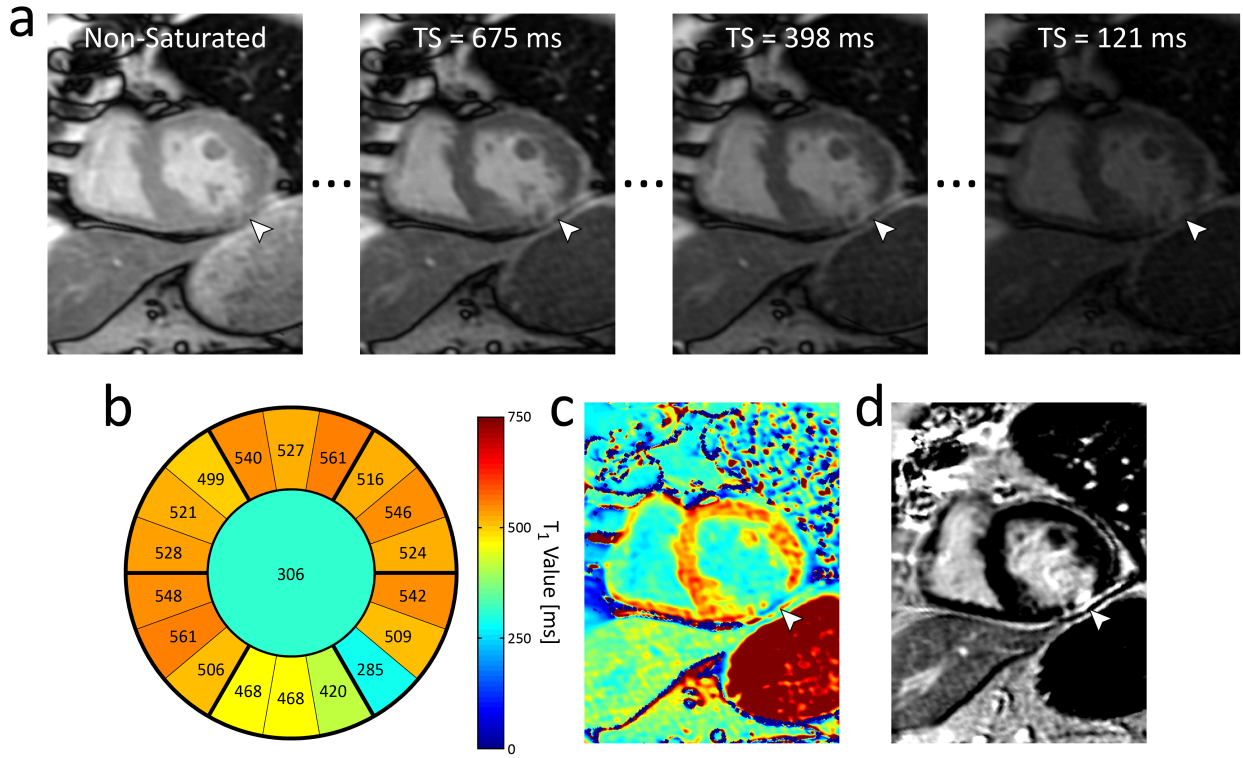

Figure 3.6: T_1 mapping in a heart failure subject 33 minutes following contrast. **(a)** SASHA images at various saturation recovery times with hyperintensity visible in the inferior wall (white arrow). A bull's-eye plot **(b)** of myocardial (circumferential segments) and blood (central circle) T_1 values and parametric T_1 map **(c)** both show reduced myocardial T_1 values in the inferior wall. **(d)** Late gadolinium enhancement image showing transmural ischemic pattern scarring in the inferior wall (white arrow).

by 29% and 17% respectively over the same interval.

Baseline blood T_1 values from the time-course sub-study were not significantly related to heart rate when controlling for gender from multiple regression analysis. However, a significant difference in baseline blood T_1 values was found between men (1605±65 ms) and women (1724±62 ms) when controlling for heart rate (mean 64±13 bpm, range 45–90 bpm). Baseline myocardial T_1 values showed no significant difference with gender or heart rate.

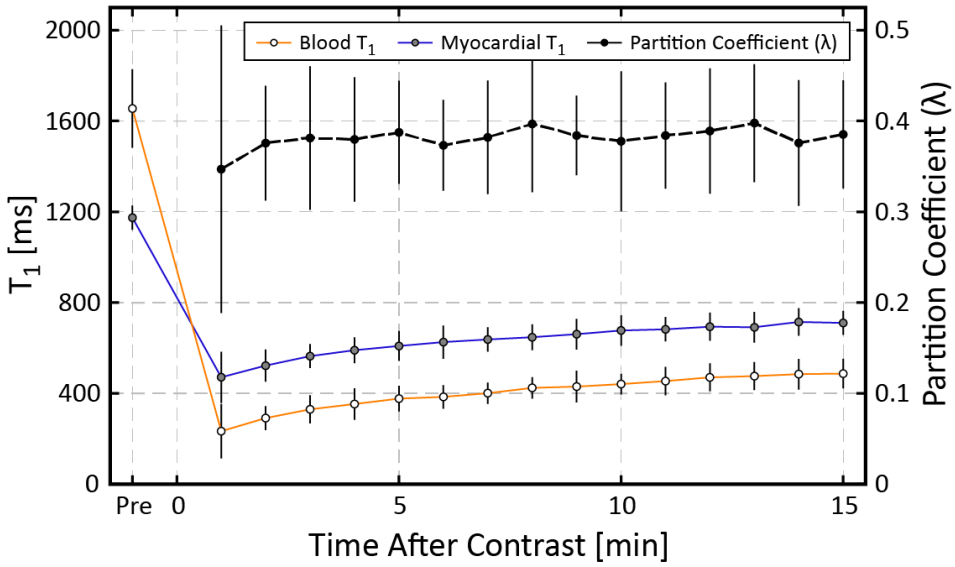

Figure 3.7: Post-contrast time-course of myocardial T_1, blood T_1, and partition coefficient (λ) in 19 healthy volunteers. Vertical lines represent two standard deviations above and below average values at each time point.

3.4.5 Heart Failure Sub-Study

Heart failure patients had reduced systolic function, larger end-diastolic volumes, and larger end-systolic volumes. Compared to controls, remote myocardial segments without focal scarring in heart failure patients had statistically higher pre-contrast myocardial T_1 values and increased λ, but post-contrast myocardial T_1 values were not statistically different (Table 3.2). In the 4 subjects with late enhancement focal scarring, scarred segments had statistically significantly higher pre-contrast myocardial T_1 values (1292±33 vs. 1214±34 ms), lower post-contrast myocardial T_1 values (483±25 vs. 534±25 ms), and significantly increased λ (0.54±0.07 vs. 0.42±0.04) compared to non-scarred segments.

3.4.6 Inter- and Intra-Observer Reproducibility

Myocardial and blood T_1 measurements had excellent inter- and intra-observer coefficients of variation of less than 2.6% and intra-class correlations of 1.00 for all. The derived partition coefficient (λ) had slightly higher inter- and intra-observer CV of 4.7% and 4.9% respectively and an ICC of 0.90 for both.

3.5 Discussion

This study has described and validated a simple and accurate approach to blood and myocardial T_1 mapping that can be performed in a single 10-heartbeat breath-hold. Based on numerical simulations and phantom experiments, the accuracy of SASHA T_1 values is independent of absolute T_1, T_2, heart rate, flip angle, and off-resonant frequencies up to $\pm$96 Hz. Furthermore, best-fit T_1 values do not require a correction factor to account for magnetization attenuation by the imaging readout.

3.5.1 Myocardial and Blood T_1 Values

Baseline myocardial T_1 values in healthy subjects showed similar variability as other T_1 mapping techniques with an overall myocardial standard deviation of $\pm$22 ms between subjects. Myocardial T_1 values in healthy subjects with SASHA (1174$\pm$27 ms) are slightly lower than previously reported values with a saturation recovery FLASH sequence (1219$\pm$72 ms [23]) but considerably higher than values with MOLLI sequences (939$\pm$24 ms [15], 947 ms [5], and 966$\pm$48 ms [16]).

Baseline blood T_1 values in the time-course and control subjects (1639$\pm$97 ms) are also higher than previously reported values using MOLLI (1518 ms [5]) and saturation recovery FLASH (1516$\pm$21 ms [23]) sequences. Measurement of blood T_1 in these studies as well as the current study was performed within the left ventricular cavity where inflow errors may arise. In MOLLI sequences, the delay of several heart-beats between inversion and imaging for long TI images may cause distant non-inverted blood to be imaged, resulting in an apparent decrease in T_1 values. Shorter TS times used in SASHA reduce the likelihood of non-saturated blood being imaged, and thus inflow errors are expected to be diminished. Additionally, previous studies have reported a considerable range of blood T_1 values in healthy subjects with a negative relationship between hematocrit and T_1 [34, 35]. This is consistent with data from the time-course subjects in this study, where females had higher blood T_1 values compared to men (1724$\pm$62 ms vs. 1605$\pm$65 ms), likely as a result of the lower hematocrit values expected in women.

The difference in blood T_1 values between the SASHA and MOLLI sequences is consistent with a known 4–10% MOLLI T_1 underestimation in phantoms studies, with larger T_1 errors found at longer absolute T_1 values [14–16]. The even larger difference in myocardial T_1 values can also be partially explained by previous reports of greater MOLLI T_1 underestimation in short T_2 tissues such as the myocardium [20, 21]. However, the almost 20% discrepancy observed for in-vivo myocardial T_1 values requires further investigation. MOLLI sequences are also known to have heart rate dependencies that change with the sampling scheme employed [5, 16], although correction algorithms have been proposed [36]. By comparison, the accuracy of SASHA T_1 values has been shown to be independent of absolute T_1s, T_2s, flip angle and heart rates.

3.5.2 Partition Coefficient

In the post-contrast time-course subjects, λ remained constant while myocardial and blood T_1 values increased with imaging time after contrast delivery as gadolinium was cleared from the blood and tissue. Insensitivity of λ with imaging time is consistent with previous studies [4, 5, 11] and confirms λ as a more robust metric of the underlying extracellular volume fraction than post-contrast myocardial T_1 values alone. The dependence of post-contrast blood and tissue T_1 on measurement time observed in the current study likely contributes to the lack of statistical significance in post-contrast myocardial T_1 values between the heart failure and control group, despite a statistically higher λ in patients (Table 3.2). In particular, the later post-contrast imaging time in patients would result in an increase in post-contrast myocardial T_1 values that is independent of λ.

Heart failure patients had significantly higher λ in scarred segments compared to remote myocardium, consistent with replacement fibrosis, and higher λ in remote myocardium than controls, consistent with increased interstitial fibrosis expected in heart failure [26]. Calculated λ was also similar in the healthy time-course and control populations, despite potential differences in myocardial T_1 values expected due to dissimilar contrast agents, contrast dosage, and imaging times after contrast. However, direct comparison of these groups is confounded by age differences, as λ has been shown to change with age [18].

SASHA-derived λ values for healthy subjects in the current study (0.38 ± 0.04) are smaller than previously reported values of 0.41 ± 0.06 using an IR-FLASH technique at 3T [11] and 0.43 ± 0.03 using a hybrid MOLLI technique with gadoteridol [5]. While λ reflects a physiologic parameter that is ideally independent of measurement technique, comparisons of λ between studies is difficult due to the propagation of sequence dependent T_1 errors to the derived λ. In particular, T_2 dependent errors in MOLLI-derived T_1 values may result in

systematic T_1 errors that are different in blood and myocardium due to their different T_2 values. Also, while λ was similar between the two contrast agents used in this study, this may not hold true for all gadolinium based contrast agents. Finally, reported changes in contrast agent relaxivity with field strength [37] may further confound direct comparisons.

3.5.3 Inter- and Intra-Observer Reproducibility

Myocardial and blood T_1 measurements had low inter- and intra-observer coefficients of variation and excellent intra-class correlations, similar previously reported values for MOLLI [38]. Higher CVs and lower ICCs for the derived partition coefficient may be related to the reduced range of values for lambda compared to the large range of T_1 values found pre- and post-contrast. ICCs in this study were better than those previously reported for a study using the MOLLI sequence, where ICC was 0.82 using Gd-BOPTA and 0.63 using Gd-DTPA [39]. In all cases, the reproducibility CVs in this study were approximately half the variation found in each value for the healthy population.

3.5.4 Image Quality

A small percentage of myocardial sectors were excluded from analysis due to unclear boundaries of the myocardium with neighbouring blood or epicardial fat, both of which have greatly different T_1 values than myocardium. In ROI based analysis where SNR is less of a limitation, reducing slice thickness may be useful by reducing partial voluming effects. As with any sequence using a bSSFP readout, occasional image artifacts including ghosting and banding were present, with one SASHA data set unanalyzable due to artifacts. Banding artifacts are exacerbated in the presence of metallic implants or poor shimming and result in complex changes to signal intensities that may produce unreliable SASHA T_1 values. In the time-course data, the overall segment exclusion rate of 4% was comparable to 3% exclusion rate reported for MOLLI [17], which is not surprising given the similarity in single-shot bSSFP readouts used in both sequences.

3.5.5 T_1 Variability and Pulse Sequence Limitations

The normalized inter-quartile range (IQR divided by median) is a metric of in-vivo variability that includes the effects of SNR as well as other factors such as residual image misregistration from motion despite image registration and physiologic spatial variability in T_1, particularly in the patient population. At sufficiently high SNRs where the distribution of T_1 error is approximately normal, the CV is approximately equal to normalized IQR divided

by 1.35. The average measured myocardial normalized IQR of 8.1% is thus approximately equivalent to a CV of 6.0%, comparable to previously reported CVs of 6–8% for MOLLI in-vivo [14, 16].

In the worst case scenario where T_1 variability is due entirely to noise alone, the Monte Carlo simulation results can be used to estimate lower bounds for SNR in the non-saturated image using Fig. 3.4. The average normalized IQR of 8.1±3.0% in the myocardium and 6.0±2.3% in the blood measured in-vivo correspond to a minimum myocardial SNR of 49 and blood SNR of 74 at a heart rate of 60 bpm (marked data points, Fig. 3.4). A similar myocardial SNR value of 46 has been reported using a single-shot bSSFP readout [40]. However, the use of smaller voxels and a T_2 preparation pulse in this referenced study suggests that higher SNR values are achievable.

At these estimated lower bounds of SNR for our study groups, Monte Carlo simulation results suggest systematic overestimation of T_1 values is less than 0.5%, even at a heart rate of 100 bpm (Fig. 3.4). However, SNR may be diminished if flip angle is reduced due to SAR limitations, if receiver coils are farther away from the myocardium in larger subjects, or other practical limitations in clinical settings. At low SNR values, SASHA T_1 values will be unreliable due to systematic overestimation and increased variability, as illustrated in Fig. 3.4. Figure 3.4 can also be used to determine the minimum SNR required to attain a desired level of precision and accuracy in SASHA T_1 values. For example, if the normalized IQR is to be kept below 15% (equivalent to an 11% CV), with median error less than 1% in the myocardium, a minimum SNR of 40 in the non-saturated SASHA image must be attained.

Systematic overestimation at low SNR values is likely related to the Rician distribution, where the signal intensity in short TS time images is increased due to the magnitude image reconstruction. It is possible that phase sensitive reconstruction of SASHA images could therefore reduce systematic bias at low SNR values, as low signal intensities with noise would follow an unbiased Gaussian distribution instead.

Non-ideal saturation pulse efficiency (η_{actual}) or incomplete spoiling may result in systematic errors in SASHA due to the memory effect of incomplete saturation, and the SASHA sequence could also potentially be made more robust with the use of alternate saturation preparation pulses. However, nearly ideal saturation was measured in all phantoms, and a similarly robust in-vivo saturation efficiency with a 3-pulse composite saturation has been previously demonstrated at 3T [41]. Therefore, the dependence on η_{actual} is not a practical limitation of the SASHA method.

As a bSSFP based sequence, SASHA is sensitive to off-resonant frequency errors, although simulations showed negligible best-fit T_1 errors for off-resonant frequencies from ±96 Hz, which is 2.7 times the reported peak-to-peak variation of 70 Hz found across the

myocardium at 1.5T [42]. However, larger errors were found when off-resonance reached ±0.36/TR (±137 Hz), which may be more likely at higher field strength as variations of up to 130 Hz have been reported at 3T [43]. In these and other cases where off-resonance may be an issue, reducing the TR increases the range of absolute off-resonance frequencies where SASHA has minimal errors.

3.5.6 Study Limitations

Our study is limited by relatively small numbers of subjects imaged, particularly in the heart failure sub-study. While our results are consistent with previous findings, further studies are needed to better characterize changes found in heart failure. Direct comparisons of SASHA to standard MOLLI sequences were not made in this study but are the subject of ongoing research.

As with previous studies with in-vivo calculations of the blood-tissue partition coefficient, this study makes several common assumptions about contrast agent kinetics. First, the contrast agent relaxivity is assumed not to differ between blood and tissue and thus cancels out in the calculation of λ, although there is evidence to suggest this may not hold true at higher field strengths [37]. Secondly, it is assumed that contrast concentration between the blood and tissue have reached equilibrium in all post-contrast measurements. Simulations have shown blood-tissue concentration equilibrium is reached 3 minutes after a contrast bolus for tissue blood flow above 0.5 $mL{\cdot}min^{-1}{\cdot}g^{-1}$ [11], and a study comparing bolus contrast administration to a continuous infusion of contrast agent has shown similar λ values between them [5]. However, it is possible that lower calculated λ values in this study for the time-course sub-study before the 3 minute mark are due to non-equilibrium conditions. Lastly, it is assumed that water exchange between tissue compartments is in the fast exchange regime [44].

In general, λ provides only a measure of extracellular volume fraction and not fibrosis itself. The extracellular volume fraction (ECV) can be better estimated by correcting the partition coefficient for the blood hematocrit [7], although this was not available for subjects in this study. While post-contrast myocardial T_1, λ, and ECV have been correlated with fibrosis in patients following heart transplantation [2] and with hypertrophic cardiomyopathy [3], other disease processes that increase extracellular volume would also present as reduced post-contrast myocardial T_1, increased λ, and increased ECV.

3.6 Conclusions

The proposed saturation recovery single shot acquisition (SASHA) sequence allows for simple and fast in-vivo measurements of myocardial and blood T_1 values. Numerical simulations suggest the accuracy of measured T_1 values are independent of absolute T_1, T_2, heart rate, and flip angle, and spin echo experiments verified its accuracy in phantoms with physiologic T_1 and T_2 values. Potential sources of error include off-resonance, incomplete saturation preparation and low SNR, which result in increasing variability and overestimation of T_1. SASHA is an excellent candidate for future T_1 mapping applications, but further studies and comparisons with existing T_1 mapping sequences are needed to establish its robustness in clinical patient populations.

3.7 Appendix: Origin of Apparent Changes in Saturation Efficiency in SASHA

The measured signal intensity in each SASHA image is determined by a combination of saturation recovery preparation and the balanced steady-state free precession (bSSFP) readout.

3.7.1 Saturation Recovery Preparation

The longitudinal magnetization for each SASHA image after saturation recovery preparation is characterized by a three-parameter exponential recovery curve:

$$M(0) = 1 - \eta_{actual} e^{\frac{-(TS-\Delta)}{T_1}} \tag{3.4}$$

where η_{actual} is the saturation efficiency ($\eta_{\text{actual}} = 1$ for perfect saturation), TS is the conventional definition of saturation recovery time, from the end of the saturation pulse to the center of k-space, Δ is the time from the start of imaging to the center of k-space, and (TS-Δ) is the time from the end of the saturation pulse to the start of imaging.

For the non-saturated image in SASHA, $M(0) = 1$.

Eq. 3.4 can be re-written as:

$$M(0) = 1 - \eta_{actual} e^{\frac{-(TS-\Delta)}{T_1}}$$

$$M(0) = 1 - \eta_{actual} e^{\frac{\Delta}{T_1} - \frac{TS}{T_1}}$$

$$M(0) = 1 - (e^{\frac{\Delta}{T_1}})\eta_{actual}e^{-\frac{TS}{T_1}} \tag{3.5}$$

The offset factor Δ may also be expressed in terms of bSSFP sequence parameters:

$$\Delta = (n-1)TR + TE \tag{3.6}$$

where n is the number of RF pulses to the center of k-space, TR is the repetition time, and TE is the echo time.

3.7.2 Effect of a bSSFP Readout

The signal intensity (magnitude of the transverse magnetization) of a spin-system after n RF pulses in a bSSFP experiment may be approximated in the on-resonance case as [45]:

$$S(n) = \left[\sin\left(\frac{\alpha}{2}\right) M(0) - M_{\mathrm{SS}}\right] \lambda_1^n + M_{SS} \tag{3.7}$$

where:

$$\lambda_1 = E_2 \sin^2\left(\frac{\alpha}{2}\right) + E_1 \cos^2\left(\frac{\alpha}{2}\right) \tag{3.8}$$

$$E_{1,2} = e^{\frac{-TR}{T_{1,2}}} \tag{3.9}$$

$$M_{SS} = \frac{\sqrt{E_2}\,(1-E_1)\sin\alpha}{1-(E_1-E_2)\cos\alpha - E_1E_2} \tag{3.10}$$

and M_{SS} is the steady state magnetization, *M(0)* is the starting longitudinal magnetization after saturation recovery preparation, TR is the repetition time, and α is the flip angle.

Eq. 3.7 can be re-written in terms of the starting magnetization as:

$$S(n) = \left[\sin\left(\frac{\alpha}{2}\right) M(0) - M_{\mathrm{SS}}\right] \lambda_1^n + M_{SS}$$

$$S(n) = \sin\left(\frac{\alpha}{2}\right) \lambda_1^n M(0) + \left[1 - \lambda_1^n\right] M_{SS}$$

$$S(n) = aM(0) + b \tag{3.11}$$

where:

$$a = \sin\left(\frac{\alpha}{2}\right) \lambda_1^n \tag{3.12}$$

$$b = [1 - \lambda_1^n]\, M_{SS} \tag{3.13}$$

and a and b are constants determined by T_1, T_2, TR, flip angle, and n, the number of RF pulses to the center of k-space.

Eq. 3.5 and Eq. 3.11 can be combined to yield the signal at the center of k-space, S, in terms of the three-parameter exponential recovery model:

$$S = aM(0) + b$$

$$S = a\left[1 - (e^{\frac{\Delta}{T_1}})\eta_{actual}e^{-\frac{TS}{T_1}}\right] + b$$

$$S = a + b - a(e^{\frac{\Delta}{T_1}})\eta_{actual}e^{-\frac{TS}{T_1}}$$

$$S = (a+b)\left[1 - \frac{a}{a+b}(e^{\frac{\Delta}{T_1}})\eta_{actual}e^{-\frac{TS}{T_1}}\right]$$

$$S = A\left(1 - \eta_{apparent}e^{-\frac{TS}{T_1}}\right) \tag{3.14}$$

where:

$$A = a + b \tag{3.15}$$

$$\eta_{apparent} = \left(\frac{a}{a+b}e^{\frac{\Delta}{T_1}}\right)\eta_{actual} \tag{3.16}$$

The apparent saturation efficiency (η_{apparent}) thus reflects not only the actual saturation efficiency (η_{actual}), but is also influenced by T_1, T_2, and pulse sequence parameters, as given by equations 3.6, 3.8, 3.9, 3.10, 3.12, 3.13.

3.7.3 Effect of a Flip Angle Distribution

A realistic slice excitation profile contains a distribution of flip angles and the total signal is a weighted sum of SASHA experiments performed with different flip angles. This can be represented as:

$$S' = \sum_{i=1}^{n} w_i S_i \tag{3.17}$$

where there are n experiments indexed by i, each with a different flip angle, and w_i are the weighting coefficients that define the flip angle distribution. The signal intensity for each flip angle experiment is described by Eq. 3.14, where η_{apparent} is flip angle dependent, while

the exponential term, exp(-TS/T_1), is not. Eq. 3.17 can be rewritten as:

$$S' = \sum w_i \left[A_i \left(1 - \eta_{\text{apparent}_i} e^{\frac{-\text{TS}}{T_1}} \right) \right]$$

$$S' = \sum w_i A_i - \left(\sum w_i A_i \eta_{\text{apparent}_i} \right) e^{\frac{-\text{TS}}{T_1}}$$

$$S' = \sum w_i A_i \left[1 - \left(\frac{\sum w_i A_i \eta_{\text{apparent}_i}}{\sum w_i A_i} \right) e^{\frac{-\text{TS}}{T_1}} \right]$$

$$S' = A' \left(1 - \eta'_{\text{apparent}} e^{\frac{-\text{TS}}{T_1}} \right) \tag{3.18}$$

where:

$$A' = \sum w_i A_i \tag{3.19}$$

$$\eta'_{\text{apparent}} = \frac{\sum w_i A_i \eta_{\text{apparent}}}{\sum w_i A_i} \tag{3.20}$$

Therefore, the total signal intensity from a SASHA experiment with a flip angle distribution can still be represented by a three-parameter exponential recovery model.

3.8 References

[1] Erica Dall'Armellina, Stefan K Piechnik, Vanessa M Ferreira, Quang Le Si, Matthew D Robson, Jane M Francis, Florim Cuculi, Rajesh K Kharbanda, Adrian P Banning, Robin P Choudhury, Theodoros D Karamitsos, and Stefan Neubauer. Cardiovascular magnetic resonance by non contrast T1 mapping allows assessment of severity of injury in acute myocardial infarction. *Journal of cardiovascular magnetic resonance : official journal of the Society for Cardiovascular Magnetic Resonance*, 14(1):15, February 2012. pg. 59

[2] Leah Iles, Heinz Pfluger, Arintaya Phrommintikul, Joshi Cherayath, Pelin Aksit, Sandeep N Gupta, David M Kaye, and Andrew J Taylor. Evaluation of diffuse myocardial fibrosis in heart failure with cardiac magnetic resonance contrast-enhanced T1 mapping. *Journal of the American College of Cardiology*, 52(19):1574–1580, November 2008. pg. 59, pg. 59, pg. 60, pg. 80

[3] Andrew S Flett, Martin P Hayward, Michael T Ashworth, Michael Schacht Hansen, Andrew M Taylor, Perry M Elliott, Christopher McGregor, and James Charles Moon. Equilibrium contrast cardiovascular magnetic resonance for the measurement of diffuse myocardial fibrosis: preliminary validation in humans. *Circulation*, 122(2):138–144, July 2010. pg. 59, pg. 59, pg. 59, pg. 59, pg. 80

[4] Kelvin Chow, Jacqueline A Flewitt, Jordin D Green, Matthias G Friedrich, and Richard B Thompson. Characterization of myocardial T1 and partition coefficient as a function of time after gadolinium delivery in healthy subjects. *Journal of cardiovascular magnetic resonance : official journal of the Society for Cardiovascular Magnetic Resonance*, 13(Suppl 1):P31, 2011. pg. 77

[5] Erik B Schelbert, Stephen M Testa, Christopher G Meier, William J Ceyrolles, Joshua E Levenson, Alexander J Blair, Peter Kellman, Bobby L Jones, Daniel R Ludwig, David S Schwartzman, Sanjeev G Shroff, and Timothy C Wong. Myocardial extravascular extracellular volume fraction measurement by gadolinium cardiovascular magnetic resonance in humans: slow infusion versus bolus. *Journal of cardiovascular magnetic resonance : official journal of the Society for Cardiovascular Magnetic Resonance*, 13:16, 2011. pg. 60, pg. 60, pg. 76, pg. 76, pg. 77, pg. 77, pg. 77, pg. 80

[6] Daniel R Messroghli, Sven Plein, David M Higgins, Kevin Walters, Timothy R Jones,

John P Ridgway, and Mohan U Sivananthan. Human myocardium: single-breath-hold MR T1 mapping with high spatial resolution–reproducibility study. *Radiology*, 238(3):1004–1012, March 2006. pg. 59, pg. 60, pg. 60

[7] Sebastian J Flacke, S E Fischer, and C H Lorenz. Measurement of the gadopentetate dimeglumine partition coefficient in human myocardium in vivo: normal distribution and elevation in acute and chronic infarction. *Radiology*, 218(3):703–710, March 2001. pg. 59, pg. 66, pg. 80

[8] D Look and D Locker. Time Saving in Measurement of NMR and EPR Relaxation Times. *Review of Scientific Instruments*, 41(2):250–251, 1970. pg. 60

[9] R Deichmann and Axel Haase. Quantification of T1 values by SNAPSHOT-FLASH NMR imaging. *Journal of Magnetic Resonance*, 96(3):608–612, February 1992. pg. 60, pg. 60

[10] R Deichmann, D Hahn, and Axel Haase. Fast T1 mapping on a whole-body scanner. *Magnetic Resonance in Medicine*, 42(1):206–209, July 1999.

[11] Michael Jerosch-Herold, David C Sheridan, Jessica D Kushner, Deirdre Nauman, Donna Burgess, Diana Dutton, Rami Alharethi, Duanxiang Li, and Ray E Hershberger. Cardiac magnetic resonance imaging of myocardial contrast uptake and blood flow in patients affected with idiopathic or familial dilated cardiomyopathy. *American journal of physiology Heart and circulatory physiology*, 295(3):H1234–H1242, September 2008. pg. 60, pg. 60, pg. 77, pg. 77, pg. 80

[12] M Karlsson and B Nordell. Analysis of the Look-Locker T(1) mapping sequence in dynamic contrast uptake studies: simulation and in vivo validation. *Magnetic resonance imaging*, 18(8):947–954, October 2000. pg. 60

[13] Neville D Gai, Evrim B Turkbey, Saman Nazarian, Rob J van der Geest, Chia-Ying Liu, João A C Lima, and David A Bluemke. T1 mapping of the gadolinium-enhanced myocardium: adjustment for factors affecting interpatient comparison. *Magnetic Resonance in Medicine*, 65(5):1407–1415, May 2011. pg. 60

[14] Daniel R Messroghli, Aleksandra Radjenovic, Sebastian Kozerke, David M Higgins, Mohan U Sivananthan, and John P Ridgway. Modified Look-Locker inversion recovery (MOLLI) for high-resolution T1 mapping of the heart. *Magnetic Resonance in Medicine*, 52(1):141–146, July 2004. pg. 60, pg. 60, pg. 77, pg. 79

[15] Daniel R Messroghli, Andreas Greiser, Mirko Fröhlich, Rainer Dietz, and Jeanette Schulz-Menger. Optimization and validation of a fully-integrated pulse sequence for modified look-locker inversion-recovery (MOLLI) T1 mapping of the heart. *Journal of magnetic resonance imaging : JMRI*, 26(4):1081–1086, October 2007. pg. 60, pg. 76

[16] Stefan K Piechnik, Vanessa M Ferreira, Erica Dall'Armellina, Lowri E Cochlin, Andreas Greiser, Stefan Neubauer, and Matthew D Robson. Shortened Modified Look-Locker Inversion recovery (ShMOLLI) for clinical myocardial T1-mapping at 1.5 and 3 T within a 9 heartbeat breathhold. *Journal of cardiovascular magnetic resonance : official journal of the Society for Cardiovascular Magnetic Resonance*, 12:69, 2010. pg. 60, pg. 60, pg. 60, pg. 76, pg. 77, pg. 77, pg. 79

[17] Daniel R Messroghli, Kevin Walters, Sven Plein, Patrick Sparrow, Matthias G Friedrich, John P Ridgway, and Mohan U Sivananthan. Myocardial T1 mapping: application to patients with acute and chronic myocardial infarction. *Magnetic Resonance in Medicine*, 58(1):34–40, July 2007. pg. 60, pg. 78

[18] Martin Ugander, Abiola J Oki, Li-Yueh Hsu, Peter Kellman, Andreas Greiser, Anthony H Aletras, Christopher T Sibley, Marcus Y Chen, W Patricia Bandettini, and Andrew E Arai. Extracellular volume imaging by magnetic resonance imaging provides insights into overt and sub-clinical myocardial pathology. *European heart journal*, 33(10):1268–1278, May 2012. pg. 60, pg. 60, pg. 77

[19] Patrick Sparrow, Daniel R Messroghli, Scott Reid, John P Ridgway, Gavin Bainbridge, and Mohan U Sivananthan. Myocardial T1 mapping for detection of left ventricular myocardial fibrosis in chronic aortic regurgitation: pilot study. *AJR American journal of roentgenology*, 187(6):W630–5, December 2006. pg. 60

[20] Kelvin Chow, Jacqueline A Flewitt, Joseph J Pagano, Jordin D Green, Matthias G Friedrich, and Richard B Thompson. MOLLI T1 Values Have Systematic T2 and Inversion Efficiency Dependent Errors. In *Proceedings of the International Society for Magnetic Resonance in Medicine*, page 395, 2012. pg. 60, pg. 77

[21] Neville D Gai, Christian Stehning, Marcelo Nacif, and David A Bluemke. Modified Look-Locker T1 evaluation using Bloch simulations: human and phantom validation. *Magnetic Resonance in Medicine*, 69(2):329–336, February 2013. pg. 60, pg. 77

[22] Ting Song, Jeffrey A Stainsby, Vincent B Ho, Maureen N Hood, and Glenn S Slavin. Flexible cardiac T(1) mapping using a modified look-locker acquisition with saturation recovery. *Magnetic Resonance in Medicine*, 67(3):622–627, March 2012. pg. 60

[23] C M Wacker, M Bock, A W Hartlep, G Beck, G van Kaick, G Ertl, W R Bauer, and L R Schad. Changes in myocardial oxygenation and perfusion under pharmacological stress with dipyridamole: assessment using T*2 and T1 measurements. *Magnetic Resonance in Medicine*, 41(4):686–695, April 1999. pg. 60, pg. 76, pg. 76

[24] David M Higgins, John P Ridgway, Aleksandra Radjenovic, U Mohan Sivananthan, and Michael A Smith. T1 measurement using a short acquisition period for quantitative cardiac applications. *Medical physics*, 32(6):1738–1746, May 2005. pg. 60

[25] Mariell Jessup and Susan Brozena. Heart failure. *The New England journal of medicine*, 348(20):2007–2018, May 2003. pg. 60

[26] D L Mann. Mechanisms and models in heart failure: A combinatorial approach. *Circulation*, 100(9):999–1008, August 1999. pg. 60, pg. 77

[27] Donald Marquardt. An Algorithm for Least-Squares Estimation of Nonlinear Parameters. *Journal of the Society for Industrial and Applied Mathematics*, 11(2):431–441, June 1963. pg. 63

[28] Warren D Foltz, Osama Al-Kwifi, Marshall S Sussman, Jeffrey A Stainsby, and Graham A Wright. Optimized spiral imaging for measurement of myocardial T2 relaxation. *Magnetic Resonance in Medicine*, 49(6):1089–1097, June 2003. pg. 63

[29] K A Kraft, P P Fatouros, G D Clarke, and P R Kishore. An MRI phantom material for quantitative relaxometry. *Magnetic Resonance in Medicine*, 5(6):555–562, December 1987. pg. 64

[30] Peter Kellman, Andrew E Arai, Elliot R McVeigh, and Anthony H Aletras. Phase-sensitive inversion recovery for detecting myocardial infarction using gadolinium-delayed hyperenhancement. *Magnetic Resonance in Medicine*, 47(2):372–383, February 2002. pg. 65

[31] Stefan Klein, Marius Staring, Keelin Murphy, Max A Viergever, and Josien P W Pluim. elastix: a toolbox for intensity-based medical image registration. *IEEE transactions on medical imaging*, 29(1):196–205, 2010. pg. 65

[32] Manuel D Cerqueira, Neil J Weissman, Vasken Dilsizian, Alice K Jacobs, Sanjiv Kaul, Warren K Laskey, Dudley J Pennell, John A Rumberger, Thomas Ryan, Mario S Verani, American Heart Association Writing Group on Myocardial Segmentation, and Registration for Cardiac Imaging. Standardized myocardial segmentation and nomenclature

for tomographic imaging of the heart: a statement for healthcare professionals from the Cardiac Imaging Committee of the Council on Clinical Cardiology of the American Heart Association. *Circulation*, 105(4):539–542, January 2002. pg. 65

[33] Y Zur, S Stokar, and P Bendel. An analysis of fast imaging sequences with steady-state transverse magnetization refocusing. *Magnetic Resonance in Medicine*, 6(2):175–193, February 1988. pg. 67

[34] P A Janick, D B Hackney, R I Grossman, and T Asakura. MR imaging of various oxidation states of intracellular and extracellular hemoglobin. *AJNR American journal of neuroradiology*, 12(5):891–897, 1991. pg. 76

[35] Hanzhang Lu, Chekesha Clingman, Xavier Golay, and Peter C M van Zijl. Determining the longitudinal relaxation time (T1) of blood at 3.0 Tesla. *Magnetic Resonance in Medicine*, 52(3):679–682, September 2004. pg. 76

[36] Nadine Kawel, Marcelo Nacif, Anna Zavodni, Jacquin Jones, Songtao Liu, Christopher Sibley, and David Bluemke. T1 mapping of the myocardium: intra-individual assessment of post-contrast T1 time evolution and extracellular volume fraction at 3T for Gd-DTPA and Gd-BOPTA. *Journal of cardiovascular magnetic resonance : official journal of the Society for Cardiovascular Magnetic Resonance*, 14(1):26, 2012. pg. 77

[37] Puneet Sharma, Josh Socolow, Salil Patel, Roderic I Pettigrew, and John N Oshinski. Effect of Gd-DTPA-BMA on blood and myocardial T1 at 1.5T and 3T in humans. *Journal of magnetic resonance imaging : JMRI*, 23(3):323–330, March 2006. pg. 78, pg. 80

[38] Nadine Kawel, Marcelo Nacif, Anna Zavodni, Jacquin Jones, Songtao Liu, Christopher Sibley, and David Bluemke. T1 mapping of the myocardium: Intra-individual assessment of the effect of field strength, cardiac cycle and variation by myocardial region. *Journal of cardiovascular magnetic resonance : official journal of the Society for Cardiovascular Magnetic Resonance*, 14(1):27, 2012. pg. 78

[39] Nadine Kawel, Marcelo Nacif, Francesco Santini, Songtao Liu, Jens Bremerich, Andrew E Arai, and David A Bluemke. Partition coefficients for gadolinium chelates in the normal myocardium: Comparison of gadopentetate dimeglumine and gadobenate dimeglumine. *Journal of magnetic resonance imaging : JMRI*, 36(3):733–737, September 2012. pg. 78

[40] Peter Kellman, Anthony H Aletras, Christine Mancini, Elliot R McVeigh, and Andrew E Arai. T2-prepared SSFP improves diagnostic confidence in edema imaging in acute myocardial infarction compared to turbo spin echo. *Magnetic Resonance in Medicine*, 57(5):891–897, May 2007. pg. 79

[41] Daniel Kim, Oded Gonen, Niels Oesingmann, and Leon Axel. Comparison of the effectiveness of saturation pulses in the heart at 3T. *Magnetic Resonance in Medicine*, 59(1):209–215, 2008. pg. 79

[42] Scott B Reeder, A Z Faranesh, J L Boxerman, and E R McVeigh. In vivo measurement of T*2 and field inhomogeneity maps in the human heart at 1.5 T. *Magnetic Resonance in Medicine*, 39(6):988–998, June 1998. pg. 80

[43] R Noeske, F Seifert, K H Rhein, and H Rinneberg. Human cardiac imaging at 3 T using phased array coils. *Magnetic Resonance in Medicine*, 44(6):978–982, December 2000. pg. 80

[44] Kathleen M Donahue, R M Weisskoff, and D Burstein. Water diffusion and exchange as they influence contrast enhancement. *Journal of magnetic resonance imaging : JMRI*, 7(1):102–110, 1997. pg. 80

[45] Klaus Scheffler. On the transient phase of balanced SSFP sequences. *Magnetic Resonance in Medicine*, 49(4):781–783, April 2003. pg. 82

Chapter 4

Saturation Pulse Design for Quantitative Cardiac Imaging[1]

4.1 Introduction

Non-selective saturation pulses are commonly used in quantitative MRI pulse sequences to prepare longitudinal magnetization to a known zero state and generate longitudinal relaxation time (T_1) contrast for quantitative first-pass perfusion [1] or the quantification of T_1 directly. In quantitative T_1 imaging, multiple images with variable saturation recovery times are used to directly quantify T_1 values in sequences such as SRTFL [2], SAP-T1 [3], and the recently proposed SAturation recovery single-SHot Acquisition (SASHA) [4]. Saturation pulses have also been used in the saturated double angle method (SDAM) [5] and 3D T_2 mapping [6] to reset the longitudinal magnetization to a consistent state for multiple acquisitions, regardless of its initial state, instead of using long delays for full T_1 recovery.

Incomplete saturation results in errors in quantified parameters due to a combination of the assumption of perfect saturation in the analysis model and effects from the history of magnetization prior to the saturation pulse. The saturation efficiency can be quantified as the residual longitudinal magnetization (M_Z/M_0), which can range from -1 (full inversion) to 1 (no effect) with 0 for perfect saturation. For quantitative perfusion imaging, residual M_Z/M_0 results in large errors in estimated pre-contrast T_1 values which propagate to errors in the calculated contrast agent concentration and calculated tissue perfusion [7]. In the standard three-parameter exponential fit of SASHA T_1 data, saturation efficiency is a modeled parameter, but residual M_Z/M_0 still results in errors in the calculated T_1 values due to

[1] A version of this chapter has been submitted for review: Chow K, Kellman P, Spottiswoode BS, Thompson RB. Saturation Pulse Design for Quantitative Cardiac Imaging. *Mag Reson Med.* Submitted 26 August 2014.

magnetization carry-through [4]. Two-parameter fitting of SASHA data has been shown to substantially reduce variability of calculated T_1 values [8], but will give rise to larger errors in best-fit T_1 values due to the explicit assumption of ideal saturation in addition to the carry-through effects. In general, variability in M_Z/M_0 should be kept as low as possible for quantitative applications in order to minimize associated variability in derived parameters.

Composite saturation pulses consisting of trains of shaped RF pulses with numerically optimized flip angles have been designed for enhanced water suppression over narrow B_0 and B_1 ranges for spectroscopy applications at 1.5T [9] and wide ranges at 7T [10]. Hard RF pulse trains have also been proposed [11] and numerically optimized for improved performance over B_0 and B_1 ranges expected at 3T with in-vivo evaluation [12]. However, T_1 effects were not considered in these recent designs and their residual magnetization over the smaller range of commonly observed B_0 and B_1 values found at 1.5T may not be sufficient for quantitative imaging, depending on the allowable threshold of residual M_Z/M_0. Adiabatic BIR4-90 saturation pulses [13] and hybrid adiabatic-rectangular saturation pulses [14] have been proposed as a more B_0/B_1 insensitive alternative at the expense of higher specific absorption rate (SAR), but have not been specifically designed for the ranges of B_0/B_1 ranges found at 1.5 and 3T with specific residual M_Z/M_0 criteria. Also, the high B_1 field strength required to meet the adiabatic criteria may exceed the routinely achievable RF transmitter voltage. On higher B_0 field strength magnets, lower B_1 scale factors may reduce the effective B_1 field to below the adiabatic limit and result in poor performance [5, 12].

In this work, we expand upon existing literature regarding the design of saturation pulse trains and adiabatic saturation pulses with the primary goal of developing saturation pulses with less than 1% residual $|M_Z/M_0|$ over ranges of B_0 and B_1 values found at 1.5T and 3T, given the practical constraints of peak B_1 transmit field strength. An intuitive understanding of the pattern of flip angles chosen in pulse trains is developed and the performance of the proposed saturation pulses are simulated and experimentally validated in phantom experiments with wide variations in B_0 and B_1 values. The magnitude of T_1 errors for the two-parameter SASHA T_1 mapping technique is characterized as a function of M_Z/M_0.

4.2 Theory

4.2.1 Geometric Pulse Train Design

The simplest saturation pulse is a single hard RF pulse with a prescribed 90° flip angle. Complete saturation is achieved in regions with perfect B_0 and B_1 field calibration, but incomplete saturation or partial inversion results otherwise. Assuming on-resonance,

the residual M_Z/M_0 for a single hard pulse can be described more generally as $\cos(\hat{B}_1\theta)$, where $\hat{B}_1$ is a normalized scale factor and θ is the flip angle. Complete saturation occurs when $\hat{B}_1\theta$ is equal to 90° or at $\hat{B}_1 = {}^{90^\circ}/_{\theta}$. By approximating the cosine function as linear around the null, the maximum residual $|M_Z/M_0|$ can be intuitively minimized over a range of $\hat{B}_1$ values by minimizing the maximum absolute height of two triangles (Fig. 4.1a). By geometric inspection, this occurs when the null point (a) is in the middle of the optimization range. Therefore, the optimal flip angle to minimize the peak residual $|M_Z/M_0|$for a range of $\hat{B}_1$ values from $\hat{B}_{1min}$ to $\hat{B}_{1max}$ is $\theta_{\text{opt}} \approx \frac{180^\circ}{\left(\hat{B}_{1min}+\hat{B}_{1max}\right)}$.

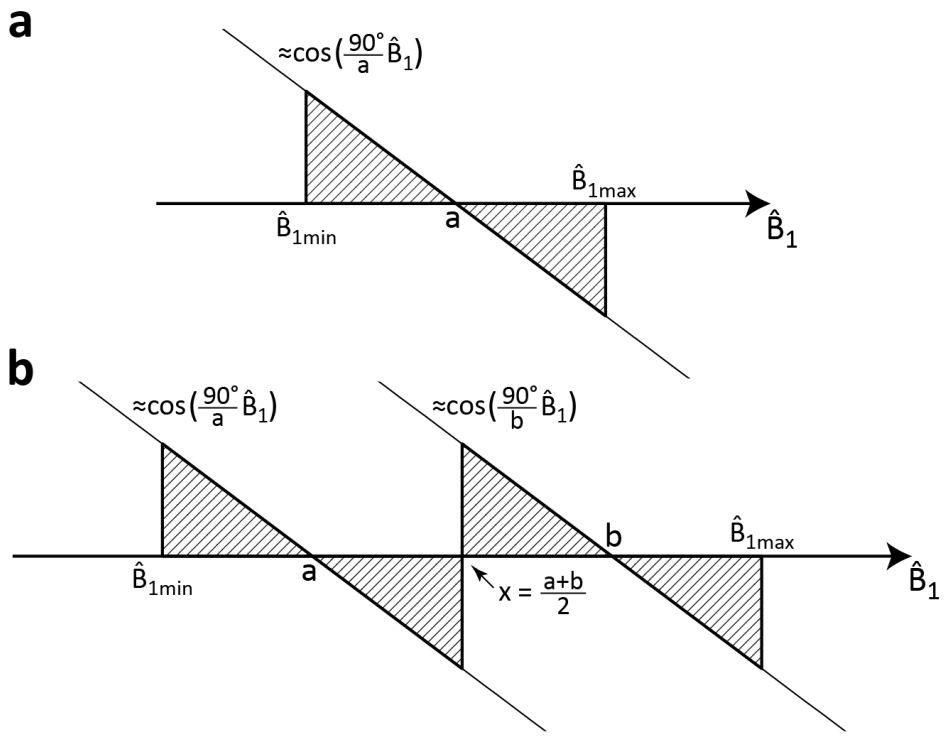

Figure 4.1: Geometric approach to pulse train design for (**a**) a single RF pulse and (**b**) two RF pulses.

This geometric minimization model can be generalized to multiple hard pulses when the residual M_Z/M_0 at a given $\hat{B}_1$ is described only by the minimum absolute valued cosine function at that location (Fig. 4.1b), i.e. ignoring the multiplicative effect of multiple overlapping cosines. Again by geometric inspection, the minimum peak absolute height for all 4 triangles occurs when the null points are at $a = {}^3/_4\hat{B}_{1min} + {}^1/_4\hat{B}_{1max}$ and $b = \hat{B}_{1max} - {}^1/_4\left(\hat{B}_{1max} - \hat{B}_{1min}\right)$. More generally, the optimal solution for n RF pulses is when the null points are evenly spaced with distance $d = \frac{\left(\hat{B}_{1min}+\hat{B}_{1max}\right)}{n}$, with the first and last null points spaced ${}^d/_2$ from $\hat{B}_{1min}$ to $\hat{B}_{1max}$, respectively.

4.3 Methods

4.3.1 B_1 Field Strength Limitations

Off-resonance effects in pulse train saturation are determined by the bandwidth of the RF pulses and results in a reduced effective $\hat{B}_1$. Bandwidth is inversely proportional to pulse duration, which is predominately limited by the maximum achievable RF amplifier voltage. On the MRI systems used in this study, a reference voltage is calculated for each subject corresponding to the transmitter voltage required to achieve a 180° flip angle with a 1 ms rectangular pulse or equivalently a B_1 field strength of 11.7 µT. The maximum achievable B_1 can be calculated by multiplying 11.7 µT by the ratio of maximum voltage to the reference voltage. The maximum achievable B_1 field strength was calculated in this way for subjects on Siemens MAGNETOM 1.5T Aera and 3T Skyra systems over an approximate period of 6 months, with information collected as quality assurance data and analysis approved by the NIH Office of Human Subject Research.

4.3.2 Spoiler Gradient Design

Spoiler gradients in between RF pulses in a saturation pulse train were designed to eliminate transverse magnetization. In contrast to previous pulse train designs where inter-pulse spoilers were polarity cycled along a single direction [11, 12, 14], inter-pulse spoilers in the proposed design were cycled along multiple gradient directions in order to dephase magnetization in all spatial directions and reduce the likelihood that spoiler gradients could be unwound during image readouts. Spoiler durations and total areas were also varied to minimize the potential formation of coherent stimulated echoes, with no two spoilers on the same axis having the same area. The implementation in this study uses a gradient strength of 24 mT/m per channel, which is achievable on most modern MRI scanners. At this strength, the minimum spoiler area in the 6 pulse train was 60 mT·ms/m, equivalent to 2π phase dispersion across 0.4 mm, with other spoiler areas and directions detailed in Fig. 4.2a. Spoiler designs for shorter pulse trains with n pulses share the same design as the first n spoiler gradients in the 6 pulse design, as shown for a 4 pulse train in Fig. 4.2b. The final trailing spoiler gradients are also of the same design, although its polarity is adjusted to maintain alternating polarity within that axis.

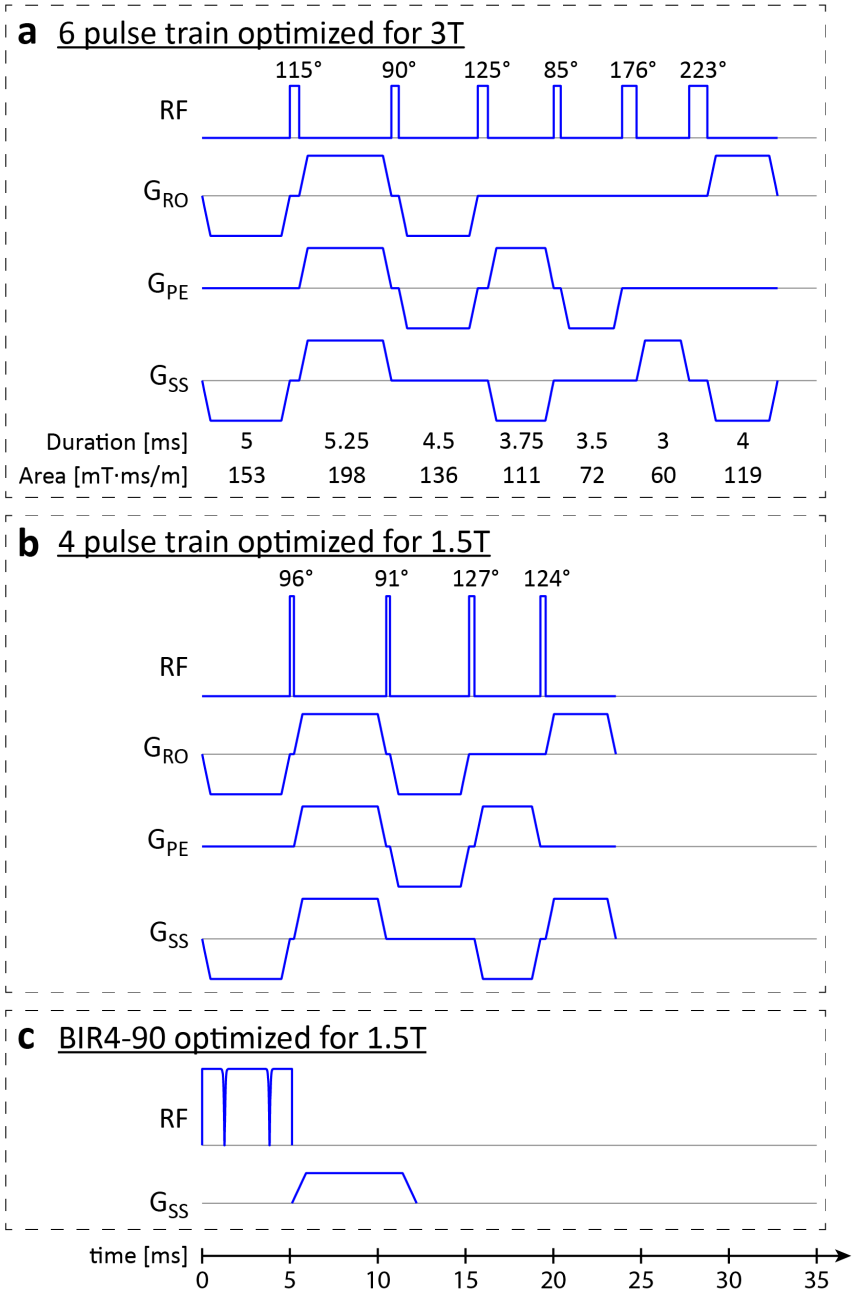

Figure 4.2: **a**. 6 pulse train numerically optimized for 3T ($\hat{B}_1 = 0.4$–1.2, $B_0 = \pm 240$ Hz, B_1 field = 14 µT), with a total duration of 32.8 ms. Gradient areas are the effective areas across all three gradient directions. **b**. 4 pulse train numerically optimized for 1.5T ($\hat{B}_1 = 0.7$–1.0, $B_0 = \pm 120$ Hz, B_1 field = 26.9 µT), with a total duration of 23.6 ms. The first four spoilers are the same for the 4 and 6 pulse trains and the last spoilers have the same pattern, but with the polarity in the slice select axis reversed to maintain alternating polarity. **c**. The optimized BIR4-90 pulse, with a total duration of 12.2 ms. All saturation pulses are shown on the same time, RF amplitude and gradient strength scale.

4.3.3 Numerical Pulse Train Design

Pulse trains were designed first under the simplified assumptions of on-resonance, perfect spoiling, and sufficiently short inter-pulse spoiler gradients such that T_1 relaxation can be ignored. Under these conditions, identical to those used for the geometric minimization model, the residual M_Z/M_0 following a train of hard pulses can be approximated as a product of multiple cosines. The peak residual $|M_Z/M_0|$ was minimized over a range of $\hat{B}_1$ values by varying an unordered set of flip angles using a Nelder-Mead numerical minimization subroutine [15] in MATLAB (R2013a; The MathWorks, Natick, USA). The starting guess for minimization was the optimal flip angle solution for the geometric minimization model. This method is termed simple numerical optimization.

Saturation pulse trains were also designed to account for off-resonance (B_0) and T_1 relaxation by numerical solution of the Bloch equations programmed in MATLAB available online at http://mrsrl.stanford.edu/~brian/blochsim. RF pulse flip angles were altered by varying their duration, using a fixed B_1 value for all pulses in order to achieve the largest possible excitation bandwidth for each pulse. In the on-scanner implementation, the maximum achievable B_1 field strength was calculated and used for every subject. For numerical optimization simulations, the typical maximum B_1 strength measured for each field strength scanner was used. Perfect spoiling was assumed, and thus the spoiler durations before the first RF pulse and after the last RF pulse were omitted. T_1 recovery was simulated during all other spoiler durations and RF pulses.

In this Bloch simulation optimization method, residual $|M_Z/M_0|$ is dependent on the flip angle order due to T_1 effects and thus direct application of standard numerical minimization algorithms was not used to avoid potential trapping in local minima. Instead, the peak residual $|M_Z/M_0|$ was minimized over a range of B_0, $\hat{B}_1$, and T_1 values by applying Nelder-Mead numerical minimization to an unordered set of flip angles. In each iteration, all possible permutations of the flip angle set were evaluated using the Bloch equation simulator over a range of B_0, $\hat{B}_1$, and T_1 values and the lowest mean residual $|M_Z/M_0|$ from all permutations was returned. The starting guess for this minimization was the flip angle set calculated using the simplified minimization described above. Overall computation time was approximately 6 minutes on a 3.6 GHz quad-core Intel Core i7 personal computer for a pulse train of 5 pulses. Source code used for this numerical minimization is available online at https://bitbucket.org/kelvinc/pulsetrainopt.

Both algorithms were applied to calculate the optimal flip angles for pulse trains ranging from 3 to 6 RF pulses. Pulse trains were optimized for 1.5T using a $\hat{B}_1$ range of 0.7–1.0 [16], a B_0 range of $\pm$120 Hz, and a maximum B_1 field strength of 26.9 µT. Pulse

trains were also optimized for 3T using a larger $\hat{B}_1$ range of 0.4–1.2 [12, 17], a B_0 range of ±240 Hz, and a maximum B_1 of 14 µT. In all Bloch simulation minimizations, the T_1 range was 200–2000 ms and T_2 was 45 ms (native myocardium).

Proposed saturation pulse trains were compared to a commonly used reference pulse train consisting of three 90° RF pulses, each with a fixed duration of 0.5 ms [11]. Spoiler durations for the reference pulse train were 1.00, 8.80, 5.86, and 1.55 ms, with a total time of 18.71 ms.

4.3.4 BIR4-90 Pulse Optimization

A BIR4-90 pulse was numerically optimized by a brute force optimization over adiabatic design parameters [18]. The pulse duration, amplitude, maximum frequency sweep, and parameters ζ and κ which define the adiabatic half passage section of the BIR4-90 defined in Equations 4 and 6 in [18] were varied and the optimum pulse was selected which achieved the best saturation over the specified range of $\hat{B}_1$ and off-resonance, i.e., best worst-case deviation. The frequency sweep parameter was varied from 4–20 kHz in 1 kHz steps, $\tan(\kappa)$ ranged from 8 to 22 in steps of 2, and ζ ranged from 8 to 30 in steps of 2. Bloch simulations assumed values for native myocardium of $T_1 = 1100$ ms and $T_2 = 45$ ms. Pulse durations between 4 and 10 ms were evaluated. The design range was ±120 Hz off-resonance and $\hat{B}_1$ ranged from 0.7 to 1.0. The peak amplitude was limited to approximately 20 µT.

4.3.5 RF Power Calculation

Relative RF energy was calculated for each saturation pulse as B_1^2 integrated over time divided by the RF energy of the 90°-90°-90° pulse train. Relative RF power was calculated as the RF energy divided by the total duration (including pre- and post-spoilers) and also normalized to the 90°-90°-90° pulse train.

4.3.6 Phantom Validation

Saturation efficiency was experimentally assessed for five saturation pulses: the reference 90°-90°-90° pulse train, the 1.5T optimized 4 pulse train, the 3T optimized 6 pulse train, the reference BIR4-90 pulse, and the optimized BIR4-90 pulse. Performance for each pulse was assessed in a Siemens 2L plastic bottle phantom (1.25g $NiSO_4 \cdot 6H_2O$ + 5g NaCl per 1000g water). The T_1 value was measured using an inversion recovery spin echo sequence with inversion times between 100 ms and 500 ms and a non-prepared image. T_2 was measured using spin echo repeated with echo times varied between 11 ms and 300 ms.

A linear spatial gradient was applied along the long axis of the phantom to assess performance as a function of off-resonance. To calculate an off-resonance (B_0) map, gradient echo images were acquired with 5 echo times (TE) between 4 and 6 ms, 3000 ms repetition time (TR), 90° flip angle, 128×44 matrix size, 400×138 mm^2 field of view, and 8 mm slice thickness. The B_0 map was generated by fitting the equation $\phi = \Delta B_0 \cdot \mathrm{TE}$ for every pixel, where ϕ is the phase of gradient echo images. To calculate an excitation $\hat{B}_1$-field map for the phantom, gradient echo images were acquired with 45°, 60°, 90°, and 120° flip angles, 3.79 ms TE, and other parameters as above. The signal intensity as a function of flip angle was simulated using a Bloch equation simulation accounting for slice profile effects [19], and a $\hat{B}_1$ map was generated by fitting the measured signal intensity to this simulated curve for every pixel.

Saturation pulse efficiency was calculated using a gradient echo sequence with 3.79 ms TE, 3000 ms TR, 90° flip angle, and other parameters as above. An image was acquired without a saturation pulse and with 4 saturation recovery times (TS = 10–40 ms) for each of the 5 saturation pulses, where TS is defined as the time from the end of the last RF pulse in the saturation and the middle of the imaging excitation RF pulse. A saturation efficiency map was generated by fitting acquired data to Eq. 4.1:

$$Signal = A\left(1 - \eta e^{\frac{-TS}{T_1}}\right) \tag{4.1}$$

where η is the saturation efficiency and residual (signed) M_Z/M_0 is equal to 1-η. These acquisitions were repeated 9 times with the flip angles of the saturation RF pulses scaled by 40–120% to emulate the effect of varied $\hat{B}_1$ values.

For each pixel of the nine resulting residual M_Z/M_0 maps, the B_0 and effective $\hat{B}_1$ (equal to $\hat{B}_1$ map multiplied by the flip angle scaling factor) could be determined, separately for each saturation pulse considered. Together, the intrinsic variation in $\hat{B}_1$ over the phantom in combination with the 9 repeated experiments with flip angle scaling from 40% to 120% yielded a wide range of effective $\hat{B}_1$ values. With the variation in B_0 provided by the linear gradient, the M_Z/M_0 values were thus directly measured over a wide range of B_0 and $\hat{B}_1$ values. The missing data within the B_0–$\hat{B}_1$ space was calculated by fitting a surface over the scattered points with a modified ridge estimator using the gridfit function [20].

4.3.7 SASHA Sequence Simulation

Bloch equation simulations of the SASHA sequence were performed with a range of residual M_Z/M_0 (-5%–5%) and relaxation values emulating myocardium (native T_1/T_2: 1175/50 ms, post-contrast T_1/T_2: 725/50 ms) and blood (native T_1/T_2: 1650/240, post-

contrast: 500/180 ms) at 1.5T [4]. Typical in-vivo SASHA acquisition parameters were used: 1.3/2.6 ms TE/TR, 70° target flip angle, 70 phase encode lines, 60 bpm simulated heart rate, 10 images with maximum 775 ms saturation recovery time (TS) and a non-saturated image. Image readout flip angles were scaled using a variable flip angle (VFA) scheme to minimize T_1 error with two parameter fitting as previously described [21]. In this scheme, the prescribed flip angle of the first 45 RF pulses was scaled by $\sin(x)$ for $\pi/90 < x < \pi/2$. Simulations used actual RF pulse waveforms and the transverse magnetization (M_{XY}) at the centre k-space readout as the image signal intensity. T_1 values were calculated by fitting simulated data to a 2-parameter exponential recovery model with assumed ideal saturation.

4.4 Results

4.4.1 B_1 Field Strength Limitations

The maximum B_1 field strength was calculated for 379 subjects on the Siemens MAGNETOM Skyra platform and 230 subjects on the Siemens MAGNETOM Aera platform. A maximum B_1 field strength of 14 µT was achievable on the 3T Skyra platform in >98% of subjects, while 26.9 µT was achievable on the 1.5T Aera platform in >99% of subjects. At a B_1 strength of 14 µT, a 90° rectangular pulse is 419 µs and the full width half maximum effective B_1 scaling is ±1334 Hz.

4.4.2 BIR4-90 Pulses

The numerically optimized BIR4-90 design used a duration of 5.12 ms, maximum B_1 field of 20.5 µT, swept over ±7 kHz, with $\zeta = 22$ and $\tan(\kappa) = 18$. This design is longer and has a lower maximum B_1 compared to the reference BIR4-90 pulse that has a 4.00 ms duration and a maximum B_1 of 25.1 µT, resulting in lower relative RF power and energy (Table 4.1). The optimized BIR4-90 design had substantially improved performance with a maximum residual $|M_Z/M_0|$ within the 1.5T optimization range 5.8× lower than the reference pulse.

4.4.3 Numerically Optimized Pulse Trains

Calculation time for the Bloch simulation numerical optimizations was less than 6 minutes for 5 pulse trains and less than 60 minutes for 6 pulse trains. The calculated flip angles for 4, 6, and 12 pulse trains optimized for both 1.5T and 3T using the geometric minimization, simple numerical optimization, and Bloch simulation optimization methods

Table 4.1: Summary of characteristics for Bloch simulation numerically optimized saturation pulses

		Flip Angle [°]	Duration [ms]	Relative RF Energy	Relative RF Power	Residual $\lvert M_Z/M_0\rvert$ [%] mean±std (max)
Reference saturation pulses	90°-90°-90°	90-90-90	18.7	1.0	1.0	2.86±2.98 (11.31)
	BIR4-90	25.1 µT (adiabatic)	11.1	11.0	18.5	0.92±0.92 (5.32)
Optimized for 1.5T B_0 = ±120 Hz $\hat{B}_1$ = 0.7 – 1.0 B_1 field = 26.9 µT	BIR4-90	20.6 µT (adiabatic)	12.2	10.0	15.2	0.30±0.14 (0.91)
	3 pulse train	90-107-126	19.5	2.7	2.6	0.40±0.21 (0.80)
	4 pulse train	96-91-127-124	23.6	3.7	3.0	0.11±0.07 (0.25)
	5 pulse train	89-106-89-145-127	27.4	4.7	3.2	0.06±0.03 (0.11)
	6 pulse train	116-99-81-92-146-139	30.6	5.7	3.5	0.02±0.01 (0.04)
Optimized for 3T B_0 = ±240 Hz $\hat{B}_1$ = 0.4 – 1.2 B_1 field = 14 µT	3 pulse train	220-136-93	20.8	2.0	1.8	4.33±2.49 (8.70)
	4 pulse train	75-103-149-213	25.0	2.4	1.8	1.99±1.22 (4.17)
	5 pulse train	99-76-120-169-220	29.2	3.0	1.9	0.64±0.41 (1.58)
	6 pulse train	115-90-125-85-176-223	32.8	3.6	2.0	0.27±0.19 (0.87)

Total duration values include post-spoiler and pre-spoilers where applicable. Residual $\lvert M_Z/M_0\rvert$ values are simulated using Bloch equation simulations and the mean, standard deviation, and maximum are calculated over the entire optimization space, i.e. B_0, $\hat{B}_1$, and T_1. Residual $\lvert M_Z/M_0\rvert$ for reference pulses was evaluated over the 1.5T B_1 range. Relative RF energy and power are normalized to a reference 90°-90°-90° pulse train as described in the methods.

(4 and 6 pulse trains only) are shown graphically in Fig. 4.3. The flip angles are plotted in ascending order for all methods — the geometric minimization and simple optimization return unordered flip angle sets, while the Bloch simulation minimization returns ordered flip angle sets for optimal performance in the presence of T_1 recovery. Flip angles are similar between the geometric and simple minimization methods with a similar distribution pattern for all pulse train lengths. Optimal flip angles calculated using Bloch simulation minimization (right column, Fig. 4.3) are similar to the other design methods for the case of the larger 3T $\hat{B}_1$ range of 0.4–1.2 (bottom row), but the Bloch simulation minimization yielded comparatively larger flip angles for the smaller 1.5T $\hat{B}_1$ range of 0.7–1.0, particularly for the 6 pulse train.

Characteristics of the Bloch simulation numerically optimized pulse trains are summarized in Table 4.1 and their simulated performance is plotted in Fig. 4.4. The reference 90°-90°-90° pulse train has poor performance at the lower end of $\hat{B}_1$ scale factors expected at 1.5T, with a residual M_Z/M_0 of 10% at a $\hat{B}_1$ of 0.7 while on-resonance, with a 1000 ms T_1. For the 1.5T optimization range, simulated residual $\lvert M_Z/M_0\rvert$ achieved the target of <1% with a pulse train length of 3, while 6 pulses were necessary to achieve this target for the 3T optimization range due to the larger $\hat{B}_1$ range of 0.4–1.2. For both $\hat{B}_1$ optimization ranges, simulated residual $\lvert M_Z/M_0\rvert$ increased rapidly outside of the optimization region. Minor off-resonance effects are seen, with larger variations with B_0 at high $\hat{B}_1$ values and for pulse trains optimized for the larger $\hat{B}_1$ range, as shown in the right hand column of Fig. 4.4. Small T_1 effects were also observed, but did not have a consistent trend over the range.

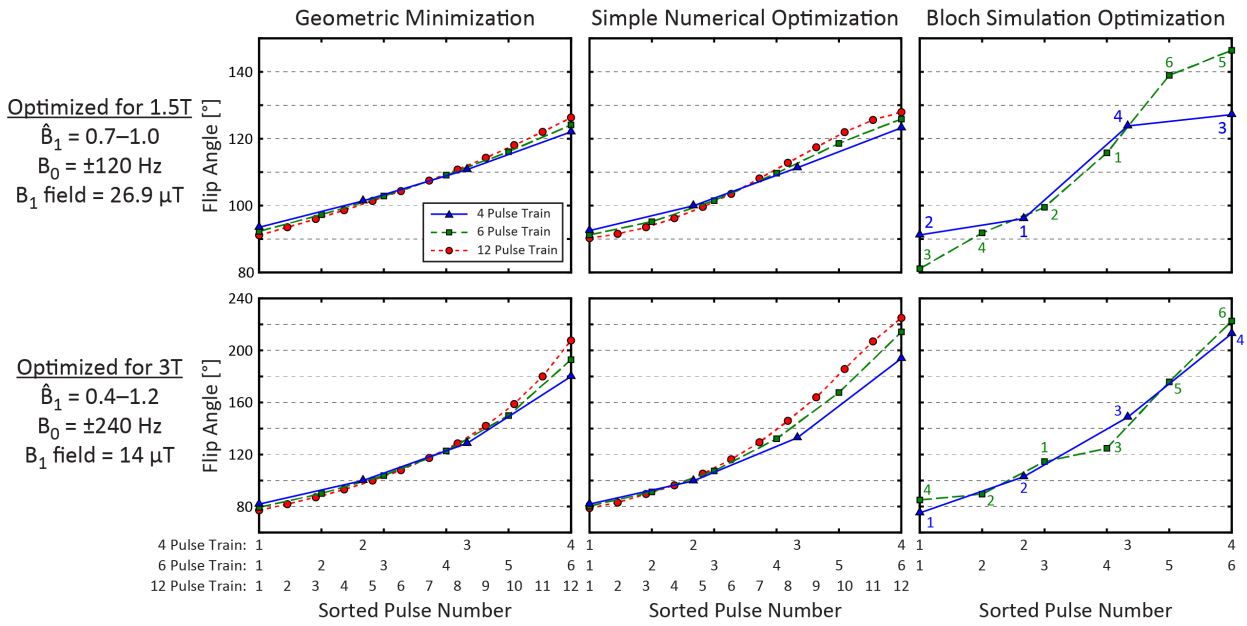

Figure 4.3: Pulse train designs optimized for 1.5T (top) and 3T (bottom) using the geometric minimization model (left), simple numerical optimization assuming on-resonance and no T_1 relaxation (middle), and Bloch simulation numerical optimization with off-resonance and T_1 effects (right). Flip angles are plotted in ascending order demonstrate the flip angle pattern and the flip angle order is labeled for the Bloch simulation optimization.

4.4.4 Pulse Train Ordering Effects

The saturation efficiency of a saturation pulse train is dependent on the order of its flip angles due to T_1 relaxation. The effect of flip angle order in pulse trains can be illustrated by characterizing the residual $|M_Z/M_0|$ for all permutations of a set of flip angles. For the 6 pulse train optimized for 3T (Table 4.1), the residual $|M_Z/M_0|$ was calculated for all 720 (i.e. 6!) flip angle permutations during the final iteration of the Bloch simulation numerical optimization algorithm. The maximum and mean residual $|M_Z/M_0|$ are calculated over the optimization range of B_0, $\hat{B}_1$, and T_1 values and plotted (Fig. 4.5) after sorting by the maximum residual $|M_Z/M_0|$. There was relatively poor correlation between the maximum and mean $|M_Z/M_0|$, as some permutations with similar maximum $|M_Z/M_0|$ had greatly different mean $|M_Z/M_0|$. The largest maximum residual $|M_Z/M_0|$ was 5.7× greater than the smallest, and the largest mean residual $|M_Z/M_0|$ was 2.6× greater than the smallest.

4.4.5 T_1 Relaxation Effects

Simulated residual M_Z/M_0 for selected saturation pulses are shown as a function of T_1 in Fig. 4.6. Performance is only weakly related to T_1 in the optimization range (200–2000

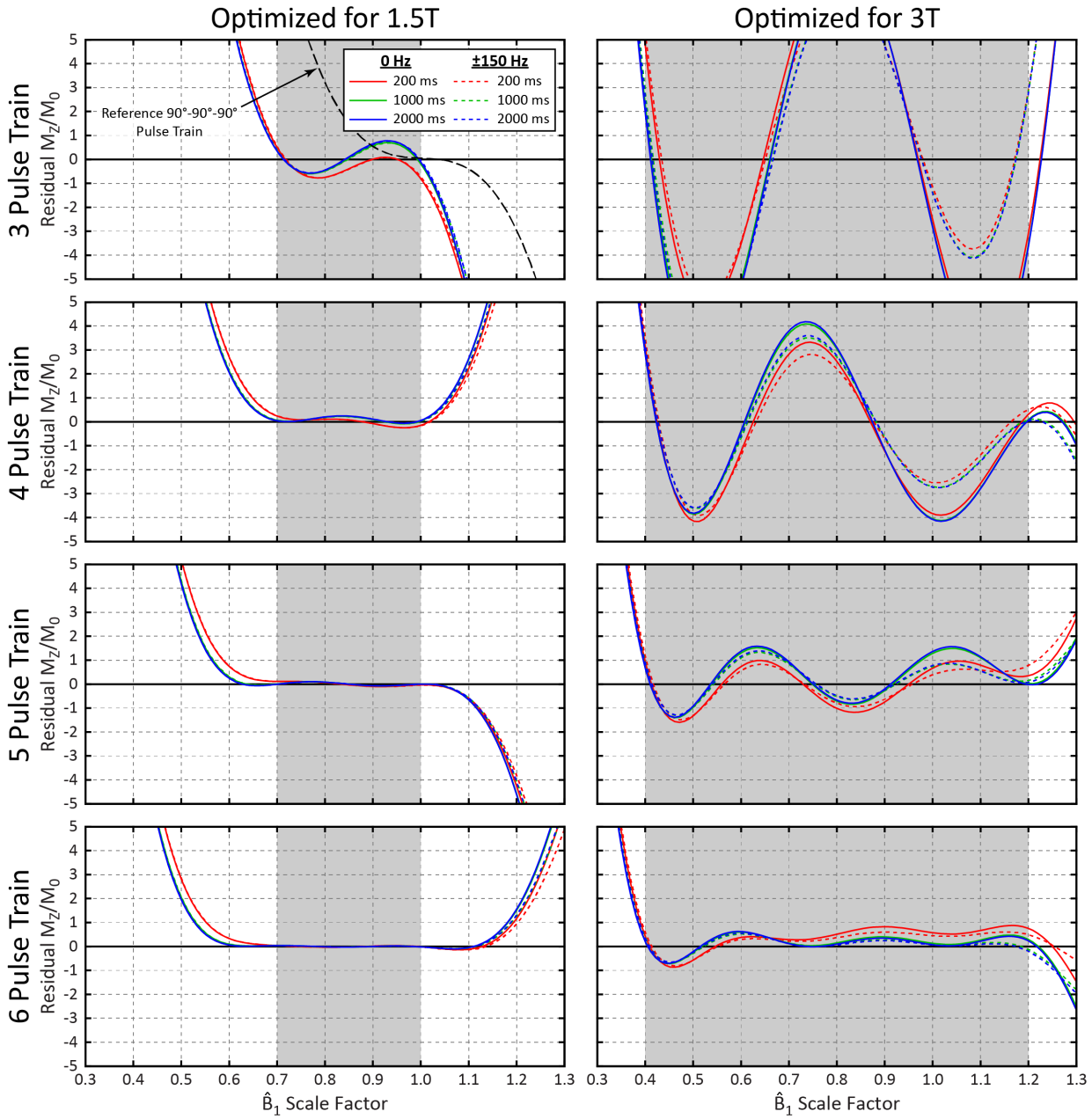

Figure 4.4: Simulated performance for pulse trains with 3–6 pulses, visualized for 3 T_1 values (colored lines) and off-resonance (B_0) values (solid vs. dashed lines). Performance for the reference 90°-90°-90° pulse train (on-resonance, 1000 ms T_1) is also shown along with the 3 pulse train optimized for 1.5T for comparison (top left).

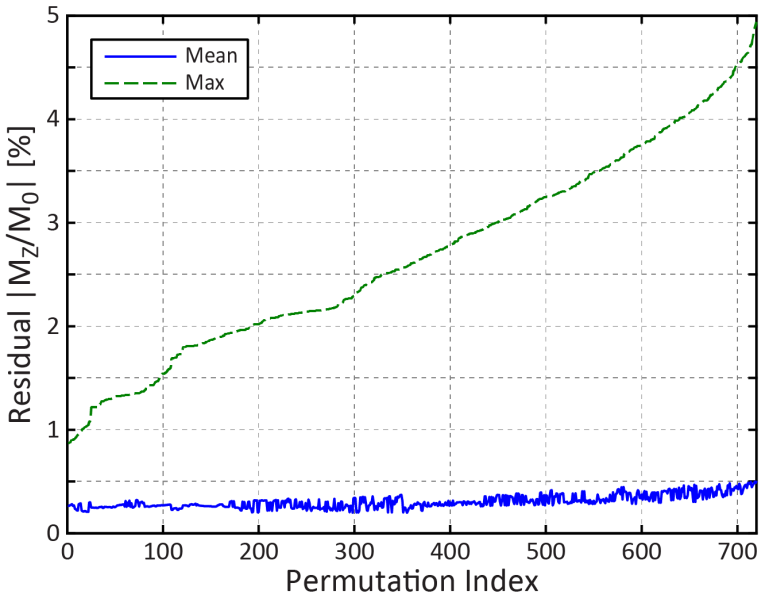

Figure 4.5: Mean and maximum simulated residual $|M_Z/M_0|$ for the 3T 6 pulse train for all 720 order permutations, sorted by maximum residual $|M_Z/M_0|$.

ms), but residual $|M_Z/M_0|$ increases rapidly for T_1 values shorter than 25 ms for all pulse trains, with divergent behavior depending on the $\hat{B}_1$ scale factor. The 90°-90°-90° train has poor performance with a $\hat{B}_1$ scale factor of 0.7, with residual $|M_Z/M_0|$ exceeding 15% for a 50 ms T_1. The 3T 6-pulse train maintains $|M_Z/M_0|<1\%$ for T_1 greater than 186 ms at ±240 Hz and for T_1 greater than 140 ms at ±120 Hz.

4.4.6 Phantom Validation

The T_1 and T_2 of the bottle phantom was measured to be 316 ms and 274 ms respectively using spin echo experiments, and the intrinsic $\hat{B}_1$ scaling factor across the image was found to range from 0.83 to 1.05. The applied linear magnetic field gradient resulted in off-resonance values from -605 to 697 Hz across the phantom. The performance of each saturation pulse as a function of B_0 and $\hat{B}_1$ scaling factor is plotted in Fig. 4.7, with the optimization range of B_0 and $\hat{B}_1$ values demarcated with a white box.

As shown in Fig. 4.7, experimentally measured residual M_Z/M_0 shows excellent agreement with simulations. The saturation pulse trains are robust to off-resonance due to the short individual pulse durations, while the BIR4-90 pulses with an overall shorter duration have tighter off-resonance constraints and more complex relationships with B_0 and $\hat{B}_1$. The reference 90°-90°-90° pulse train shows poor performance at low $\hat{B}_1$ scaling factors, even in the relatively narrow range of 0.7–1.0 expected at 1.5T. However, all proposed pulses

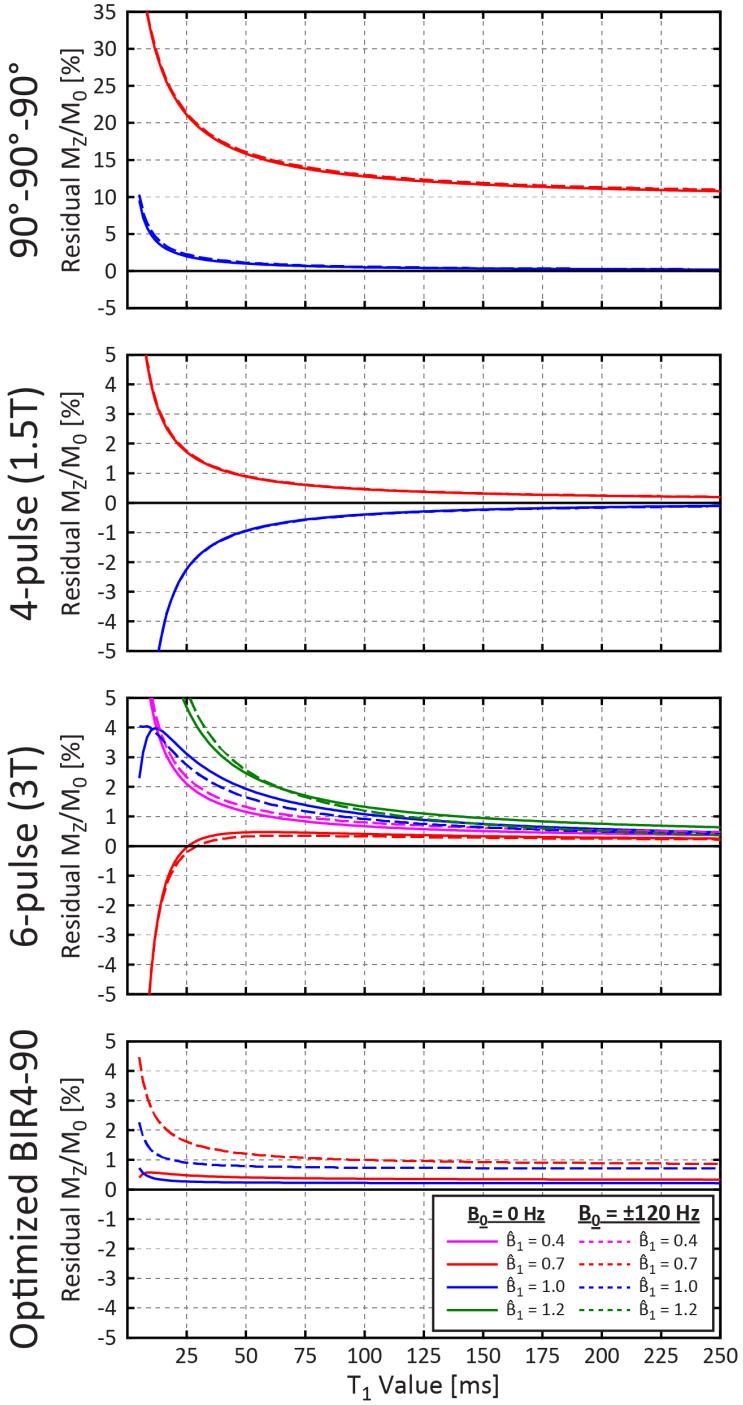

Figure 4.6: Simulated residual M_Z/M_0 for selected saturation pulses as a function of T_1 for different off-resonance (B_0) and $\hat{B}_1$ values.

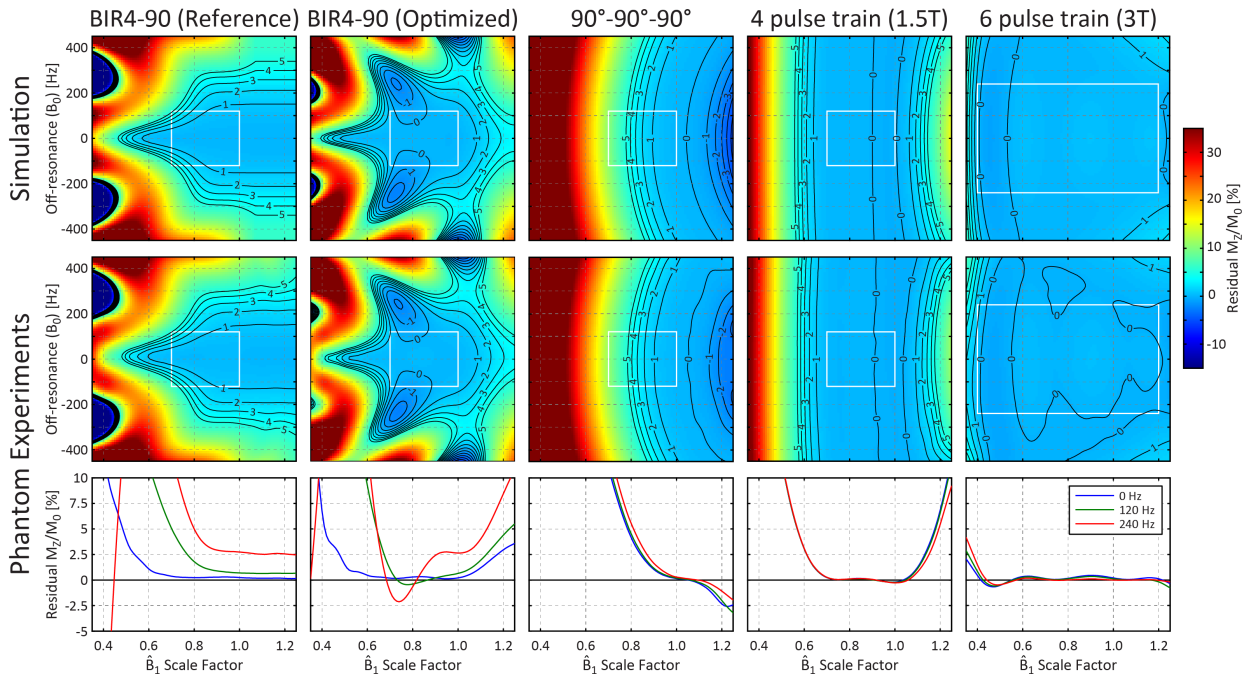

Figure 4.7: Simulated residual M_Z/M_0 (top row) and experimentally measured values (middle row) for 5 different saturation pulses as a function of $\hat{B}_1$ scale factor and off-resonance. The bottom row shows a profile of measured residual M_Z/M_0 as a function of $\hat{B}_1$ scale factor for three off-resonance frequencies.

show greatly improved performance within their respective optimization spaces (white dashed box) compared to the reference designs. The average measured residual $|M_Z/M_0|$ within these spaces was 0.24±0.16%, 0.11±0.06%, and 0.20±0.18% for the optimized BIR4-90, 4 pulse (1.5T), and 6 pulse (3T) trains respectively. All proposed pulses show excellent performance within their optimization space.

Figure 4.8 shows the relationship between residual M_Z/M_0 and simulated T_1 errors in the SASHA sequence. Simulations show that for the 2-parameter model fitting, SASHA T_1 errors increase by 1.3–1.6% for every 1% change in residual M_Z/M_0. A higher heart rate of 100 bpm results in greater SASHA T_1 errors for native (pre-contrast) T_1/T_2 values compared to 60 bpm, with negligible effects for post-contrast values. Overall, 2-parameter model fitting results in greater T_1 error dependence on residual M_Z/M_0 than 3-parameter fitting, particularly for post-contrast T_1/T_2 values.

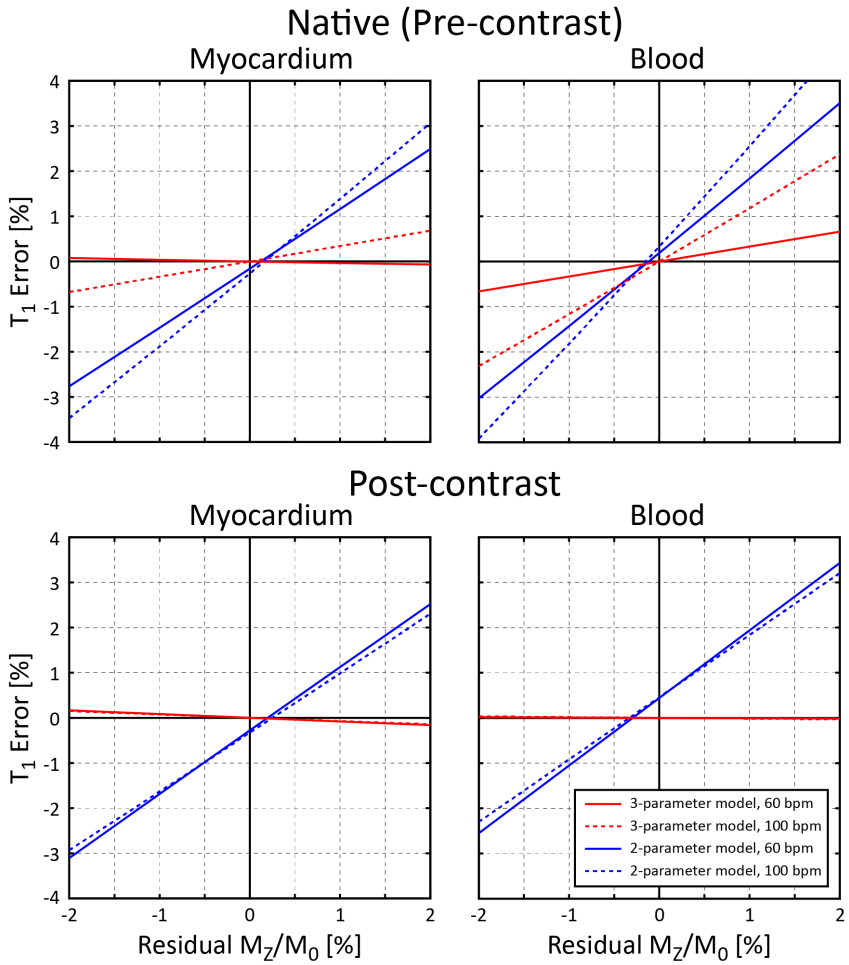

Figure 4.8: Simulated T_1 error for SASHA as a function of residual M_Z/M_0 for native (top) and post-contrast (bottom) myocardium (left) and blood (right) using 2 and 3 parameter models at 60 and 120 bpm. Input native relaxation times $T_1/T_2 = 1175/50$ ms (myocardium) and $T_1/T_2 = 1650/240$ (blood) and post-contrast relaxation times were $T_1/T_2 = 725/50$ ms (myocardium) and $T_1/T_2 = 500/180$ ms (blood).

4.5 Discussion

4.5.1 BIR4-90 Pulse Design

Experimental data in this study shows the older reference BIR4-90 saturation pulse has relatively poor performance with low $\hat{B}_1$ and high off-resonance within the range expected at 1.5T. A new optimized BIR4-90 pulse was shown to have improved performance with <1% residual $|M_Z/M_0|$ over the 1.5T optimization ranges of B_0 and $\hat{B}_1$ fields while reducing maximum B_1 field strength and resulting SAR. Although the required B_1 of 20.5 μT was achievable on the 1.5T MRI system used here, and likely most 1.5T MRI scanners, this high

B_1 amplitude may not be generally attainable on higher field systems. The SAR and B_1 may be reduced with a longer pulse duration, but this would reduce its bandwidth and thus its off-resonance performance. Furthermore, it was not possible to meet the <1% residual $|M_Z/M_0|$ criteria for the greatly expanded range of $\hat{B}_1$ values expected at 3T even with the current pulse duration. As a result, the adiabatic BIR4-90 family of saturation pulses is likely not appropriate at field strengths above 1.5T.

4.5.2 Pulse Train Design

The geometric minimization method provides a new intuitive description of the optimal flip angle patterns in pulse train design. It agrees well with the numerical optimization methods that neglect B_0 and T_1 effects except when the residual $|M_Z/M_0|$ is extremely small. While similar flip angle patterns were obtained using the full Bloch simulation numerical optimization method incorporating B_0 and T_1 effects, it was the only method that provided flip angle ordering instead of an unordered set. Flip angle ordering effects were found to be important, reducing the maximum residual $|M_Z/M_0|$ by a factor of 5.7× from the best order permutation to the worst. The evaluation of all permutations of an unordered flip angle set in the minimization subroutine provided a straightforward means of considering flip angle ordering while avoiding trapping within local minima. While this brute force approach is computationally inefficient because all permutations are evaluated in each iteration, this optimization is performed only when designing new pulse trains.

Pulse trains were designed for expected ranges of $\hat{B}_1$ values at both 1.5T and 3T, with excellent performance within those optimization ranges when a sufficient number of pulses are used. As performance decreases rapidly outside of the $\hat{B}_1$ optimization range for all pulse trains (Fig. 4.4), conservative estimates of $\hat{B}_1$ ranges were used in the design process. For the $\hat{B}_1$ range of 0.7 to 1.0 expected for 1.5T, the optimized 3 pulse train has the same number of pulses as the reference 90°-90°-90° pulse train and reduces the maximum residual $|M_Z/M_0|$ by 14×, meeting the target of <1%. The 4 pulse train has even better performance with <0.25% peak residual magnetization (0.11% mean residual signal), with minimal additional time and SAR.

The design $\hat{B}_1$ range for 3T was chosen to be 0.4–1.2 to encompass the widest range of in-vivo cardiac $\hat{B}_1$ values measured in a handful of small studies [5, 12, 17]. However, further work is needed to characterize the ranges of $\hat{B}_1$ values in larger representative populations and on different scanner platforms. A pulse train with 6 pulses was needed to achieve the criteria of <1% peak residual magnetization over this wide range of $\hat{B}_1$ values, but had excellent performance (mean residual $|M_Z/M_0|$ of 0.27%) with a total duration of only 33 ms

and 2.0× greater RF power compared to the 90°-90°-90° reference pulse train. The relatively short RF pulse durations used in the pulse trains resulted in a wide range of B_0 insensitivity for all pulse train designs, with a negligible drop in performance at ±450 Hz even with a short T_1 of 316 ms (Fig. 4.7). This will result in excellent saturation of fat signals even at 3T where the 440 Hz shift in resonant frequency would result in poor performance using even the optimized BIR4-90 pulse.

The optimization algorithm used in this study was designed to minimize the maximum residual $|M_Z/M_0|$ across the optimization space. However, previous studies of in-vivo $\hat{B}_1$ patterns have shown a Gaussian like distribution [12], and thus a weighted average during the optimization may allow better typical saturation performance or shorter pulse train lengths. The inherent flexibility of saturation pulse train parameters allows them to be further optimized for other applications. While relatively short RF pulses were selected to maximize the off-resonance performance, pulse lengths may be increased considerably to reduce peak B_1 amplitude and SAR. For example, the pulse lengths in the 3T 6 pulse design may be doubled, halving the RF energy, with a minor increase in mean residual $|M_Z/M_0|$ to 0.34±0.41%, although saturation performance with short T_1s is further reduced as maximum residual $|M_Z/M_0|$ increases to 4.4%. Additionally, while the maximum B_1 amplitude was characterized for 2 common MRI scanner models, other models and scanners by different vendors likely have different limitations. The inter-pulse spoiler durations could also be shortened to further reduce T_1 dependencies with more careful consideration of minimum spoiler areas and stimulated echo effects. This may also be useful in reducing the overall pulse duration, although the current durations were not a limiting factor in SASHA T_1 mapping or perfusion applications. While the saturation pulse trains presented here have excellent performance for common applications, the publically available optimization code can be used to design pulses for B_1 amplitude limitations and B_0, $\hat{B}_1$, and T_1 ranges for other applications and MRI scanners.

Simulations of 2-parameter fitting of SASHA data show increased sensitivity to saturation pulse performance compared to 3-parameter fitting. However, the excellent performance of the saturation pulses proposed here minimizes saturation efficiency as a source of error in SASHA T_1 mapping. The optimized saturation pulse trains also have robust performance over both a wide range of resonant frequencies and short T_1 values, and would thus likely reduce the variability of calculated parameters when used in quantitative saturation-recovery first-pass perfusion methods.

This study is limited by the lack of in-vivo data on the performance of the proposed saturation pulses. Previous in-vivo measurements of residual longitudinal magnetization have shown good agreement with phantom experiments [2, 7, 12, 14], but are limited by

inherently low signal to noise, T_1 recovery effects between saturation and imaging readout and low spatial resolution, particularly for the quantification of residual $|M_Z/M_0|$ <1% that was the goal of this study.

Gradient spoiler design and its effect on the possible formation of stimulated echoes were not studied in detail. The proposed spoiler design utilizes relatively large gradient areas played in multiple directions, with care taken to avoid duplicate gradient areas. While no stimulated echo artifacts were observed in our data, a more systematic study of stimulated echo formation is warranted.

4.6 Conclusions

This study has described the optimization of saturation pulses and validated their performance in phantom experiments across a wide range of off-resonance and $\hat{B}_1$ scale factor values. Their experimental performance was characterized by the residual M_Z/M_0 following saturation and has excellent agreement with theoretical predictions. Compared to reference saturation pulse designs, the optimized BIR4-90 pulse and pulse trains had significantly lower residual $|M_Z/M_0|$ over the range of B_0 and $\hat{B}_1$ values expected at 1.5T and 3T. Optimized saturation pulse trains are robust to off-resonance, T_1 values, and $\hat{B}_1$ scale factors, which can likely reduce the variability of calculated parameters when they are used in quantitative sequences such as SASHA T_1 mapping, saturation-recovery first-pass perfusion, and the saturated double angle methods, which rely on saturation-preparation of magnetization.

4.7 References

[1] N V Tsekos, Y Zhang, H Merkle, N Wilke, Michael Jerosch-Herold, A Stillman, and K Uğurbil. Fast anatomical imaging of the heart and assessment of myocardial perfusion with arrhythmia insensitive magnetization preparation. *Magnetic Resonance in Medicine*, 34(4):530–536, October 1995. pg. 91

[2] C M Wacker, M Bock, A W Hartlep, G Beck, G van Kaick, G Ertl, W R Bauer, and L R Schad. Changes in myocardial oxygenation and perfusion under pharmacological stress with dipyridamole: assessment using T*2 and T1 measurements. *Magnetic Resonance in Medicine*, 41(4):686–695, April 1999. pg. 91, pg. 108

[3] David M Higgins, John P Ridgway, Aleksandra Radjenovic, U Mohan Sivananthan, and Michael A Smith. T1 measurement using a short acquisition period for quantitative cardiac applications. *Medical physics*, 32(6):1738–1746, May 2005. pg. 91

[4] Kelvin Chow, Jacqueline A Flewitt, Jordin D Green, Joseph J Pagano, Matthias G Friedrich, and Richard B Thompson. Saturation recovery single-shot acquisition (SASHA) for myocardial T1 mapping. *Magnetic Resonance in Medicine*, 71(6):2082–2095, 2014. pg. 91, pg. 92, pg. 99

[5] Charles H Cunningham, John M Pauly, and Krishna S Nayak. Saturated double-angle method for rapid B1+ mapping. *Magnetic Resonance in Medicine*, 55(6):1326–1333, June 2006. pg. 91, pg. 92, pg. 107

[6] H Ding, Xu D, M M Zviman, V Sena-Weltin, L Amado, Saman Nazarian, Henry R Halperin, E R McVeigh, and D A Herzka. High Spatial Resolution Free Breathing 3D T2 Mapping for Edema Detection in Radio Frequency Ablation. *Proceedings of the International Society for Magnetic Resonance in Medicine*, 19:23, 2011. pg. 91

[7] Daniel Kim, Oded Gonen, Niels Oesingmann, and Leon Axel. Comparison of the effectiveness of saturation pulses in the heart at 3T. *Magnetic Resonance in Medicine*, 59(1):209–215, 2008. pg. 91, pg. 108

[8] Peter Kellman and Michael Schacht Hansen. T1-mapping in the heart: accuracy and precision. *Journal of cardiovascular magnetic resonance : official journal of the Society for Cardiovascular Magnetic Resonance*, 16(1):2, January 2014. pg. 92

[9] R J Ogg, P B Kingsley, and J S Taylor. WET, a T1- and B1-insensitive water-suppression method for in vivo localized 1H NMR spectroscopy. *Journal of magnetic resonance Series B*, 104(1):1–10, May 1994. pg. 92

[10] Yuehui Tao, Aaron T Hess, Graeme A Keith, Christopher T Rodgers, Alexander Liu, Jane M Francis, Stefan Neubauer, and Matthew D Robson. Optimized saturation pulse train for human first-pass myocardial perfusion imaging at 7T. *Magnetic Resonance in Medicine*, pages n/a–n/a, April 2014. pg. 92

[11] N Oesingmann, Q Zhang, and O Simonetti. Improved saturation RF pulse design for myocardial first-pass perfusion at 3T. *Journal of cardiovascular magnetic resonance : official journal of the Society for Cardiovascular Magnetic Resonance*, 6:373–374, 2004. pg. 92, pg. 94, pg. 97

[12] Kyunghyun Sung and Krishna S Nayak. Design and use of tailored hard-pulse trains for uniformed saturation of myocardium at 3 Tesla. *Magnetic Resonance in Medicine*, 60(4):997–1002, October 2008. pg. 92, pg. 92, pg. 94, pg. 97, pg. 107, pg. 108, pg. 108

[13] R S Staewen, A J Johnson, B D Ross, T Parrish, H Merkle, and Michael Garwood. 3-D FLASH imaging using a single surface coil and a new adiabatic pulse, BIR-4. *Investigative radiology*, 25(5):559–567, May 1990. pg. 92

[14] Daniel Kim, Niels Oesingmann, and Kellyanne McGorty. Hybrid adiabatic-rectangular pulse train for effective saturation of magnetization within the whole heart at 3 T. *Magnetic Resonance in Medicine*, 62(6):1368–1378, December 2009. pg. 92, pg. 94, pg. 108

[15] J A Nelder and R Mead. A Simplex Method for Function Minimization. *The Computer Journal*, 7(4):308–313, January 1965. pg. 96

[16] Peter Kellman, Daniel A Herzka, and Michael Schacht Hansen. Adiabatic inversion pulses for myocardial T1 mapping. *Magnetic Resonance in Medicine*, 71(4):1428–1434, 2014. pg. 96

[17] Kyunghyun Sung and Krishna S Nayak. Measurement and characterization of RF nonuniformity over the heart at 3T using body coil transmission. *Journal of magnetic resonance imaging : JMRI*, 27(3):643–648, March 2008. pg. 97, pg. 107

[18] Michael Garwood and Y Ke. Symmetric pulses to induce arbitrary flip angles with compensation for rf inhomogeneity and resonance offsets. *Journal of Magnetic Resonance*, 1991. pg. 97, pg. 97

[19] Jinghua Wang, Weihua Mao, Maolin Qiu, Michael B Smith, and R Todd Constable. Factors influencing flip angle mapping in MRI: RF pulse shape, slice-select gradients, off-resonance excitation, and B0 inhomogeneities. *Magnetic Resonance in Medicine*, 56(2):463–468, August 2006. pg. 98

[20] John D'Errico. Surface Fitting using gridfit, November 2005. pg. 98

[21] Kelvin Chow, Bruce Spottiswoode, Joseph J Pagano, and Richard Thompson. Improved precision in SASHA T1 mapping with a variable flip angle readout. *Journal of cardiovascular magnetic resonance : official journal of the Society for Cardiovascular Magnetic Resonance*, 16(Suppl 1):M9, 2014. pg. 99

Chapter 5

Optimization of SASHA T_1 Mapping Using Variable Flip Angle Readouts[1]

5.1 Introduction

Quantitative T_1 mapping is an increasingly utilized technique in cardiac magnetic resonance imaging (MRI) where spin-lattice relaxation times (T_1) are used as a biomarker for changes in myocardial tissue microstructure. Increased native (non-contrast) myocardial T_1 values have been correlated with disease severity and histological collagen volume fraction measurements in aortic stenosis [1], and increased native myocardial T_1 values have been observed in patients with aortic stenosis and amyloidosis and decreased T_1 values in patients with Fabry disease [2, 3]. Post-contrast T_1 measurements of myocardium and blood can be combined with native measurements to estimate the myocardial extracellular volume fraction (ECV), which has been shown to be altered in a variety of cardiovascular diseases [4] and also shown to be an independent predictor of all-cause mortality in a large study of consecutive patients referred for cardiac MRI [5].

A variety of pulse sequences have been used for in-vivo T_1 mapping such as the widely available MOdified Look-Locker Inversion recovery (MOLLI) sequence [6] and its variants [7–9]. However, MOLLI has been shown to have systematic errors that vary as a function of T_1, T_2, heart rate, inversion efficiency, off-resonance, and magnetization transfer [6, 7, 10–13, 23]. As heart rates may be systematically altered with disease states and T_2 values are increased with edema [14], MOLLI T_1 values may vary with disease due to these confounders in addition to true changes in myocardial T_1. The recently proposed SAturation

[1] A portion of this chapter has been previously published: Chow K, Spottiswoode BS, Pagano JJ, Thompson RB. Improved precision in SASHA T_1 mapping with a variable flip angle readout. *J Cardiovasc Magn Reson.* 2014;**16**(Suppl 1):M9.

recovery single-SHot Acquisition (SASHA) sequence has been shown to accurately measure T_1 values without systematic errors due to T_1, T_2, heart rate, flip angle, off-resonance, and magnetization transfer [13, 15]. However, SASHA T_1 values have greater variability than MOLLI due to the smaller dynamic range of signal intensities with saturation recovery preparation [16].

SASHA data is traditionally analyzed by fitting measured signal intensities to a three-parameter exponential recovery curve:

$$Signal = A\left(1 - \eta e^{\frac{-TS}{T_1}}\right) \tag{5.1}$$

where A is a scaling factor, η is a variable saturation efficiency, TS is the saturation recovery time, and T_1 is the spin-lattice relaxation time. A two-parameter fit with assumed perfect saturation efficiency (η=1) has been shown to reduce SASHA best-fit T_1 variability, but introduces systematic T_1 errors when $\eta \neq 1$ [16]. These errors may be the result of poor saturation pulse performance, which has an intuitive and direct effect on the true η. However, the magnetization perturbation caused by the balanced steady-state free precession (bSSFP) readout also results in a change in the *apparent* η when fitting SASHA data. As a result, even with perfect saturation pulses, significant changes in apparent η are observed for SASHA data due to the effect of the bSSFP readout and depend on T_1, T_2, flip angle, and the number of phase encode lines [15].

Variable flip angle (VFA) readouts, where the RF flip angle is modulated over the echo train, have long been used in gradient echo imaging to control the point spread function by shaping the signal response during the echo train [17], particularly to maximize signal yield in hyperpolarized imaging [18]. VFA designs with bSSFP readouts have also been designed achieve a constant signal intensity profile for reduced blurring caused by signal intensity changes in the approach to equilibrium [19] and hyperpolarized imaging [20] and to increase T_2 contrast [21]. We propose that a VFA implementation can be designed using simulations to reduce the bSSFP magnetization perturbation, thus reducing the change in apparent η and improving the accuracy of 2-parameter SASHA. The accuracy and variability of 2-parameter SASHA-VFA is evaluated against the standard SASHA and MOLLI sequences in phantom experiments and healthy volunteers.

5.2 Methods

5.2.1 Variable Flip Angle Readout Design Simulations

The change in apparent saturation efficiency for SASHA data can be reduced by decreasing the flip angle of the bSSFP readout [15] at the expense of reduced signal to noise. We hypothesize that a variable flip angle (VFA) readout pattern with reduced flip angles for RF pulses at the beginning of the readout can also be used to reduce the change in apparent η and increase the accuracy of 2-parameter SASHA. The modulation function chosen in our implementation was a partial sinusoid (from zero to the first peak) applied over a variable number of RF pulses to achieve a smooth transition to constant flip angle RF pulses, although a variety of other modulation functions could also be chosen. Specifically, the first n RF pulses were scaled by $\sin(x)$, where x is linearly spaced between $\pi/2n < x < \pi/2$ and n is termed the VFA length. The first 5 readouts were discarded due to low signal, matching the number of dummy readouts commonly used for standard constant flip angle (CFA) readouts. The flip angle schedule of a VFA readout is plotted and compared to a CFA readout in Fig. 5.1a. The first 5 catalyzation pulses in the CFA readout had scaling factors of 10, 30, 50, 70, and 90% of the target flip angle. Echo numbering used below does not include the 5 catalyzation pulses.

The off-resonance performance of CFA and VFA readouts was characterized by analyzing the time-course of transverse magnetization (M_{XY}) over the readout train. Bloch equations were performed of both CFA and VFA bSSFP readouts with the following input parameters: 1175/50 ms T_1/T_2, representative of native myocardium, 1.3 ms echo time (TE), 2.6 ms repetition time (TR), -250–250 Hz off-resonance, 70° target flip angle, a typical VFA length of 50 pulses, and 72 total readout RF pulses not including the first 5 dummy pulses. Simulations accounted for slice profile effects by simulation of the actual RF waveform from the scanner.

The propensity for image artifacts with each readout was investigated by quantifying the oscillations in magnitude ($|M_{XY}|$) and phase ($\angle M_{XY}$) of M_{XY} over time. Specifically, the difference between sequential echoes was calculated for each, and subtracted from a best-fit 5^{th} order polynomial in order to remove slowly varying changes in magnitude and phase that are not artifact generating. The average change in magnitude and phase differences ($\Delta|M_{XY}|$ and $\Delta(\angle M_{XY})$ respectively) was calculated as a function of off-resonance as a metric of image artifact performance.

The amount of spatial blurring caused by an image readout can be quantified using its point-spread function (PSF). The PSF was calculated for CFA and VFA readouts as the

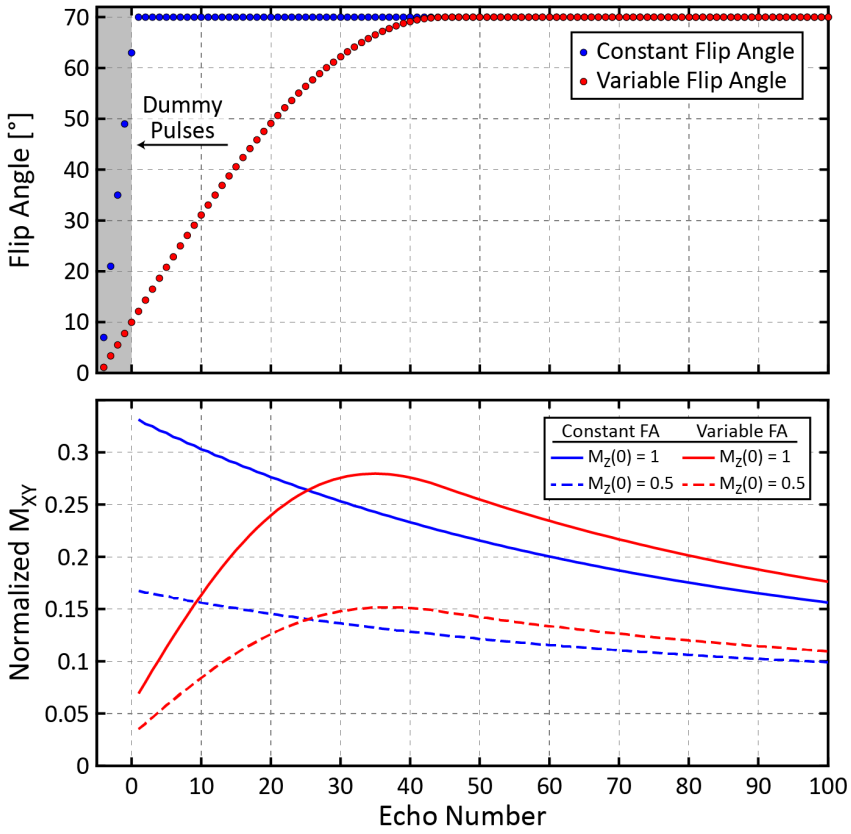

Figure 5.1: **a)** Flip angle pattern for a variable flip angle (VFA) scheme with a VFA length of 50 and a constant flip angle (CFA) scheme. **b)** Simulated transverse magnetization for VFA and CFA schemes with starting Mz of 1 and 0.5 using native myocardium T_1/T_2 values (1175/50ms).

Fourier transform of the signal intensity (M_{XY}) over the single-shot readout. Calculations were performed for Bloch equation simulations with parameters as above but on-resonance, with additional simulations for native blood T_1/T_2 values (1650/240 ms) and starting normalized longitudinal magnetization (M_Z) values of 0, 0.5, and 1.0 to emulate the effect of various saturation recovery preparations in the SASHA sequence. The full-width half-maximum (FWHM) was calculated for each PSF as a metric of image blurring.

Signal intensity in a single-shot readout is determined by the magnitude of M_{XY} during the centre k-space readout, the position of which is affected by the imaging matrix size, field of view, phase encoding order, and image acceleration techniques such as GRAPPA [22], or partial Fourier in the phase encode direction. The optimum VFA length was evaluated as a function of center k-space position by assessing its effect on SNR, blood-tissue contrast, and SASHA T_1 error.

Bloch equation simulations of the SASHA sequence used typical in-vivo SASHA ac-

quisition parameters: 1.3/2.6 ms TE/TR, 70° target flip angle, 70 total phase encode lines, 60 bpm simulated heart rate, 10 images with maximum 775 ms saturation recovery time (TS) and a non-saturated anchor image. Simulations were repeated with CFA readouts and over a range of VFA lengths (10–100 pulses), center k-space positions (1–45th echo in steps of 2), and relaxation values emulating myocardium (native T_1/T_2: 1175/50 ms, post-contrast T_1/T_2: 500/47 ms) and blood (native T_1/T_2: 1650/240, post-contrast: 300/145 ms) at 1.5T. Image intensity was taken as M_{XY} at center k-space to calculate relative SNR between VFA and CFA readouts and blood-tissue contrast in native and post-contrast settings. A 2-parameter model was fit to simulated SASHA data and the error in best-fit T_1 values was calculated. An empirical formula was designed using these data to calculate the optimal VFA length for each center k-space position.

5.2.2 Phantom Experiments

Accuracy of the SASHA-VFA readout was assessed in 14 $NiCl_2$-doped agarose phantoms. Gold standard relaxometry spin echo experiments were performed with common sequence parameters: 15 ms TE, 10 s TR, 192×90 matrix size, 300×141 mm field of view (FOV), 8 mm slice thickness, and a single line of k-space acquired per excitation. Saturation recovery spin echo experiments used the same optimized BIR-4 saturation pulse (Chapter 4) as the SASHA sequence with similar TS times (10 images with 100–1000 ms) and a non-prepared image. Gold standard T_1 values and actual η measurements for the saturation pulse were calculated by fitting data to Eq. 5.1. T_2 values were calculated by fitting a 2-parameter exponential decay model to spin echo data with 7 TEs spanning 25–250 ms:

$$Signal = Ae^{\frac{-TE}{T_2}} \tag{5.2}$$

SASHA-VFA T_1 measurements were performed with common acquisition parameters: 1.51/3.02 ms TE/TR, 70° target flip angle, 256×150 matrix size, 340×255 mm field of view, 8 mm slice thickness, 78% phase resolution, 7/8th phase partial Fourier, GRAPPA rate 2 parallel acceleration with 36 "extra" ACS lines acquired in a separate heartbeat, 72 phase encode lines per image, 1085 Hz/pixel bandwidth, 60 bpm simulated heart rate, optimized BIR-4 saturation, 10 images with 200–800 ms TS and a non-saturated image. SASHA-VFA was acquired with VFA lengths between 10 and 100 pulses, and with 5, 15, and 25 dummy readouts discarded prior to the start of k-space acquisition. All acquisitions were repeated 3 times to reduce noise in calculated values. Additional Bloch simulations using experimental acquisition parameters, spin-echo T_1 and T_2 values, and measured η values in each phantom were also used to predict 2-parameter SASHA T_1 errors.

5.2.3 In-Vivo Studies

Four healthy volunteers were imaged on a 1.5T Siemens Avanto MRI scanner (Siemens Healthcare; Erlangen, Germany) with written informed consent and institutional review board approval. T_1 mapping was performed on a mid-ventricular short-axis slice using SASHA-CFA, SASHA-VFA, and MOLLI. Common image readout parameters for all sequence were: 1.01/2.44 ms TE/TR, 112×192 matrix size, 270×360 mm^2 field of view, rate 2 GRAPPA with 24 in-place ACS reference lines, 78% phase resolution, 7/8 partial Fourier, and 28 lines to the center of k-space with a total imaging duration of ~175 ms. SASHA-CFA and SASHA-VFA used a target flip angle 70°with ramping functions described above, and MOLLI used a target flip angle of 35° with 5 linearly ramped startup pulses as described for SASHA-CFA. SASHA datasets were acquired with 9 images having equally spaced TIs from 165–780 ms following BIR-4 saturation, plus a non-saturated image. MOLLI data was acquired with a 5-(3)-3 configuration, 120 ms TI start, 80 ms TI increment, 35° flip angle, and a tan/tanh adiabatic inversion pulse [23]. All images were motion corrected using a variational motion correction algorithm with synthetic image estimation [24].

5.2.4 Image Analysis

T_1 maps were calculated using both 2 and 3-parameter models (Eq. 5.1) for SASHA-CFA and SASHA-VFA. MOLLI T_1 maps were calculated using the standard method with a 3-parameter model:

$$Signal = A - Be^{-TI/T_1^*} \tag{5.3}$$

and applying the Look-Locker correction [25]:

$$Signal = \left(B/A - 1\right) T_1^* \tag{5.4}$$

For phantom images, a region of interest was manually drawn for each phantom. For in-vivo acquisitions, endocardial and epicardial contours were manually drawn using raw images and T_1 maps for guidance. The inferior right ventricular insertion point was defined to segment the short axis slice into 18 circumferential segments, with three sub-segments corresponding to each standardized AHA segment. A separate ROI was traced in the left ventricular blood pool. The mean and standard deviation of T_1 values was calculated across all pixels contained within each ROI or segment. Calculated values from SASHA-VFA data were averaged across the 3 repetitions. All analysis was performed with custom MATLAB software (R2013a; The MathWorks, Natick, USA).

5.2.5 Statistics

Continuous variables are reported as mean ± standard deviation unless otherwise indicated. Paired two-tailed Student's t-tests were used to assess statistical significance between T_1 values calculated with 2-parameter and 3-parameter models for CFA and VFA acquisitions.

5.3 Results

5.3.1 Variable Flip Angle Readout Performance

As shown in Fig. 5.1b, the VFA readout has slightly increased simulated signal yield after the 25th echo compared to the CFA readout for native myocardial T_1 and T_2 values, but CFA has a more uniform signal intensity profile over time. Simulated transverse magnetization for CFA and VFA readouts as a function of off-resonance is shown in Fig. 5.2a. Larger temporal oscillations are seen in the CFA $|M_{XY}|$ as off-resonance increases, with both VFA and CFA readouts experiencing signal dropouts at 192 Hz, which is the 1/2TR bSSFP band. Magnetization oscillations in the CFA readout are more apparent in the delta $|M_{XY}|$, where at 150 Hz (Fig. 5.2b), changes in normalized $|M_{XY}|$ of up to 0.12 are seen between sequential echoes in the first 20 echoes, which is approximately 22% of its absolute intensity. Oscillations in $\Delta|M_{XY}|$ are seen to also persist for the later echoes while oscillations for the VFA readout are negligible after the 20th echo. Significant oscillations are observed in $\angle M_{XY}$ when off-resonant, with phase differences of up 15° between sequential echoes throughout the CFA readout at 150 Hz. Significantly fewer oscillations are observed for the VFA readout, again with negligible phase changes after the 20th echo.

The average absolute $\Delta|M_{XY}|$ and absolute $\Delta(\angle M_{XY})$ over the entire 72 echo readout (after high-pass filtering are shown as a function of off-resonance in Fig. 5.3. The constant flip angle readout has significantly higher average changes in both magnitude and phase compared to the variable flip angle readout for the vast majority of off-resonance values and the average values for the CFA readout also have a more complex relationship with off-resonance than the VFA readout.

Figure 5.4 shows simulated $|M_{XY}|$ for the VFA and CFA readouts are shown for native myocardial and blood relaxation values, assuming on-resonance and various starting M_Z values. The transverse magnetization is more uniform over the echo train for the CFA readout than the VFA readout, consistent with results shown in Fig. 5.1 and 5.2. The PSFs are similarly shaped for both readouts, with the VFA readout having a larger FWHM in all

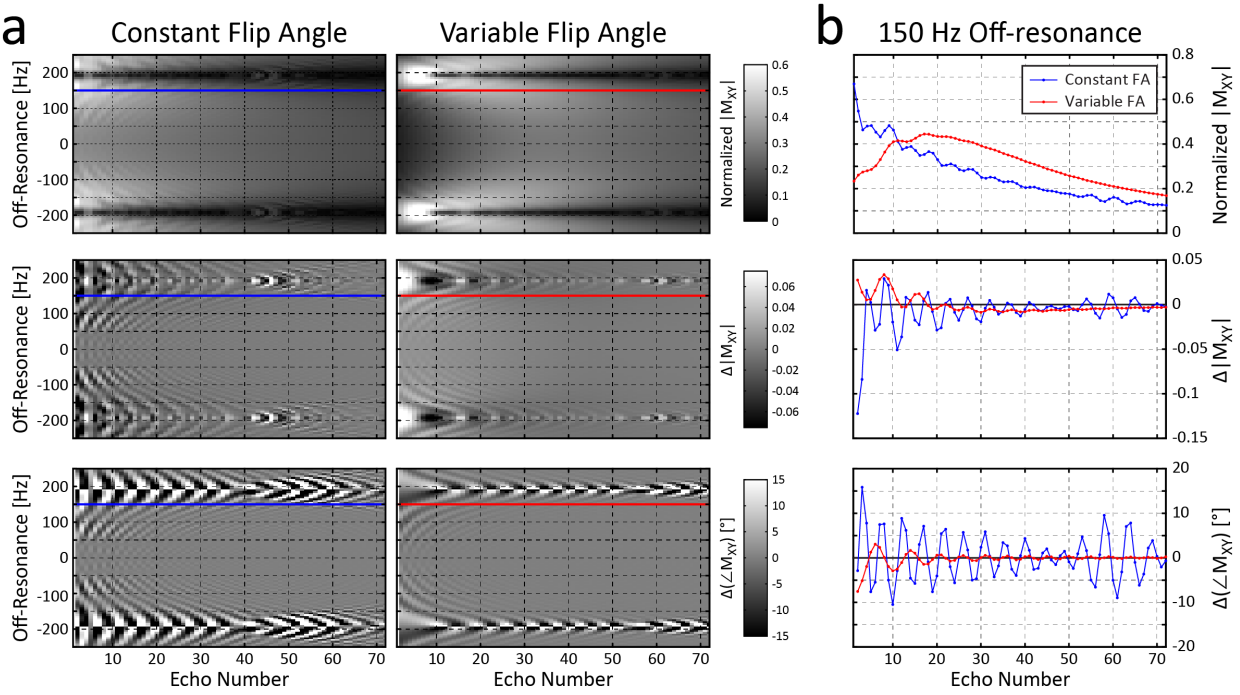

Figure 5.2: **a)** Simulated transverse magnetization (M_{XY}) for constant flip angle and variable flip angle schemes as a function of off-resonance for $T_1/T_2 = 1175/50$ ms (native myocardium). Delta magnitude ($|M_{XY}|$) and delta phase ($\angle M_{XY}$) are calculated as the difference over time (echo number). **b)** Simulated $|M_{XY}|$, $\Delta|M_{XY}|$, and $\Delta(\angle M_{XY})$ at 150 Hz off-resonance for both CFA and VFA readouts.

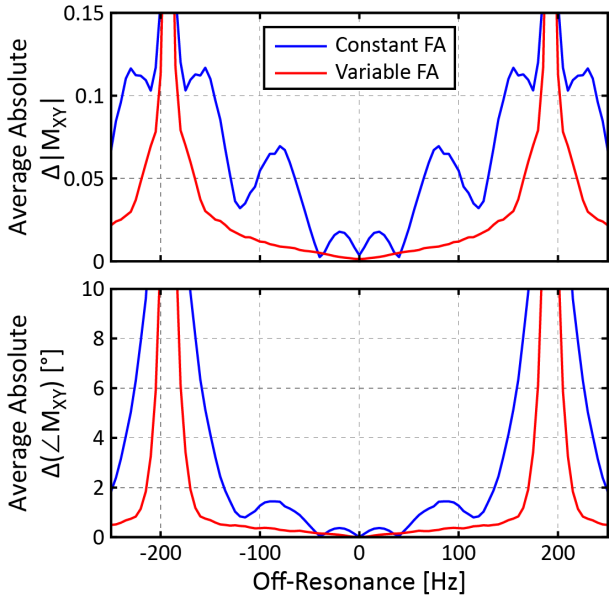

Figure 5.3: Average absolute delta |Mxy| and absolute delta phase of Mxy over the entire readout as a function of off-resonance.

cases. The ratio of FWHM between VFA and CFA readouts varied depending on the T_1 and T_2 values as well the starting M_Z, with the VFA having a FHWM 4–15% wider than the CFA readout for the simulations shown in Fig. 5.4.

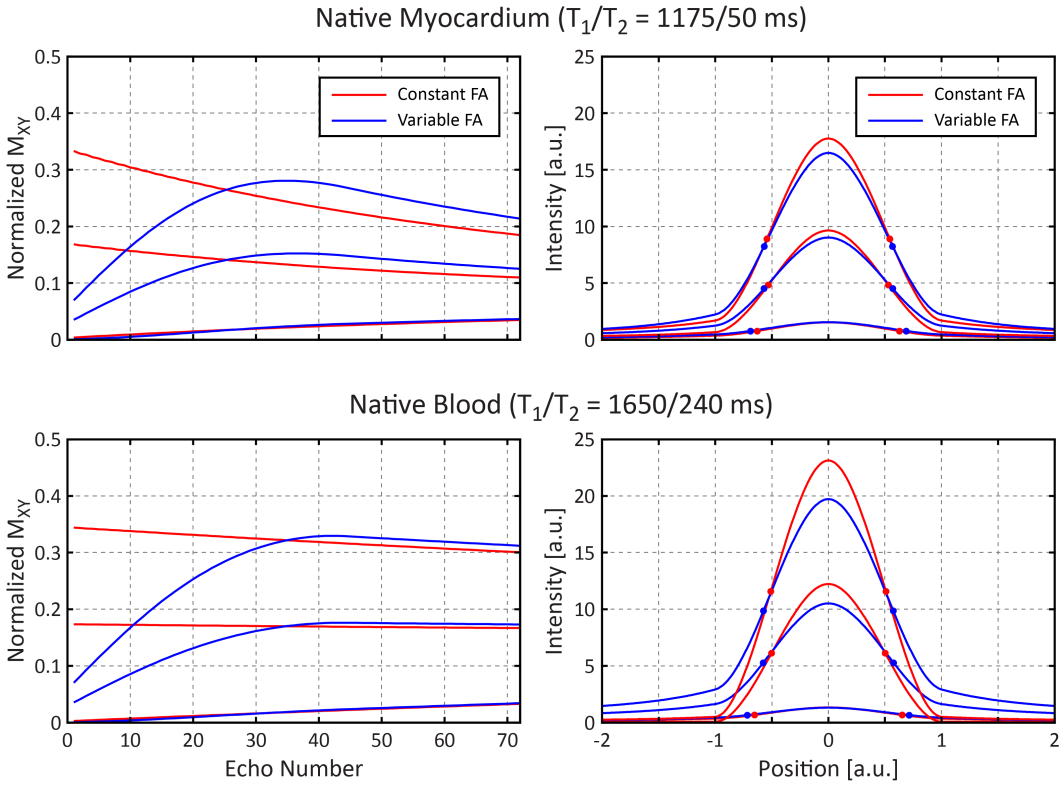

Figure 5.4: Simulated M_{XY} for native myocardium and blood T_1 and T_2 values using CFA and VFA readout (left) and the corresponding point spread functions (right). Simulations assumed on-resonance and had starting normalized M_Z values of 0, 0.5, and 1. Circles indicate the full-width half-max position for each point spread function.

5.3.2 Variable Flip Angle Length Optimization

Simulation results used to determine the optimal VFA length are summarized in Fig. 5.5. Typical center k-space locations are between the 25th and 35th echo, indicated with white lines. The VFA readout generally has reduced signal intensity compared to the CFA readout in native blood (Fig. 5.5a), but SNR increases are seen in native myocardium when the VFA length is longer than approximately double the echo number. Similar trends are observed in all saturation recovery images in both native and post-contrast settings.

Figure 5.5b shows the simulated blood-tissue contrast as a function of echo number and VFA length, with simulated contrast for CFA shown below each plot. Blood-tissue contrast decreases with increasing VFA length for the non-saturated image in both native and

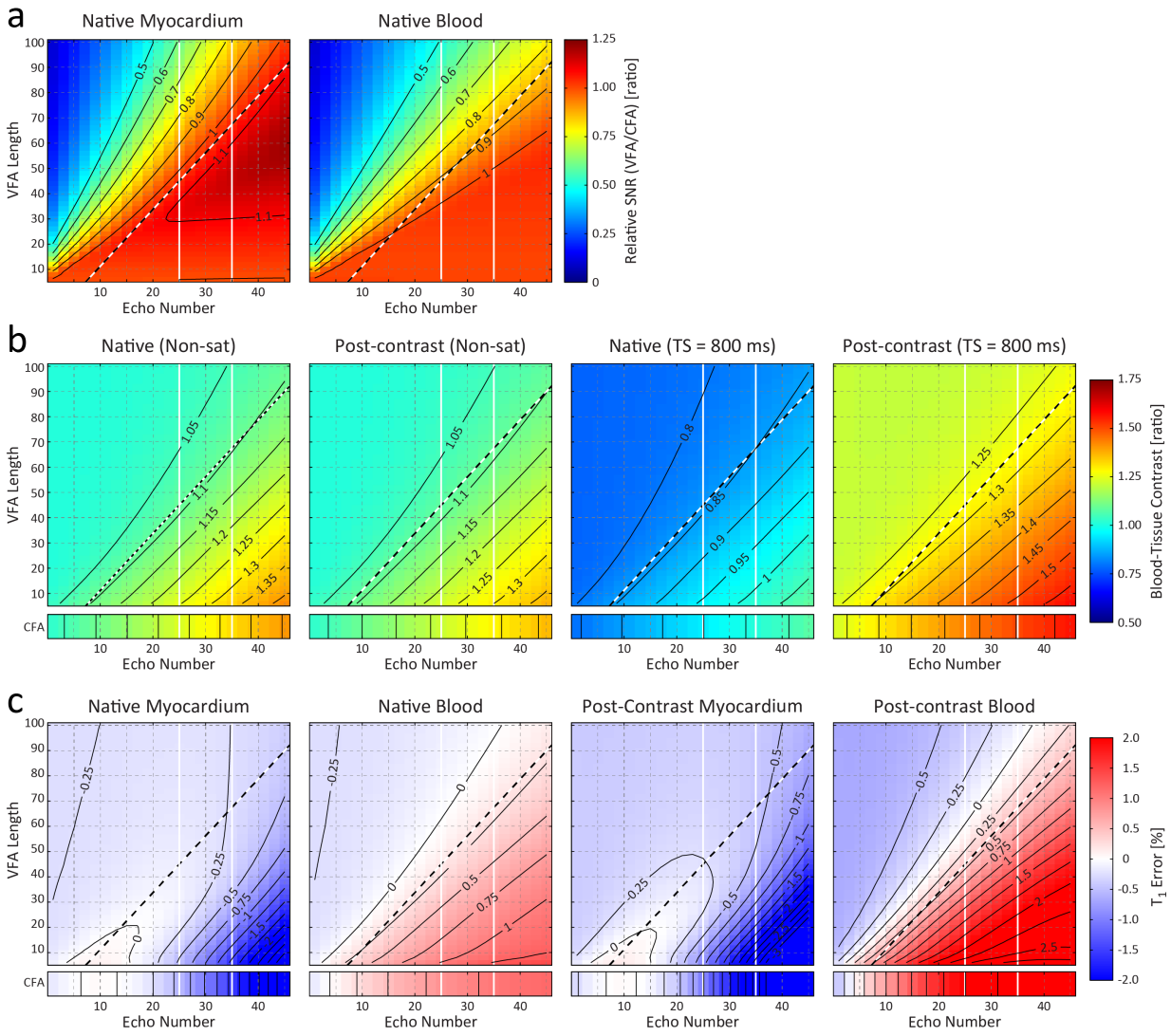

Figure 5.5: Simulations of VFA performance as a function of center k-space location and VFA length. **a)** SNR of VFA image relative to CFA readout for native myocardium (T_1/T_2 = 1175/50 ms) and blood (T_1/T_2 = 1650/240 ms). **b)** Blood-tissue contrast with the VFA and CFA readouts for the native and post-contrast (myocardium T_1/T_2 = 500/47 ms, blood T_1/T_2 = 300/145 ms) settings for both a non-saturated and saturation recovery (TS = 800 ms) image. **c)** Error in 2-parameter model calculations of T_1 with VFA and CFA readouts. Dashed black and white diagonal line on each plot shows the optimal VFA length as described in Eq. 5.5.

post-contrast settings as well as all saturation recovery images post-contrast. Native blood-tissue contrast is reversed in the 800 ms TS image, with myocardium generally having higher signal intensities than blood. This trend was consistent for all other saturation recovery times and blood-tissue contrast improved with increasing VFA length.

Figure 5.5c shows the simulated SASHA T_1 error using a 2-parameter model as a function of echo number and VFA length, with simulated error for CFA shown separately below each plot. Two-parameter model fitting of SASHA data generally resulted in underestimation of true T_1 values for myocardial relaxation values and overestimation for blood relaxation values, with larger errors post-contrast for both. The magnitude of these errors is increased with later echo numbers and is reduced with increasing VFA length.

An empirical formula for the optimum VFA length as a function of center k-space echo number was designed to keep the magnitude of T_1 error to less than 1% and slightly increase the native myocardial SNR compared to the CFA readout (white and black dashed lines, Fig. 5.5):

$$\text{VFA length} = 2.25 * \text{center k-space} - 11.25 \tag{5.5}$$

5.3.3 Phantom Experiments

The measured saturation efficiency of the optimized BIR-4 pulse in the 14 phantoms was 0.995±0.002. 2-parameter SASHA T_1 errors are shown as a function of VFA length in Fig. 5.6, with gold standard spin-echo T_1 and T_2 values listed in the legend. T_1 errors were larger with later center k-space positions and with shorter VFA lengths. 2-parameter SASHA T_1 values in phantoms with shorter myocardial-like T_2 values (blue circles and lines) were generally underestimated and had larger magnitudes of error, up to -8%, compared to phantoms with longer blood-like T_2 values (red circles and lines), which had smaller, but overestimated T_1 errors. Experimental results had good agreement with simulations, as shown in Fig. 5.6 (circles vs. lines, respectively) are re-plotted in Fig. 5.7. The average difference between experimental and simulated 2-parameter SASHA T_1 errors was 0.3±1.4% T_1 error. The average T_1 error with 3-parameter SASHA-VFA for all center k-space locations and VFA lengths was -0.8±0.7%.

Accuracy of 2-parameter SASHA-VFA with different center k-space locations for 4 phantoms with relaxation values similar to native and post-contrast myocardium and blood is summarized in Fig. 5.8. In the absence of SASHA-CFA data, results are shown for a VFA length of 10 pulses (red bars), which has similar performance to a CFA readout (Fig. 5.5c). Results are also shown for VFA lengths that are the nearest multiple of 10 to the optimum length proposed in Eq. 5.5 (blue bars). Small errors of less than ~1% were

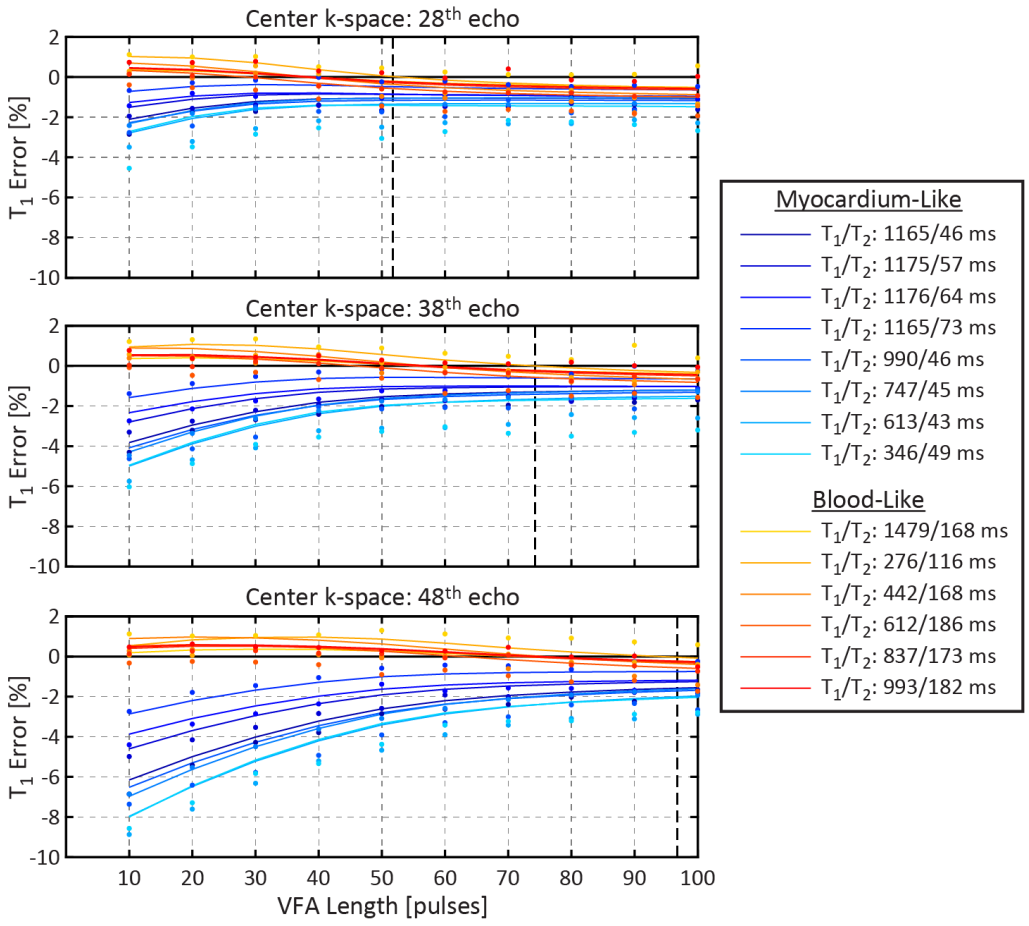

Figure 5.6: Error in 2-parameter SASHA T_1 values as a function of VFA length for various center k-space locations. Lines indicate simulated error and dots indicate measured values. T_1 and T_2 values in the legend are from spin-echo experiments. Myocardial-like (short T_2) phantoms are shown in blues while blood-like (long T_2) phantoms are shown in reds. Vertical black dashed lines show the optimal VFA length (Eq. 5.5) for each center k-space location.

found for phantoms with blood-like relaxation values in all cases. The short VFA length of 10 results in underestimation of myocardial T_1 values that increases with center k-space position up to -7% error when the center of k-space is at the 48th echo. Near-optimal VFA lengths significantly reduced the magnitude of these errors to less than -2% error for all center k-space locations. Good agreement was found between measured results and simulations for all cases. Additional simulations using an ideal saturation pulse (light blue striped bars) show that T_1 errors are greater than the <1% target due to imperfect saturation.

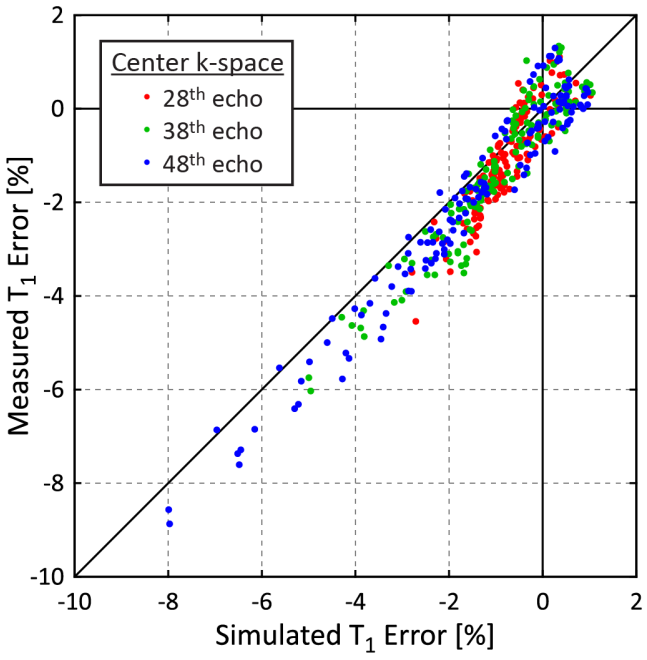

Figure 5.7: Measured T_1 error as a function of simulated T_1 error with 2-parameter SASHA and VFA lengths from 10–100 pulses in 14 phantoms. Diagonal line indicates the unity line.

5.3.4 In-Vivo Studies

In-vivo myocardial and blood T_1 values in the 4 healthy volunteers are summarized in Table 5.1. Mean myocardial T_1 values were similar between SASHA-CFA and SASHA-VFA, regardless of 2-parameter or 3-parameter model fitting. The average standard deviation and coefficient of variation was lower for VFA readouts than CFA and also for 2-parameter model T_1 values compared to 3-parameter. Blood T_1 values were higher with 2-parameter fitting for both CFA and VFA readouts, but the coefficient of variation was reduced. The average coefficient of variation was lower in the blood pool for VFA readouts compared to CFA readouts.

Typical in-vivo images and T_1 maps from one of the volunteers are shown in Fig. 5.9. Improved blood-tissue contrast is seen with VFA in the 580 ms TS images (left) while reduced contrast is seen in the non-saturated images (middle). An artifact in the inferior right ventricular wall (red arrow) in the CFA images is not present in the VFA images. The T_1 map calculated using a 2-parameter model for SASHA-VFA is visibly less noisy than the T_1 map calculated using the 3-parameter model typically used for SASHA-CFA (right).

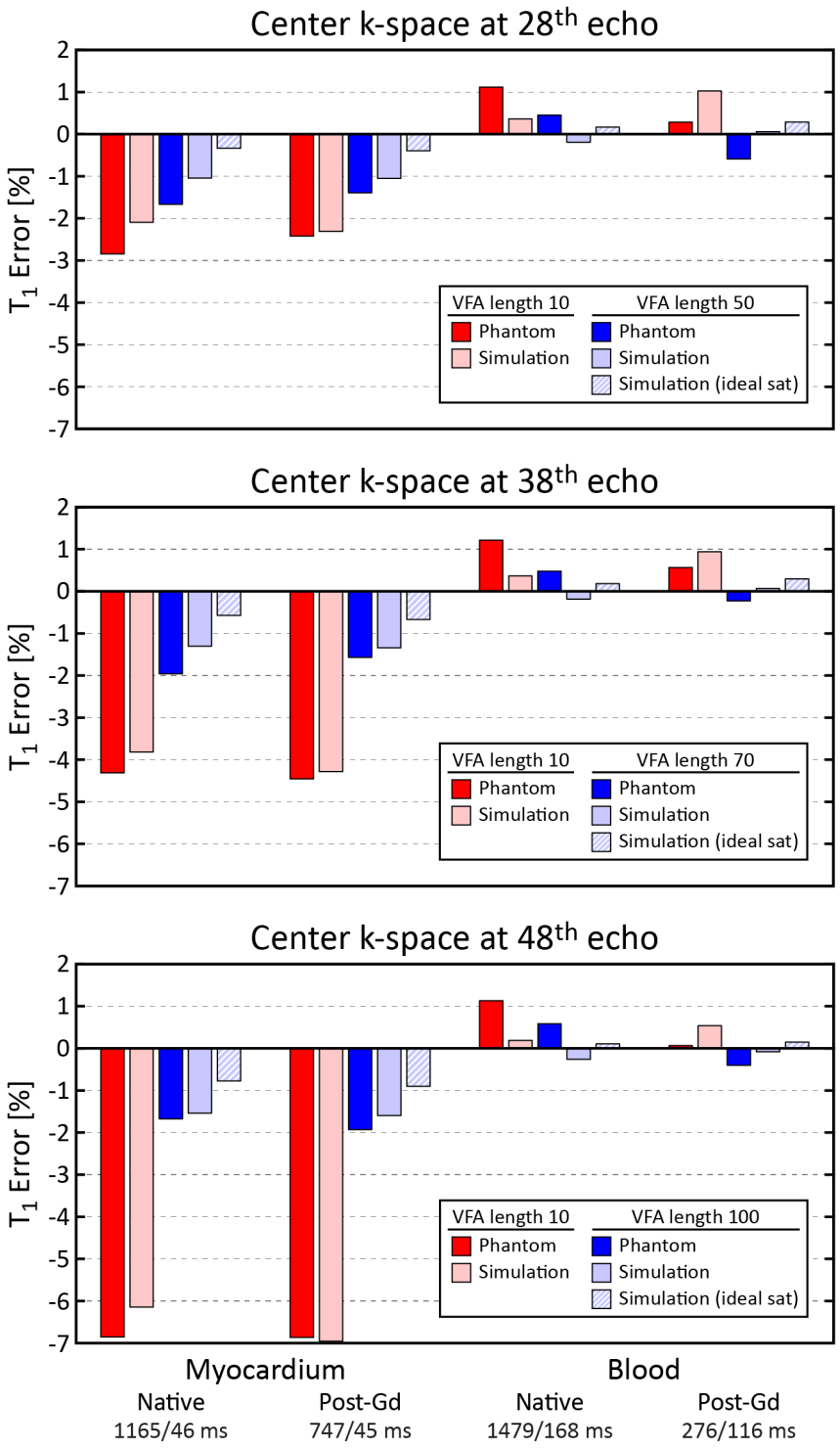

Figure 5.8: Measured and simulated T_1 error with 2-parameter SASHA-VFA for phantoms with relaxation values similar to native and post-contrast myocardium and blood. Results for a VFA length of 10 (red bars) are similar those expected for a CFA readout (Fig. 5.5c). Longer VFA lengths (blue bars) are the nearest multiple of 10 to the proposed optimum VFA length in Eq. 5.5. Light blue striped bars show results for simulations using ideal saturation efficiency instead of measured saturation efficiency.

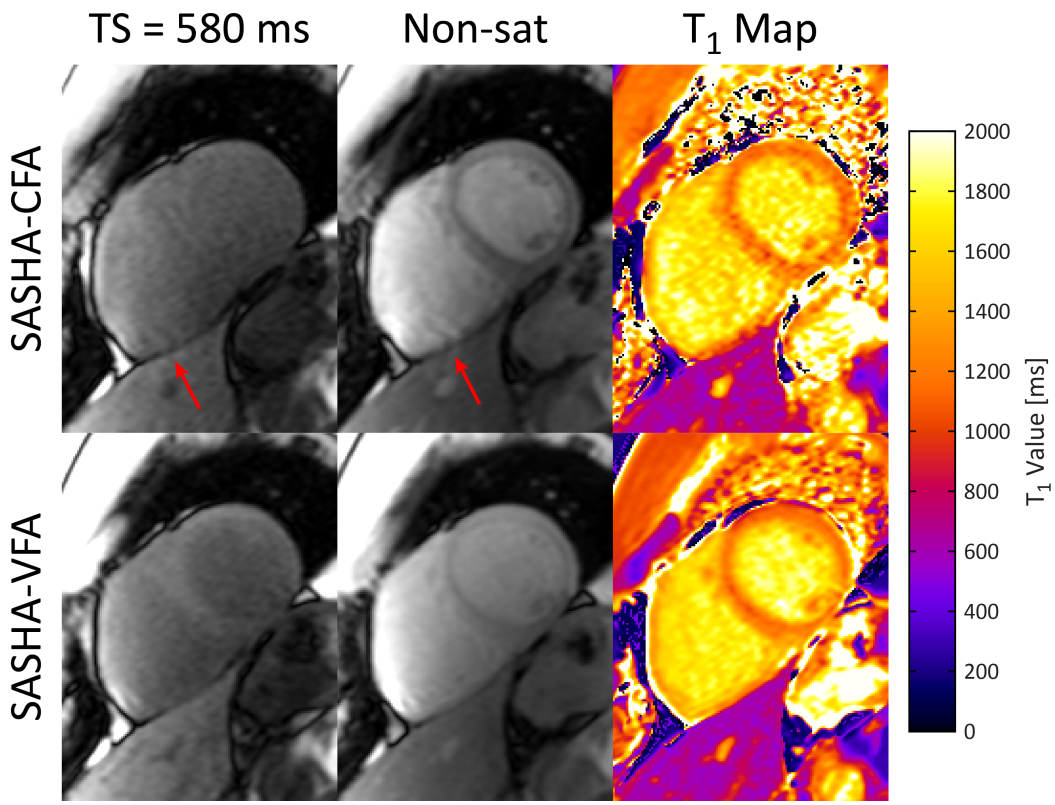

Figure 5.9: SASHA-CFA (top) and SASHA-VFA (bottom) images from a healthy volunteer. VFA images have improved blood-tissue contrast in the saturation recovery image (left) but poorer blood-tissue contrast in the non-saturated image. A ghosting artifact in the right ventricle on CFA images (red arrow) is not visible in VFA images. The 2-parameter SASHA-VFA T_1 map (bottom right) is visibly less noisy than the 3-parameter SASHA-CFA T_1 map (top right).

5.4 Discussion

5.4.1 Accuracy of 2-parameter SASHA T_1 Values

The variable flip angle design proposed in this study was shown to improve the accuracy of 2-parameter SASHA T_1 values compared to the standard constant flip angle readout. T_1 values with 2-parameter SASHA-CFA are overestimated for long T_2 values such as in the blood pool but underestimated for short T_2 values in the myocardium depending on the center k-space position. Image acquisitions used in this study reduced the center k-space position to the 28^{th} echo at a relatively large 256 matrix size using a combination of 75% phase field of view, 78% phase resolution, $7/8^{th}$ partial Fourier, and a GRAPPA acquisition where the ACS lines are acquired in a separate heartbeat in order to achieve true rate 2 acceleration. This early center k-space position keeps the magnitude of 2-parameter SASHA-CFA to less

than ~2%, however this high level of acceleration may not be achievable or desirable in all settings. For example, a 100% phase field of view may be unavoidable for some patients due to slice orientation, which increases the center k-space to the 38th echo. If 24 GRAPPA ACS lines are acquired in-line with each image, as is more commonly done, in addition to a 100% phase field of view, the center k-space increases even further to the 44th echo. Reduction in the amount of acceleration from phase resolution and partial Fourier factors may also be helpful in reducing effects of image blurring in the phase encode direction. The proposed VFA scheme allows much later center k-space locations while maintaining the magnitude of 2-parameter SASHA errors to less than 1%.

5.4.2 Variable Flip Angle Readout Performance

Variable flip angle readouts have improved off-resonance characteristics compared to constant flip angle readouts, with substantially lower amplitude oscillations in the magnitude and phase between sequential echoes of the simulated transverse magnetization. This smoother signal evolution over k-space, particularly in the signal phase, results in less image artifacts, as illustrated in Fig. 5.9. A recent study at 3T [12] found off-resonance >150Hz in 39% of subjects, indicating that the signal oscillations shown in Fig. 5.2 are not uncommon at 3T when using standard CFA readouts. While off-resonance values of ±150 Hz would be quite large for the myocardium at 1.5T, ghosting artifacts from fat can likely be reduced by VFA readouts, as fat is 220 Hz off-resonance at 1.5T.

The lower signal amplitudes at the beginning of VFA readouts results in 4–15% broader point spread functions than for CFA readouts thus increased image blurring. However, the increase in FWHM did not result in a noticeable decrease in image sharpness in in-vivo images, although the blood-tissue contrast in non-saturation images was significantly reduced as predicted by Fig. 5.5b.

The reduced blood-tissue contrast in the non-saturated VFA image is due slightly increased myocardial SNR and reduced blood SNR (Fig. 5.5a). This reduces the visibility the endocardial border in in-vivo images, although identification was still possible in all cases. The poorer blood tissue contrast also did not appear to affect the accuracy of the motion correction algorithm used, as the high contrast at the heart/lung boundary is likely sufficient. Reduced contrast may actually be beneficial in T_1 quantification, as the smaller amplitude difference at the blood/tissue boundary lessens the Gibbs' ringing artifact, which results in T_1 errors as the ringing is not consistent between individual images when they have different contrast [16]. The reduced contrast may also be helpful in ameliorating errors from partial voluming effects, as the signal intensity is less altered when a myocardial voxel is

partially contaminated by blood. While blood tissue contrast is reduced in the non-saturated VFA image, contrast is noticeably increased in the native saturation recovery images where the endocardial boundary is not routinely identifiable in CFA images (Fig. 5.9). This may provide some additional information for manual contouring or assisting motion correction algorithms.

The optimal VFA length as described in Eq. 5.5 was chosen with consideration of SNR, blood-tissue contrast, as well as T_1 error in both native and post-contrast conditions. However, different VFA lengths could be use for native and post-contrast imaging to obtain further benefits from the VFA readout. For example, increasing the VFA length could reduce the systematic errors in post-contrast blood T_1 values, where shorter T_1 values increase the signal intensity in the saturation recovery images and thus the reduced SNR is less detrimental. For native imaging, the VFA length could be reduced to improve blood-tissue contrast and increase myocardial SNR, thus reducing myocardial T_1 variability at the expense of slightly larger T_1 errors in native blood.

Furthermore, the VFA optimization presented here considered only a sinuisoid pattern with variable lengths in order to reduce the optimization complexity. Different VFA shapes including other smooth analytic functions or algorithmically calculated schemes based on work by Worters *et al.* [19] may provide further benefits in SNR, contrast, or T_1 error.

5.4.3 Phantom Experiments

Phantom data in this study had good agreement with simulations. Due to a programming error, SASHA-CFA data was not acquired in the phantom experiments and thus a direct comparison between SASHA-CFA and SASHA-VFA could not be performed. However, simulations showed similar performance between VFA readouts with a short length of 10 pulses and CFA readouts (Fig. 5.5), and thus served as a suitable surrogate comparison of T_1 accuracy. The magnitude of T_1 overestimation in the post-contrast blood phantom (Fig. 5.8) is less than suggested by Fig. 5.5, however had good agreement with simulations using the gold standard measured phantoms T_1 and T_2 values. This discrepancy is thus likely due to the different relaxation values between the simulations shown in Fig. 5.5 and the actual phantom relaxation values.

5.4.4 In-Vivo Studies

In-vivo data from this study was limited to native T_1 mapping in a small sample size that were all imaged with a small phase field of view and thus the center k-space position was at the 28^{th} echo. Due to the relatively early center k-space position in these acquisitions,

simulations predict a relatively small error in 2-parameter fitting of SASHA-CFA data and thus minimal accuracy benefit in using SASHA-VFA. Further studies with a later center k-space position from a larger field of view more typical for clinical subjects may reveal more systematic differences between 2-parameter SASHA-CFA and SASHA-VFA, particularly in post-contrast settings where 2-parameter T_1 errors are larger.

While there were no significant errors in myocardial T_1 values with 2-parameter fitting with acquisition parameters used, the VFA readout alone reduced the coefficient of variation in T_1 in both the myocardium and blood pool. The increased precision can partially be attributed to the predicted increase in SNR with VFA readouts (Fig. 5.5a), but simulations predict a decrease in SNR for the blood pool, which was confirmed by relatively decreased signal intensity. Instead, the improved precision is likely due to reduced variability in the signal intensity within the blood pool, as shown in the raw images in Fig. 5.9. This is consistent with the reduction in overall image artifacts with the VFA readout that can appear as both well-defined shapes as well as hazy ghosting.

5.4.5 Limitations

VFA readouts were designed to reduce the error in calculated T_1 values when using a 2-parameter model by reducing the change in apparent saturation efficiency caused by the bSSFP readout. However, poor saturation pulses with non-ideal *actual* saturation efficiency results in T_1 errors through the direct effect of fitting data to a model with incorrect η, but also due to magnetization history effects between heartbeats. Two-parameter fitting is much more sensitive to errors due to poor saturation efficiency, with 1.3–1.6% T_1 error for every 1% error in true saturation efficiency (Chapter 4), compared to less than 0.3% T_1 error at a heart rate of 60 bpm when using a 3-parameter fit. Thus 2-parameter SASHA-VFA requires robust saturation, which can be achieved using saturation pulse trains, with an average measured $\eta_{|\text{actual}}$ of 0.9981±0.0018 in a phantom with B_1=0.4–1.2 and off-resonance values between ±240 Hz, as described further in Chapter 4.

A 3-parameter fit can also still be used to calculate T_1 values from SASHA-VFA data, but without the benefit of reduced variability gained by fitting one less parameter. Instead, a 3-parameter fit with SASHA-VFA data is more robust to imperfect saturation as described above, and maintains the accuracy of the original 3-parameter SASHA technique, removing the minor residual systematic errors introduced by 2-parameter fitting, as shown in Fig. 5.5c. Thus a 3-parameter fit may be used as an internal consistency check of SASHA-VFA data. If T_1 values calculated using 3-parameter fitting are systematically different from those with 2-parameter fitting, it suggests that the 2-parameter T_1 values are incorrect due to the poor

Table 5.1: Myocardial and blood T_1 values in 4 healthy volunteers

	Myocardium			Blood		
	Mean [ms]	Standard Deviation [ms]	Coefficient of Variation [%]	Mean [ms]	Standard Deviation [ms]	Coefficient of Variation [%]
SASHA-CFA (3p)	1174.0 ± 16.3	58.5 ± 4.0	5.0 ± 0.3	1658.3 ± 72.0	74.9 ± 7.2	4.5 ± 0.6
SASHA-CFA (2p)	1176.7 ± 28.8	46.6 ± 4.3	4.0 ± 0.3	1721.8 ± 72.0	56.0 ± 12.3	3.3 ± 0.9
SASHA-VFA (3p)	1169.0 ± 23.3	49.7 ± 6.0	4.3 ± 0.5	1670.2 ± 118.9	61.1 ± 14.9	3.7 ± 0.9
SASHA-VFA (2p)	1163.8 ± 18.5	37.3 ± 2.7	3.2 ± 0.2	1703.9 ± 111.6	47.0 ± 3.8	2.8 ± 0.3
MOLLI	996.1 ± 14.2	33.2 ± 2.3	3.3 ± 0.2	1596.7 ± 74.5	32.4 ± 4.2	2.1 ± 0.3

Values are reported as the mean ± standard deviation across subjects.

saturation pulses or residual bSSFP related errors such as those shown in Fig. 5.5.

5.5 Conclusions

A variable flip angle (VFA) readout scheme was designed and optimized for SASHA T_1 mapping, with consideration of SNR, blood-tissue contrast, and T_1 errors. The proposed VFA scheme reduces the magnitude of SASHA T_1 errors resulting from 2-parameter fitting, particularly in readouts where the center of k-space is acquired later in the echo train. Reduced incidence of image artifacts with the VFA readout and improved myocardial SNR resulted in lower variability of calculated T_1 values with the VFA readout alone. Combined with 2-parameter model fitting, SASHA-VFA has a coefficient of variation similar to that of the commonly used MOLLI sequence while maintaining superior accuracy.

5.6 References

[1] Sacha Bull, Steven K White, Stefan K Piechnik, Andrew S Flett, Vanessa M Ferreira, Margaret Loudon, Jane M Francis, Theodoros D Karamitsos, Bernard D Prendergast, Matthew D Robson, Stefan Neubauer, James Charles Moon, and Saul G Myerson. Human non-contrast T1 values and correlation with histology in diffuse fibrosis. *Heart (British Cardiac Society)*, 99(13):932–937, July 2013. pg. 113

[2] Daniel M Sado, Steven K White, Stefan K Piechnik, Sanjay M Banypersad, Thomas Treibel, Gabriella Captur, Marianna Fontana, Viviana Maestrini, Andrew S Flett, Matthew D Robson, Robin H Lachmann, Elaine Murphy, Atul Mehta, Derralynn Hughes, Stefan Neubauer, Perry M Elliott, and James Charles Moon. Identification and assessment of Anderson-Fabry disease by cardiovascular magnetic resonance non-contrast myocardial T1 mapping. *Circulation: Cardiovascular Imaging*, 6(3):392–398, May 2013. pg. 113

[3] Richard B Thompson, Kelvin Chow, Aneal Khan, Alicia Chan, Miriam Shanks, Ian Paterson, and Gavin Y Oudit. T mapping with cardiovascular MRI is highly sensitive for Fabry disease independent of hypertrophy and sex. *Circulation: Cardiovascular Imaging*, 6(5):637–645, September 2013. pg. 113

[4] Daniel M Sado, Andrew S Flett, Sanjay M Banypersad, Steven K White, Viviana Maestrini, Giovanni Quarta, Robin H Lachmann, Elaine Murphy, Atul Mehta, Derralynn A Hughes, William J McKenna, Andrew M Taylor, Derek J Hausenloy, Philip Nigel Hawkins, Perry M Elliott, and James Charles Moon. Cardiovascular magnetic resonance measurement of myocardial extracellular volume in health and disease. *Heart (British Cardiac Society)*, 98(19):1436–1441, October 2012. pg. 113

[5] Timothy C Wong, Kayla Piehler, Christopher G Meier, Stephen M Testa, Amanda M Klock, Ali A Aneizi, Jonathan Shakesprere, Peter Kellman, Sanjeev G Shroff, David S Schwartzman, Suresh R Mulukutla, Marc A Simon, and Erik B Schelbert. Association between extracellular matrix expansion quantified by cardiovascular magnetic resonance and short-term mortality. *Circulation*, 126(10):1206–1216, September 2012. pg. 113

[6] Daniel R Messroghli, Aleksandra Radjenovic, Sebastian Kozerke, David M Higgins, Mohan U Sivananthan, and John P Ridgway. Modified Look-Locker inversion recovery

(MOLLI) for high-resolution T1 mapping of the heart. *Magnetic Resonance in Medicine*, 52(1):141–146, July 2004. pg. 113, pg. 113

[7] Stefan K Piechnik, Vanessa M Ferreira, Erica Dall'Armellina, Lowri E Cochlin, Andreas Greiser, Stefan Neubauer, and Matthew D Robson. Shortened Modified Look-Locker Inversion recovery (ShMOLLI) for clinical myocardial T1-mapping at 1.5 and 3 T within a 9 heartbeat breathhold. *Journal of cardiovascular magnetic resonance : official journal of the Society for Cardiovascular Magnetic Resonance*, 12:69, 2010. pg. 113, pg. 113

[8] Erik B Schelbert, Stephen M Testa, Christopher G Meier, William J Ceyrolles, Joshua E Levenson, Alexander J Blair, Peter Kellman, Bobby L Jones, Daniel R Ludwig, David S Schwartzman, Sanjeev G Shroff, and Timothy C Wong. Myocardial extravascular extracellular volume fraction measurement by gadolinium cardiovascular magnetic resonance in humans: slow infusion versus bolus. *Journal of cardiovascular magnetic resonance : official journal of the Society for Cardiovascular Magnetic Resonance*, 13:16, 2011.

[9] Jason J Lee, Songtao Liu, Marcelo S Nacif, Martin Ugander, Jing Han, Nadine Kawel, Christopher T Sibley, Peter Kellman, Andrew E Arai, and David A Bluemke. Myocardial T1 and extracellular volume fraction mapping at 3 tesla. *Journal of cardiovascular magnetic resonance : official journal of the Society for Cardiovascular Magnetic Resonance*, 13:75, 2011. pg. 113

[10] Kelvin Chow, Jacqueline A Flewitt, Joseph J Pagano, Jordin D Green, Matthias G Friedrich, and Richard B Thompson. T2-dependent errors in MOLLI T1 values: simulations, phantoms, and in-vivo studies. *Journal of cardiovascular magnetic resonance : official journal of the Society for Cardiovascular Magnetic Resonance*, 14(Suppl 1):P281, 2012. pg. 113

[11] Neville D Gai, Christian Stehning, Marcelo Nacif, and David A Bluemke. Modified Look-Locker T1 evaluation using Bloch simulations: human and phantom validation. *Magnetic Resonance in Medicine*, 69(2):329–336, February 2013.

[12] Peter Kellman, Daniel A Herzka, Andrew E Arai, and Michael Schacht Hansen. Influence of Off-resonance in myocardial T1-mapping using SSFP based MOLLI method. *Journal of cardiovascular magnetic resonance : official journal of the Society for Cardiovascular Magnetic Resonance*, 15:63, 2013. pg. 128

[13] Matthew D Robson, Stefan K Piechnik, Elizabeth M Tunnicliffe, and Stefan Neubauer. T1 measurements in the human myocardium: The effects of magnetization transfer on

the SASHA and MOLLI sequences. *Magnetic Resonance in Medicine*, July 2013. pg. 113, pg. 114

[14] C B Higgins, R Herfkens, M J Lipton, R Sievers, P Sheldon, L Kaufman, and L E Crooks. Nuclear magnetic resonance imaging of acute myocardial infarction in dogs: alterations in magnetic relaxation times. *The American journal of cardiology*, 52(1):184–188, July 1983. pg. 113

[15] Kelvin Chow, Jacqueline A Flewitt, Jordin D Green, Joseph J Pagano, Matthias G Friedrich, and Richard B Thompson. Saturation recovery single-shot acquisition (SASHA) for myocardial T1 mapping. *Magnetic Resonance in Medicine*, 71(6):2082–2095, 2014. pg. 114, pg. 114, pg. 115

[16] Peter Kellman and Michael Schacht Hansen. T1-mapping in the heart: accuracy and precision. *Journal of cardiovascular magnetic resonance : official journal of the Society for Cardiovascular Magnetic Resonance*, 16(1):2, January 2014. pg. 114, pg. 114, pg. 128

[17] J P Mugler, F H Epstein, and J R Brookeman. Shaping the signal response during the approach to steady state in three-dimensional magnetization-prepared rapid gradient-echo imaging using variable flip angles. *Magnetic Resonance in Medicine*, 28(2):165–185, December 1992. pg. 114

[18] L Zhao, R Mulkern, C H Tseng, D Williamson, S Patz, R Kraft, R L Walsworth, F A Jolesz, and M S Albert. Gradient-echo imaging considerations for hyperpolarized 129Xe MR. *Journal of magnetic resonance Series B*, 113:179–183, 1996. pg. 114

[19] Pauline W Worters and Brian A Hargreaves. Balanced SSFP transient imaging using variable flip angles for a predefined signal profile. *Magnetic Resonance in Medicine*, 64(5):1404–1412, November 2010. pg. 114, pg. 129

[20] Martin H Deppe and Jim M Wild. Variable flip angle schedules in bSSFP imaging of hyperpolarized noble gases. *Magnetic Resonance in Medicine*, 67(6):1656–1664, June 2012. pg. 114

[21] Dominik Paul, Michael Markl, Hans-Peter Fautz, and Jürgen Hennig. T2-weighted balanced SSFP imaging (T2-TIDE) using variable flip angles. *Magnetic Resonance in Medicine*, 56(1):82–93, July 2006. pg. 114

[22] Mark A Griswold, Peter M Jakob, Robin M Heidemann, Mathias Nittka, Vladimir Jellus, Jianmin Wang, Berthold Kiefer, and Axel Haase. Generalized autocalibrating partially parallel acquisitions (GRAPPA). *Magnetic Resonance in Medicine*, 47(6):1202–1210, June 2002. pg. 116

[23] Peter Kellman, Daniel A Herzka, and Michael Schacht Hansen. Adiabatic inversion pulses for myocardial T1 mapping. *Magnetic Resonance in Medicine*, 71(4):1428–1434, 2014. pg. 113, pg. 118

[24] Hui Xue, Saurabh Shah, Andreas Greiser, Christoph Guetter, Arne Littmann, Marie-Pierre Jolly, Andrew E Arai, Sven Zuehlsdorff, Jens Guehring, and Peter Kellman. Motion correction for myocardial T1 mapping using image registration with synthetic image estimation. *Magnetic Resonance in Medicine*, 67(6):1644–1655, June 2012. pg. 118

[25] R Deichmann and Axel Haase. Quantification of T1 values by SNAPSHOT-FLASH NMR imaging. *Journal of Magnetic Resonance*, 96(3):608–612, February 1992. pg. 118

Chapter 6

Discussion and Conclusions

6.1 Summary

This thesis analytically described the MOLLI T_1 mapping sequence using a time-weighted average model of relaxation and described the development of a new SASHA T_1 mapping sequence that is robust to many of MOLLI's systematic sources of error.

Chapter 2 proposed a time-weighted average model of relaxation in the MOLLI sequence. This model was shown to be extremely accurate in Bloch equation simulations with a single flip angle and demonstrate that multi-exponential relaxation occurs during each imaging readout of the MOLLI sequence. Approximations for this multi-exponential relaxation in the TWA model showed good agreement in the apparent relaxation time constant T_1^* with experimentally measured values over a wide range of heart rates and flip angles. This model provides an intuitive and analytic model for understanding the relationship between apparent T_1^* and the true T_1 in MOLLI for the first time since it was first published over 10 years ago [1]. Further work on the TWA model may be able to incorporate the effects of off-resonance and magnetization transfer, but may also facilitate the development of a more accurate way of calculating T_1 values from MOLLI data.

Chapter 3 presented the original SASHA sequence with 3-parameter fitting as an accurate T_1 mapping technique robust to T_1, T_2, flip angle, and heart rate through a theoretical derivation, simulations, and phantom experiments. Subsequent studies have confirmed SASHA's robustness to these factors [2, 3] as well as magnetization transfer [4], but have noted that it has substantially poorer precision than the MOLLI sequence. A 2-parameter model assuming ideal saturation efficiency was shown to improve SASHA's precision at the expense of introducing small systematic biases [3].

Chapters 4 and 5 improved the accuracy of 2-parameter model fitting of SASHA data by addressing factors that affect the assumed ideal saturation efficiency. Existing

non-selective saturation pulses were shown to be insufficient over the ranges of expected conditions, particularly variations in B_1 fields, and new hard pulse trains were designed to achieve robust saturation performance over B_0, B_1, and T_1 ranges at both 1.5T and 3T, with experimental measured residual longitudinal magnetization of less than 1%. The variable flip angle readout proposed in Chapter 5 reduces the bSSFP weighting on the measured signal intensity, thereby reducing change in apparent saturation efficiency. Together, these improvements enable the assumption of ideal saturation efficiency required for accurate T_1 estimates from SASHA with a 2-parameter model. Preliminary data shown in Chapter 5 suggests 2-parameter SASHA-VFA data can be used to quantify T_1 values to within 1% accuracy and has a similar coefficient of variation as compared to MOLLI.

6.2 T_1 Measurements and Fibrosis

In a clinical setting, T_1 mapping derived metrics, i.e. native and post-contrast myocardial T_1, λ, and ECV, are increasingly being proposed as surrogate biomarkers for the assessment of myocardial fibrosis. Thus the true goal is not necessarily the accurate quantification of T_1 values themselves, but the accurate quantification of a biomarker for fibrosis. Thus it can be argued that while MOLLI T_1 values have systematic errors, they still reflect changes in the true T_1 (native and post-contrast) that are altered with fibrosis. However, these sources of error result in random and systematic variability in MOLLI T_1 values.

6.2.1 Random and Systematic Errors in T_1 Measurements

MOLLI's sources of error can be broadly categorized as patient independent or dependent. For example, MOLLI T_1 values have a strong dependence with flip angle [5] and off-resonance [6], both of which depend mostly on RF coil design, field strength, and field shimming. MOLLI is also known to be sensitive to the efficiency of its inversion pulse [7], which may vary between sequence implementations. All MOLLI sequences exhibit dependencies on T_2 values [8–10] and magnetization transfer effects [4], and standard MOLLI sequences with 3 recovery heartbeats between Look-Locker sets are moderately heart rate dependent [3, 11].

At best, these sources of errors simply result in increased random variability in the MOLLI T_1 values. However, they may also lead to systematically different T_1 values that can be misinterpreted as differences in fibrosis. For example, observed spatial patterns in MOLLI T_1 values [12, 13] may be explained by systematic B_0 and B_1 variations over the heart [6, 14] but could be misinterpreted as regional fibrosis. Systematically increased heart

rates with disease or reduced heart rates with therapy could result in correlations or group difference that are entirely independent of fibrosis. Myocardial T_2 values may be altered with edema [15] or iron overload [16] and magnetization transfer effects are influenced by the macromolecular concentration, all of which indicate a pathological condition, but may also be independent of fibrosis. T_1-mapping derived ECV values are calculated using both myocardial and blood T_1 values in both native and post-contrast states, all of which may have different systematic errors, further complicating interpretation the effect of systematic T_1 errors on ECV values.

Given the potential for misinterpretation, proper analysis of MOLLI data should therefore use multivariate statistics with each of MOLLI's systematic dependencies as a covariate. However this approach is entirely impractical in nearly all contexts, as it would require additional time-consuming measurements of each of these variables. Additionally, the increase in the number of covariates and variability in their measurements would likely substantially increase the number of subjects required to achieve the same statistical power. Instead, it may be more realistic to simply minimize as many sources of error when possible during the data acquisition and carefully interpret possible T_1 differences if any of the possible confounders are likely to be altered between comparison groups.

MOLLI's sensitivity to acquisition parameters make it ill-suited for multi-site studies, particular with multiple MRI scanner vendors due to the variations in sequence implementation such as RF pulse profiles, B_0 shimming, B_1 calibration, inversion pulse selection, and calculation of TI time. A recent study comparing MOLLI T_1 values between 5 scanners at both 1.5T and 3T field strengths from Phillips and Siemens vendors found that a difference in T_1 accuracy of 4% between sites using the same vendor at 3T, and up to a 6% difference in T_1 accuracy between different vendors at 3T [17]. Poor inter-site agreement between MOLLI T_1 values hinders the creation of reference ranges for normal healthy myocardial T_1 values, and the current consensus statement on T_1 mapping suggests that site-specific normal ranges be established, greatly increasing the barrier to entry for clinical users.

However, MOLLI's high precision can be used to its advantage in single center studies or serial follow-up studies if the acquisition parameters are tightly controlled. For example, while the MOLLI sequence has evolved with improved sampling patterns that reduce its heart-rate dependence [3], improved the inversion efficiency with new pulses [7], and used higher resolutions to avoid partial voluming [3], the ShMOLLI sequence [12] has remained consistent to its original implementation. As the vast majority of ShMOLLI data is acquired by a small group of researchers in a limited number of sites, they have been able to carefully prevent any modification of sequence parameters including field of view and phase resolution. Healthy control data from their group has shown normal myocardial ShMOLLI T_1 values

of 962±25 ms in 342 subjects [18], and the low coefficient of variation allows more sensitive thresholds for detecting abnormalities.

The SASHA sequence with a 3-parameter model has been shown to be a highly accurate sequence with none of systematic biases that MOLLI has (i.e. T_1, T_2, flip angle, number of phase encode lines, off-resonance, and magnetization transfer), and minimal dependence on saturation efficiency [3, 4, 6, 19]. Preliminary data presented in Chapter 5 suggest that T_1 values from 2-parameter SASHA-VFA have similar coefficients of variation to MOLLI while being accurate to within 1% of true T_1 values. Although the relative variability of the MOLLI and 2-parameter SASHA-VFA sequence requires confirmation in larger studies, the lack of *systematic* bias that makes it much stronger candidate for widespread usage. This should enable the identification of normative ranges for myocardial SASHA T_1 values that are implementation insensitive, thus obviating the need for site-specific controls. Insensitivity to sequence parameters is of particular appeal in multi-center studies where data heterogeneity is an unavoidable reality.

6.2.2 Sensitivity and Specificity of T_1 and ECV Measurements

It has been suggested that sensitivity to T_2 and magnetization transfer (MT) effects are advantageous to MOLLI in that they improve its sensitivity to pathological changes [4], as edema and macromolecular concentration alterations are likely of clinical utility. This pragmatic perspective is appealing, but it must also consider that increased sensitivity to pathological changes other than fibrosis result in a corresponding reduction in specificity to fibrosis alone. For example, native myocardial ShMOLLI T_1 values have been correlated with injury severity in acute myocardial infarction [20, 21] and with T_2^* in iron overload [22]. However, given that there are known T_2 changes with both myocardial edema [15] and iron overload [16], it is likely the observed ShMOLLI T_1 changes are at least partially due to changes in T_2 instead of true T_1. This highlights the utility of ShMOLLI in applications where T_2 is altered but also the non-specificity of ShMOLLI T_1 changes. In patients with an abnormal native ShMOLLI T_1 value without a known clinical diagnosis, it is difficult to determine whether the T_1 value is changed due to increased fibrosis, edema, iron, or the other systematic sources of error described in the previous section.

Fibrotic remodeling in chronic infarction are accompanied by alterations in MT effects [23] and both MT [24] and T_2 [15] are altered with edema in acute infarction. Reduced MT effects and increased T_2 values both serve to reduce systematic T_1 underestimation and increase measured MOLLI T_1 values. As fibrosis also results in increased native T_1 values and decreased post-contrast T_1 values, T_2 and MT effects increase the difference between

normal myocardium and its surroundings in the native state and reduce the difference in the post-contrast state. Thus while fibrosis is likely to be more conspicuous on native MOLLI T_1 values than unbiased SASHA T_1 values, the net result on MOLLI ECV values, derived from both native and post-contrast measurements, is complex and not well known.

6.2.3 Interpretation of T_1 and ECV Measurements

It is important to appreciate that even true native myocardial T_1 values are reflective of the general microstructural environment and not entirely specific to fibrosis. Increased T_1 with fibrosis likely reflect an increase in the extracellular volume, thus increasing T_1 by increasing the free water fraction as described in Section 1.4.4. An increase in extracellular volume due to edema is likely to increase native T_1 values in a similar way, and other non-fibrosis pathologies likely cause changes in native T_1 values that have yet to be properly quantified.

Contrast-enhanced T_1 measures such as post-contrast myocardial T_1, partition coefficient, and ECV are more direct measurements of the true extracellular volume because the change in T_1 is caused by the accumulation of contrast agent in the extracellular space. However even these metrics do not reflect fibrosis itself, but rather the expansion of extracellular space due to fibrosis, and edematous expansion of the extracellular space is still indistinguishable from fibrosis.

6.3 Limitations

The utility of the SASHA sequence in quantifying myocardial fibrosis is limited by a relatively small number of studies using it. Although there have been multiple published studies correlating fibrosis measurements using MOLLI and other T_1 mapping sequences with histology [25–29], it is still necessary to establish that SASHA is able to do the same. The SASHA sequence with the original constant flip angle readout was also reported to be more susceptible to artifacts than the MOLLI sequence [3]. Although the variable flip angle (VFA) readout proposed in Chapter 5 showed a reduction in artifacts for a small sample of 4 people, image quality with SASHA-VFA requires further testing in a larger group of more challenging, clinically relevant subjects.

The 2-parameter model significantly reduces the variability of calculated SASHA T_1 values, but the standard deviation of 2-parameter SASHA-VFA T_1 values is still higher than MOLLI. However, preliminary in-vivo data suggests that the coefficient of variation with SASHA-VFA is similar to MOLLI due to the lower T_1 values with MOLLI. Further study is

needed to determine whether the variability in 2-parameter SASHA-VFA hinders its ability to detect pathological changes in myocardial T_1 values. The SASHA sequence is more flexible in the number of images that can be acquired, and the variability may be further reduced if needed by increasing the number of acquired images at the expense of a longer breath-hold.

The time-weighted average (TWA) relaxation model of MOLLI presented in Chapter 2 provides an intuitive and analytic description of the measured apparent T_1^*. However, the model is currently of limited practical application in calculating the true T_1 value, as the current derivation requires a priori knowledge of T_2 and flip angle and is unstable to errors in those assumptions. Further work is required to determine if the TWA model can be used create a more stable and accurate way of calculating true T_1 values from MOLLI data.

Although T_1 mapping has generally been used to assess diffuse myocardial fibrosis, spatial resolution of existing techniques may still be a limiting factor. Partial-voluming of blood or fat can alter the measured T_1 value at the edges of the myocardium, particularly for oblique short axis slices, and Gibbs ringing due to signal intensity differences can cause artifactual spatial patterns in T_1 values. Single-shot techniques such as MOLLI and SASHA are commonly acquired with a matrix size of 192 in the readout dimension, resulting in 1.9–2.0 mm^2 in-plane resolution. The resolution can be increased to use a 256 matrix with 1.4–1.6 mm^2 in-plane resolution by using more aggressive parallel acceleration techniques such as Generalized Autocalibrating Partially Parallel Acquisitions (GRAPPA) [30] with the auto-calibration signal (ACS) reference lines in a separate heart-beat. However, further increases in spatial resolution by increasing the matrix size are likely to bring only mild gains due to increased cardiac motion over the longer imaging duration. Reduced slice thicknesses have also been used to diminish partial voluming effects, although increased variability in calculated T_1 values associated with reduced SNR of smaller voxel sizes is also likely to at least partially negate some of the benefits of increased resolution. T_1 mapping applications such as imaging of the thin-walled right ventricle and smaller hearts in pediatric populations where higher resolutions are needed will require alternative approaches such as segmented imaging, 3D imaging, or other categories of image acceleration such as compressed sensing [31].

6.4 Recent Developments in SASHA T_1 mapping

6.4.1 Selection of SASHA Saturation Recovery Times

The choice of TS times in the SASHA sequence determines the sampling of the T_1 saturation recovery curve and the variability of calculated best-fit T_1 values. The original

sampling scheme proposed in Chapter 3 linearly spaces TS times from the shortest possible TS time, where the saturation pulse is played immediately before the imaging readout, to the longest possible TS time, with the saturation pulse immediately following the ECG trigger. This uniform sampling pattern allows the maximum number of images to be acquired within a fixed duration. Longer TS times can be obtained by playing the image readout in the RR interval following the saturation pulse, as previously described for the SR-TFL sequence [32] and more recently in SMART$_1$Map [33]. However, the advantage of sampling a greater portion of the recovery curve is partially negated by the reduced number of samples. The overall effect on T_1 variability is affected by the T_1 value itself (as the magnitude of recovery for a given TS time depends on T_1) as well as the choice of a 2 or 3-parameter exponential recovery model.

Sampling strategies for a 2-parameter model were recently investigated with the aim of minimizing the variability best-fit T_1 values [34]. The optimal TS times were chosen using brute force optimization with constraints on the total imaging duration and accounting for the reduced number of samples with multi-heartbeat TS times. A sampling strategy with fixed TS times, i.e. all saturation recovery images with the same TS time in addition to the first non-saturation anchor image, was found to reduce the T_1 standard deviation by ~10% compared to a uniform sampling pattern. The optimum fixed TS time was 600 ms for native T_1 values and a 190 ms TS time for post-contrast T_1 values. When used with a 2-parameter model, multi-heartbeat TS times found to have greater T_1 variability compared to both fixed and uniform sampling.

The optimal TS pattern for a 3-parameter model with variable saturation efficiency has also been determined using brute-force optimization without multi-heartbeat TS times [35]. The authors found that the optimal sampling pattern had two sets of fixed TS times, one at the shortest possible TS time, and one as close to the T_1 value as permitted by the heart rate. The difference in optimal sampling strategies between 2 and 3-parameter models is likely due to the need to also estimate the saturation efficiency in the 3-parameter model. The short TS time cluster allows for better estimation of this parameter, whereas these low SNR data points are less useful when the saturation efficiency is assumed in the 2-parameter model.

6.5 Future Directions

6.5.1 MOLLI and the TWA Model

The TWA model can likely be further expanded to incorporate the effects of off-resonance and magnetization transfer as an increase in the driven relaxation rate R_1', making it a more complete model of relaxation during a realistic MOLLI experiment. The current description of the relationship between apparent T_1^* and the true T_1 uses only the apparent T_1^* from measured data and requires assumptions about the T_2, flip angle, and its slice profile. However, with an assumption about the initial magnetization following an inversion pulse, the apparent steady-state magnetization can be readily extracted from experimental data at no additional cost. This could potentially be used to generate a correction factor similar to the currently used Look-Locker correction factor, resulting in a more stable method for calculating true T_1 values. The MOLLI sequence could also be potentially modified to acquire supplementary information used to calculate true T_1 values, such as directly measuring the driven R_1'. It remains to be seen whether these improvements can entirely remove MOLLI's sources of error, although it is likely that they could be significantly reduced with an improved correction factor or through modifications made to the sequence acquisition.

6.5.2 Segmented Acquisitions

Segmented acquisitions overcome the limited diastasis imaging window by separating each image into segments that can be acquired in separate heartbeats. As the total segmented acquisition time is increased by the segmentation factor, navigator-gated free-breathing acquisitions are generally used. Segmented MOLLI acquisitions require that all segments within a Look-Locker set be acquired at the same respiratory phase in order to ensure the same magnetization history. This is often done by verifying the respiratory phase of each image within the 3–5 heartbeat set and discarding the set if the respiratory phase change exceeds a specified threshold, which may occur frequently for fast or irregular respiratory patterns. Additionally, the inversion times of images after the first image of a Look-Locker set are heart-rate dependent, and thus heart rate variability results in inconsistent TI times between segments. Implementations of segmented MOLLI have overcome these challenges by using shortened Look-Locker sets [36] and an adaptive algorithm to acquire sparse data for compressed sensing reconstruction and end acquisition when a specific threshold of image quality and predicted T_1 variability is reached [37].

SASHA is more amenable to segmented acquisitions than MOLLI, as the saturation pulse acts to make each saturation recovery image acquisition independent. With saturation

recovery time typically less than the R-R interval, acquisitions can be respiratory triggered instead of retrospectively accepted/discarded, leading to higher acquisition efficiency. Segmented SASHA acquisitions may also be more time efficient, as the saturation pulse enables saturation recovery images to be acquired in every heartbeat while the respiratory phase is at the target position, although longer delays are necessary to allow full magnetization recovery between segments of the non-saturated anchor image.

Segmented acquisitions are particularly useful for higher resolutions readouts that would exceed the diastasis imaging window if acquired in a single shot. This approach also enables 3-dimensional acquisitions, which have higher SNR and allow thinner slices than 2-dimensional acquisitions. Shorter imaging durations with segmented acquisitions may also be useful in subjects with fast heart rates, where significant cardiac motion over typical 150–200 ms single-shot imaging duration often results in image blurring or artifacts. These improvements over single-shot imaging may be essential to T_1 imaging in pediatric populations, where fast heart rates and inability to perform breath-holds make current sequences ineffective.

6.5.3 Alternative Image Reconstruction

Like most parametric mapping techniques, SASHA and MOLLI sequences acquire an image series with different T_1-weighting but of the same object. This information redundancy is well suited for compressed sensing (CS) image reconstruction [31] and can significantly increase the acquisition acceleration factor beyond the typical 2–3 from parallel imaging techniques such as GRAPPA [30] and SENSE [38]. CS image reconstruction has been used in the Accelerated and Navigator-Gated Look-Locker Imaging for Cardiac T_1 Estimation (ANGIE) variant of the MOLLI sequence to reduce acquisition time and achieve higher spatial resolution. Compressed sensing can also be used to reconstruct T_1 maps instead of generating intermediate raw images [39, 40], further improving acceleration factors.

6.6 Conclusions

The ubiquitous presence of fibrosis in cardiac disease is likely to drive widespread adoption of T_1 mapping into clinical practice if it can be robustly measured and shown to be clinically useful. The widely used MOLLI T_1 mapping sequence has been validated against histological fibrosis measurements and correlated with various metrics of cardiac remodeling in numerous patient populations. However, systematic sources of error with the MOLLI sequence can confound interpretation about the source of T_1 changes and complicate multi-

site studies where different sequence implementations result in different reference T_1 ranges. The time-weighted average model of relaxation provides an analytic understanding of these sources of error and could potentially be further developed to more accurately calculate T_1 values from MOLLI data.

The SASHA sequence developed in this thesis is an alternative T_1 mapping sequence without many of MOLLI's systematic sources of error. A 2-parameter exponential recovery model assuming ideal saturation efficiency was shown to significantly reduce variability when calculating SASHA T_1 values, but resulted in systematic errors when applied to the original SASHA sequence. Improvements to saturation pulse design and variable flip angle readouts were shown to reduce systematic errors in 2-parameter SASHA to less than 1% with the coefficient of variation similar to MOLLI. Further development of SASHA using segmented readouts could enable high-resolution 3D T_1 maps and expand its utility into pediatric populations.

6.7 References

[1] Daniel R Messroghli, Aleksandra Radjenovic, Sebastian Kozerke, David M Higgins, Mohan U Sivananthan, and John P Ridgway. Modified Look-Locker inversion recovery (MOLLI) for high-resolution T1 mapping of the heart. *Magnetic Resonance in Medicine*, 52(1):141–146, July 2004. pg. 136

[2] Sébastien Roujol, Sebastian Weingärtner, Murilo Foppa, Kelvin Chow, Keigo Kawaji, Long H Ngo, Peter Kellman, Warren J Manning, Richard B Thompson, and Reza Nezafat. Accuracy, Precision, and Reproducibility of Four T1 Mapping Sequences: A Head-to-Head Comparison of MOLLI, ShMOLLI, SASHA, and SAPPHIRE. *Radiology*, 272(3):683–689, April 2014. pg. 136

[3] Peter Kellman and Michael Schacht Hansen. T1-mapping in the heart: accuracy and precision. *Journal of cardiovascular magnetic resonance : official journal of the Society for Cardiovascular Magnetic Resonance*, 16(1):2, January 2014. pg. 136, pg. 136, pg. 137, pg. 138, pg. 138, pg. 139, pg. 140

[4] Matthew D Robson, Stefan K Piechnik, Elizabeth M Tunnicliffe, and Stefan Neubauer. T1 measurements in the human myocardium: The effects of magnetization transfer on the SASHA and MOLLI sequences. *Magnetic Resonance in Medicine*, July 2013. pg. 136, pg. 137, pg. 139, pg. 139

[5] Daniel R Messroghli, Andreas Greiser, Mirko Fröhlich, Rainer Dietz, and Jeanette Schulz-Menger. Optimization and validation of a fully-integrated pulse sequence for modified look-locker inversion-recovery (MOLLI) T1 mapping of the heart. *Journal of magnetic resonance imaging : JMRI*, 26(4):1081–1086, October 2007. pg. 137

[6] Peter Kellman, Daniel A Herzka, Andrew E Arai, and Michael Schacht Hansen. Influence of Off-resonance in myocardial T1-mapping using SSFP based MOLLI method. *Journal of cardiovascular magnetic resonance : official journal of the Society for Cardiovascular Magnetic Resonance*, 15:63, 2013. pg. 137, pg. 137, pg. 139

[7] Peter Kellman, Daniel A Herzka, and Michael Schacht Hansen. Adiabatic inversion pulses for myocardial T1 mapping. *Magnetic Resonance in Medicine*, 71(4):1428–1434, 2014. pg. 137, pg. 138

[8] Kelvin Chow, Jacqueline A Flewitt, Joseph J Pagano, Jordin D Green, Matthias G Friedrich, and Richard B Thompson. MOLLI T1 Values Have Systematic T2 and Inversion Efficiency Dependent Errors. In *Proceedings of the International Society for Magnetic Resonance in Medicine*, page 395, 2012. pg. 137

[9] Kelvin Chow, Jacqueline A Flewitt, Joseph J Pagano, Jordin D Green, Matthias G Friedrich, and Richard B Thompson. T2-dependent errors in MOLLI T1 values: simulations, phantoms, and in-vivo studies. *Journal of cardiovascular magnetic resonance : official journal of the Society for Cardiovascular Magnetic Resonance*, 14(Suppl 1):P281, 2012.

[10] Neville D Gai, Christian Stehning, Marcelo Nacif, and David A Bluemke. Modified Look-Locker T1 evaluation using Bloch simulations: human and phantom validation. *Magnetic Resonance in Medicine*, 69(2):329–336, February 2013. pg. 137

[11] Jason J Lee, Songtao Liu, Marcelo S Nacif, Martin Ugander, Jing Han, Nadine Kawel, Christopher T Sibley, Peter Kellman, Andrew E Arai, and David A Bluemke. Myocardial T1 and extracellular volume fraction mapping at 3 tesla. *Journal of cardiovascular magnetic resonance : official journal of the Society for Cardiovascular Magnetic Resonance*, 13:75, 2011. pg. 137

[12] Stefan K Piechnik, Vanessa M Ferreira, Erica Dall'Armellina, Lowri E Cochlin, Andreas Greiser, Stefan Neubauer, and Matthew D Robson. Shortened Modified Look-Locker Inversion recovery (ShMOLLI) for clinical myocardial T1-mapping at 1.5 and 3 T within a 9 heartbeat breathhold. *Journal of cardiovascular magnetic resonance : official journal of the Society for Cardiovascular Magnetic Resonance*, 12:69, 2010. pg. 137, pg. 138

[13] Toby Rogers, Darius Dabir, Islam Mahmoud, Tobias Voigt, Tobias schaeffter, Eike Nagel, and Valentina O Puntmann. Standardization of T1 measurements with MOLLI in differentiation between health and disease – the ConSept study. *Journal of cardiovascular magnetic resonance : official journal of the Society for Cardiovascular Magnetic Resonance*, 15(1):78, September 2013. pg. 137

[14] Kyunghyun Sung and Krishna S Nayak. Measurement and characterization of RF nonuniformity over the heart at 3T using body coil transmission. *Journal of magnetic resonance imaging : JMRI*, 27(3):643–648, March 2008. pg. 137

[15] C B Higgins, R Herfkens, M J Lipton, R Sievers, P Sheldon, L Kaufman, and L E Crooks. Nuclear magnetic resonance imaging of acute myocardial infarction in dogs: alterations

in magnetic relaxation times. *The American journal of cardiology*, 52(1):184–188, July 1983. pg. 138, pg. 139, pg. 139

[16] Maciej W Garbowski, John-Paul Carpenter, Gillian Smith, Michael Roughton, Mohammed H Alam, Taigang He, Dudley J Pennell, and John B Porter. Biopsy-based calibration of T2* magnetic resonance for estimation of liver iron concentration and comparison with R2 Ferriscan. *Journal of cardiovascular magnetic resonance : official journal of the Society for Cardiovascular Magnetic Resonance*, 16(1):40, June 2014. pg. 138, pg. 139

[17] Fabio S Raman, Nadine Kawel-Boehm, Neville D Gai, Melanie Freed, Jing Han, Chia Ying Liu, João A C Lima, David A Bluemke, and Songtao Liu. Modified look-locker inversion recovery T1 mapping indices: assessment of accuracy and reproducibility between magnetic resonance scanners. *Journal of cardiovascular magnetic resonance : official journal of the Society for Cardiovascular Magnetic Resonance*, 15:64, 2013. pg. 138

[18] Stefan K Piechnik, Vanessa M Ferreira, Adam J Lewandowski, Ntobeko Ab Ntusi, Rajarshi Banerjee, Cameron Holloway, Mark Bm Hofman, Daniel M Sado, Viviana Maestrini, Steven White, Merzaka Lazdam, Theodoros D Karamitsos, James Charles Moon, Stefan Neubauer, Paul Leeson, and Matthew D Robson. Normal variation of magnetic resonance T1 relaxation times in the human population at 1.5T using ShMOLLI. *Journal of cardiovascular magnetic resonance : official journal of the Society for Cardiovascular Magnetic Resonance*, 15(1):13, January 2013. pg. 139

[19] Kelvin Chow, Jacqueline A Flewitt, Jordin D Green, Joseph J Pagano, Matthias G Friedrich, and Richard B Thompson. Saturation recovery single-shot acquisition (SASHA) for myocardial T1 mapping. *Magnetic Resonance in Medicine*, 71(6):2082–2095, 2014. pg. 139

[20] Erica Dall'Armellina, Stefan K Piechnik, Vanessa M Ferreira, Quang Le Si, Matthew D Robson, Jane M Francis, Florim Cuculi, Rajesh K Kharbanda, Adrian P Banning, Robin P Choudhury, Theodoros D Karamitsos, and Stefan Neubauer. Cardiovascular magnetic resonance by non contrast T1 mapping allows assessment of severity of injury in acute myocardial infarction. *Journal of cardiovascular magnetic resonance : official journal of the Society for Cardiovascular Magnetic Resonance*, 14(1):15, February 2012. pg. 139

[21] Vanessa M Ferreira, Stefan K Piechnik, Erica Dall'Armellina, Theodoros D Karamitsos, Jane M Francis, Robin P Choudhury, Matthias G Friedrich, Matthew D Robson, and Stefan Neubauer. Non-contrast T1-mapping detects acute myocardial edema with high diagnostic accuracy: a comparison to T2-weighted cardiovascular magnetic resonance. *Journal of cardiovascular magnetic resonance : official journal of the Society for Cardiovascular Magnetic Resonance*, 14(1):42, June 2012. pg. 139

[22] Daniel M Sado, Viviana Maestrini, Stefan K Piechnik, Sanjay M Banypersad, Steven K White, Andrew S Flett, Matthew D Robson, Stefan Neubauer, Cono Ariti, Andrew Arai, Peter Kellman, Jin Yamamura, Bjoern P Schoennagel, Farrukh Shah, Bernard Davis, Sara Trompeter, Malcolm Walker, John Porter, and James Charles Moon. Noncontrast myocardial T1mapping using cardiovascular magnetic resonance for iron overload. *Journal of magnetic resonance imaging : JMRI*, pages n/a–n/a, August 2014. pg. 139

[23] Clifford R Weiss, Anthony H Aletras, James F London, Joni L Taylor, Frederick H Epstein, Ralf Wassmuth, Robert S Balaban, and Andrew E Arai. Stunned, Infarcted, and Normal Myocardium in Dogs: Simultaneous Differentiation by Using Gadolinium-enhanced Cine MR Imaging with Magnetization Transfer Contrast. *Radiology*, 226(3):723–730, 2003. pg. 139

[24] Oliver M Weber, Peter Speier, Klaus Scheffler, and Oliver Bieri. Assessment of magnetization transfer effects in myocardial tissue using balanced steady-state free precession (bSSFP) cine MRI. *Magnetic Resonance in Medicine*, 62(3):699–705, 2009. pg. 139

[25] Leah Iles, Heinz Pfluger, Arintaya Phrommintikul, Joshi Cherayath, Pelin Aksit, Sandeep N Gupta, David M Kaye, and Andrew J Taylor. Evaluation of diffuse myocardial fibrosis in heart failure with cardiac magnetic resonance contrast-enhanced T1 mapping. *Journal of the American College of Cardiology*, 52(19):1574–1580, November 2008. pg. 140

[26] Elizabeth Kehr, Megan Sono, Sumeet S Chugh, and Michael Jerosch-Herold. Gadolinium-enhanced magnetic resonance imaging for detection and quantification of fibrosis in human myocardium in vitro. *The international journal of cardiovascular imaging*, 24(1):61–68, 2008.

[27] Andrew S Flett, Martin P Hayward, Michael T Ashworth, Michael Schacht Hansen, Andrew M Taylor, Perry M Elliott, Christopher McGregor, and James Charles Moon. Equilibrium contrast cardiovascular magnetic resonance for the measurement of diffuse

myocardial fibrosis: preliminary validation in humans. *Circulation*, 122(2):138–144, July 2010.

[28] Daniel R Messroghli, Sarah Nordmeyer, Thore Dietrich, Olaf Dirsch, Elena Kaschina, Kostas Savvatis, Darach O H-Ici, Christoph Klein, Felix Berger, and Titus Kuehne. Assessment of diffuse myocardial fibrosis in rats using small-animal look-locker inversion recovery t1 mapping. *Circulation: Cardiovascular Imaging*, 4(6):636–640, November 2011.

[29] Sacha Bull, Steven K White, Stefan K Piechnik, Andrew S Flett, Vanessa M Ferreira, Margaret Loudon, Jane M Francis, Theodoros D Karamitsos, Bernard D Prendergast, Matthew D Robson, Stefan Neubauer, James Charles Moon, and Saul G Myerson. Human non-contrast T1 values and correlation with histology in diffuse fibrosis. *Heart (British Cardiac Society)*, 99(13):932–937, July 2013. pg. 140

[30] Mark A Griswold, Peter M Jakob, Robin M Heidemann, Mathias Nittka, Vladimir Jellus, Jianmin Wang, Berthold Kiefer, and Axel Haase. Generalized autocalibrating partially parallel acquisitions (GRAPPA). *Magnetic Resonance in Medicine*, 47(6):1202–1210, June 2002. pg. 141, pg. 144

[31] Michael Lustig, David Donoho, and John M Pauly. Sparse MRI: The application of compressed sensing for rapid MR imaging. *Magnetic Resonance in Medicine*, 58(6):1182–1195, November 2007. pg. 141, pg. 144

[32] C M Wacker, M Bock, A W Hartlep, G Beck, G van Kaick, G Ertl, W R Bauer, and L R Schad. Changes in myocardial oxygenation and perfusion under pharmacological stress with dipyridamole: assessment using T*2 and T1 measurements. *Magnetic Resonance in Medicine*, 41(4):686–695, April 1999. pg. 142

[33] Glenn S Slavin, Maureen N Hood, Vincent B Ho, and Jeffrey A Stainsby. Breath-Held Myocardial T1 Mapping Using Multiple Single-Point Saturation Recovery. In *Proceedings of the International Society for Magnetic Resonance in Medicine*, page 1244, 2012. pg. 142

[34] Peter Kellman, Hui Xue, Kelvin Chow, Bruce S Spottiswoode, Andrew E Arai, and Richard B Thompson. Optimized saturation recovery protocols for T1-mapping in the heart: influence of sampling strategies on precision. *Journal of cardiovascular magnetic resonance : official journal of the Society for Cardiovascular Magnetic Resonance*, 16(1):55, September 2014. pg. 142

[35] Mehmet Akçakaya, Sebastian Weingärtner, Sébastien Roujol, and Reza Nezafat. On the selection of sampling points for myocardial T1 mapping. *Magnetic Resonance in Medicine*, May 2014. pg. 142

[36] Tobias Voigt, Tobias schaeffter, Rene Botnar, Jouke Smink, and Markus Henningsson. Three-Dimensional MOLLI For Myocardial T1 Mapping Using Respiratory Navigation and Inversion Time Gating. *Proceedings of the International Society for Magnetic Resonance in Medicine*, 21:258, 2013. pg. 143

[37] Bhairav B Mehta, Xiao Chen, Kenneth C Bilchick, Michael Salerno, and Frederick H Epstein. Accelerated and navigator-gated look-locker imaging for cardiac t1 estimation (ANGIE): Development and application to T1 mapping of the right ventricle. *Magnetic Resonance in Medicine*, February 2014. pg. 143

[38] K P Pruessmann, M Weiger, M B Scheidegger, and Peter Boesiger. SENSE: sensitivity encoding for fast MRI. *Magnetic Resonance in Medicine*, 42(5):952–962, November 1999. pg. 144

[39] Mariya Doneva, Peter Börnert, Holger Eggers, Christian Stehning, Julien Sénégas, and Alfred Mertins. Compressed sensing reconstruction for magnetic resonance parameter mapping. *Magnetic Resonance in Medicine*, 64(4):1114–1120, October 2010. pg. 144

[40] Julia V Velikina, Andrew L Alexander, and Alexey Samsonov. Accelerating MR parameter mapping using sparsity-promoting regularization in parametric dimension. *Magnetic Resonance in Medicine*, 70(5):1263–1273, 2013. pg. 144

Complete Bibliography

[1] World Health Organization. Global status report on noncommunicable diseases 2010. Technical report, Geneva, 2011.

[2] Statistics Canada. Mortality, Summary List of Causes 2009. Technical report, July 2012.

[3] A S Go, D Mozaffarian, V L Roger, E J Benjamin, J D Berry, M J Blaha, S Dai, E S Ford, C S Fox, S Franco, H J Fullerton, C Gillespie, S M Hailpern, J A Heit, V J Howard, M D Huffman, S E Judd, B M Kissela, S J Kittner, D T Lackland, J H Lichtman, L D Lisabeth, R H Mackey, D J Magid, G M Marcus, A Marelli, D B Matchar, D K McGuire, E R Mohler, C S Moy, M E Mussolino, R W Neumar, G Nichol, D K Pandey, N P Paynter, M J Reeves, P D Sorlie, J Stein, A Towfighi, T N Turan, S S Virani, N D Wong, D Woo, M B Turner, and on behalf of the American Heart Association Statistics Committee and Stroke Statistics Subcommittee. Heart Disease and Stroke Statistics–2014 Update: A Report From the American Heart Association. *Circulation*, 129(3):e28–e292, January 2014.

[4] M A Bernstein, K F King, and X J Zhou. *Handbook of MRI Pulse Sequences*. Elsevier Science, 2004.

[5] F Bloch. Nuclear Induction. *Physical Review*, 70(7-8):460–474, October 1946.

[6] N Bloembergen, E Purcell, and R Pound. Relaxation Effects in Nuclear Magnetic Resonance Absorption. *Physical Review*, 73(7):679–712, April 1948.

[7] Gary D Fullerton, Janet L Potter, and N Carol Dornbluth. NMR relaxation of protons in tissues and other macromolecular water solutions. *Magnetic resonance imaging*, 1(4):209–226, 1982.

[8] J R Zimmerman and W E Brittin. Nuclear Magnetic Resonance Studies in Multiple Phase Systems: Lifetime of a Water Molecule in an Adsorbing Phase on Silica Gel. *The Journal of Physical Chemistry*, 61(10):1328–1333, October 1957.

[9] D Look and D Locker. Time Saving in Measurement of NMR and EPR Relaxation Times. *Review of Scientific Instruments*, 41(2):250–251, 1970.

[10] R Deichmann and Axel Haase. Quantification of T1 values by SNAPSHOT-FLASH NMR imaging. *Journal of Magnetic Resonance*, 96(3):608–612, February 1992.

[11] Michael Jerosch-Herold, David C Sheridan, Jessica D Kushner, Deirdre Nauman, Donna Burgess, Diana Dutton, Rami Alharethi, Duanxiang Li, and Ray E Hershberger. Cardiac magnetic resonance imaging of myocardial contrast uptake and blood flow in patients affected with idiopathic or familial dilated cardiomyopathy. *American journal of physiology Heart and circulatory physiology*, 295(3):H1234–H1242, September 2008.

[12] Craig S Broberg, Sumeet S Chugh, Catherine Conklin, David J Sahn, and Michael Jerosch-Herold. Quantification of diffuse myocardial fibrosis and its association with myocardial dysfunction in congenital heart disease. *Circulation: Cardiovascular Imaging*, 3(6):727–734, November 2010.

[13] Peter Schmitt, Mark A Griswold, Peter M Jakob, Markus Kotas, Vikas Gulani, Michael Flentje, and Axel Haase. Inversion recovery TrueFISP: quantification of T(1), T(2), and spin density. *Magnetic Resonance in Medicine*, 51(4):661–667, April 2004.

[14] Ankur Gupta, Vivian S Lee, Yiu-Cho Chung, James S Babb, and Orlando P Simonetti. Myocardial Infarction: Optimization of Inversion Times at Delayed Contrast-enhanced MR Imaging. *Radiology*, 233(3):921–926, December 2004.

[15] J S Detsky, Jeffrey A Stainsby, R Vijayaraghavan, John J Graham, A J Dick, and G A Wright. Inversion-recovery-prepared SSFP for cardiac-phase-resolved delayed-enhancement MRI. *Magnetic Resonance in Medicine*, 58(2):365–372, July 2007.

[16] Kim A Connelly, Jay S Detsky, John J Graham, Gideon Paul, Ram Vijayaragavan, Alexander J Dick, and Graham A Wright. Multicontrast late gadolinium enhancement imaging enables viability and wall motion assessment in a single acquisition with reduced scan times. *Journal of magnetic resonance imaging : JMRI*, 30(4):771–777, October 2009.

[17] M Pop, V Ramanan, F Yang, L Zhang, S Newbigging, N Ghugre, and G Y1 Wright. High resolution 3D T1*-mapping and quantitative image analysis of gray zone in chronic fibrosis. *Biomedical Engineering, IEEE Transactions on*, PP(99):1–1, 2014.

[18] Daniel R Messroghli, Aleksandra Radjenovic, Sebastian Kozerke, David M Higgins, Mohan U Sivananthan, and John P Ridgway. Modified Look-Locker inversion recovery (MOLLI) for high-resolution T1 mapping of the heart. *Magnetic Resonance in Medicine*, 52(1):141–146, July 2004.

[19] Stefan K Piechnik, Vanessa M Ferreira, Erica Dall'Armellina, Lowri E Cochlin, Andreas Greiser, Stefan Neubauer, and Matthew D Robson. Shortened Modified Look-Locker Inversion recovery (ShMOLLI) for clinical myocardial T1-mapping at 1.5 and 3 T within a 9 heartbeat breathhold. *Journal of cardiovascular magnetic resonance : official journal of the Society for Cardiovascular Magnetic Resonance*, 12:69, 2010.

[20] Jason J Lee, Songtao Liu, Marcelo S Nacif, Martin Ugander, Jing Han, Nadine Kawel, Christopher T Sibley, Peter Kellman, Andrew E Arai, and David A Bluemke. Myocardial T1 and extracellular volume fraction mapping at 3 tesla. *Journal of cardiovascular magnetic resonance : official journal of the Society for Cardiovascular Magnetic Resonance*, 13:75, 2011.

[21] Erik B Schelbert, Stephen M Testa, Christopher G Meier, William J Ceyrolles, Joshua E Levenson, Alexander J Blair, Peter Kellman, Bobby L Jones, Daniel R Ludwig, David S Schwartzman, Sanjeev G Shroff, and Timothy C Wong. Myocardial extravascular extracellular volume fraction measurement by gadolinium cardiovascular magnetic resonance in humans: slow infusion versus bolus. *Journal of cardiovascular magnetic resonance : official journal of the Society for Cardiovascular Magnetic Resonance*, 13:16, 2011.

[22] Peter Kellman and Michael Schacht Hansen. T1-mapping in the heart: accuracy and precision. *Journal of cardiovascular magnetic resonance : official journal of the Society for Cardiovascular Magnetic Resonance*, 16(1):2, January 2014.

[23] Kelvin Chow, Jacqueline A Flewitt, Joseph J Pagano, Jordin D Green, Matthias G Friedrich, and Richard B Thompson. MOLLI T1 Values Have Systematic T2 and Inversion Efficiency Dependent Errors. In *Proceedings of the International Society for Magnetic Resonance in Medicine*, page 395, 2012.

[24] Neville D Gai, Christian Stehning, Marcelo Nacif, and David A Bluemke. Modified Look-Locker T1 evaluation using Bloch simulations: human and phantom validation. *Magnetic Resonance in Medicine*, 69(2):329–336, February 2013.

[25] Daniel R Messroghli, Andreas Greiser, Mirko Fröhlich, Rainer Dietz, and Jeanette Schulz-Menger. Optimization and validation of a fully-integrated pulse sequence for

modified look-locker inversion-recovery (MOLLI) T1 mapping of the heart. *Journal of magnetic resonance imaging : JMRI*, 26(4):1081–1086, October 2007.

[26] Kelvin Chow, Joseph J Pagano, and Richard B Thompson. An Intuitive Model of Several Factors Affecting Accuracy of MOLLI T1 Values. In *Proceedings of the International Society for Magnetic Resonance in Medicine*, 2013.

[27] Peter Kellman, Daniel A Herzka, and Michael Schacht Hansen. Adiabatic inversion pulses for myocardial T1 mapping. *Magnetic Resonance in Medicine*, 71(4):1428–1434, 2014.

[28] Peter Kellman, Daniel A Herzka, Andrew E Arai, and Michael Schacht Hansen. Influence of Off-resonance in myocardial T1-mapping using SSFP based MOLLI method. *Journal of cardiovascular magnetic resonance : official journal of the Society for Cardiovascular Magnetic Resonance*, 15:63, 2013.

[29] Matthew D Robson, Stefan K Piechnik, Elizabeth M Tunnicliffe, and Stefan Neubauer. T1 measurements in the human myocardium: The effects of magnetization transfer on the SASHA and MOLLI sequences. *Magnetic Resonance in Medicine*, July 2013.

[30] C B Higgins, R Herfkens, M J Lipton, R Sievers, P Sheldon, L Kaufman, and L E Crooks. Nuclear magnetic resonance imaging of acute myocardial infarction in dogs: alterations in magnetic relaxation times. *The American journal of cardiology*, 52(1):184–188, July 1983.

[31] Oliver M Weber, Peter Speier, Klaus Scheffler, and Oliver Bieri. Assessment of magnetization transfer effects in myocardial tissue using balanced steady-state free precession (bSSFP) cine MRI. *Magnetic Resonance in Medicine*, 62(3):699–705, 2009.

[32] Hans J de Haas, Eloisa Arbustini, Valentin Fuster, Christopher M Kramer, and Jagat Narula. Molecular imaging of the cardiac extracellular matrix. *Circulation research*, 114(5):903–915, February 2014.

[33] Nathan Mewton, Chia Ying Liu, Pierre Croisille, David A Bluemke, and João A C Lima. Assessment of myocardial fibrosis with cardiovascular magnetic resonance. *Journal of the American College of Cardiology*, 57(8):891–903, February 2011.

[34] C A Souders, S L K Bowers, and T A Baudino. Cardiac Fibroblast: The Renaissance Cell. *Circulation research*, 105(12):1164–1176, December 2009.

[35] Gabriela Kania, Przemyslaw Blyszczuk, and Urs Eriksson. Mechanisms of cardiac fibrosis in inflammatory heart disease. *Trends in cardiovascular medicine*, 19(8):247–252, November 2009.

[36] Hossein Ardehali, Edward K Kasper, and Kenneth L Baughman. Diagnostic approach to the patient with cardiomyopathy: Whom to biopsy. *American heart journal*, 149(1):7–12, 2005.

[37] Raymond Y Kwong and Hema Korlakunta. Diagnostic and prognostic value of cardiac magnetic resonance imaging in assessing myocardial viability. *Topics in magnetic resonance imaging : TMRI*, 19(1):15–24, February 2008.

[38] O P Simonetti, R J Kim, D S Fieno, H B Hillenbrand, E Wu, J M Bundy, J P Finn, and R M Judd. An improved MR imaging technique for the visualization of myocardial infarction. *Radiology*, 218(1):215–223, 2001.

[39] Raymond J Kim, David S Fieno, Todd B Parrish, Kathleen Harris, Enn-Ling Chen, Orlando Simonetti, Jeffrey Bundy, J Paul Finn, Francis J Klocke, and Robert M Judd. Relationship of MRI Delayed Contrast Enhancement to Irreversible Injury, Infarct Age, and Contractile Function. *Circulation*, 100(19):1992–2002, November 1999.

[40] Edwin Wu, Robert M Judd, John D Vargas, Francis J Klocke, Robert O Bonow, and Raymond J Kim. Visualisation of presence, location, and transmural extent of healed Q-wave and non-Q-wave myocardial infarction. *The Lancet*, 357(9249):21–28, January 2001.

[41] Peter Kellman, Andrew E Arai, Elliot R McVeigh, and Anthony H Aletras. Phase-sensitive inversion recovery for detecting myocardial infarction using gadolinium-delayed hyperenhancement. *Magnetic Resonance in Medicine*, 47(2):372–383, February 2002.

[42] Kathleen M Donahue, R M Weisskoff, and D Burstein. Water diffusion and exchange as they influence contrast enhancement. *Journal of magnetic resonance imaging : JMRI*, 7(1):102–110, 1997.

[43] C S Landis, X Li, F W Telang, P E Molina, I Palyka, G Vetek, and C S Springer. Equilibrium transcytolemmal water-exchange kinetics in skeletal muscle in vivo. *Magnetic Resonance in Medicine*, 42(3):467–478, September 1999.

[44] C S Landis, X Li, F W Telang, J A Coderre, P L Micca, W D Rooney, L L Latour, G Vétek, I Pályka, and C S Springer. Determination of the MRI contrast agent concentration time course in vivo following bolus injection: effect of equilibrium transcytolemmal water exchange. *Magnetic Resonance in Medicine*, 44(4):563–574, October 2000.

[45] Otavio R Coelho-Filho, François-Pierre Mongeon, Richard Mitchell, Heitor Moreno, Wilson Nadruz, Raymond Y Kwong, and Michael Jerosch-Herold. Role of transcytolemmal water-exchange in magnetic resonance measurements of diffuse myocardial fibrosis in hypertensive heart disease. *Circulation: Cardiovascular Imaging*, 6(1):134–141, 2013.

[46] Andrew S Flett, Martin P Hayward, Michael T Ashworth, Michael Schacht Hansen, Andrew M Taylor, Perry M Elliott, Christopher McGregor, and James Charles Moon. Equilibrium contrast cardiovascular magnetic resonance for the measurement of diffuse myocardial fibrosis: preliminary validation in humans. *Circulation*, 122(2):138–144, July 2010.

[47] Steven K White, Daniel M Sado, Marianna Fontana, Sanjay M Banypersad, Viviana Maestrini, Andrew S Flett, Stefan K Piechnik, Matthew D Robson, Derek J Hausenloy, Amir M Sheikh, Philip Nigel Hawkins, and James Charles Moon. T1 Mapping for Myocardial Extracellular Volume Measurement by CMR: Bolus Only Versus Primed Infusion Technique. *JACC: Cardiovascular Imaging*, 6(9):955–962, April 2013.

[48] James Charles Moon, Daniel R Messroghli, Peter Kellman, Stefan K Piechnik, Matthew D Robson, Martin Ugander, Peter D Gatehouse, Andrew E Arai, Matthias G Friedrich, Stefan Neubauer, Jeanette Schulz-Menger, and Erik B Schelbert. Myocardial T1 mapping and extracellular volume quantification: a Society for Cardiovascular Magnetic Resonance (SCMR) and CMR Working Group of the European Society of Cardiology consensus statement. *Journal of cardiovascular magnetic resonance : official journal of the Society for Cardiovascular Magnetic Resonance*, 15:92, 2013.

[49] Martin R Prince, Honglei Zhang, Zhitong Zou, Ronald B Staron, and Paula W Brill. Incidence of immediate gadolinium contrast media reactions. *AJR American journal of roentgenology*, 196(2):W138–43, February 2011.

[50] Zhitong Zou, Hong Lei Zhang, Giles H Roditi, Tim Leiner, Walter Kucharczyk, and Martin R Prince. Nephrogenic systemic fibrosis review of 370 biopsy-confirmed cases. *JACC: Cardiovascular Imaging*, 4(11):1206–1216, November 2011.

[51] Daniel M Sado, Andrew S Flett, Sanjay M Banypersad, Steven K White, Viviana Maestrini, Giovanni Quarta, Robin H Lachmann, Elaine Murphy, Atul Mehta, Derralynn A Hughes, William J McKenna, Andrew M Taylor, Derek J Hausenloy, Philip Nigel Hawkins, Perry M Elliott, and James Charles Moon. Cardiovascular magnetic resonance measurement of myocardial extracellular volume in health and disease. *Heart (British Cardiac Society)*, 98(19):1436–1441, October 2012.

[52] Martin Ugander, Abiola J Oki, Li-Yueh Hsu, Peter Kellman, Andreas Greiser, Anthony H Aletras, Christopher T Sibley, Marcus Y Chen, W Patricia Bandettini, and Andrew E Arai. Extracellular volume imaging by magnetic resonance imaging provides insights into overt and sub-clinical myocardial pathology. *European heart journal*, 33(10):1268–1278, May 2012.

[53] Leah Iles, Heinz Pfluger, Arintaya Phrommintikul, Joshi Cherayath, Pelin Aksit, Sandeep N Gupta, David M Kaye, and Andrew J Taylor. Evaluation of diffuse myocardial fibrosis in heart failure with cardiac magnetic resonance contrast-enhanced T1 mapping. *Journal of the American College of Cardiology*, 52(19):1574–1580, November 2008.

[54] Alicia Maria Maceira, Jayshree Joshi, Sanjay Kumar Prasad, James Charles Moon, Enrica Perugini, Idris Harding, Mary Noelle Sheppard, Philip Alexander Poole-Wilson, Philip Nigel Hawkins, and Dudley John Pennell. Cardiovascular magnetic resonance in cardiac amyloidosis. *Circulation*, 111(2):186–193, January 2005.

[55] Sebastian J Flacke, S E Fischer, and C H Lorenz. Measurement of the gadopentetate dimeglumine partition coefficient in human myocardium in vivo: normal distribution and elevation in acute and chronic infarction. *Radiology*, 218(3):703–710, March 2001.

[56] Daniel R Messroghli, Kevin Walters, Sven Plein, Patrick Sparrow, Matthias G Friedrich, John P Ridgway, and Mohan U Sivananthan. Myocardial T1 mapping: application to patients with acute and chronic myocardial infarction. *Magnetic Resonance in Medicine*, 58(1):34–40, July 2007.

[57] Sairia Dass, Joseph J Suttie, Stefan K Piechnik, Vanessa M Ferreira, Cameron J Holloway, Rajarshi Banerjee, Masliza Mahmod, Lowri Cochlin, Theodoros D Karamitsos, Matthew D Robson, Hugh Watkins, and Stefan Neubauer. Myocardial tissue characterization using magnetic resonance noncontrast t1 mapping in hypertrophic and dilated cardiomyopathy. *Circulation: Cardiovascular Imaging*, 5(6):726–733, November 2012.

[58] Vanessa M Ferreira, Stefan K Piechnik, Erica Dall'Armellina, Theodoros D Karamitsos, Jane M Francis, Robin P Choudhury, Matthias G Friedrich, Matthew D Robson, and Stefan Neubauer. Non-contrast T1-mapping detects acute myocardial edema with high diagnostic accuracy: a comparison to T2-weighted cardiovascular magnetic resonance. *Journal of cardiovascular magnetic resonance : official journal of the Society for Cardiovascular Magnetic Resonance*, 14(1):42, June 2012.

[59] Sacha Bull, Steven K White, Stefan K Piechnik, Andrew S Flett, Vanessa M Ferreira, Margaret Loudon, Jane M Francis, Theodoros D Karamitsos, Bernard D Prendergast, Matthew D Robson, Stefan Neubauer, James Charles Moon, and Saul G Myerson. Human non-contrast T1 values and correlation with histology in diffuse fibrosis. *Heart (British Cardiac Society)*, 99(13):932–937, July 2013.

[60] Daniel M Sado, Steven K White, Stefan K Piechnik, Sanjay M Banypersad, Thomas Treibel, Gabriella Captur, Marianna Fontana, Viviana Maestrini, Andrew S Flett, Matthew D Robson, Robin H Lachmann, Elaine Murphy, Atul Mehta, Derralynn Hughes, Stefan Neubauer, Perry M Elliott, and James Charles Moon. Identification and assessment of Anderson-Fabry disease by cardiovascular magnetic resonance noncontrast myocardial T1 mapping. *Circulation: Cardiovascular Imaging*, 6(3):392–398, May 2013.

[61] Richard B Thompson, Kelvin Chow, Aneal Khan, Alicia Chan, Miriam Shanks, Ian Paterson, and Gavin Y Oudit. T mapping with cardiovascular MRI is highly sensitive for Fabry disease independent of hypertrophy and sex. *Circulation: Cardiovascular Imaging*, 6(5):637–645, September 2013.

[62] Elizabeth Kehr, Megan Sono, Sumeet S Chugh, and Michael Jerosch-Herold. Gadolinium-enhanced magnetic resonance imaging for detection and quantification of fibrosis in human myocardium in vitro. *The international journal of cardiovascular imaging*, 24(1):61–68, 2008.

[63] Christopher A Miller, Josephine H Naish, Paul Bishop, Glyn Coutts, David Clark, Sha Zhao, Simon G Ray, Nizar Yonan, Simon G Williams, Andrew S Flett, James Charles Moon, Andreas Greiser, Geoffrey J M Parker, and Matthias Schmitt. Comprehensive Validation of Cardiovascular Magnetic Resonance Techniques for the Assessment of Myocardial Extracellular Volume. *Circulation: Cardiovascular Imaging*, 6(3):373–383, May 2013.

[64] Marianna Fontana, Steve K White, Sanjay M Banypersad, Daniel M Sado, Viviana Maestrini, Andrew S Flett, Stefan K Piechnik, Stefan Neubauer, Neil Roberts, and James Charles Moon. Comparison of T1 mapping techniques for ECV quantification. Histological validation and reproducibility of ShMOLLI versus multibreath-hold T1 quantification equilibrium contrast CMR. *Journal of cardiovascular magnetic resonance : official journal of the Society for Cardiovascular Magnetic Resonance*, 14:88, 2012.

[65] Timothy C Wong, Kayla Piehler, Christopher G Meier, Stephen M Testa, Amanda M Klock, Ali A Aneizi, Jonathan Shakesprere, Peter Kellman, Sanjeev G Shroff, David S Schwartzman, Suresh R Mulukutla, Marc A Simon, and Erik B Schelbert. Association between extracellular matrix expansion quantified by cardiovascular magnetic resonance and short-term mortality. *Circulation*, 126(10):1206–1216, September 2012.

[66] C G Brilla, R C Funck, and H Rupp. Lisinopril-mediated regression of myocardial fibrosis in patients with hypertensive heart disease. *Circulation*, 102(12):1388–1393, September 2000.

[67] Erica Dall'Armellina, Stefan K Piechnik, Vanessa M Ferreira, Quang Le Si, Matthew D Robson, Jane M Francis, Florim Cuculi, Rajesh K Kharbanda, Adrian P Banning, Robin P Choudhury, Theodoros D Karamitsos, and Stefan Neubauer. Cardiovascular magnetic resonance by non contrast T1 mapping allows assessment of severity of injury in acute myocardial infarction. *Journal of cardiovascular magnetic resonance : official journal of the Society for Cardiovascular Magnetic Resonance*, 14(1):15, February 2012.

[68] Kelvin Chow, Jacqueline A Flewitt, Jordin D Green, Matthias G Friedrich, and Richard B Thompson. Characterization of myocardial T1 and partition coefficient as a function of time after gadolinium delivery in healthy subjects. *Journal of cardiovascular magnetic resonance : official journal of the Society for Cardiovascular Magnetic Resonance*, 13(Suppl 1):P31, 2011.

[69] Daniel R Messroghli, Sven Plein, David M Higgins, Kevin Walters, Timothy R Jones, John P Ridgway, and Mohan U Sivananthan. Human myocardium: single-breath-hold MR T1 mapping with high spatial resolution–reproducibility study. *Radiology*, 238(3):1004–1012, March 2006.

[70] R Deichmann, D Hahn, and Axel Haase. Fast T1 mapping on a whole-body scanner. *Magnetic Resonance in Medicine*, 42(1):206–209, July 1999.

[71] M Karlsson and B Nordell. Analysis of the Look-Locker T(1) mapping sequence in dynamic contrast uptake studies: simulation and in vivo validation. *Magnetic resonance imaging*, 18(8):947–954, October 2000.

[72] Neville D Gai, Evrim B Turkbey, Saman Nazarian, Rob J van der Geest, Chia-Ying Liu, João A C Lima, and David A Bluemke. T1 mapping of the gadolinium-enhanced myocardium: adjustment for factors affecting interpatient comparison. *Magnetic Resonance in Medicine*, 65(5):1407–1415, May 2011.

[73] Patrick Sparrow, Daniel R Messroghli, Scott Reid, John P Ridgway, Gavin Bainbridge, and Mohan U Sivananthan. Myocardial T1 mapping for detection of left ventricular myocardial fibrosis in chronic aortic regurgitation: pilot study. *AJR American journal of roentgenology*, 187(6):W630–5, December 2006.

[74] Ting Song, Jeffrey A Stainsby, Vincent B Ho, Maureen N Hood, and Glenn S Slavin. Flexible cardiac T(1) mapping using a modified look-locker acquisition with saturation recovery. *Magnetic Resonance in Medicine*, 67(3):622–627, March 2012.

[75] C M Wacker, M Bock, A W Hartlep, G Beck, G van Kaick, G Ertl, W R Bauer, and L R Schad. Changes in myocardial oxygenation and perfusion under pharmacological stress with dipyridamole: assessment using T*2 and T1 measurements. *Magnetic Resonance in Medicine*, 41(4):686–695, April 1999.

[76] David M Higgins, John P Ridgway, Aleksandra Radjenovic, U Mohan Sivananthan, and Michael A Smith. T1 measurement using a short acquisition period for quantitative cardiac applications. *Medical physics*, 32(6):1738–1746, May 2005.

[77] Mariell Jessup and Susan Brozena. Heart failure. *The New England journal of medicine*, 348(20):2007–2018, May 2003.

[78] D L Mann. Mechanisms and models in heart failure: A combinatorial approach. *Circulation*, 100(9):999–1008, August 1999.

[79] Donald Marquardt. An Algorithm for Least-Squares Estimation of Nonlinear Parameters. *Journal of the Society for Industrial and Applied Mathematics*, 11(2):431–441, June 1963.

[80] Warren D Foltz, Osama Al-Kwifi, Marshall S Sussman, Jeffrey A Stainsby, and Graham A Wright. Optimized spiral imaging for measurement of myocardial T2 relaxation. *Magnetic Resonance in Medicine*, 49(6):1089–1097, June 2003.

[81] K A Kraft, P P Fatouros, G D Clarke, and P R Kishore. An MRI phantom material for quantitative relaxometry. *Magnetic Resonance in Medicine*, 5(6):555–562, December 1987.

[82] Stefan Klein, Marius Staring, Keelin Murphy, Max A Viergever, and Josien P W Pluim. elastix: a toolbox for intensity-based medical image registration. *IEEE transactions on medical imaging*, 29(1):196–205, 2010.

[83] Manuel D Cerqueira, Neil J Weissman, Vasken Dilsizian, Alice K Jacobs, Sanjiv Kaul, Warren K Laskey, Dudley J Pennell, John A Rumberger, Thomas Ryan, Mario S Verani, American Heart Association Writing Group on Myocardial Segmentation, and Registration for Cardiac Imaging. Standardized myocardial segmentation and nomenclature for tomographic imaging of the heart: a statement for healthcare professionals from the Cardiac Imaging Committee of the Council on Clinical Cardiology of the American Heart Association. *Circulation*, 105(4):539–542, January 2002.

[84] Y Zur, S Stokar, and P Bendel. An analysis of fast imaging sequences with steady-state transverse magnetization refocusing. *Magnetic Resonance in Medicine*, 6(2):175–193, February 1988.

[85] P A Janick, D B Hackney, R I Grossman, and T Asakura. MR imaging of various oxidation states of intracellular and extracellular hemoglobin. *AJNR American journal of neuroradiology*, 12(5):891–897, 1991.

[86] Hanzhang Lu, Chekesha Clingman, Xavier Golay, and Peter C M van Zijl. Determining the longitudinal relaxation time (T1) of blood at 3.0 Tesla. *Magnetic Resonance in Medicine*, 52(3):679–682, September 2004.

[87] Nadine Kawel, Marcelo Nacif, Anna Zavodni, Jacquin Jones, Songtao Liu, Christopher Sibley, and David Bluemke. T1 mapping of the myocardium: intra-individual assessment of post-contrast T1 time evolution and extracellular volume fraction at 3T for Gd-DTPA and Gd-BOPTA. *Journal of cardiovascular magnetic resonance : official journal of the Society for Cardiovascular Magnetic Resonance*, 14(1):26, 2012.

[88] Puneet Sharma, Josh Socolow, Salil Patel, Roderic I Pettigrew, and John N Oshinski. Effect of Gd-DTPA-BMA on blood and myocardial T1 at 1.5T and 3T in humans. *Journal of magnetic resonance imaging : JMRI*, 23(3):323–330, March 2006.

[89] Nadine Kawel, Marcelo Nacif, Anna Zavodni, Jacquin Jones, Songtao Liu, Christopher Sibley, and David Bluemke. T1 mapping of the myocardium: Intra-individual

assessment of the effect of field strength, cardiac cycle and variation by myocardial region. *Journal of cardiovascular magnetic resonance : official journal of the Society for Cardiovascular Magnetic Resonance*, 14(1):27, 2012.

[90] Nadine Kawel, Marcelo Nacif, Francesco Santini, Songtao Liu, Jens Bremerich, Andrew E Arai, and David A Bluemke. Partition coefficients for gadolinium chelates in the normal myocardium: Comparison of gadopentetate dimeglumine and gadobenate dimeglumine. *Journal of magnetic resonance imaging : JMRI*, 36(3):733–737, September 2012.

[91] Peter Kellman, Anthony H Aletras, Christine Mancini, Elliot R McVeigh, and Andrew E Arai. T2-prepared SSFP improves diagnostic confidence in edema imaging in acute myocardial infarction compared to turbo spin echo. *Magnetic Resonance in Medicine*, 57(5):891–897, May 2007.

[92] Daniel Kim, Oded Gonen, Niels Oesingmann, and Leon Axel. Comparison of the effectiveness of saturation pulses in the heart at 3T. *Magnetic Resonance in Medicine*, 59(1):209–215, 2008.

[93] Scott B Reeder, A Z Faranesh, J L Boxerman, and E R McVeigh. In vivo measurement of T*2 and field inhomogeneity maps in the human heart at 1.5 T. *Magnetic Resonance in Medicine*, 39(6):988–998, June 1998.

[94] R Noeske, F Seifert, K H Rhein, and H Rinneberg. Human cardiac imaging at 3 T using phased array coils. *Magnetic Resonance in Medicine*, 44(6):978–982, December 2000.

[95] Klaus Scheffler. On the transient phase of balanced SSFP sequences. *Magnetic Resonance in Medicine*, 49(4):781–783, April 2003.

[96] J P Felmlee and R L Ehman. Spatial presaturation: a method for suppressing flow artifacts and improving depiction of vascular anatomy in MR imaging. *Radiology*, 164(2):559–564, August 1987.

[97] N V Tsekos, Y Zhang, H Merkle, N Wilke, Michael Jerosch-Herold, A Stillman, and K Uğurbil. Fast anatomical imaging of the heart and assessment of myocardial perfusion with arrhythmia insensitive magnetization preparation. *Magnetic Resonance in Medicine*, 34(4):530–536, October 1995.

[98] Kelvin Chow, Jacqueline A Flewitt, Jordin D Green, Joseph J Pagano, Matthias G Friedrich, and Richard B Thompson. Saturation recovery single-shot acquisition

(SASHA) for myocardial T1 mapping. *Magnetic Resonance in Medicine*, 71(6):2082–2095, 2014.

[99] Charles H Cunningham, John M Pauly, and Krishna S Nayak. Saturated double-angle method for rapid B1+ mapping. *Magnetic Resonance in Medicine*, 55(6):1326–1333, June 2006.

[100] H Ding, Xu D, M M Zviman, V Sena-Weltin, L Amado, Saman Nazarian, Henry R Halperin, E R McVeigh, and D A Herzka. High Spatial Resolution Free Breathing 3D T2 Mapping for Edema Detection in Radio Frequency Ablation. *Proceedings of the International Society for Magnetic Resonance in Medicine*, 19:23, 2011.

[101] R J Ogg, P B Kingsley, and J S Taylor. WET, a T1- and B1-insensitive water-suppression method for in vivo localized 1H NMR spectroscopy. *Journal of magnetic resonance Series B*, 104(1):1–10, May 1994.

[102] Yuehui Tao, Aaron T Hess, Graeme A Keith, Christopher T Rodgers, Alexander Liu, Jane M Francis, Stefan Neubauer, and Matthew D Robson. Optimized saturation pulse train for human first-pass myocardial perfusion imaging at 7T. *Magnetic Resonance in Medicine*, pages n/a–n/a, April 2014.

[103] N Oesingmann, Q Zhang, and O Simonetti. Improved saturation RF pulse design for myocardial first-pass perfusion at 3T. *Journal of cardiovascular magnetic resonance : official journal of the Society for Cardiovascular Magnetic Resonance*, 6:373–374, 2004.

[104] Kyunghyun Sung and Krishna S Nayak. Design and use of tailored hard-pulse trains for uniformed saturation of myocardium at 3 Tesla. *Magnetic Resonance in Medicine*, 60(4):997–1002, October 2008.

[105] R S Staewen, A J Johnson, B D Ross, T Parrish, H Merkle, and Michael Garwood. 3-D FLASH imaging using a single surface coil and a new adiabatic pulse, BIR-4. *Investigative radiology*, 25(5):559–567, May 1990.

[106] Daniel Kim, Niels Oesingmann, and Kellyanne McGorty. Hybrid adiabatic-rectangular pulse train for effective saturation of magnetization within the whole heart at 3 T. *Magnetic Resonance in Medicine*, 62(6):1368–1378, December 2009.

[107] J A Nelder and R Mead. A Simplex Method for Function Minimization. *The Computer Journal*, 7(4):308–313, January 1965.

[108] Kyunghyun Sung and Krishna S Nayak. Measurement and characterization of RF nonuniformity over the heart at 3T using body coil transmission. *Journal of magnetic resonance imaging : JMRI*, 27(3):643–648, March 2008.

[109] Michael Garwood and Y Ke. Symmetric pulses to induce arbitrary flip angles with compensation for rf inhomogeneity and resonance offsets. *Journal of Magnetic Resonance*, 1991.

[110] Jinghua Wang, Weihua Mao, Maolin Qiu, Michael B Smith, and R Todd Constable. Factors influencing flip angle mapping in MRI: RF pulse shape, slice-select gradients, off-resonance excitation, and B0 inhomogeneities. *Magnetic Resonance in Medicine*, 56(2):463–468, August 2006.

[111] John D'Errico. Surface Fitting using gridfit, November 2005.

[112] Kelvin Chow, Bruce Spottiswoode, Joseph J Pagano, and Richard Thompson. Improved precision in SASHA T1 mapping with a variable flip angle readout. *Journal of cardiovascular magnetic resonance : official journal of the Society for Cardiovascular Magnetic Resonance*, 16(Suppl 1):M9, 2014.

[113] Kelvin Chow, Jacqueline A Flewitt, Joseph J Pagano, Jordin D Green, Matthias G Friedrich, and Richard B Thompson. T2-dependent errors in MOLLI T1 values: simulations, phantoms, and in-vivo studies. *Journal of cardiovascular magnetic resonance : official journal of the Society for Cardiovascular Magnetic Resonance*, 14(Suppl 1):P281, 2012.

[114] J P Mugler, F H Epstein, and J R Brookeman. Shaping the signal response during the approach to steady state in three-dimensional magnetization-prepared rapid gradient-echo imaging using variable flip angles. *Magnetic Resonance in Medicine*, 28(2):165–185, December 1992.

[115] L Zhao, R Mulkern, C H Tseng, D Williamson, S Patz, R Kraft, R L Walsworth, F A Jolesz, and M S Albert. Gradient-echo imaging considerations for hyperpolarized 129Xe MR. *Journal of magnetic resonance Series B*, 113:179–183, 1996.

[116] Pauline W Worters and Brian A Hargreaves. Balanced SSFP transient imaging using variable flip angles for a predefined signal profile. *Magnetic Resonance in Medicine*, 64(5):1404–1412, November 2010.

[117] Martin H Deppe and Jim M Wild. Variable flip angle schedules in bSSFP imaging of hyperpolarized noble gases. *Magnetic Resonance in Medicine*, 67(6):1656–1664, June 2012.

[118] Dominik Paul, Michael Markl, Hans-Peter Fautz, and Jürgen Hennig. T2-weighted balanced SSFP imaging (T2-TIDE) using variable flip angles. *Magnetic Resonance in Medicine*, 56(1):82–93, July 2006.

[119] Mark A Griswold, Peter M Jakob, Robin M Heidemann, Mathias Nittka, Vladimir Jellus, Jianmin Wang, Berthold Kiefer, and Axel Haase. Generalized autocalibrating partially parallel acquisitions (GRAPPA). *Magnetic Resonance in Medicine*, 47(6):1202–1210, June 2002.

[120] Hui Xue, Saurabh Shah, Andreas Greiser, Christoph Guetter, Arne Littmann, Marie-Pierre Jolly, Andrew E Arai, Sven Zuehlsdorff, Jens Guehring, and Peter Kellman. Motion correction for myocardial T1 mapping using image registration with synthetic image estimation. *Magnetic Resonance in Medicine*, 67(6):1644–1655, June 2012.

[121] Sébastien Roujol, Sebastian Weingärtner, Murilo Foppa, Kelvin Chow, Keigo Kawaji, Long H Ngo, Peter Kellman, Warren J Manning, Richard B Thompson, and Reza Nezafat. Accuracy, Precision, and Reproducibility of Four T1 Mapping Sequences: A Head-to-Head Comparison of MOLLI, ShMOLLI, SASHA, and SAPPHIRE. *Radiology*, 272(3):683–689, April 2014.

[122] Toby Rogers, Darius Dabir, Islam Mahmoud, Tobias Voigt, Tobias schaeffter, Eike Nagel, and Valentina O Puntmann. Standardization of T1 measurements with MOLLI in differentiation between health and disease – the ConSept study. *Journal of cardiovascular magnetic resonance : official journal of the Society for Cardiovascular Magnetic Resonance*, 15(1):78, September 2013.

[123] Maciej W Garbowski, John-Paul Carpenter, Gillian Smith, Michael Roughton, Mohammed H Alam, Taigang He, Dudley J Pennell, and John B Porter. Biopsy-based calibration of T2* magnetic resonance for estimation of liver iron concentration and comparison with R2 Ferriscan. *Journal of cardiovascular magnetic resonance : official journal of the Society for Cardiovascular Magnetic Resonance*, 16(1):40, June 2014.

[124] Fabio S Raman, Nadine Kawel-Boehm, Neville D Gai, Melanie Freed, Jing Han, Chia Ying Liu, João A C Lima, David A Bluemke, and Songtao Liu. Modified look-locker inversion recovery T1 mapping indices: assessment of accuracy and reproducibility between magnetic resonance scanners. *Journal of cardiovascular magnetic*

resonance : official journal of the Society for Cardiovascular Magnetic Resonance, 15:64, 2013.

[125] Stefan K Piechnik, Vanessa M Ferreira, Adam J Lewandowski, Ntobeko Ab Ntusi, Rajarshi Banerjee, Cameron Holloway, Mark Bm Hofman, Daniel M Sado, Viviana Maestrini, Steven White, Merzaka Lazdam, Theodoros D Karamitsos, James Charles Moon, Stefan Neubauer, Paul Leeson, and Matthew D Robson. Normal variation of magnetic resonance T1 relaxation times in the human population at 1.5T using ShMOLLI. *Journal of cardiovascular magnetic resonance : official journal of the Society for Cardiovascular Magnetic Resonance*, 15(1):13, January 2013.

[126] Daniel M Sado, Viviana Maestrini, Stefan K Piechnik, Sanjay M Banypersad, Steven K White, Andrew S Flett, Matthew D Robson, Stefan Neubauer, Cono Ariti, Andrew Arai, Peter Kellman, Jin Yamamura, Bjoern P Schoennagel, Farrukh Shah, Bernard Davis, Sara Trompeter, Malcolm Walker, John Porter, and James Charles Moon. Non-contrast myocardial T1mapping using cardiovascular magnetic resonance for iron overload. *Journal of magnetic resonance imaging : JMRI*, pages n/a–n/a, August 2014.

[127] Clifford R Weiss, Anthony H Aletras, James F London, Joni L Taylor, Frederick H Epstein, Ralf Wassmuth, Robert S Balaban, and Andrew E Arai. Stunned, Infarcted, and Normal Myocardium in Dogs: Simultaneous Differentiation by Using Gadolinium-enhanced Cine MR Imaging with Magnetization Transfer Contrast. *Radiology*, 226(3):723–730, 2003.

[128] Daniel R Messroghli, Sarah Nordmeyer, Thore Dietrich, Olaf Dirsch, Elena Kaschina, Kostas Savvatis, Darach O H-Ici, Christoph Klein, Felix Berger, and Titus Kuehne. Assessment of diffuse myocardial fibrosis in rats using small-animal look-locker inversion recovery t1 mapping. *Circulation: Cardiovascular Imaging*, 4(6):636–640, November 2011.

[129] Michael Lustig, David Donoho, and John M Pauly. Sparse MRI: The application of compressed sensing for rapid MR imaging. *Magnetic Resonance in Medicine*, 58(6):1182–1195, November 2007.

[130] Tobias Voigt, Tobias schaeffter, Rene Botnar, Jouke Smink, and Markus Henningsson. Three-Dimensional MOLLI For Myocardial T1 Mapping Using Respiratory Navigation and Inversion Time Gating. *Proceedings of the International Society for Magnetic Resonance in Medicine*, 21:258, 2013.

[131] Bhairav B Mehta, Xiao Chen, Kenneth C Bilchick, Michael Salerno, and Frederick H Epstein. Accelerated and navigator-gated look-locker imaging for cardiac t1 estimation (ANGIE): Development and application to T1 mapping of the right ventricle. *Magnetic Resonance in Medicine*, February 2014.

[132] K P Pruessmann, M Weiger, M B Scheidegger, and Peter Boesiger. SENSE: sensitivity encoding for fast MRI. *Magnetic Resonance in Medicine*, 42(5):952–962, November 1999.

[133] Mariya Doneva, Peter Börnert, Holger Eggers, Christian Stehning, Julien Sénégas, and Alfred Mertins. Compressed sensing reconstruction for magnetic resonance parameter mapping. *Magnetic Resonance in Medicine*, 64(4):1114–1120, October 2010.

[134] Julia V Velikina, Andrew L Alexander, and Alexey Samsonov. Accelerating MR parameter mapping using sparsity-promoting regularization in parametric dimension. *Magnetic Resonance in Medicine*, 70(5):1263–1273, 2013.